Diagnostic Study of Steady State Advanced Fuel (D-D and D-3He) Fusion in an IEC Device

Krupakar Murali Subramanian

December 2004

UWFDM-1267

Ph.D. thesis.

FUSION TECHNOLOGY INSTITUTE

UNIVERSITY OF WISCONSIN

MADISON WISCONSIN

Diagnostic Study of Steady State Advanced Fuel (D-D and D-3He) Fusion in an IEC Device

Krupakar Murali Subramanian

Fusion Technology Institute
University of Wisconsin
1500 Engineering Drive
Madison, WI 53706

http://fti.neep.wisc.edu

December 2004

UWFDM-1267

Ph.D. thesis.

DIAGNOSTIC STUDY OF STEADY STATE ADVANCED FUEL (D-D AND D-^{3}He) FUSION IN AN IEC DEVICE

by

Krupakar Murali Subramanian

A dissertation submitted in partial fulfillment of the
requirements for the degree of

Doctor of Philosophy

(Physics)

at the

UNIVERSITY OF WISCONSIN, MADISON

2004

University of Wisconsin, Madison

DIAGNOSTIC STUDY OF STEADY STATE ADVANCED FUEL (DD AND D-^{3}He) FUSION IN AN IEC DEVICE

By Krupakar Murali Subramanian

Co-Chairs of the Supervisory Committee: Professor Stewart Prager
(Department of Physics) and
Professor Gerald L. Kulcinski
(Department of Nuclear Engineering
& Engineering Physics)

Abstract

The ionized fusion fuels (D-D & D-^{3}He) have been accelerated to fusion velocities using two concentric grids maintained at a high potential difference in an Inertial Electrostatic Confinement (IEC) device. Though the gridded IEC device currently has a low efficiency ($Q \equiv$ fusion power/input power $\sim 10^{-5}$), the energetic protons and neutrons generated within this device can be used for many near-term applications, such as medical isotope production, landmine detection, neutron activation analysis, etc. The present work is centered upon understanding the operation of the device and finding new ways to increase the overall efficiency.

The steady state fusion of D-^{3}He fuel in an IEC device was successfully studied. At a pressure of ~2 mtorr the source of such reactions was identified to be principally beam-target reactions and was theoretically explained using the Monte Carlo – Stopping and Range of Ions in Matter (SRIM) code. The first simultaneous measurement of DD and D-^{3}He protons was accomplished during the present thesis work that confirmed that D-^{3}He fusion reactions indeed occur in an IEC device. A new pressure independent diagnostic was invented to measure the average ion energy. That diagnostic uses the D-D proton energy spectra from a single loop cathode grid and the SRIM code predictions. A second diagnostic called the eclipse disc was co-invented to characterize the various fusion regimes in an IEC device. This diagnostic verified

that a converged core fusion source exists for the DD reactions but the D-^{3}He reactions that are principally embedded source reactions. A third diagnostic called the chordwire was invented to study the effects of various sources of electrons – thermionic, photo and field emission electrons, that decrease the efficiency of the device. This diagnostic also helped map the ion flux into the cathode in 2D, besides helping identify the high performance grid materials (W-25%Re and pure Re). Understanding the electron current contributions helped correct previous recirculation ion current equation in the literature. Sequential grid construction experiments where a new loop was added in a sequence (in various orientations) while monitoring the performance of the grid showed fusion rate saturation of the fusion rate with just a 3 loop grid. Hence, further increases in symmetry of the grid are deemed unnecessary. It was also found that the fusion occurred mostly in the microchannels that form in the regions where the cathode field is a minimum (i.e., in the open areas between the wires). This is an important conclusion because all earlier work had assumed a uniform spherical volume source of incoming ions and this work suggests otherwise. A new method of calibration was derived using the non-uniform volume source that takes into account the surface area of the detector visible to the protons that are born anywhere within the IEC chamber.

As a consequence of the above research and valuable input from others in the IEC group, at UW Madison, there has been an increase in D-^{3}He rate by 5 orders of magnitude, in a span of 4 yrs, while those of the D-D reaction rate increased by 3 orders of magnitude.

Approval:

_____	_____
Professor Stewart Prager	Professor Gerald L. Kulcinski

Dedication

I dedicate this dissertation work to my motherland INDIA and United States of America. Former taught me ethics, discipline, family values and persistence while the latter gave me the opportunity and research experience.

ACKNOWLEDGMENTS

I feel indebted and wishes to express sincere thanks to my thesis advisor Prof. Gerald L. Kulcinski for his support and guidance in every step of the way that lead to the successful completion of this dissertation work. His organization skills, together with the knowledge in nuclear engineering inspired me in every possible way.

If there were one person without whose help I would not have completed this dissertation work on time, it is Prof. John Santarius. I would like to thank him heartily for all his help, discussions and timely feedback.

I would also like to thank Prof. Stewart Prager from Department of Physics for having readily agreed to be my acting advisor. His feedback on preparing the thesis report is gratefully acknowledged.

Prof. Noah Hershkowitz is a one of a kind professor from whom the author learnt ways to address various problems in plasma physics in a systematic manner. He played a crucial role in setting my research targets for my dissertation work. His help is gratefully acknowledged.

I would also like to express thanks to Mr. Bob Ashley, for all his help in the lab. His experience is something that I always counted on. The help from my colleagues Ross Radel, Ben Cipiti, Greg Piefer, John Weidner, Dave Boris, Alex Wehmeyer and Tracy Uchytil is gratefully acknowledged. I had enjoyed their company to the fullest, be it a conference trip or just running the experiment in the lab, the experiences were all memorable. The author would like to thank every one of them for their help and feedback during research meetings and informal discussions.

On the administrative side Sue Ann Hubanks, Linda Kraft, and Joan LePain have made all the research related transactions an easy process. Dennis Bruggink had been helpful in retrieving some of the lost files, scanning information and fixing computer related problems. I would like to express my gratitude to each and every one of them.

I feel honored to have Prof. Paul Terry and Prof. Carry Forest on my dissertation committee. Their feedback on the dissertation work is gratefully acknowledged and appreciated. Discussions with Prof. G. A. Emmert were both insightful and helpful, I wish to express my thanks to him.

I would also like to express my deep sense of gratitude to University of Wisconsin, Madison, for its hospitality towards international students and the best education possible in plasma physics. I express my sincere thanks from the bottom of my heart to the Grainger Foundation and the Greatbatch Foundation for having supported the research and providing the much needed funds to carry out the present research.

My parents always provided the support and motivation needed for successful completion of this dissertation to me, I couldn't have done it without them. My sister, brother in law and two little nieces were all very helpful and supportive during my entire dissertation work, I simply cannot thank them enough. I would also like to express gratitude to my in-laws for being very supportive and encouraging in difficult times.

Finally, I would like to thank my wife and our little son (8 months old at the time of completion of this dissertation) for all the help, support, and encouragement they have showered on me during my dissertation work, most importantly for being patient and understanding with me at all times.

TABLE OF CONTENTS

Table of Contents ***Page***

Table of Figures

Page

Chapter 1

Chapter 2

Chapter 3

Chapter 4

Chapter 5

Chapter 7

Chapter 9

Chapter 10

Chapter 11

Chapter 12

Chapter 13

Table of Tables

Page

Chapter 4

Chapter 5

Chapter 7

Chapter 9

Chapter 10

Chapter 11

Chapter 12

Chapter 13

Appendix B

Chapter 1: Introduction

Fusion is attractive for being a potentially inexpensive, environmentally friendly, and practically unlimited power source. However, the central problem of creating useful controllable nuclear fusion reactions among ions is the necessity of confining a sufficient density of energetic ions at a sufficiently high temperature for an acceptable time. This would ensure that the reaction rate density between the ions is high enough to be useful for both power generation and to overcome radiative, collisional and other losses that may be associated with the particles' confinement at high energy.

Inertial Electrostatic Confinement (IEC) is an alternate confinement concept to Magnetic (Tokamaks, Stellarators, etc.) and Inertial (laser, heavy and light ions) fusion. Because of the inherent difficulties in non-electric inertial and magnetic means for confining ions (for near term applications), researchers at the University of Wisconsin, Madison and a few other groups around the world have pursued the IEC concept. A more direct means of providing energy to fusion fuels and achieving high density is available through use of electric fields for ion acceleration and spherically convergent geometries for their densification by such motion.[1] In an IEC device with spherical geometry, a negative potential is maintained through a nearly transparent spherical cathode in the center of the device. Positive ions introduced at the outer edge of this system will "fall down" the radial electric field toward the center, gaining energy

and speed with nearly 100% efficiency in the process. This technique is very promising and appealing since it has immediate applications even at gain Q (ratio of output power to input power) << 1, besides a possibility of power production in the long run. An IEC device has many near-term applications such as isotope production for medical applications, oil well logging, diamond processing, Boron Neutron Capture Therapy (BNCT), tunable x-ray source, calibration source for tokamaks, land mine detection, etc. as shown in Figure1.1.

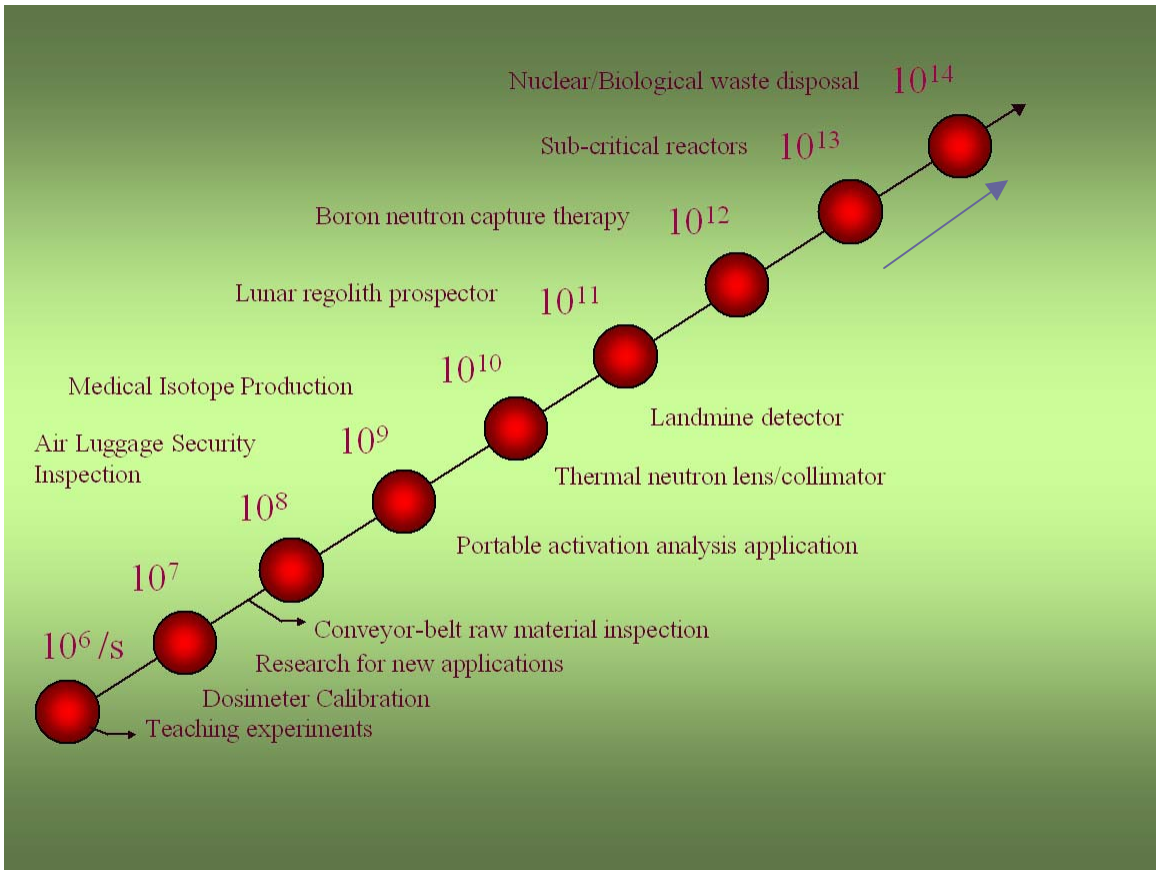

Figure 1.1 The number of applications of the IEC device increases with increasing (efficiency) fusion reaction rate (10^n s^{-1} where n = 6 to 14 is shown).

This kind of increasing applicability of a fusion device (figure 1.1) with increasing reactivity is very attractive and has many near term commercial applications.[2,3,4] It is noteworthy

that IEC is the first fusion confinement concept to be commercialized.[5] However, the efficiency of this fusion scheme cannot be increased without understanding this device and the various reaction mechanisms.

1.1 Motivation of Research

The purpose of this research has been to understand the underlying physics of operation of this device through experiments backed by appropriate computer simulations that have led to significant improvements in the IEC device's performance.

Fusion occurs everywhere inside an IEC device, however the relative distributions differ. A thorough understanding of such a distribution would pay off in the form of new applications and would also allow the researchers to conceive new ways to improve the efficiency of the device. The relative distribution of the fusion reactions within the IEC device is expected to depend on the chamber pressure and the fuel used. If experiments are directed to classify these reactions, not only would we be able to calibrate the device properly but also come up with new applications (Ben Cipiti used the results of such a study to increase the efficiency of the medical isotope production rate[6]). It would also be helpful to measure the average ion energy so that device optimization could be eventually accomplished.

To increase the efficiency of the device it is important to operate the device at higher voltage and hence new techniques need to be developed to handle high voltages in such compact devices. Operating the device at peak reaction cross-section would help increase the fusion reactivity significantly. For this purpose, it is important to be able to operate at higher input voltages and hence the components of the device should be able to withstand such feral environments. The cathode grid must be able to operate at higher temperatures, which would

allow much higher power operation of the device since the power radiated by the cathode increases as 4^{th} power of the temperature. Hence new materials are required to replace the old stainless-steel grids. This new material should also have minimum associated sputtering because the sputtered material tends to get deposited on the high voltage stalk and eventually causes surface breakdown thus limiting the operational capability of the device. Once this problem is fixed, the next problem to be addressed is the standoff capability of the high voltage stalk. In general this is accomplished by using high standoff material with appropriate dimensions.

Once the above-mentioned challenges are fixed we would then be limited by the physics of operation of the device. A thorough understanding of the ion flow dynamics into the cathode grid would be highly desirable. If the ion flux distribution into the cathode grid is known, one could invent new techniques to homogenize such a distribution to realize a higher fusion rate. For this purpose a systematic study of the effect of transparency is required. It would be helpful to determine if gargantuan efforts are required to increase the symmetry/transparency of the cathode grid, if not it would save both time and money.

The power supply is incapable of differentiating between an electron current (electrons leaving the grid) and an ion current (ions recombining and causing a electron loss on the surface of the cathode). It only measures the sum of the two currents and hence an inadvertent increase in one of the two currents would inevitably cause a decrease in the other. Unfortunately it is always the electron current that increases and hence the ion current is adversely affected, causing the overall fusion rate to decrease. A clear understanding of various electron current contributions would allow the researcher to fix such drains on the system eventually leading to a

higher efficiency of the device. Another factor that influences the fusion reactivity is the impurity concentration inside an IEC chamber.

Finally if there is any discrepancy in the uniform ion flux distribution assumption (around the cathode grid) it must be accommodated in the calculations of the calibration factor. A clear understanding of the fusion rate distribution would allow one to correlate theoretical predictions with experimental results, which have in general differed significantly. The fusion rate observed experimentally has always exceeded those predicted theoretically.[7,8]

1.2 References

[1] R. P.Ashley, G.L. Kulcinski, J. F. Santarius, S. Krupakar Murali, G. Piefer and R. Radel, "Steady-State D-^{3}He Proton Production in an IEC Fusion Device," Fusion Technology, **44**, 564 (2001).

[2] Kulcinski, G. L., "Near Term Commercial Opportunities from Long Range Fusion Research," Fusion Technology **30**, p. 411, 1996.

[3] G. L. Kulcinski, "Non-Electric Applications of Fusion Energy – An Important Precursor to Commercial Electric Power," Fusion Technology 34, 477 (1998).

[4] G. L. Kulcinski, and J.F. Santarius, " New Opportunities for Fusion in the 21st Century – Advanced fuels," Fusion Technology, Vol. 39, Mar. (2001).

[5] G. Miley, and J. Sved, "The IEC Star-Mode Fusion Neutron Source for NAA – Status and Next-Step Designs, Proceedings, IRRMA '99, Raleigh, NC, October 3-8 (1999)

[6] Ben Cipiti, PhD thesis, University of Wisconsin, Madison (2004).

[7] J. F. Santarius, University of Wisconsin-Madison, private communications (2002), see also "Modeling the UW IEC Experiment," presented at the 4th U.S. – Japan Workshop on Inertial Electrostatic Confinement, March 25-26, 2004, Kyoto, Japan.

[8] M. Ohnishi, Y. Yamamoto, M. Hasegawa, K. Yoshikawa and G. H. Miley, "Study on Inertial Electrostatic Confinement Fusion as a Portable Neutron Source," Fusion Engineering and Design, **42**, 207 (Sep. 1998).

Chapter 2.0: Brief History of the IEC Device

In 1963 O. A. Lavrentyev[1] in the USSR first published a paper on electrostatic confinement of fusion plasma. Though P. T. Farnsworth conceived a similar scheme independently in the USA for electrostatic fusion in the early 1950s, it was not made public until he received a patent in 1966.[2] Farnsworth conceived of using a gridded system to generate a spherically converged plasma target for fusion, thus avoiding the target deterioration. Solid targets deteriorate quickly due to high currents reaching the target, while a gridded system has a much higher recirculation current for the same grid current. R. L. Hirsch[3] further investigated this device using ion guns. Though initial efforts were directed towards power production, it was soon realized that gridded systems could not reach breakeven without melting the central grid and accompanying high (grid) erosion.

To handle the grid erosion and heating problem, Bussard[4] and Krall[5] proposed the use of a quasi-spherical magnetic field to replace the grid, thus creating a virtual cathode (Polywell®) by confining electrons. However, the Polywell® suffers potentially from electron loss through the cusp fields, and to improve the electron confinement properties a Penning-like trap was proposed[6] and investigated theoretically[7] and experimentally.[8,9,10]

Rider[11] and Nevins[12], theoretically analyzed the IEC systems and concluded that these devices could not reach breakeven due to the very large recirculation powers required to overcome the thermalizing effect of ion-ion collisions and sustain the non-Maxwellian ion profile in velocity space. However, these studies lack a self-consistent collisional treatment of the ion distribution function in velocity space, crucial for adequately estimating the fusion rate and the recirculating power.

A recent attempt to identify efficient regimes of operation of Penning IEC devices using a bounce-averaged Fokker-Planck (BAFP) model showed that breakeven is possible in these devices, although the fusion power densities are small.[13] The underlying problem is that for non-thermal systems the coulomb scattering cross-sections are larger than the fusion cross-sections. Thus, it can take more energy to maintain the non-thermal distributions than the device produces in fusion power. However, this problem is avoided if the plasma is in local thermodynamic equilibrium (LTE).

Theoretical work by Barnes and Nebel[14,15] has suggested that a tiny oscillating ion cloud may undergo a self-similar collapse in a harmonic oscillator potential formed by a uniform electron background. A remarkable feature of these oscillations is that the plasma remains in LTE at all times.[14,16] By tuning the external radio-frequency (rf) electric fields to this naturally occurring mode, it is then possible to heat the ions to obtain very high densities and temperatures simultaneously during the collapse phase of the oscillation through adiabatic compression. Theoretical projections indicate that such a scheme is highly effective and may result in net fusion energy gain even for fuels such as D-D.[17]

A major uncertainty in this oscillating plasma scheme is the dynamics and stability of the background electrons in the virtual cathode. It has been shown that the oscillating ion

cloud (referred to as the Periodically Oscillating Plasma Sphere or POPS) is stable to multi-dimensional perturbations.[14] On the other hand, recent work based on the electron fluid equations has demonstrated that the required electron cloud for POPS is susceptible to an instability that is analogous to the Raleigh-Taylor mode present in fluid mechanics.[18] Fortunately, solutions of the marginal stability profiles indicate that stable electron density profiles that are sufficiently close to those required for POPS do exist as one approaches the Brillouin Limit as well as in the limit of large Debye length to plasma radius (λ_D/a). In the kinetic limit, a simple two-stream analysis suggests that the mode may be absolutely stable at a finite value of $\lambda_D/a \sim 1$.

In conclusion, many interesting electrostatic confinement concepts are now being envisaged. Although, the gridless devices aim for high gain (Q) fusion, the gridded IEC devices are still useful at low Q, and hence these gridded systems are still maintaining the interest of various researchers.

The gridded Inertial Electrostatic Confinement (IEC) device does not require magnetic coils for plasma confinement, allowing it to be lightweight and hence portable, although radiation shields will sometimes be needed. The gridded IEC device has many near term applications even without reaching breakeven ($Q << 1$)[19,20] such as neutron activation analysis,[21,22,23] tunable X-ray source,[24] Ion propulsion,[25] radioisotope production,[26] oil well logging,[27] and nondestructive evaluation.[28] The IEC device also has other projected applications at high Q, such as neutron sources for fusion materials testing, tritium production,[29] subcritical reactors,[30] nuclear and chemical/biological waste management,[31] space propulsion[32] etc.

Because IEC fusion devices are not restricted to D-T fusion, there is also much less of a problem of neutron activation. A key feature of the gridded IEC device is that the steady state burning of advanced fuels[33] (that operate on neutron lean reactions) such as D-^{3}He and potentially ^{3}He-^{3}He and p-^{11}B, is possible. The various fusion reactions (1st and 2nd generation fuels) currently realized in the UW and other IEC devices are shown in Figure 2.1. Future work towards the realization of 3rd generation fuel fusion, Figure 2.2, is under way. It is also important to note that the number of applications of this device increases with the reaction rate. In order to increase the fusion productivity a clear understanding of the physics of operation of the device is required.

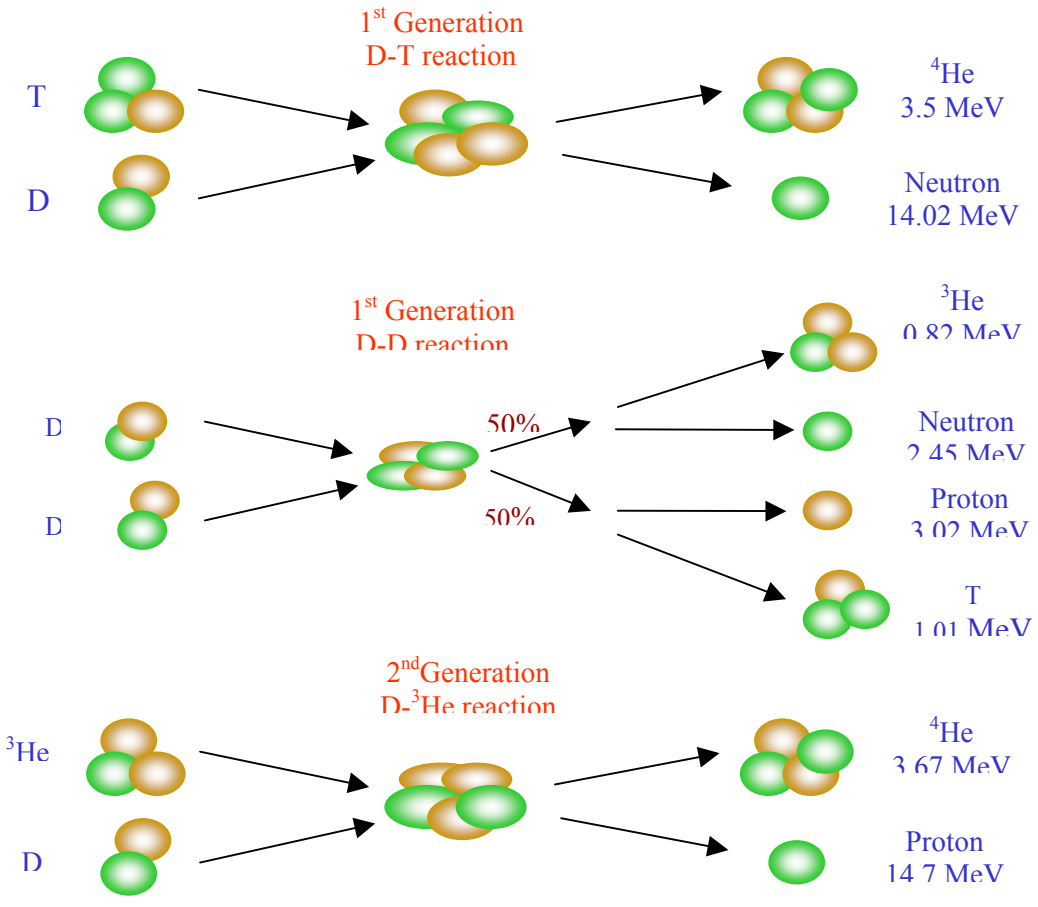

Figure 2.1 Steady-state fusion reactions achieved in an IEC device

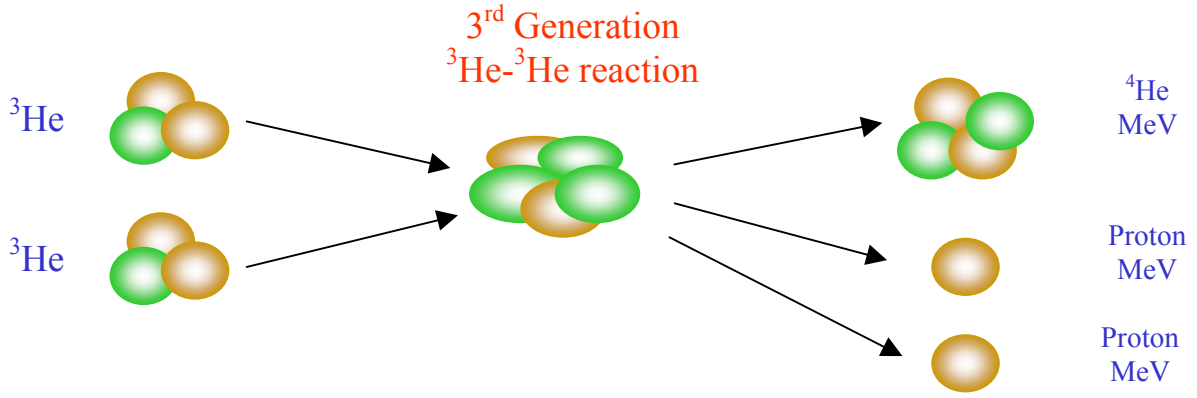

Figure 2.2 The 3rd generation ^3He – ^3He fuel is difficult to attain because much higher cathode voltages (~400 kV) are required to realize this reaction.

2.1 References

[1] O. A. Lavrent'ev, Uk. Fiz. Zh. 8, 440 (1963).

[2] P. Farnsworth, "Electric discharge device for producing interactions between nuclei," U.S. Patent 3,258,402, June 28, 1966.

[3] R. Hirsch, J. Appl. Phys., vol. 38, p. 4522, 1967

[4] R. W. Bussard, Fusion Technol. 19, 273 (1991).

[5] N. A. Krall, Fusion Technol. 22, 42 (1992).

[6] D. C. Barnes, T. B. Mitchell, and M. M. Schauer, Phys. Plasmas 4, 1745 (1997).

[7] D. C. Barnes, Phys. Plasmas 6, 4472 (1999).

[8] T. B. Mitchell, M. M. Schauer, and D. C. Barnes, Phys. Rev. Lett. 78, 58 (1997).

[9] M. M. Schauer, T. B. Mitchell, M. H. Holtzscheiter, and D. C. Barnes, Rev. Sci. Instrum. 68, 3340 (1997).

[10] D. C. Barnes, M. M. Schauer, K. R. Umstadter et al., Phys. Plasmas 7, 1693 (2000).

[11] T. H. Rider, Phys. Plasmas 2, 1853 (1995).

[12] W. M. Nevins, Phys. Plasmas **2**, 3804 (1995).

[13] L. Chacon, G. H. Miley, D. C. Barnes and D. A. Knoll, "Energy gain calculations in Penning fusion systems using a bounce-averaged Fokker-Planck model," Phys. Plasmas, Vol. 7, No. 11:4547- 4560 (2000).

[14] D. C. Barnes, and R. A. Nebel, Phys. Plasmas **5**, 2498 (1998).

[15] R. A. Nebel and D. C. Barnes, Fusion Technology **38**, 28 (1998).

[16] R. A. Nebel, and J. M. Finn, Phys. Plasmas **7**, 839 (2000).

[17] R. A. Nebel and D. C. Barnes, Fusion Technology **38**, 28 (1998).

[18] R. A. Nebel, and J. M. Finn, Phys. Plasmas 8, 1505 (2001).

[19] G. L. Kulcinski, "Near Term Commercial Opportunities from Long Range Fusion Research," Fusion Technology **30**, p. 411, 1996.

[20] G. L. Kulcinski, "Non-Electric Applications of Fusion Energy – An Important Precursor to Commercial Electric Power," Fusion Technology **34**, **Part 2**, p. 477, 1998.

[21] G. L. Kulcinski et al., "Overview of Neutron/Proton Source Applications from IEC Fusion Devices," Trans. Of the ANS, **77**, 507, 1997.

[22] G. H. Miley, Y. Gu, M. Ohnisi, Y. Yamamoto, M. Hasegawa, and K. Yoshikawa, "Potential Well Structure and Scaling Studies for the IEC," International Sherwood Fusion Theory Confernce, Madison, WI, April 23-26, 1997.

[23] A. J. Caffrey, J.D. Cole, R.J. Gehrke and R.C. Greenwood, "Chemical warfare agent and high explosive identification by spectroscopy of neutron-induced gamma rays," IEEE Trans. On Nucl. Sci., Vol. 39, pp 1422-1426, 1992.

[24] Y. Gu, and G. H. Miley, "Spherical IEC Device as a Tunable X-ray Source," Bulletin APS, **11**, 185.

[25] G. H. Miley, B. Bromley, B. Jurczyk, and Y. Gu, (1997) "Progress in IEC Research for near-Term Thrusters and Future Fusion Propulsion," NASA JPL Space Propulsion Research Workshop, Pasadena, CA, May 20-22.

[26] G. L. Kulcinski and J. F. Santarius, "New Opportunities for Fusion in the 21st Century – Advanced fuels," Fusion Tech. Vol. 39, Mar. 2001.

[27] R. E. Chrien, "Practical uses of neutron capture gamma-ray spectroscopy," Ch. 7 in Neutron Radiative Capture, R.E. Chrien, ed. Pergamon Press, Oxford, 1984.

[28] R. A. Anderl, J. K. Hartwell, J. H. Nadler, "Development of an IEC neutron source for NDE," Proc. 16th IEEE/NPSS Symp. Fusion Eng. G. H. Miley and C. M. Elliott. Eds. Piseataway, NJ: IEEE 1996, PP. 1486-1489.

[29] W. M. Stacey, et al., "A Tokamak Tritium Production Reactor," Fusion Tech. **32**, 563, 1997.

[30] G. H. Miley, T. H. Bauer, H. Hora, J. Nadler,"Converging beam neutron source for driving a sub-critical fission reactor," Proc. Of ICONE 8, 8th Intern. Conf. On Nuclear Engineering, April 2-6, 2000, Baltimore, MD, USA.

[31] W. Gough and B. Eastland, "Near Term Recycling Option Using Fusion Grade Plasmas," IECNES 91, Trans. Of Fusion Technology, **20**, Part 2 (1991).

[32] S. Krupakar Murali, "Inertial Electrostatic Confinement Reactor Based Fusion Ash Impact Propulsion System" ANS Transactions 2002, June 9-13, Hollywood, Florida.

[33] Kulcinski, G. L. and Santarius J. F., "New Opportunities for Fusion in the 21st Century – Advanced Fuels," Fusion Technology, Vol. 39, 480 – 485, Mar. 2001.

Chapter 3.0: Experimental Facility

The University of Wisconsin (UW) IEC device, figure 3.1, consists of a cylindrical vacuum vessel made of aluminum with internal dimensions of 91 cm diameter and 65 cm height. A picture of the device in operation is shown in figure 3.2. The pumping system consists of a Leybold Trivac® rotary vane roughing pump and DynaTech® turbo pump to allow base pressures ~ 1-10 x 10^{-7} torr. Although the base pressure is measured using an MKS® ion gauge, higher pressures during chamber venting are measured using a capacitive manometer (Baratron® gauge). The fuel gas is fed to the chamber through two MKS Mass-Flow controllers for both D_2 and ^3He gases. The electronic flow controllers allow fine adjustment of the gas flow up to 50 sccm (standard cubic centimeter per minute) into the chamber. During runs, the chamber pressure is monitored using an MKS Baratron® pressure transducer. In one mode of operation, the device is run at 2 ± 0.5 mtorr. An SRS CIS 200 residual gas analyzer (RGA) allows real time gas composition measurement, for monitoring the impurity levels. It also allows one to maintain a predetermined fuel ratio $D_2/^3He$ if required by the experiment.

The central grid (cathode) is typically 10 cm in diameter. Unique to this experiment is the selection of tungsten alloy (W-25%Re) as the grid material since it is a refractory material

and can be spot-welded. With this grid, the previously prevalent sputtering (of a stainless-steel grid) is drastically reduced and the low power operation limitation is relaxed. The outer grid (anode) is, however, fabricated from stainless steel (SS) wire and is generally connected to ground. In some experiments a third intermediate SS grid (35 cm dia.) is used; this grid is covered with a SS mesh (~ 1 mm spacing). A RF power source (operated at 345 kHz) is connected to both the outer and the intermediate grid through a matching transformer.

A high voltage stalk conducts large negative voltages from the power supply to the central grid. The present design is a 2 cm dia. cylinder made of BN with a 3 mm dia. Mo wire running along the central axis. The voltage power supply is a Hipotronics^{TM} supply with maximum capability of 200 kV and 75 mA. Plasma is generated inside the chamber using a set of three equally spaced (120^{o} apart) electron emitters placed outside the outer grid. The voltage to the filaments (-30 V to -250 V) and hence the electrons emitted by the filaments is controlled through a variac. The efficiency of these filaments in ionizing the ambient gas in the chamber is improved by rectifying the AC power fed to the filaments, followed by the application of controlled DC bias that aids better current control.

The neutrons generated by the D-D reactions are detected using a ^{3}He filled neutron detector enclosed by a paraffin shield that thermalizes all neutrons before detection,[1] as shown in Figure 3.3. This detector is calibrated using a standard Pu-Be source. For this purpose the source is placed in the center of the chamber and is calibrated approximating a point source.

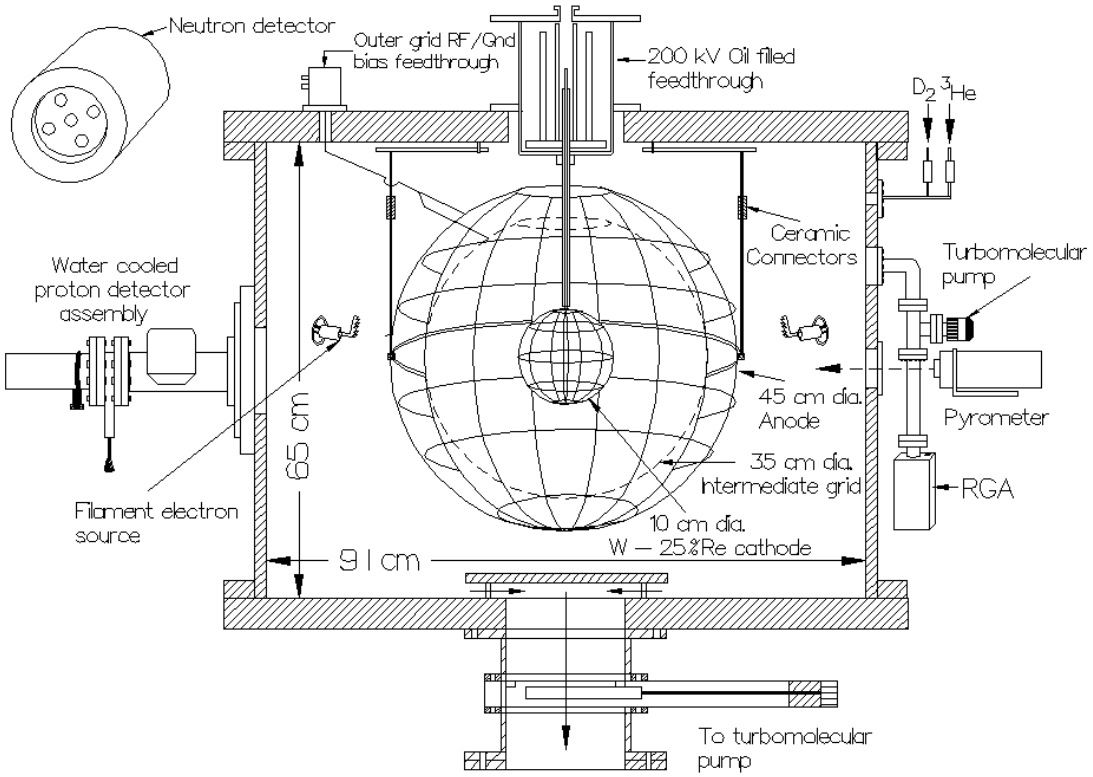

Figure 3.1 Sectional view of the IEC device at University of Wisconsin, Madison. All figures are not to scale unless specifically mentioned.

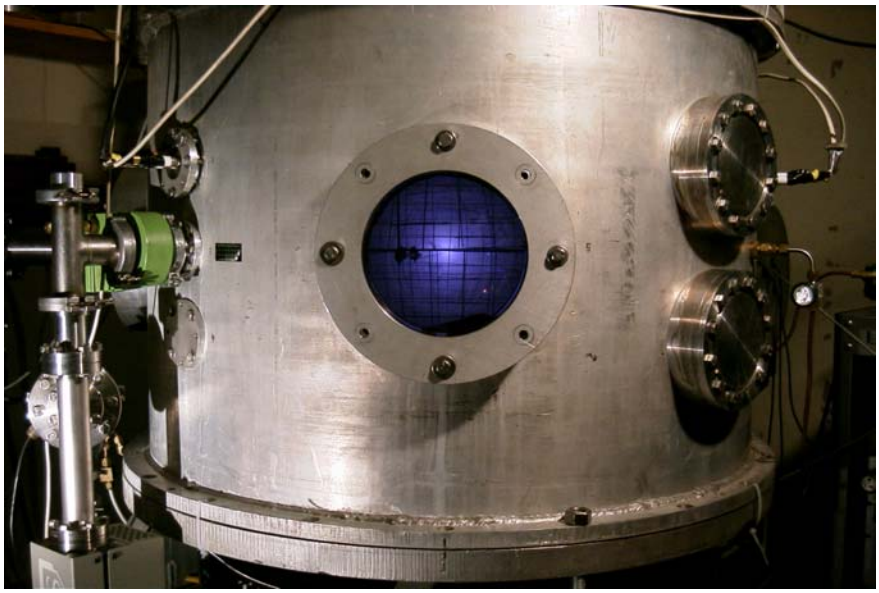

Figure 3.2 Picture of an IEC chamber in operation

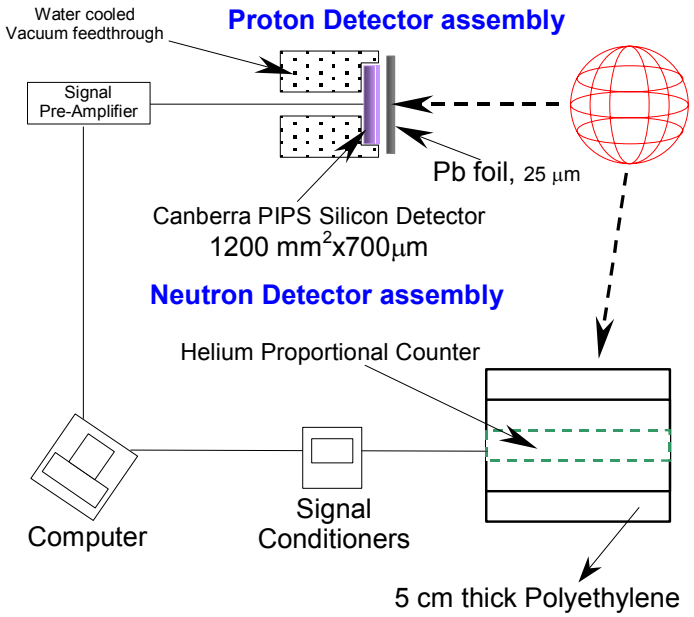

Figure 3.3 Diagnostics used for detecting the fusion products.

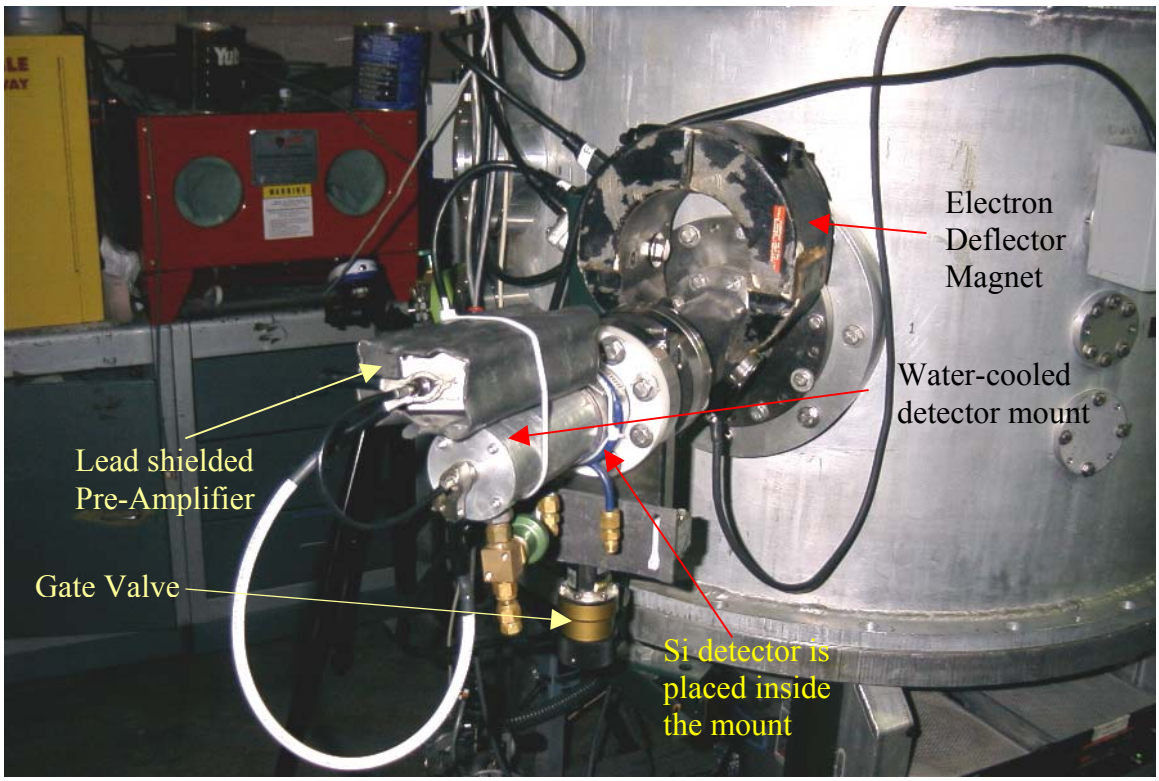

Figure 3.4 The Proton detector mounted on the UW IEC device.

The protons are detected using an Ortec® 1200 mm^2 silicon detector mounted on a water cooled vacuum feedthrough, on a port facing the center of the chamber, and accompanying multichannel analyzer software. The detector itself is shielded from visible light using thin Pb foil that keeps the background noise at tolerable levels and also allows simultaneous detection of D-D and D-^{3}He protons.[2] A picture of the proton detector assembly is shown in figure 3.4. A deflector magnet scoops out electrons from the radiation (protons, x rays and other fusion products) reaching the detector, thus further reducing the background noise.

A video camera is connected to a computer in the control room that allows visual monitoring of the operation through a view port. The view port itself is protected from the sputtered material using a transparent glass shield. A Raytek® Marathon MR pyrometer can be pointed to different areas on the cathode to determine temperatures from 700^{o}C to 1800^{o}C with temperature resolution of 1^{o}C. The whole IEC assembly and the related diagnostics are housed inside a room with 1 m thick concrete walls and a 5 cm thick (1500 kg) lead door, for radiation shielding.

3.1 References

[1] L. V. East, and R. B. Walton, "Polyethylene Moderated ^{3}He Neutron Detectors," Nucl. Inst. and methods, 72 (1969), pg. 161-166.

[2] R. P. Ashley, G. L. Kulcinski, J. F. Santarius, S. Krupakar Murali, G. Piefer, and R. Radel, "Steady state D-^{3}He proton production in an IEC fusion device," 14th ANS topical meeting on the Technology of Fusion Energy, Park city, UT, Oct. 15-19, 2000.

Chapter 4.0: IEC Operational Principle

Based on the ionization source used there are three different modes of operation of the IEC device:

4.1 Grounded outer grid mode of operation

4.2 Radio Frequency (RF) ionization supported mode.

4.3 Outer grid biased mode

4.1 Grounded Outer grid mode

Two concentric grids are used in this mode. The central grid is ~92% transparent and the outer grid is ~85% transparent. While the outer grid (anode) is connected to ground, a high voltage (negative) is applied to the central grid that acts as the cathode. Ionization of the ambient gas in the source regime outside the anode is achieved through electron impact ionization. The electrons are emitted by set of three filaments (biased to -50 to -200 V, for efficient electron emission) as explained in the Chapter 2.0. The electrons emitted by the filaments move towards the grounded anode and as they intercept neutral gas in their path, ionization occurs. The ions

thus created see the cathode potential (once inside the outer grid) and are accelerated towards the central grid, thus picking up fusion relevant energies. These ions cause fusion in five different source regimes as explained in Chapter 5.0. All the experiments performed in the present dissertation are in these modes.

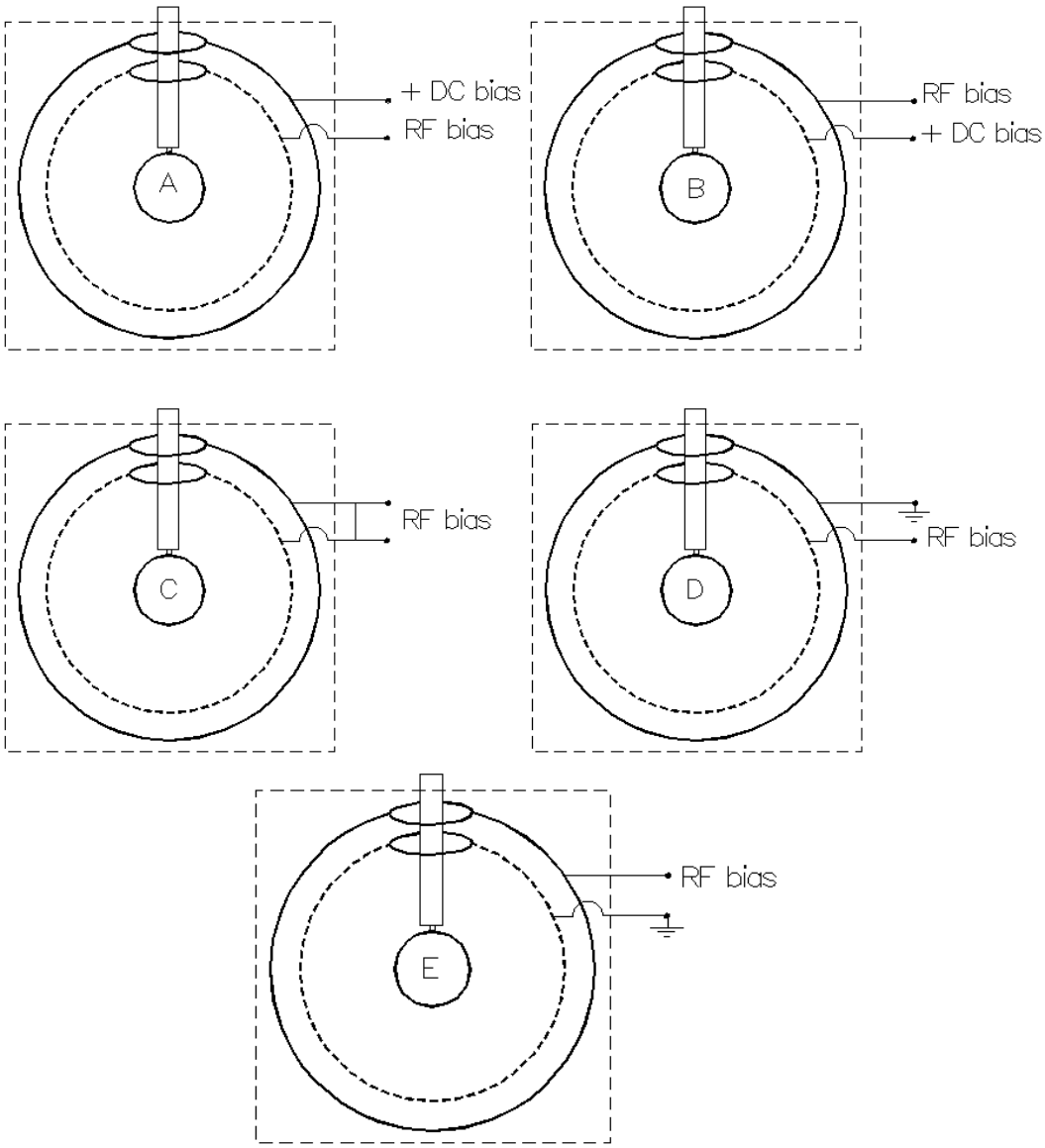

Figure 4.1 The RF bias configurations tested on the UW IEC device (chamber walls are always at ground potential and the cathode is at a negative potential).

Table 4.1 Stability of plasma with various (intermediate & central) grid bias configurations

Configuration	*Intermediate grid*	*Outer grid*	*Stability of plasma at ~ 2 mtorr, -35 kV, 40 mA*
A	RF signal	+DC bias	Stable
B	+DC bias	RF signal	Unstable
C	RF signal	RF signal	Stable
D	RF signal	Ground	Unstable
E	Ground	RF signal	Stable but requires higher RF power

4.2 RF ionization supported mode

In this mode of operation, the intermediate grid and the outer grid are connected together to an RF power supply[1] through an RF amplifier (gain ~ 1000) and an isolation transformer with the following primary to secondary voltage ratio $V_{out}/V_{in} = 3/11$. A fine mesh (with Debye length spacing of ~1 mm) around the intermediate grid allows the electrons to be confined around this grid. As these electrons oscillate about the intermediate grid they produce uniform ionization around the central grid. Several other configurations of the RF signal were experimented with, as shown in Table 4.1 and represented pictorially in Figure 4.1. The stability of these modes varied with the configuration as explained below.

In the configuration (A) shown in Figure 4.1 a +DC bias is applied to the outer grid and the RF signal is applied to the intermediate grid (with fine mesh on it). The plasma was stable (able to sustain) at 35 kV, 40 mA and 2 mtorr chamber pressure. The ions produced by the RF signal (typical frequency of operation was 243 kHz, at 50-100W amplified output power fed to the IEC chamber) on either side of the intermediate grid see a falling potential towards the central grid.

In the configuration (B) the plasma is unstable because the ions produced around the outer grid now see an increasing potential and have a tendency to go towards the chamber walls (pushed away from the central grid).

In configuration (C) the RF is applied to both the grids simultaneously and any ions produced around these grids see the negative potential of the central grid and are pulled towards the central grid, thus sustaining the plasma. A typical frequency response plot for configuration(C) is shown in Figure 4.2. At increasingly higher voltages a lower RF frequency (hence less power) is required to maintain the plasma. This is because the ions cause a cascade of ionizations on their way to the central grid; the higher cathode voltage tends to accelerate most of these ions generated by ion-impact ionization to high enough energies to cause even more ionization, hence RF power can now be reduced to keep the ion current constant. Electron impact ionization (released from central grid or from regions close to it) cross-section tends to decrease with increasing voltage and hence their contribution to the over all ionization can be neglected.

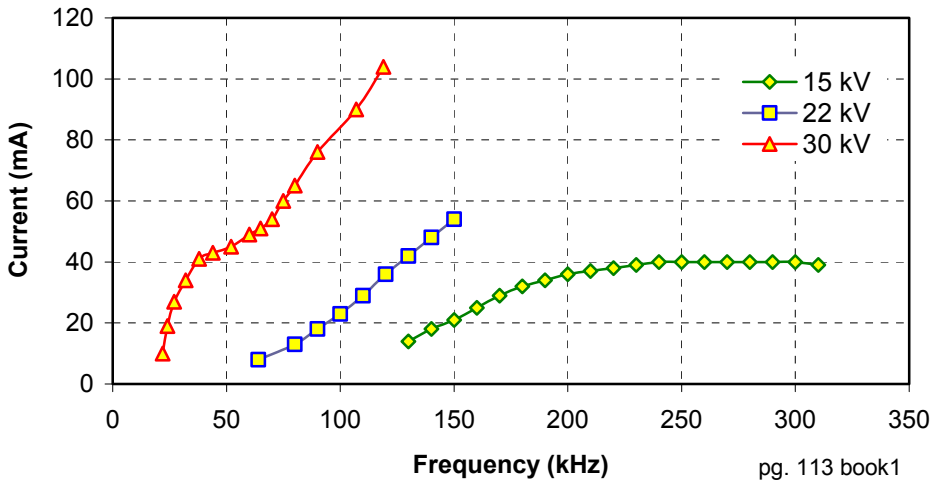

Figure 4.2 Frequency vs. Grid current plot at various central grid voltages at 2.5 mtorr shows a lower frequency input requirement at higher cathode voltage.

In the configuration (D) the outer grid is connected to ground and this tends to cause the plasma to be unstable because the ions generated near the intermediate grid see a slow falling potential (Child-Langmuir potential in the first 5 cm towards the central grid) towards the central grid, while the ground potential of the outer grid is closer to this grid. Hence the ions have a greater chance of moving towards the outer grid than towards the central grid.

In the configuration (E) when the intermediate grid is connected to ground the plasma is sustained but at an increased RF input power. This is because the ions moving towards the central grid are mostly intercepted by the (fine mesh) intermediate grid and the RF power supply has to compensate for the lost ions to keep the total number of ions moving towards the central grid constant and hence higher RF input power is required. Although experiments were conducted with several of the configurations mentioned above and it was observed that better current controllability is obtained when compared to the traditional filament electron ionization source. Unfortunately, this idea had to be shelved (for the time being) due to the parasitic noise associated with RF that tends to skew both the proton and neutron readings (especially at higher input powers). The RF power tends to couple with the Si detector through electrons in the plasma and the neutron detector sees the RF from the unshielded IEC device and the RF power supply. Hence in an effort to understand the physics behind the operation of this device, it was decided not to use RF for present experimental purposes.

4.3 Outer Grid bias mode

This mode is derived from the previous RF ionization supported mode and cannot exist independently. An RF signal is applied to the outer grid as in configuration (B) and the

intermediate grid is biased to a DC voltage. It was observed that when the DC bias was maintained at –50 V there was no plasma (at –30 kV input voltage and ~ 2 mtorr chamber pressure). However, as this bias was increased gradually to +50 V, the plasma initiated, and as the voltage was further increased the RF power had to be decreased to maintain the grid current constant. At +157.6 V the RF had to be completely turned off and the small bias voltage on the intermediate grid sustained the plasma. This could be caused due to two reasons, first, the electrons trapped in the positive well created around the intermediate grid form a new ionization source that is able to sustain the plasma and the second, the low energy ions that tend to escape the chamber through upscattering[2] now see a positive potential at the intermediate grid and are turned back. Ion upscattering losses are caused by ions picking up sufficient kinetic energy via Coulomb collisions to surmount the well and be lost from the system. The ions that would have been lost without this bias voltage now form a new ionization source that create a cascade of ion-impact ionization on their return trip to the central grid. The first explanation is more plausible from the observation that the plasma is not initiated without initially using either the RF source or the filament electron source.

4.4 References

[1] Robert Breun, University of Wisconsin, Madison, Private communications, 1999.

[2] T. H. Rider, Phys. Plasmas **2**, 1853 (1995)

Chapter 5.0: Experiments with the Eclipse Disc Diagnostic

Ions produced through ionization of the ambient gas inside the IEC chamber (through various modes explained below) are subsequently accelerated towards the negatively charged central grid. During the acceleration the ions (irrespective of their source of origin) gain fusion relevant energies. There are several modes by which fusion is known to occur in an IEC device (as illustrated in figure 5.1), namely:

1. Converged-core (beam-beam), [1]
2. Embedded (beam-target),[1]
3. Volume source (charge-exchange – neutral),[1]
4. Beam-background reactions that occur near and inside the cathode
5. Wall-surface reactions (charge-exchange – target).

In the Converged-Core mode, the ions converge inside the central grid and form a dense core. The streaming ions interact and cause fusion, primarily in the central region of the cathode.

The Embedded Source reactions occur between accelerated ions and those trapped in the wire. These reactions occur on the outer surface layers of the grid wire because the range of the 100 kV $^{3}He^{+}$ ions in the W-25%Re is ~0.25 μm.

The Volume Source reactions occur everywhere inside the IEC device. In this mode the energetic ions charge-exchange with the background gas and the resulting fast neutrals undergo fusion with the neutral gas inside the chamber.

The Beam-Background reactions occur principally between the recirculating ions near the central grid and the background gas. Because Child-Langmuir like potentials prevail in the plasma the ions gain most of their energy close to the central grid and as these ions recirculate they run into background gas and cause fusion.

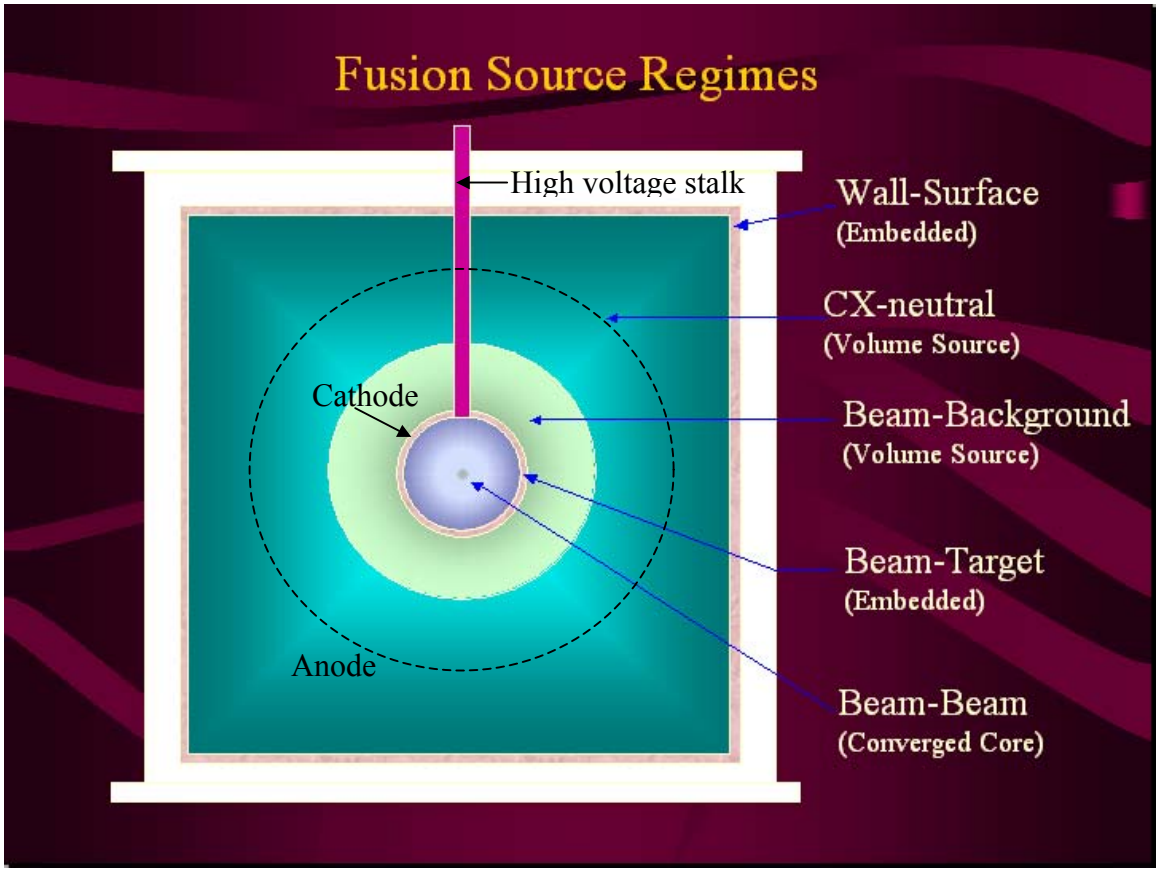

Fig. 5.1 Various fusion source regions in an IEC device.

The Wall-Surface reactions occur between the atoms trapped in the surface layers of the chamber walls and the charge-exchanged neutrals. Although the wall source reactions appear not to be important (at the present power levels), it is speculated that at higher currents and longer runs, the ^{3}He concentration trapped in the surface layers of the chamber walls would increase, and could potentially form stationary targets to the charge exchanged neutral deuterium atoms streaming outwards and thereby cause fusion to occur on the wall surface.

Depending on the fuel, chamber pressure, power level of operation and the kind of ionization source used, each of these source modes becomes important. For instance, at low pressures, the converged core and the embedded reactions dominate, but at higher pressures, the volume source dominates.

In the following sections several experiments conducted to understand the various source regimes are reported.

5.1 Eclipse disc diagnostic

There are two ways by which the fusion regimes can be studied: In the first method, the instrument measuring the fusion rate focuses on a particular region of interest, while the second method involves blocking off the region of interest and measuring the fusion rate from the unblocked region. The difference between the fusion rates measured with and without blocking the region of interest gives the fusion rate from that region. Since it is much easier to block the region of interest, a new diagnostic known as Eclipse disc was developed.[2] This diagnostic is so named because the discs manufactured using aluminum foil (0.5 mm thick) eclipse the region of interest in front of the proton detector (the region between the eclipse disc and the far wall).

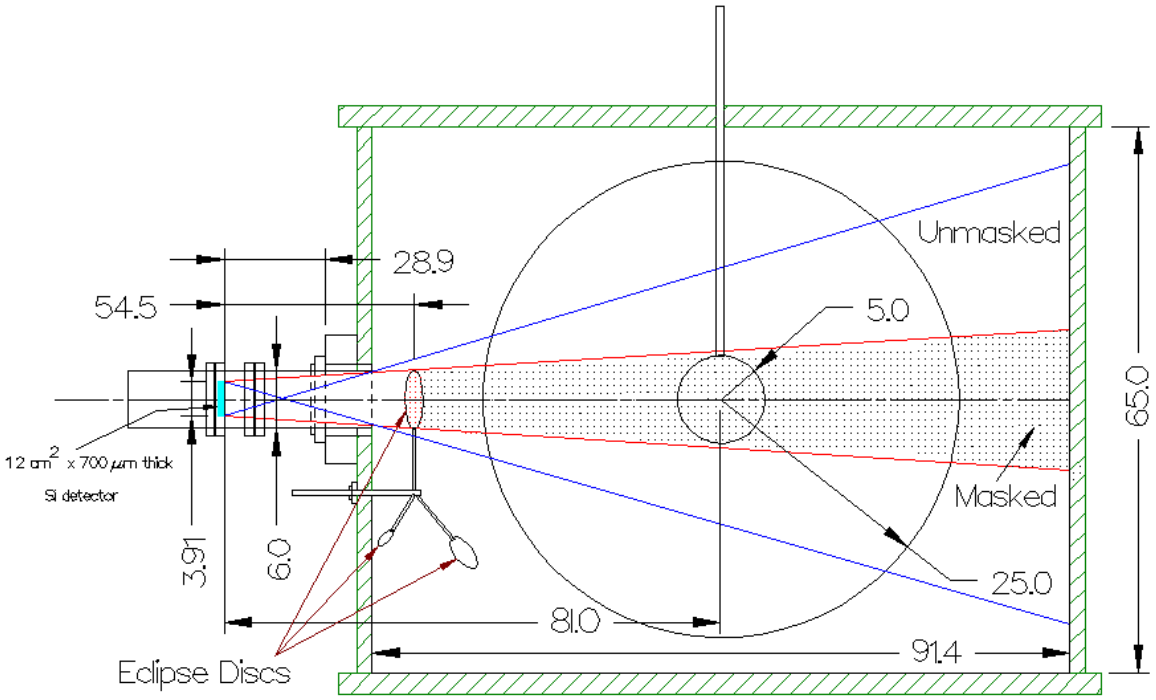

Fig. 5.2 Schematic of an eclipse disc diagnostic mounted on a port of the IEC chamber. Figure not to scale.

Three different discs – large (4.0 cm diameter), intermediate (2.4 cm) and small (1.1 cm) were used for the experiment shown schematically in figure 5.2. The volumes blocked by each of these discs and the 2D area projected at the center of the cathode calculations is given in Appendix A. These eclipse discs can be positioned before the proton detector by rotating a lever from outside the chamber. The eclipse disc masks all the D-D fusion protons generated between it and the far wall and it is this volume that forms the region of interest. It is important to note that no fusion reactions occur between the eclipse disc and the proton detector since this disc stops all the ions and the charge exchanged neutrals.

An interesting aspect of these discs is that they do not completely block the energetic D-^{3}He protons, only attenuate their energies. These attenuated protons show up as a different energy peak in the proton energy spectrum, such as shown in figure 5.3. This is an important

consequence of the eclipse disc because an independent confirmation of the protons coming from a region of interest is obtained from this peak.

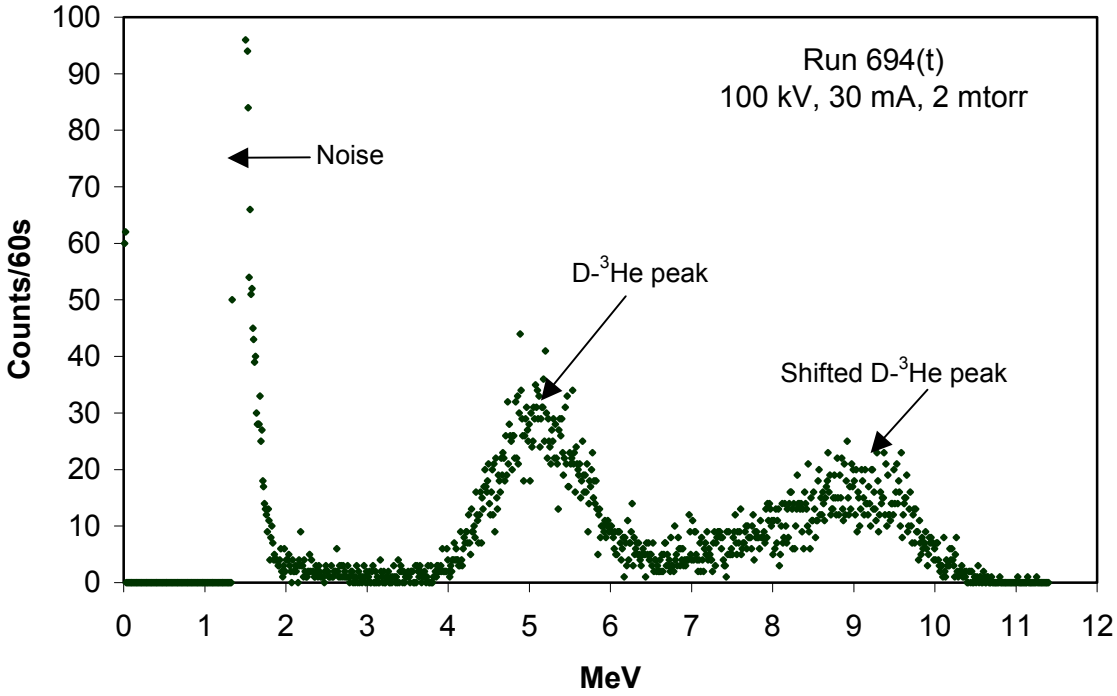

Figure 5.3 A double peak is observed when D-^{3}He fuel is used in conjunction with an intermediate eclipse disc.

The eclipse disc blocks most of the D-D protons (a few make it through the unmasked region), but it allows the D-^{3}He protons from the unmasked wires and also the masked portions through. Those coming from the masked portion show up as a second peak in the proton energy spectrum, figure 5.3. This is because the detector has a Bragg peak response as shown in figure 5.4. As the D-^{3}He protons lose energy, the amount of energy they deposit increases up to the Bragg peak value which in the present case for the 700 μm thick Si detector is 10 MeV beyond which the energy deposited would once again begin to decrease; see chapter (4) for further information.

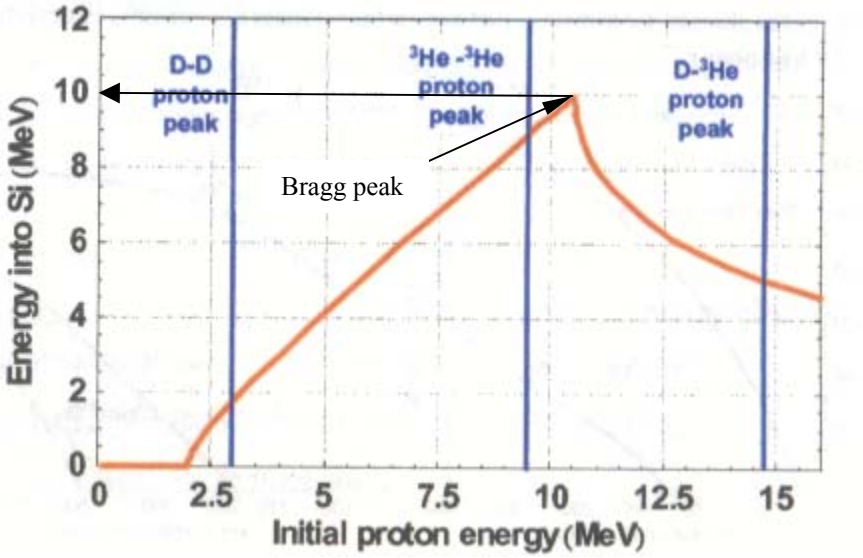

Figure 5.4 As the initial energy of D-^{3}He protons decreases, it deposits more energy into the 700 μm thick Si detector up to a maximum of 10 MeV (Bragg peak), beyond which the proton deposits lesser energy.[3]

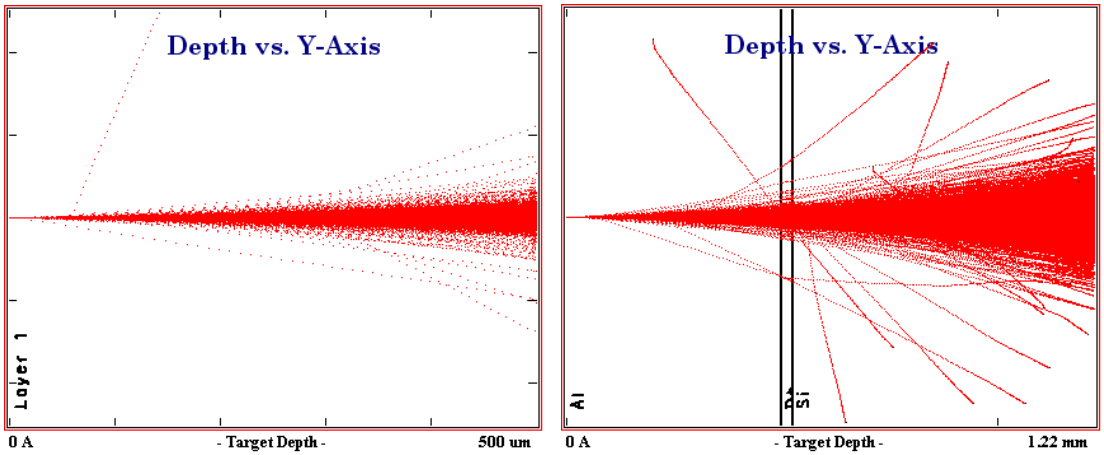

Figure 5.5 Scattering of the D-^{3}He protons as they pass through (a) Al (0.5 mm thick) and (b) Al (0.5mm) + Pb (25 μm) + Si detector (700 μm), Al disc is shown close to Pb foil but is in fact 51 cm away from the Pb foil, hence some of the scattered protons could be lost before they reach the Pb foil.

Figure 5.5 shows the D-^{3}He proton scatter that causes the protons to ultimately deposit more energy into the detector. As the protons pass through the eclipse disc, the energy distribution on the exit end of the Al foil appears as shown in figure 5.5.

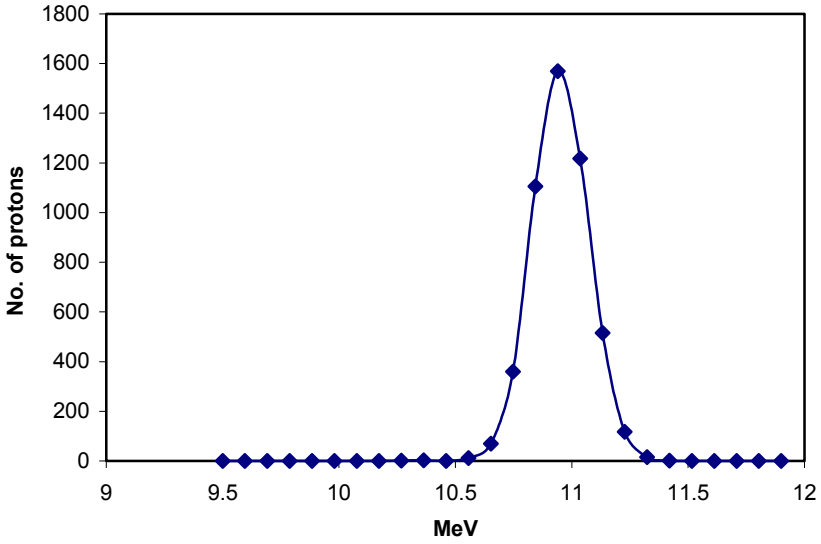

Figure 5.6 Energy distribution of the 14.7 MeV protons (exiting the 0.5 mm thick Al disc) calculated using SRIM

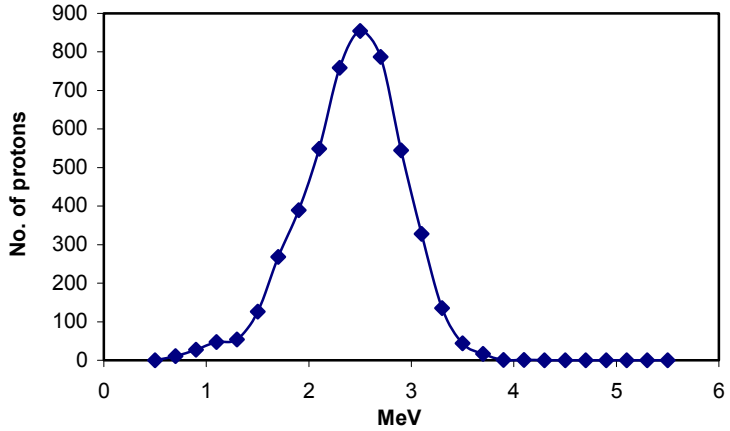

Figure 5.7 Energy distribution of the protons exiting the Si detector in figure 5.5 (b).

As observed from figure 5.7, the protons have lower energy upon exiting the detector and hence these protons have deposited more energy (difference of energy peaks from figure 5.6 and figure 5.7) into the detector thus showing up at a higher energy level as shifted peak in figure 5.3.

5.2 Experiments using eclipse disc

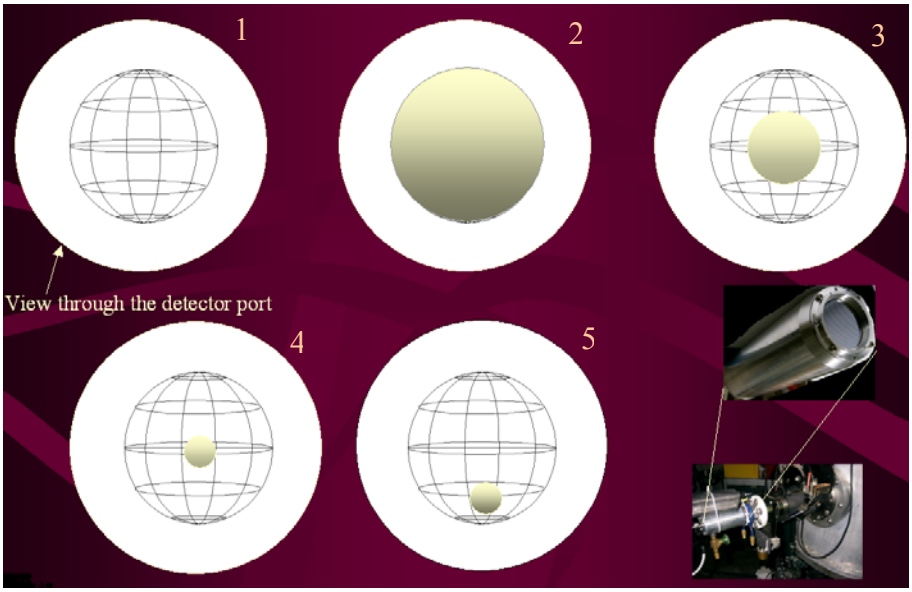

Figure 5.8 (1) Unobstructed view through the detector port (2) Large disc eclipsing the entire cathode (3) Intermediate disc eclipsing the cathode (4) Small disc eclipsing the core of the central grid (5) Offset small disc eclipsing an arbitrary region of the cathode.

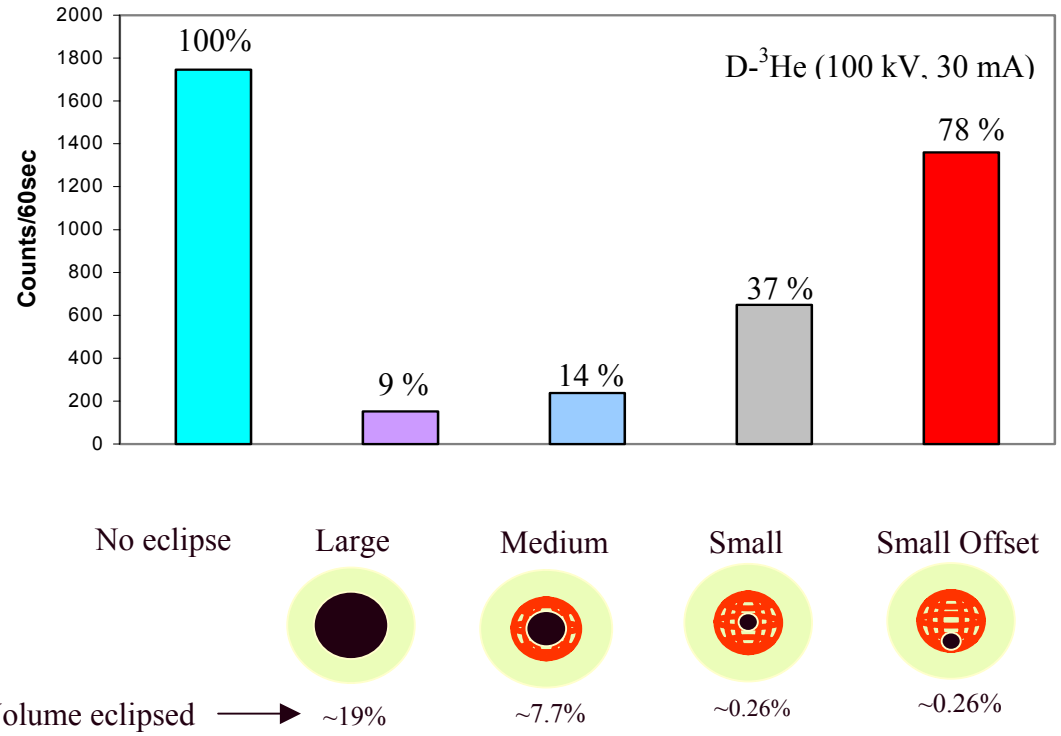

Figure 5.9 Typical D-D proton count variation (integrating over all energies) with eclipse discs in an IEC device with D-^{3}He fuel at 100 kV, 30 mA. (See Appendix A for eclipsed volume calculations). Also see reference 4.

Several experiments were performed using the eclipse disc diagnostic. In one set of experiments all three discs mentioned above were used as shown in figure 5.8 (where the view through the detector port with various discs is also illustrated). The results of these experiments performed with D-^{3}He fuel mixture are shown in figure 5.9 (Also see ref. 4).

Although D-^{3}He fuel is used in an IEC device, parasitic D-D reactions always occur alongside the D-^{3}He reactions. This aspect has been exploited in the present set of experiments to isolate and understand the contributions of the volume, embedded and converged core regions. Figure 5.9 also shows the approximate volume eclipsed by each of the discs. The no eclipse case (as illustrated in the figure 5.8) is normalized to 100% and all the other counts are relative to this value. When the large eclipse disc is used, this disc eclipses 19% of the volume visible to the proton detector (total unmasked volume, figure 5.1), and as a result of this, more than 90% of the D-D protons are blocked. With the intermediate disc that eclipses 7.7% of the volume, and hence 86% of the D-D protons are blocked (14% shows up at the detector). With the small disc that eclipses just 0.26% of the volume about 63% of the D-D protons are blocked (37% shows up), this indicates that D-D reactions are predominant in the core region of the IEC device. The offset disc data that still eclipses 0.26% of the volume further supports this, and it now blocks only 22% of the D-D reactions (78% shows up). In order to understand the D-^{3}He reaction contributions a comparative study is performed below.

The fusion occurring in each of the source regimes (tabulated below), contribute a certain percentage to the overall fusion rate detected by the Si detector. The 74% counts from the DD converged core means that this source regime contributes 74% of the total protons detected by the Si detector. The total contributions of each of the source regimes are tabulated in Table 5.2.

Table 5.1 Fusion source regime contributions to the overall proton rate detected by the Si detector. Error in these contributions is ± 2%.

Fusion source regime	**DD**	**D-^{3}He**
Converged core (x)*	75 %	11 %
Embedded (y)	15 %	89 %
Volume (z)	10 %	Negligible
Wall surface	Negligible	Negligible

As shown in figure 5.10 a comparison of the D-D reactions with D-^{3}He reactions shows several new features. The large disc blocks most of the D-D reactions and almost all of the D-^{3}He protons. The D-^{3}He protons that get through the eclipse disc show up as a shifted peak, figure 5.3 (a), some D-^{3}He protons are however lost as they are scattered away by the eclipse disc. This suggests that most of the D-^{3}He reactions are contributions of either the converged core or the embedded reactions.

The intermediate disc blocks 55% of the D-^{3}He protons and approximately 48% show up as the shifted proton peak. With the small eclipse disc, only 10% of the D-^{3}He protons are blocked and even with the offset disc only 8% of the protons are blocked. Hence the D-^{3}He reactions are dominated by the embedded reactions. This is the first confirmed evidence that D-^{3}He reactions are predominantly embedded reactions. Although the fraction of ^{3}He ions is small in the D-^{3}He mixture (D-^{3}He reactions are rare in the volume of the device due to penning ionization effect[5]), those ions that survive quickly embed themselves on the surface of the cathode grid wires forming stationary targets for the oncoming D_2^+ ions. Another independent

* See chapter 13, where the values of x, y and z (eqn. 13.20) are used to find the calibration factor.

experiment performed using the solid targets[6] provided further evidence that the D-^{3}He reactions are embedded (beam-target reactions) in nature.

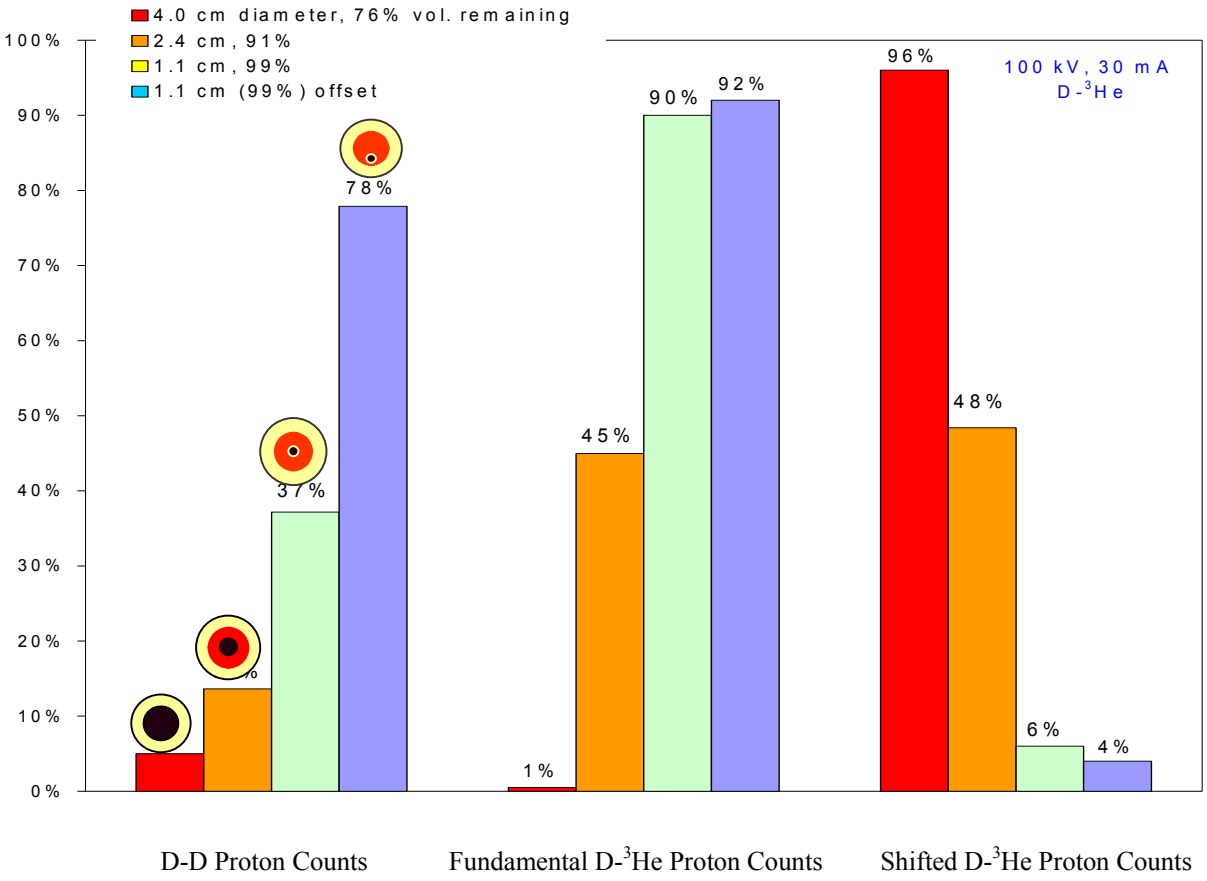

Figure 5.10 Percent of protons detected by the detector corresponding to each of the eclipse discs.

A disadvantage with this technique is that the eclipse discs are not highly selective, in other words they block more than the regions of interest. For instance, if the large disc is used in front of the proton detector to block the central grid, it not only blocks the contributions of the embedded fusion from the wires and the converged core but also the volume source behind and in front of the central grid that fall in the masked region, see figure 5.1.

5.3 Conclusions

Eclipse experiments (with D-^{3}He fuel) revealed that a converged core exists for the D-D reactions and not for D-^{3}He reactions (is negligible). The distribution of these contributions as measured using the eclipse disc diagnostic for the range 40 kV to 100 kV at 30 mA and ~**2 mtorr** chamber pressure are tabulated below:

Table 5.2 Fusion source regime distributions in an IEC device.

Fusion source regime	**DD**	**D-^{3}He**
Converged core (x)	20 – 22%	5 – 7 %
Embedded (y)	5 – 8 %	93 – 96 %
Volume (z)	67 – 70%	Negligible
Wall surface	Negligible	Negligible

The broadening of the D-D and D-^{3}He proton energy peaks is predominantly caused by Doppler and scatter broadening. While the DD protons deposit all their energy (after loosing some to the Pb foil) into the Si detector, the D-^{3}He protons deposit energy only partially. Detailed experimental measurements and Monte Carlo simulation of the proton energy peaks are reported in Chapter 7.0.

5.4 References

[1] Thorson T.A., R. D. Durst, R. J. Fonck, and A. C. Sontag, "Fusion Reactivity Characterization of a Spherically Convergent Ion Focus," Vol. 38, Nuclear Fusion, No. 4 (1998).

[2] R. P.Ashley, G.L. Kulcinski, J. F. Santarius, S. Krupakar Murali, G. Piefer, B. B. Cipiti and R. Radel, "Recent progress in steady state fusion using D-^{3}He," Fusion Science and Technology, **44**, 559 (Sep. 2003).

[3] J. F. Sanatarius, Private communications, University of Wisconsin, Madison, (2003).

[4] R. P. Ashley, G. L. Kulcinski, J. F. Santarius, S. Krupakar Murali, G. Piefer, B. B. Cipiti, R. F. Radel, "Recent progress in steady state fusion of D-^{3}He in an IEC device," 5th US-Japan Workshop, Madison, WI (2003) USA.

[5] Penning F M, "Glow Discharge at Low Gas Pressures Between Coaxial Cylinders in an Axial Magnetic Field," Physica **3**, 873-894 (1936).

[6] Ben B. Cipiti, PhD Thesis, University of Wisconsin, Madison, 2004.

Chapter 6.0: Fusion convergence measurements inside the central grid through small eclipse scan

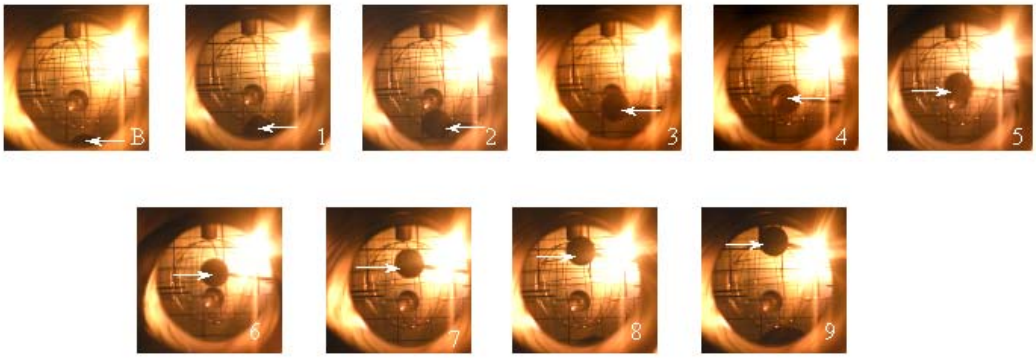

Figure 6.1 Pictures taken through the detector port of the small disc at various locations. The bright light in the background comes from the filament electron source in the far end.

The set of experiments described in this chapter is an extension of the offset small eclipse disc experiment (explained earlier in chapter 5.0), wherein the small disc is scanned all the way across the central grid in small increments as shown in figure 6.1.

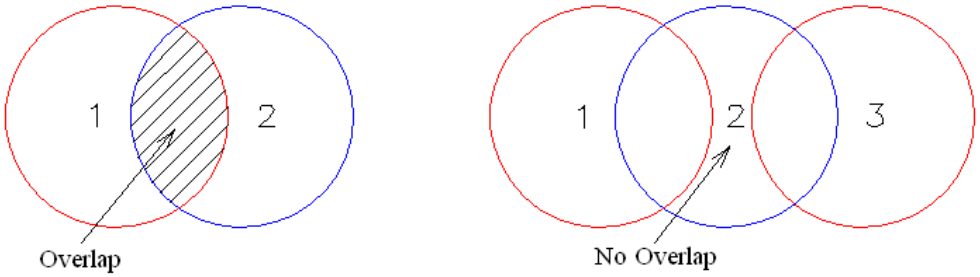

Figure 6.2 There is ~50% overlap between two consecutive discs [red (1) and blue (2)] but not between every other disc position [in red (1) & (3)].

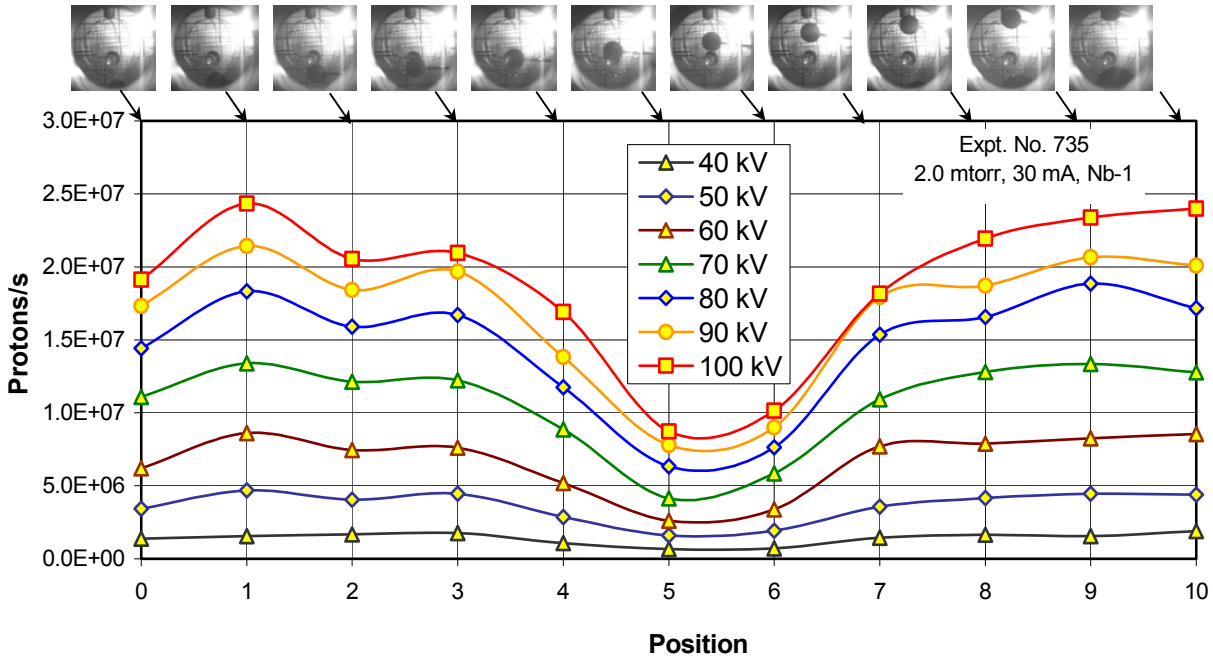

Figure 6.3 Protons/s at various voltages vs. position.

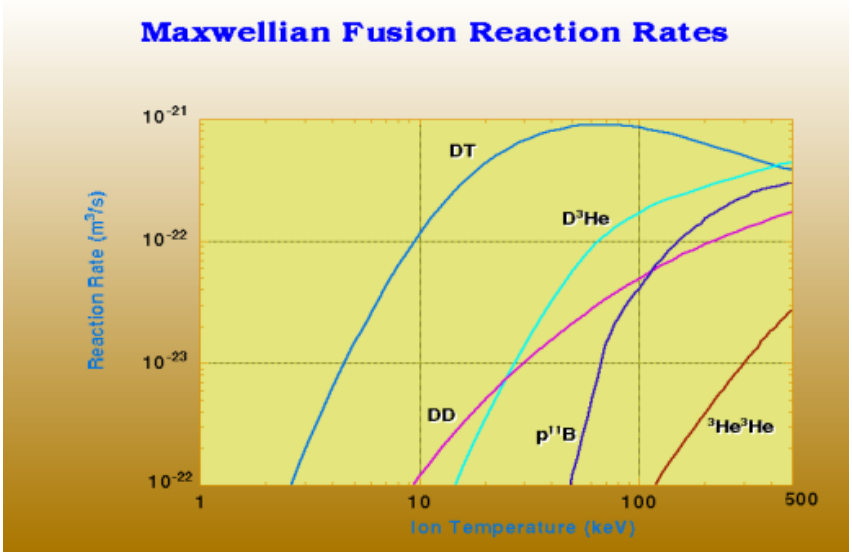

Figure 6.4 Fusion reaction rate vs. ion temperature

The area blocked by the disc in each position overlaps with the previous area, but there is no overlap between alternate disc positions as shown in figure 6.2. Proton and neutron data are recorded at each position of the disc, figure 6.3 shows the plot of protons/s vs. position of the

eclipse disc at various voltages. It is observed that the protons/s converge at position 5, showing that converged core contributions exist for D-D reactions. The magnitude of the proton rate (protons/s) values increase with voltage because the ion energy (and hence the reaction cross-section) increases with voltage, see figure 6.4.

6.1 Effects of voltage and pressure on the fusion convergence

The proton rate shows the convergence (more protons produced in the core) as the disc scans the central grid. Interestingly, when the protons are normalized to 1 the proton counts show a regular structure and even more interesting is the fact that other than the counts at 40 kV, all the counts seem to show a dip at the position (2) in figure 6.5. If only half the grid were scanned (assuming symmetry) this dip could be easily mistaken to be a double well[1] structure. The statistical variation in the operational parameters could cause such anomalous structures in figure 6.5.

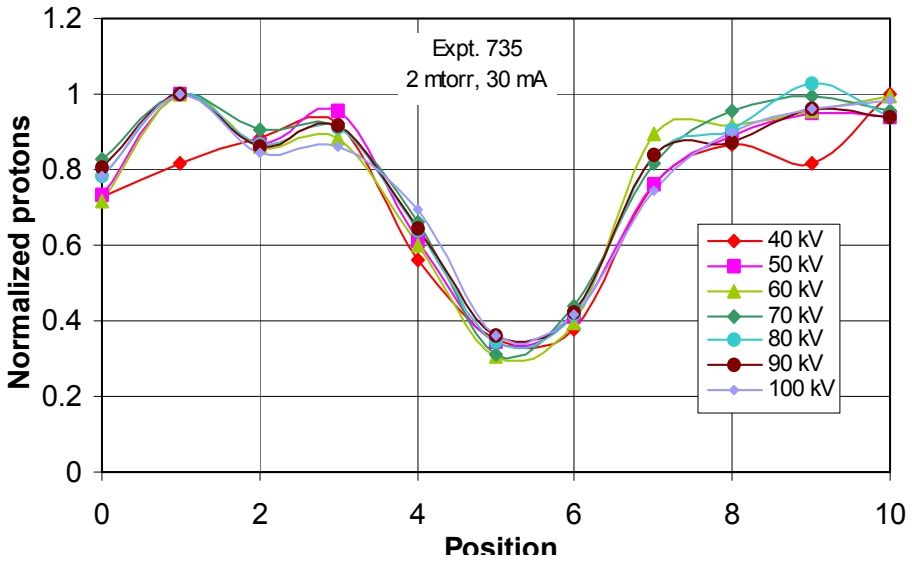

Figure 6.5 Normalized proton count vs. position at various voltages

To verify that this is the case a simple technique was conceived. The neutron data is independent of the position of the disc and would increase or decrease with the total number of protons because the branching ratio for the D-D reactions is very close to 50% as shown in figure 3.1. Any changes in the neutron counts may be caused due to variations in any of the following: grid temperature, chamber pressure, drifts in grid voltage and/or drifts in current.

6.1.1 Proton/Neutron (P/N) ratio

If the total number of proton/s (P) were divided by the (simultaneously recorded) total number of neutrons (N) at a given position of the disc, then the variation of this parameter (P/N ratio) with the position of the disc would be a true indicator of any anomalous behavior of the protons generated in the central grid region. This is because the branching ratio of the DD reactions to produce either protons or neutrons is 50%, see figure 3.1.

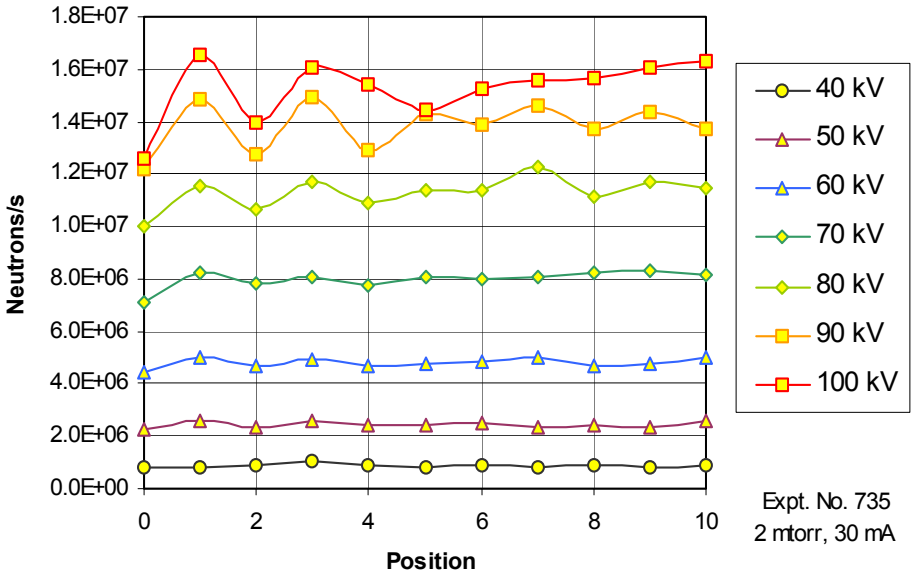

Figure 6.6 Neutrons/s at various voltages vs. position

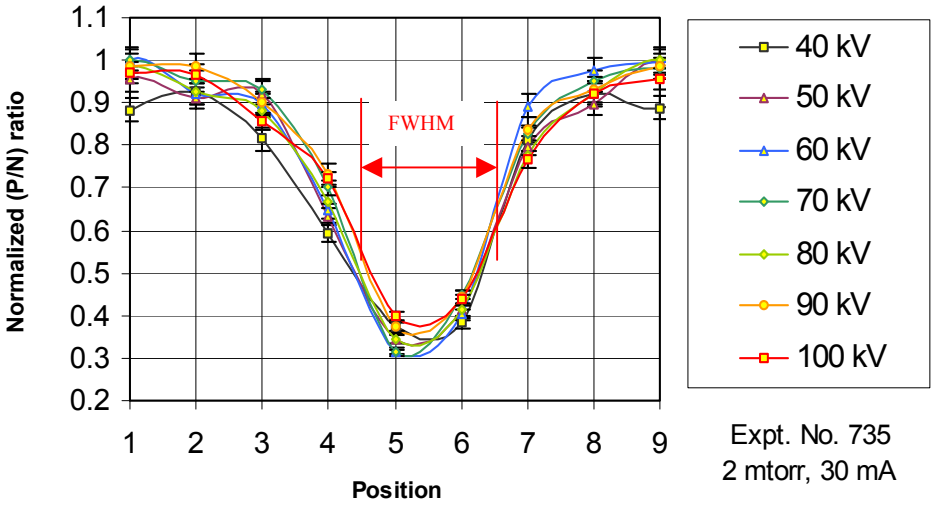

Figure 6.7 Normalized (P/N) ratio vs. position at various voltages.

The P/N ratio assumes a constant calibration factor i.e., constant contributions from each type of source with voltage and current (which seems to be valid for voltages below 100 kV, beyond which experiments were not performed).

Figure 6.6 is a plot of the neutrons/s vs. position. The counts are not constant during a given scan and hence a P/N ratio would account for the statistical variations during the experiment. Neutron counts tend to track the statistical variations just as the protons do and hence a ratio of the two would normalize any statistical variations.

Although pressure normalized proton data is being used for a proton collimation study in the literature,[1] the P/N ratio should be preferred because it accounts for all the parameters that vary during the experiment (not just the pressure).

Figure 6.7 shows the P/N ratios normalized to the maximum value in a particular scan (at a constant volage) vs. position at various voltages. The figure 6.7 shows that there is no significant improvement in convergence with voltage. The overall reaction rate increases but the relative number of reactions that occurs in the core of the device remains the same. The dip that

we had seen earlier at the position 2 no longer exists in the P/N ratio scan and is concluded to be an artifact of the experiment, created by the variation in the parameters such as chamber pressure, drifts in the cathode voltage and drifts in the cathode current.

The error bars for figure 6.7 are generated by dividing the maximum proton count [(original) counts + sqrt(counts)] by minimum neutron counts [(original)counts – sqrt(counts)] at a particular voltage. There is negligible error in the x direction because the eclipse positions are repeatable.

There is ~50% overlap between consecutive disc positions as illustrated in figure 6.2, it is evident from figure 6.7 that the converged core boundary lies between the positions 5 and 6, where the number of counts masked is the maximum. Since the counts do not return to the maximum value as in position 4, the converged core is still eclipsed in position (7).

Approximating the volume eclipsed by the small disc to be a cylinder (see Appendix A) of diameter 1.1 cm, the upper limit of the diameter of the converged core is the separation distance of the overlap regions shown in figure 6.2, it seems that the size of the converged core diameter is less than 0.55 cm.

Figure 6.8 shows the pressure scan of the P/N ratio at various chamber pressures. There is minimal variation up until position 6 beyond which the P/N ratio increases for the low pressure operation (~1 ± 0.1 mtorr). This aspect is not understood well. The pressure was maintained around 0.95 mtorr for the scan from position 0 to 4. Beyond this point the pressure was slightly lower at ~0.85 mtorr average chamber pressure, but the pressure variation is small and hence is ruled out to be the cause of the anomalous behavior.

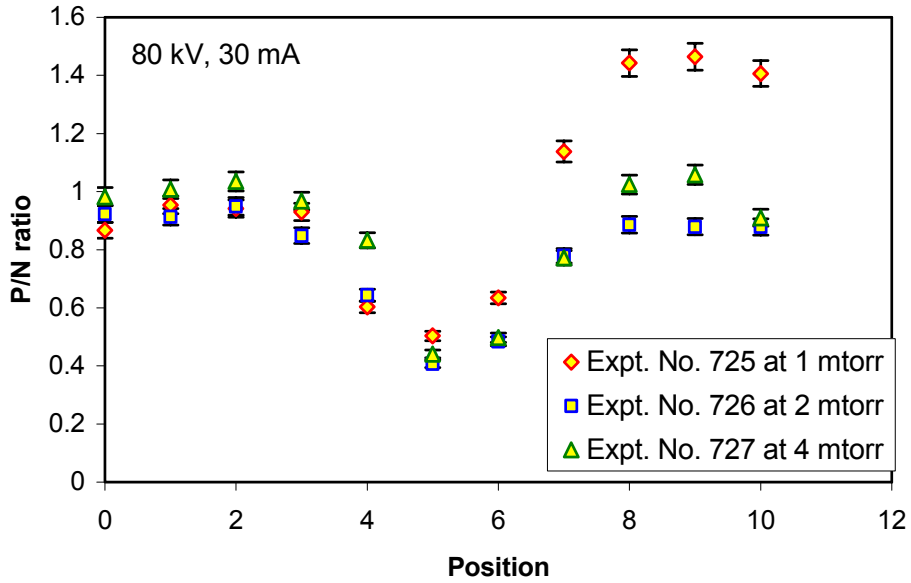

Figure 6.8 The P/N ratios scan does not show significant variation in the lower half scan (from position 0 to 5) and shows an increasing trend from (position 6 to 12) only for the 1 mtorr chamber pressure operation.

Since the eclipse scans seem to remain constant for the voltage range 40 kV to 100 kV at 30 mA and also for a pressure range of 1 to 4 mtorr, the calibration factor derived later in chapter 13 would be applicable to the entire range.

It is noteworthy that Gu's work[2] using a proton-detector-collimating assembly with micro holes in the collimator allowing only certain protons to get through, is the reverse of the above-mentioned technique. Hence the equations derived for the collimating assembly are also applicable here with a few modifications, such as instead of protons detected, here the difference of proton measurements before and after the eclipse is in position could be used. The Abel inversion technique may then be used to translate the proton-rate data into the desired radial proton-rate density profile. However, this was not done for the present dissertation work and is a suggested topic for future study. Other applications of the eclipse disc scan technique are elaborated in later chapters of this dissertation work.

6.2 References

[1] Gu Yibin, PhD Thesis, University of Illinois at Urbana-Champaign (2002).

[2] Yibin Gu and G. H. Miley, "Experimental Study of Potential Structure in a Spherical IEC Fusion Device," IEEE Trans. Plasma Sci., Vol. 28, No. 1, pg. 331 – 346, Feb. 2000.

Chapter 7.0: Calculations of energy deposition in a Si detector

Protons are generated in various fusion reactions as explained in Chapter (2.0). These protons are detected using a 700 μm thick silicon detector, also explained in Chapter (2.0). The fundamental information carriers in the semiconductor detectors are electron-hole pairs created along the path taken by the charged particle (primary radiation or secondary particle) through the detector. The electron-hole pair motion in an applied electric field in the form of surface barriers generates the basic electrical signal from the detector.

One potential disadvantage of surface barriers in Si detectors is their sensitivity to light.[1] The thin entrance windows of the Si detector are optically transparent, and photons striking the detector surface can reach the active volume. The energy of visible light photons of 2 – 4 eV is greater than the bandgap energy of most semiconductors, and electron-hole pairs can therefore be produced by photon interactions. Normal room lighting produces a very high noise level, but a 25 μm Pb foil used in front of the Si detector acts as a barrier to suppress the visible light even though it is nearly transparent to X-rays (beyond 50 keV).

The protons generated in a fusion reaction are monoenergetic but the peaks detected by the Si detector are broadened due to several reasons: firstly, Doppler broadening due to the reactant velocity distribution as explained in section 7.1; secondly, the collisional broadening that occurs due to the proton scattering as the D-D protons pass through the Pb foil geometry and the D-^{3}He protons pass through the Pb + Si detector geometry; and finally, there is the broadening due to the small portion of the proton energy transferred to recoil nuclei rather than to electrons. These low-energy recoil nuclei lose their energy in inelastic collisions with surrounding atoms and form almost no additional electron-hole pairs. If the fraction of energy lost in this manner were constant for each proton, there would be no effect on energy resolution. However, this energy loss is subject to large fluctuations since it is influenced by a few relatively large events.[1] However, the latter contribution (and the contributions mentioned below) to broadening of the proton energy peaks is neglected in the present study.

Other contributions to peak broadening are the effects of incomplete charge collection and variations in the energy lost by the particle in dead layers at the detector surface.[2] The noise level from the detector-preamplifier-amplifier combination is dominated by fluctuations in the detector leakage current, the inherent preamplifier noise, and the characteristics of the field effect transistor used in the input stage of the preamplifier.

The collisional broadening depends on the initial energy of the proton, which in turn is governed by the Doppler broadening, and these two effects appear simultaneously. All the other sources of peak broadening are normally independent of each other; the square of each Full Width Half Maximum (FWHM) value that would theoretically be observed for each source separately can be summed together to give the overall FWHM.

7.1 Doppler broadening of the proton energy peak

Different deuterium (D_2^+) ions (assuming the concentration of D^+ and D_3^+ is small) inside the IEC have different velocities in the direction of the observer owing to the spherical symmetry of the IEC device. The cumulative result of this velocity distribution is a smearing or broadening of the proton energy lineshape. It is convenient to view the broadened lineshape as being made up of a large number of "energy packets" centered at different velocities throughout the lineshape, figure 7.1. The individual energy packet at a particular velocity 'v' is the contribution of that fraction of atoms whose Doppler-shifted resonance frequencies lie within a small range of frequencies about 'v'. Many such packets added together produce the smooth Doppler-broadened lineshape.

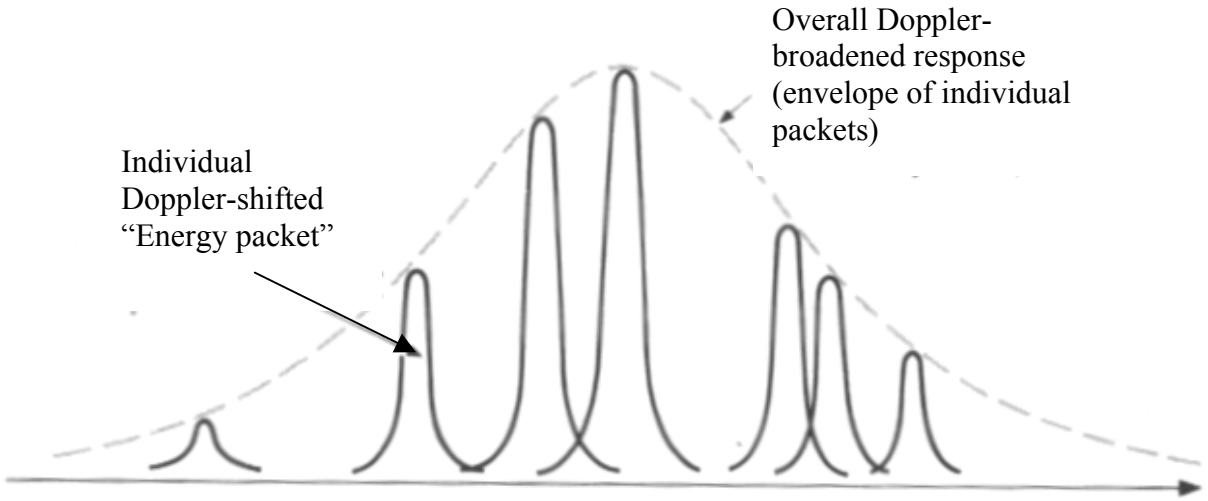

Figure 7.1 The Doppler-broadened lineshape is made up of the superposition of a large number of individual "energy packets," which are the contributions from different groups of atoms with different Doppler velocities.[3]

Initially the neutral particle (D_2) is at rest in the lab frame and it sees a deuteron coming towards it with a velocity V_D. After the fusion reaction a proton leaves the rest frame of the reacting particles at an angle 'θ', as shown in the figure 7.2. But the rest frame of the reacting particles is itself moving with respect to the lab frame with velocity V_{CM}, figure 7.2.

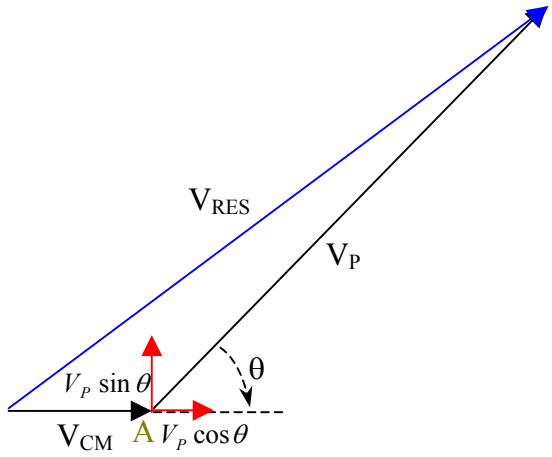

Figure 7.2 The protons detected by the detector have Doppler shifted velocities. A fusion event at the point 'A' causes a proton to be generated at an angle 'θ' to the direction of motion. Other products of fusion are not shown in the figure.

The protons generated in the fusion are now energy shifted with respect to the reactant velocities and it is this energy that the detector detects. A fusion product that enters a detector will possess the combined velocity of the fusion reaction (constant 3.02 MeV) plus the center-of-mass velocity of the reacting ions, figure 7.2. Since the fusion product has the information about the reactant atom's energy, this information can be extracted from the linear Doppler broadening effect as explained in the subsequent Chapter (8.0).

7.2 Doppler shifted energy calculations

Assuming projectile-target mode with a stationary target and V_{cm} the center-of-mass velocity, the resulting fusion-product's energy, E_{tot} (as seen by the Si detector) is calculated as follows:

The velocity of the proton in the rest frame is given by:

$$V_p = \sqrt{\frac{2E_f}{m_f}} \tag{7.1}$$

where E_f is the proton's energy (3.02 MeV for DD) and m_f is the fusion product's mass (here it is the proton mass). For head-on collisions, both the reacting particles have energy (say E_a & E_b) with $E_b = 0$ for a stationary target (a valid assumption for neutral background), and masses (m_a & m_b) and the center of mass (CM) velocity (V_{CM}) is given by:

$$V_{CM} = \sqrt{2}\left(\frac{m_a + m_b}{m_a m_b}\right)^{1/2} (E_a + E_b)^{1/2} \tag{7.2}$$

The number of fusion products with the respective energy, weights the energy range. In the lab frame the resultant velocity (V_{RES}) of the proton due to the center of mass velocity effect (see figure 7.2) is given by:

$$V_{RES}^2 = \left(V_p \cos\theta + V_{cm}\right)^2 + {V_p}^2 \sin^2\theta \tag{7.3}$$

Hence the total energy of the proton that the detector sees is now given by:

$$E_{tot} = \frac{1}{2} m_f V_{RES}{}^2 = \frac{m_f}{2}\left(\frac{2E_f}{m_f} + V_{CM}{}^2 + 2V_{CM}\sqrt{\frac{2E_f}{m_f}}\cos\theta \right) \qquad (7.4)$$

where E_{tot} is the energy of the ion before going through the Pb foil or the detector and 'θ' is the angle between the V_{CM} and the fusion-product's velocity (directed towards each other = 0^o).

A simple code was developed to calculate the initial Doppler broadening of the proton energies see figure 7.3 and the resultant energy deposited into the detector, figure 7.4.[4] The collisional broadening of these energy peaks is not predicted by this code and is caused by the presence of the Pb foil in the front of the detector.

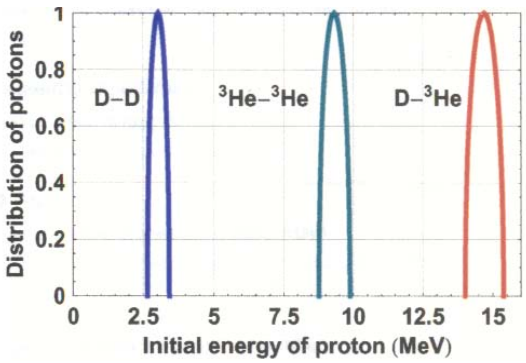

Figure 7.3 Initial doppler-shifted energy of the protons (for 100 keV reactant energy) from the IEC device before going through the 25 μm thick Pb foil or the 700 μm thick Si detector.

As the protons enter the Pb foil they get scattered and lose some energy to the foil before depositing their energy into the detector. The energies deposited into the Si detector vary according to the initial energies of the protons, and depending on the thickness of the detector, this energy varies as shown in figure 7.4.

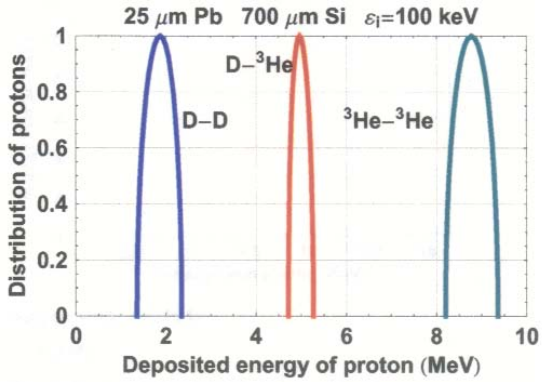

Figure 7.4 The energy deposited by the protons into the 700 μm thick Si detector is all of the energy for the D-D and ^{3}He – ^{3}He reactions and about ⅓ rd of the incident energy from the D-^{3}He reactions.

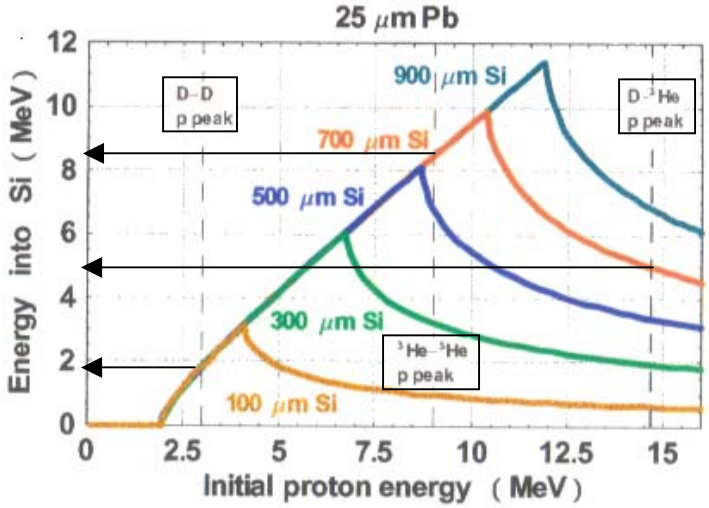

Figure 7.5 The energy deposited into the Si detector of various thicknesses vs. the initial proton energy. A 700 μm Si detector seems to be the best choice for maximum separation of the three proton peaks coming from D-D, D-^{3}He and ^{3}He – ^{3}He reactions.[4]

Depending on the thickness of the Si detector, the energetic protons tend to escape the Si detector without depositing all their energy, so it is likely that the energy peaks generated by various protons could show up at the same location (eg., 100 μm, in figure 7.5). Hence, an appropriate Si detector thickness must be selected to isolate the contributions due to various fusion reactions. This is especially crucial for D-D and D-^{3}He reactions since both these

reactions occur simultaneously when D-^{3}He fuel is used (in the present case a suitable value is 700 μm). As shown in figure 7.5, a proton from the D-^{3}He reaction has an initial energy of 14.7 MeV but it deposits only ~5 MeV into the 700 μm thick Si detector and the rest of the energy is in the form of the kinetic energy of the proton as it exits the detector.

A simple calculation of the energy deposition into the detector appears as shown in figure 7.4. The final responses (in the absence of collisional broadening) are Doppler broadened sine functions. A comparison between this prediction figure 7.4, and the experimental data in figure 7.13 show discrepancy (0.87 MeV for D-D and 0.47 MeV for D-^{3}He) in the FWHM values. This is because the predictions in figure 7.4 do not account for the broadening due to scattering collisions in the Pb foil and the Si detector. This is accomplished in the present study using the Monte Carlo – Stopping and Range of Ions in Matter (SRIM) code.[5]

SRIM is a group of programs that calculates the stopping and range of ions (10 eV – 2 GeV/amu) into matter using a full quantum mechanical treatment of ion-atom collisions.[6] This calculation has been made very efficient by the use of statistical algorithms that allow the ion to make jumps between calculated collisions and then averaging electron shells. The ion has long-range interactions creating electron excitations and overlapping electron shells. These are described by including a description of the target's collective electronic structure and inter-atomic bond structure when the calculation is set up. The charge state of the ion within the target is described using the concept of effective charge, which includes a velocity dependent charge state and long range screening due to the collective electron sea of the target. Such details in the SRIM calculations increase the accuracy of the collisional broadening calculations.

TRIM (the Transport of Ions in Matter) code included in the SRIM mentioned above is a comprehensive program that accepts complex targets made of compound materials with up to eight layers, each of different materials. This code (TRIM) calculates the final 3D distribution of the ions and also all kinetic phenomena associated with the ions' energy loss: target damage, sputtering, ionization, and phonon production. All target atom cascades in the target are followed in detail.

7.3 Algorithm for calculation of the total DD proton energy broadening

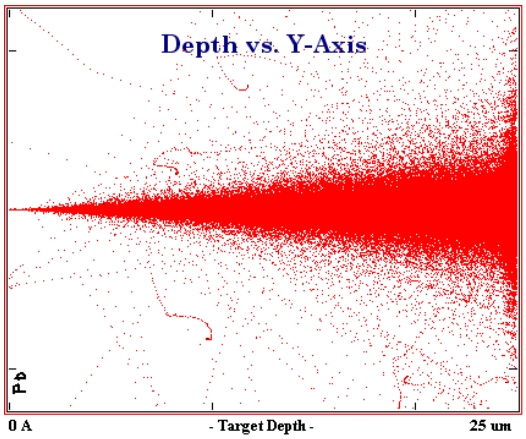

Figure 7.6 Distribution of the scattered D-D protons in a Pb foil shows very little backscattering but the forward scattering is high and hence these protons lose a lot of energy to the 25 mm thick Pb foil when compared to the energetic D-^{3}He protons.

Protons generated from the fusion reactions D-D and D-^{3}He were treated separately. In order to account for the broadening caused by collisions for the protons from the D-D reactions, the following algorithm was used:

1. The Doppler-broadened energy peak for D-D in figure 7.3 is divided into equally spaced energy bins.

2. The same number of particles (5,000 per bin) is used as input to the TRIM code, and each set of the protons is given the energy value of a single energy bin. Using 10,000 particles ensured that the final result had only ~1.4 % error.

3. The energy distribution of the particles at the exit end of the Pb foil is thus computed. The energy distribution observed for the D-D protons exiting the Pb foil is the same as the energy deposited into the Si detector since these protons deposit all their energy into the detector upon exiting the Pb foil. An example of the proton scatter is given in figure 7.6 and the angular distribution is given in figure 7.7

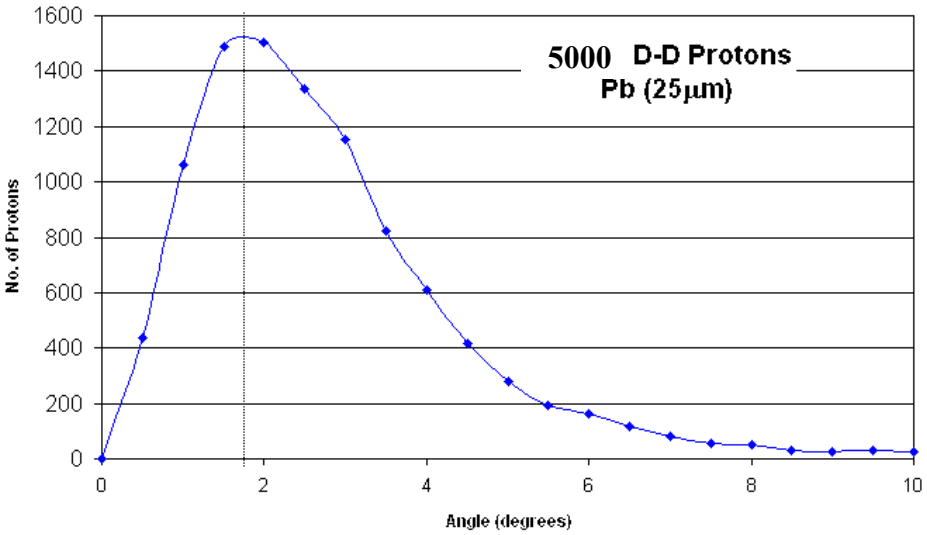

Figure 7.7 Angular distribution of the scattered D-D protons in a 25 μm Pb foil.

4. The energy distribution peak thus generated is weighted (multiplied by) by the corresponding sinθ value in table 7.1

Table 7.1 Energy bin (input) values for the D-D protons. The output peaks are weighted to the Sinθ (second column) value corresponding to each of the energies.

Sl. No.	Sin θ	Ein
1	0.130526	2.65
2	0.382683	2.67
3	0.608761	2.72
4	0.793353	2.79
5	0.92388	2.88
6	0.991445	2.98
7	0.991445	3.08
8	0.92388	3.18
9	0.793353	3.27
10	0.608761	3.34
11	0.382683	3.39
12	0.130526	3.42

5. The process repeats step 1 through step 4 until the peaks are generated for each of the energy bins.

6. A profile of the peaks thus generated represents the overall Doppler and collision broadened energy peak for the D-D protons. Following the above algorithm the data generated is plotted in figure 7.7.

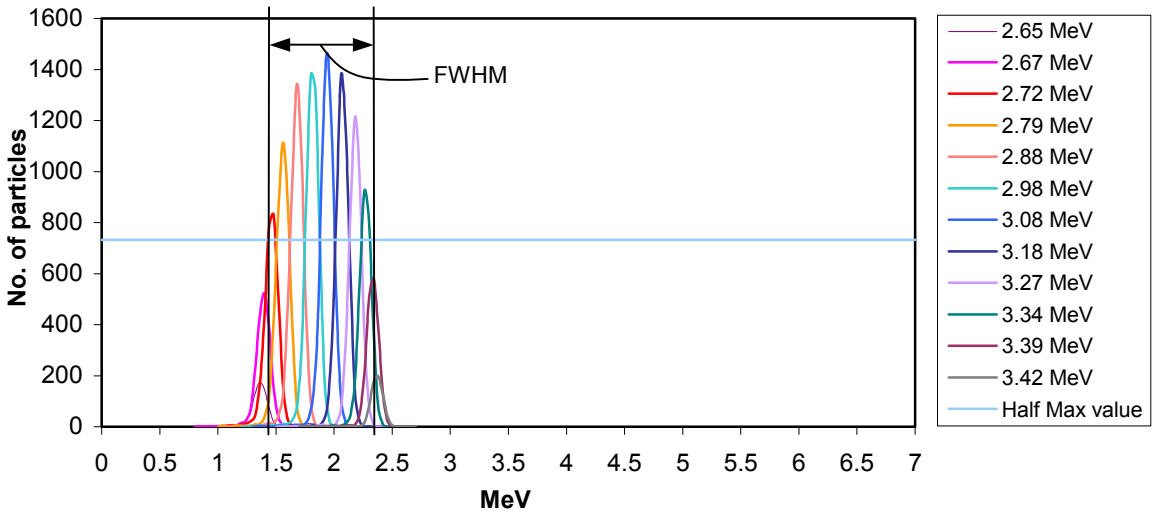

Figure 7.8 SRIM prediction of Doppler and collision broadened D-D proton energy peak.

7.4 Algorithm for calculation of the total D-^{3}He proton energy broadening

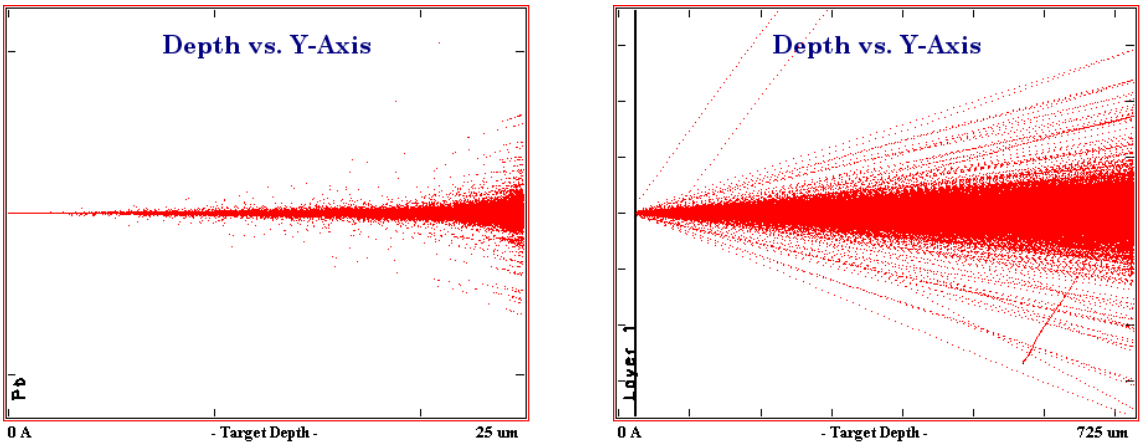

Figure 7.9 (a) Distribution of the scattered D-^{3}He protons in a Pb foil (b) The proton scatter in the Si detector. Although Pb foil is used, since the input file has the position information, the computation starts only at the boundary of the Pb foil where the Si detector boundary begins.

For D-^{3}He the situation is a little more complicated since the D-^{3}He protons deposit only partial amount of their initial energy. The following algorithm was used in generating the Doppler and collision broadened D-^{3}He proton energy peak:

1. The Doppler-broadened energy peak for D-^{3}He in figure 7.3 is divided into equally spaced energy bins.
2. 5000 particles (to speed up the process) are used as input to the TRIM code, and each set of the protons is given the energy value of a single energy bin from step 1. The choice of 5000 particles per bin ensured that the error was at a tolerable limit of ~1.4%.
3. The energy distribution of the particles at the exit end of the Pb foil is computed and saved (E_{Pb}). For example, the scattering of the energetic (14.7 MeV) protons is shown in figure 7.9(a) and the angular distribution of the scattered particles is shown in figure 7.10.

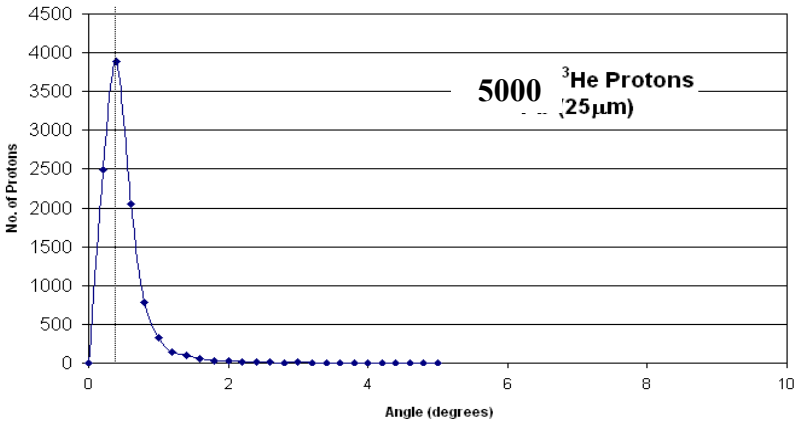

Figure 7.10 Angular distribution of the scattered D-^{3}He protons exiting a 25 μm Pb foil.

4. E_{Pb} is used as the input to the TRIM code for the Si detector geometry. Each of the 5000 particles in E_{Pb} is run through the Si detector geometry and a second energy distribution E_{Si} is generated at the exit of the Si detector. A sample of the scattered proton distribution is shown in figure 7.9(b).
5. The energy distribution E_{Si} for the $P_{D\text{-}^3He}$ is then saved for all the 5000 particles.
6. The energy deposited into the Si detector is then computed $E_{det} = E_{Pb} - E_{Si}$ as shown in figure 7.11.
7. Steps 1 through 6 are repeated until all the energy bins are used

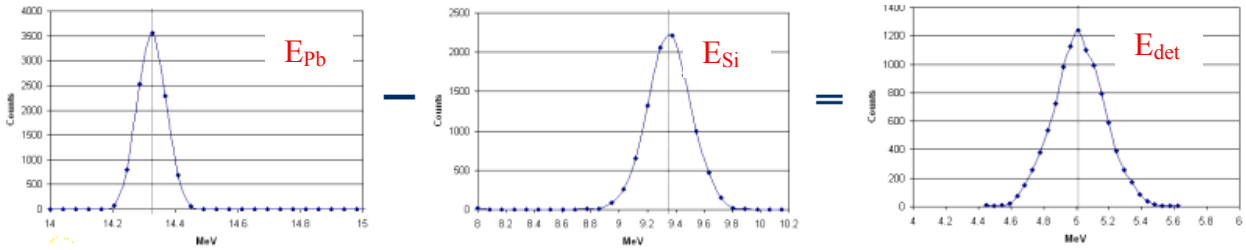

Figure 7.11 The difference between the proton energy after it has exited the Pb foil with that after exiting the Pb + Si detector geometry is the energy deposited into the Si detector.

Table 7.2 Energy bin (input) values for the D-^{3}He protons. The output peaks are weighted to the Sinθ (second column) value corresponding to each of the energies.

Sl. No.	Sin θ	Ein
1	0.130526	14.01
2	0.382863	14.07
3	0.608761	14.14
4	0.793353	14.27
5	0.92388	14.43
6	0.991445	14.60
7	0.991445	14.78
8	0.92388	14.90
9	0.793353	15.11
10	0.608761	15.23
11	0.382683	15.32
12	0.130526	15.37

8. Each of the peaks (E_{det}) generated is weighted by the corresponding $\sin\theta$ value from table 7.2. The profile of these weighted peaks gives the overall Doppler and collision broadened energy peaks for the D-^{3}He protons as shown in figure 7.12.

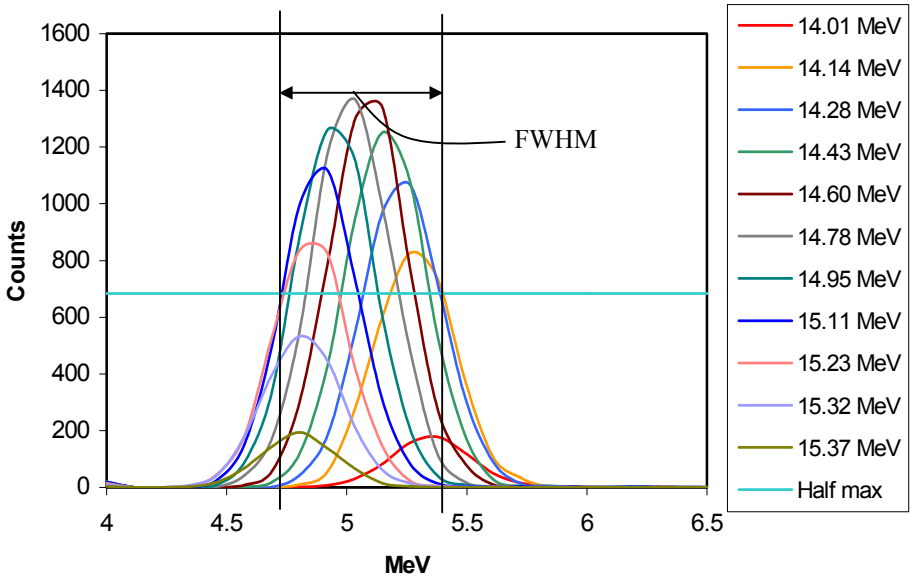

Figure 7.12 SRIM prediction of Doppler and collision broadened D-^{3}He proton energy peak.

The FWHM values of the Doppler-shift and collision broadened peaks computed using SRIM in figure 7.8 & 7.12 are compared with the experimental data figure 7.13 in the

table 7.3. The error in the experimental data is the inverse of square root of the number of particles detected.

Table 7.3. Experimental and theoretical values agree well, but the errors might be large since there is scatter in the proton's experimental data, figure 7.13.

Proton Peak	Experimental value	Predicted value
D - D	2 x HWHM ~ 1 MeV ± 0.1 MeV	0.95 MeV ±0.01 MeV
D – ^{3}He	FWHM ~ 0.8 MeV ± 0.1 MeV	0.7 MeV ± 0.01 MeV

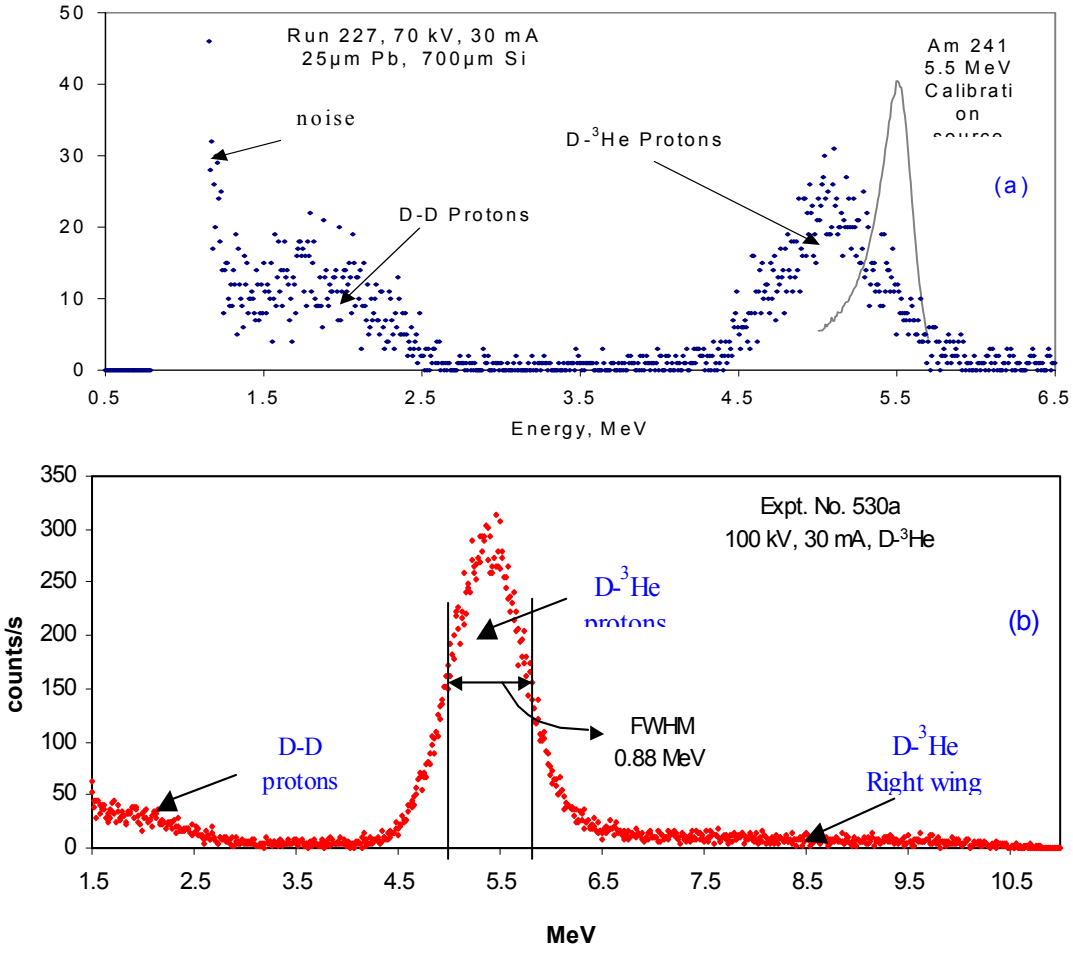

Figure 7.13 (a) First simultaneous measurement of D-D and D-^{3}He peaks in an IEC device. Data acquired for 60s. (b) Data collected using the 700 µm thick Si detector with 25 µm thick Pb foil in the front, in an IEC device (with D_2 + ^{3}He fuel) shows the D-D and D-^{3}He peaks simultaneously. As predicted earlier the 14.7 MeV D-^{3}He proton peak shows up at ~ 5 MeV. The D-^{3}He proton peak shows broadening (right wing). Data was acquired for 420s.

Figure 7.13 (a) illustrates the first simultaneous measurement of DD and D-^{3}He protons that established that D-3He reactions do occur in the IEC device. Figure 7.13 (b) shows the simultaneous measurement of DD and D-^{3}He protons in an IEC device with D-^{3}He fuel, at 100 kV, 30 mA. The D-D peak is weaker than the D-^{3}He peak, because only a small fraction of the D-^{3}He fuel (depending on fuel ratio, chamber pressure, etc.) undergoes D-D reactions. An interesting feature noticed in almost all the D-^{3}He proton spectra is the "right wing" shown in figure 7.13. This broadening of the D-^{3}He proton peak is above noise level and is observed to taper off beyond 10 MeV. This is not created by the ^{3}He-^{3}He reactions because the cross-section values for the ^{3}He-^{3}He reactions are small.

The average range of ^{3}He atoms at 100 kV energy in the cathode grid wire is ~0.25 μm, while that of deuterium ions is ~ 0.5 μm as shown in figure 7.14. Hence, most D-^{3}He reactions would occur in the first 0.25 μm thick surface layer of the cathode grid wire.

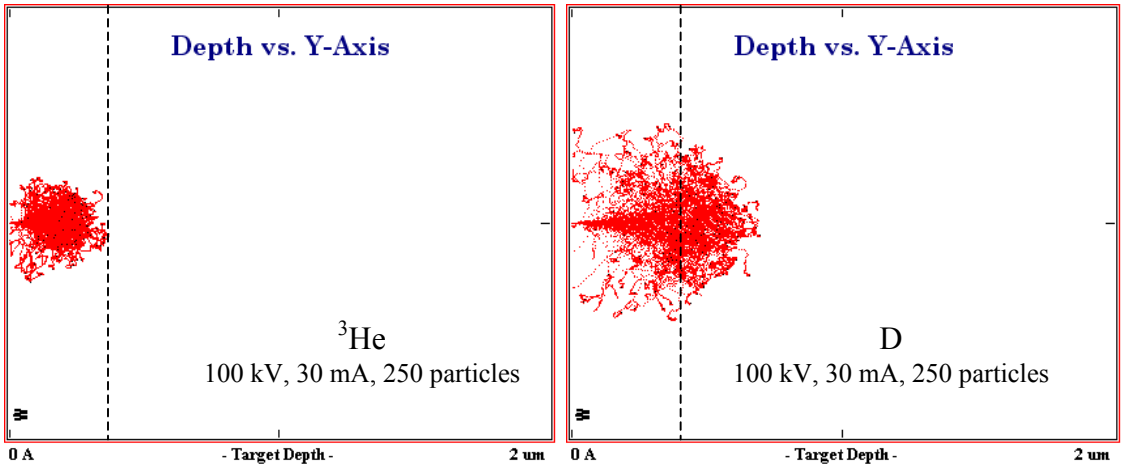

Figure 7.14 SRIM predictions of the ion (D^+ & $^3He^+$) scatter in W. Since the maximum depth at which ^{3}He exists is 0.25 μm, all D-^{3}He reactions occur above this depth. Although diffusion may occur.

A proton from a D-^{3}He fusion event at any point C, as shown in figure 7.15 has equal probability of liberation in all directions. The protons liberated in the direction CA have to go through the maximum thickness of the grid material before being detected by the Si detector. Any protons generated to the left of point C in figure 7.15 would have to go through even more material (transmit) and hence would lose relatively more energy to the grid wires.

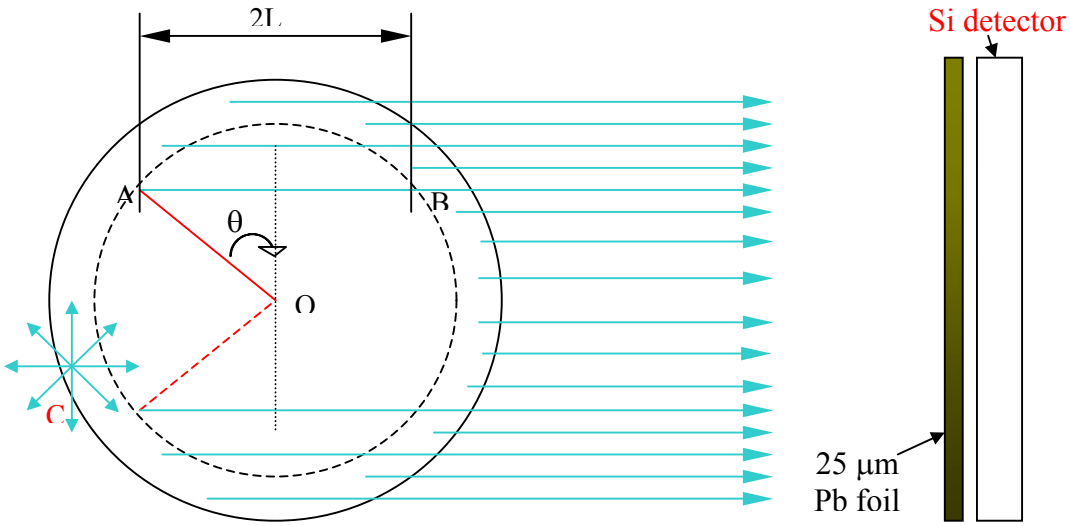

Figure 7.15 Cross-section of the W-25%Re wire. D-^{3}He protons are born isotropically on the surface of the grid wires as shown at the point C. Protons born behind the wire have to pass through greater thickness of material before reaching the detector. Figure not to scale.

The fusion occurs everywhere on the surface of the grid wire, and hence the protons would have to go through various thicknesses of the wire. Since the protons going through an effectively higher thickness of the grid wire are concentrated close to the two poles of the wire (top and bottom orientations with respect to the detector), such protons contribute to the right wing of the D-^{3}He peak as shown in figure 7.13. There are few counts beyond 10 MeV because of the Bragg peak response of the Si detector explained in the Section (7.2).

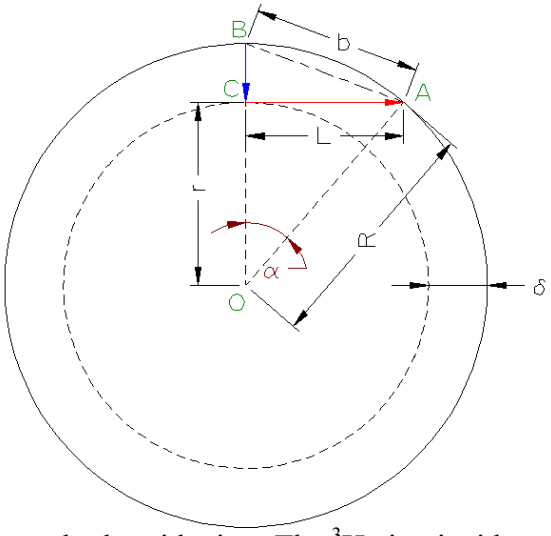

Figure 7.16 Cross-section of the cathode grid wire. The ^{3}He ion incident from the top of the wire deposits its energy into the wire along BC and finally comes to a rest at the point C (at a depth δ). Figure not to scale.

The maximum effective thickness L (as shown in figure 7.16), through which the D-^{3}He proton generated at the point C has to pass before reaching the Pb foil in front of the detector is given by

$$L^2 = R^2 - (R - x)^2 \Rightarrow L = \sqrt{2Rx - x^2} \qquad (7.1)$$

If x = δ (the range of $^3He^+$ ions in the W25%Re grid wires), then neglecting the second order (δ^2) term ($\because \delta << R$) we get

$$L \approx \sqrt{2R\delta} \qquad (7.2)$$

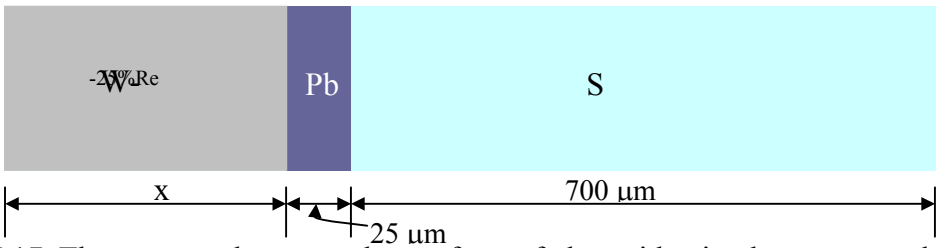

Figure 7.17 The protons born on the surface of the grid wire have to go through different thicknesses of the grid wire before reaching the Si detector.

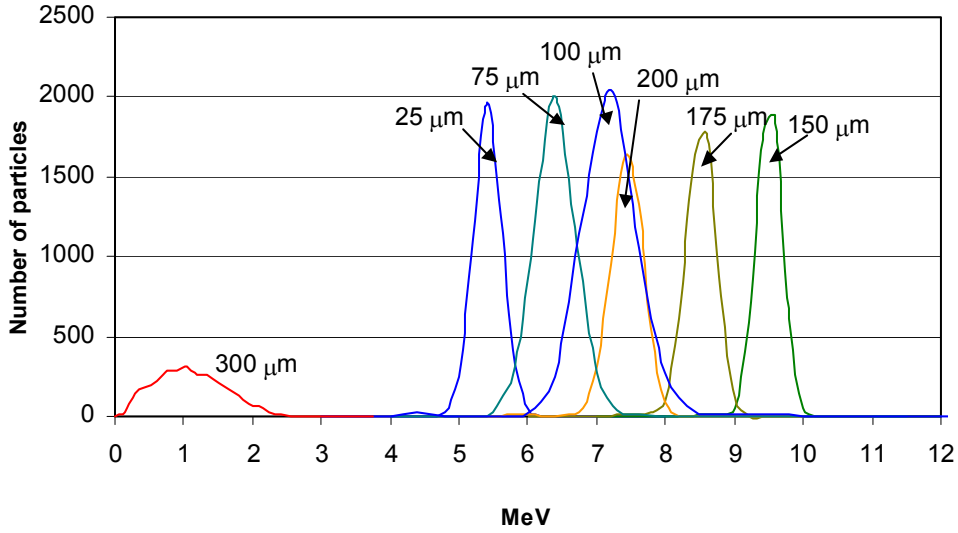

Figure 7.18 As the thickness of the wire increases the energy deposited into the proton detector increases up to a maximum of 10 MeV and then it decreases.

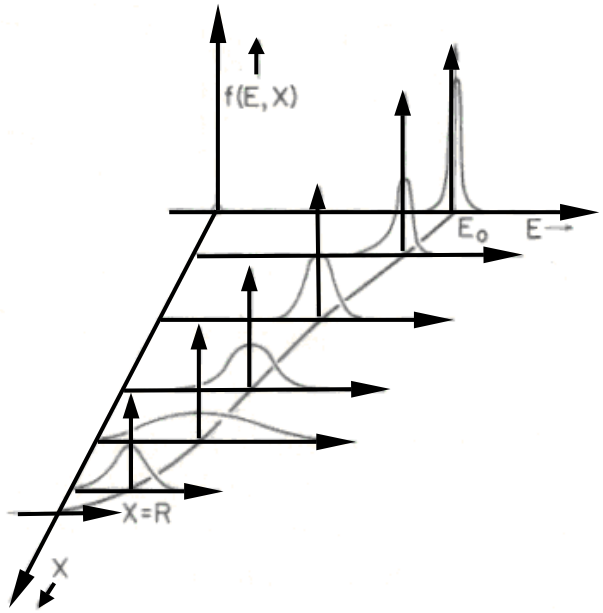

Figure 7.19 Plots of energy distribution of a beam of initially monoenergetic charged particles at various penetration distances. E is the particle energy and X is the distance along the track.[7]

With this understanding that the protons have to transmit not only through the Pb foil and the Si detector, but also the grid wire we now calculate the energy deposited into the Si detector. With the geometry shown in the figure 7.17 below and the algorithm explained earlier for the D-

^{3}He protons (section 7.4) using the SRIM code the energy deposited into the Si detector is computed. The peaks generated using 5000 particles in the SRIM code for various values of x (=25 μm, 100 μm, 150 μm, 175 μm, 200 μm and 300 μm) are plotted in figure 7.18. From figure 7.18 it is observed that up until x ~ 150 μm the energy deposited into the Si detector increases, beyond which the energy deposited decreases because of the energy staggering Bragg peak response of the proton detector explained earlier in Section 7.2. The variation of the energy peak and its width would vary with thickness of the wire through which the protons have to pass, as shown in figure 7.19.

Assuming 'δ' is small, the maximum distance through which the D-^{3}He protons would have to traverse before reaching the detector 2L is 300 μm, see figure 7.17 and figure 7.18. The protons born on the side facing the detector do not have enough material to attenuate their energies and hence contribute to the main peak. But those protons born behind the front face of the wire (with respect to the detector) as shown in figure 7.15 including some of those born at an angle see more material than δ before exiting the wire. The energy that the D-^{3}He protons lose to the grid material are responsible for the counts that show up in the right wing of figure 7.13.

The angle θ in the figure 7.15 is given by $\theta = \sin^{-1}\left(\frac{L}{R}\right)$ where $L \approx \sqrt{2Rx - x^2}$ from equation 7.1. Substituting L = 150 μm and R = 838 μm, we get θ ≈ 10.3^o. Hence the right wing in the figure 7.13 is mostly coming from the two sections behind the front face of the detector spanning a total angle of 20.6^o. The total number of counts that come from the front face of the grid wire without any attenuation show up in the D-^{3}He peak at 5.5 MeV, while those protons born in the rear of the grid wire that get attenuated by the grid wire show up as the right wing in

figure 7.13. Since the number of protons that make it to the detector from behind the grid wire is a small fraction of the total number of protons, besides spreading over the energy range of 0 – 10 MeV, the overall intensity of the right wing is low. The ratio of protons from the main peak to those from the right wing in figure 7.13 is ~ 10. Though, the right wing is only 10% of the total counts, it is important to understand where they originate. This knowledge would be more helpful for applications such as medical isotope production where the reactions occurring on the surface of a tube are used to create the positron emission tomography (PET) isotopes.[8]

7.5 Conclusions

The major causes of the proton energy peak broadening from both DD and D-^{3}He reactions are identified to be Doppler effect and scattering in the material it transmits through. Two algorithms were developed to predict the observed (DD and D-^{3}He) proton energy broadening. Using these algorithms the above-mentioned broadening mechanisms were simulated using the Monte Carlo - SRIM code and confirmed experimentally.

The anomalous extreme broadening (right wing) of the D-^{3}He proton energy peak is theoretically proved to be caused by the protons born on the rear side of the wire (with respect to the Si detector). Hence the whole energy spectrum of the DD and D-^{3}He protons is now understood and explained. The agreement between the theoretical predictions and the experimental data is within ~10%.

7.5 References

[1] G. F. Knoll, "Radiation Detection and Measurement," Third edition, (2000) pg. 377.

[2] Z. Kis et al., Nucl. Instrum. Meth. **A418**, 374 (1998)

[3] D.C. O'shea, W. R. Callen and W. T. Rhodes, "Introduction to lasers and their applications," Addison-Wesley publishing company, 1977, pg. 82.

[4] J. F. Santarius, Private communications, 2002.

[5] J. F. Ziegler, "The Stopping and Range of Ions in Matter," Instruction manual, Ver. 96.xx, Feb. 25, (2004)

[6] J. F. Ziegler, J. P. Biersack and U. Littmark, "The Stopping and Range of Ions in Solids," Pergamon Press, New York, 1996.

[7] B. Wilken and T. A. Fritz, Nucl. Instrum. Meth. **138**, 331 (1976).

[8] B. Cipiti and G. L. Kulcinski, "Embedded D-3He fusion reactions and medical isotope production in an inertial electrostatic confinement device," Fusion Technology and Science, Vol. 44, Sep. 2003.

Chapter 8.0: Measurement of average ion energy in an IEC device

A recent effort to measure the average ion energy[1] in a linear IEC device involved the use of Doppler-shift visible spectroscopy of H_3^+ ions due to charge exchange reactions. The ambient pressure in the chamber was relatively high, 10 – 16 mtorr, which aided the formation of H_3^+ ions, and also the intensity of light from the core plasma was high in this pressure regime.

It was found that the ion energy distribution consisted of a non-Maxwellian directional component, as well as a spatially isotropic Maxwellian distribution.[2] The directional components consisted of three broadened energy peaks belonging to H_3^+ (20%), H_2^+ (60%), and H^+ (20%).[3] These ions had approximately 20% of the cathode potential.

However, at lower pressures of operation, as in the present case (2 mtorr), the above distribution of various ion concentrations will not remain constant. Since the visible light coming out of the core is very faint and the background reflections of the filament light dominates the spectrum, this method is not very attractive at low pressures.

A new technique is developed that uses the Doppler broadening of the proton energy peaks to determine the average ion energy. This technique is independent of pressure because it

is free of the visible light from the plasma, which in general requires high-pressure operation of the IEC device.

8.1 Linear Doppler broadening of the proton energy peak as a diagnostic to measure the average ion energy in an IEC device

The protons generated in various fusion reactions mentioned in Chapter (2) have information about the reactant energy in the form of a Doppler shift in the energy. Since the reacting ions have velocities in all directions, a uniform Doppler broadened peak is usually observed in an IEC device.

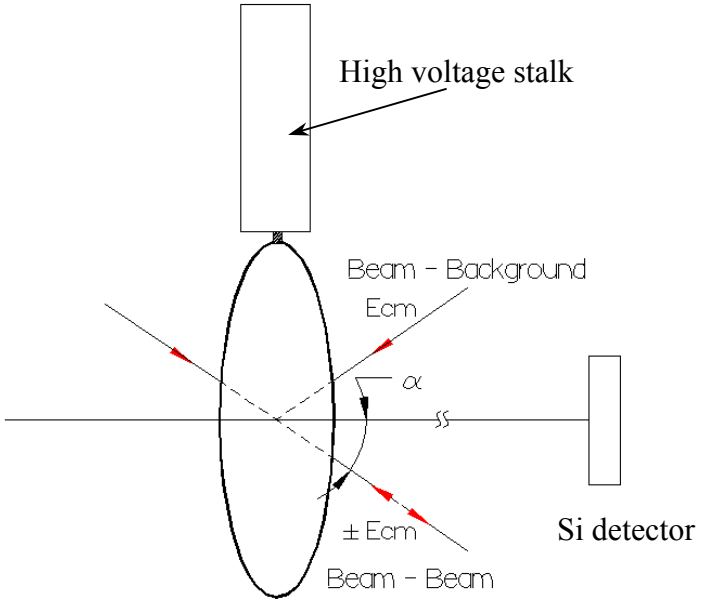

Figure 8.1 Single loop grid oriented face-on with the Si detector

The linear Doppler broadening is observed only when the ions recirculate (oscillate) along a straight line (or close to a straight line). However, such ion recirculation along a straight line cannot be accomplished using a spherical cathode grid. Hence, the spherical grid is replaced by a single loop of 10 cm diameter wire, made of W-25%Re (same material as the grid) as shown in figure 8.1.

With the single loop configuration (figure 8.1) the ion velocity distribution becomes linear as shown in figure 8.2 and is reflected in the proton energy peak that shows a doublet feature (explained later).

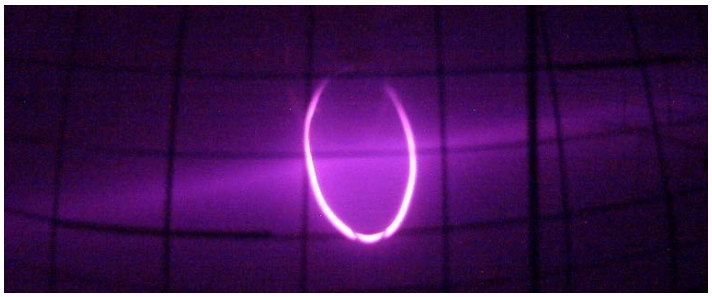

Figure 8.2 Picture of the recirculating ion flow using single loop grid at relatively high pressure (7.5 mtorr, 10 kV, 5 mA).

In the geometry shown in figure 8.1 (also see figure 8.2) the ions recirculate in paths that are close to a straight line, so the angle α is small. Hence we may set $\theta = \alpha \approx 0$ in eqn. 7.4. This gives two values for E_{tot} as shown in eqn. 8.1.

$$E_{tot} = \frac{m_f}{2}\left(\frac{2E_f}{m_f} + V_{cm}{}^2 \pm 2V_{cm}\sqrt{\frac{2E_f}{m_f}}\right) \qquad (8.1)$$

Hence a double peak is observed in the proton data. However, these two peaks are not very distinct and a rather dispersed double peak distribution is observed in the experimental data, figure 8.3. This is because the ions are not monoenergetic. Through the present model we can determine the most probable energy of the ions which is close to the average ion energy within the plasma. In the present model we assume that all reactions are beam-background reactions, where the neutral is stationary and an energetic recirculating ion undergoes fusion with it (see Chapter 7.0 for further details).

The double peaks observed in figure 8.2 at 50 kV, 10 mA, 2 mtorr are not of equal height, the low energy peak is shorter; because the protons falling in this energy range tend to lose more energy to the Pb foil in front of the Si detector than the high-energy protons. This is supported by the SRIM output data as shown in figure 8.3. Two peaks per reactant energy (assuming E_f equals 50 keV and 30 keV) are plotted along with the raw proton data from the Si detector in figure 8.4.

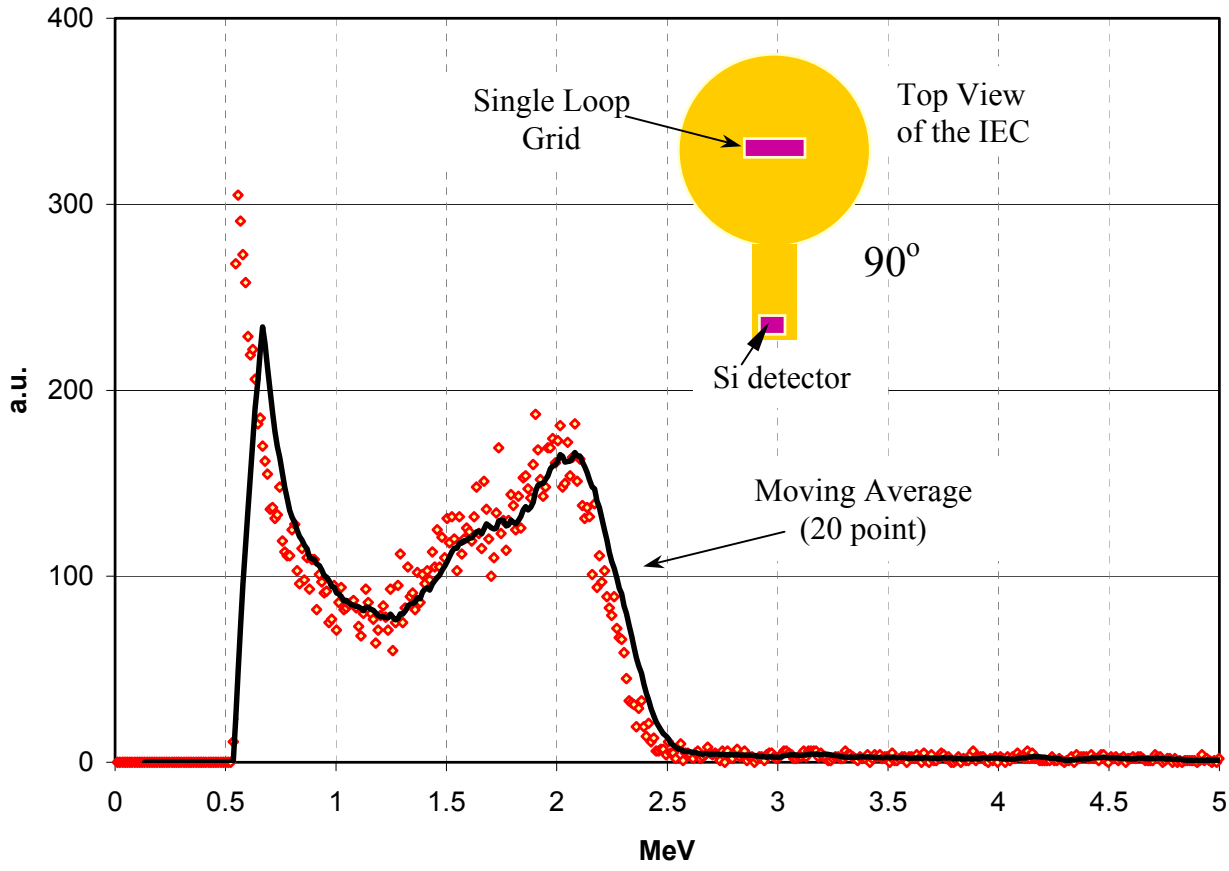

Figure 8.3 A double peak is observed in the D-D proton data for 50 kV applied voltage when a single loop is used as the central grid with face-on orientation (90°). A 20 point moving average fit to the proton data shows a double peak feature at ~1.7 MeV and ~2.0 MeV. (The peak to the left is noise.)

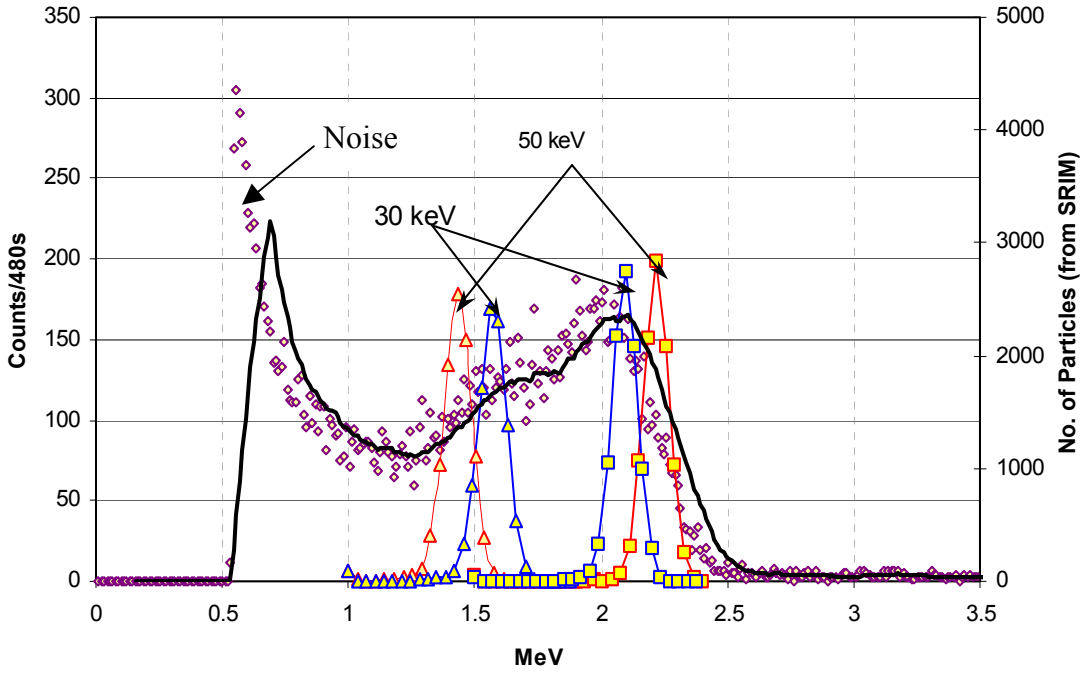

Figure 8.4 Doppler-shifted and collision broadened proton energy peaks of protons generated using the SRIM code are plotted along with the raw data. A 20 point moving average fit is performed for the raw data. The peak to the left is noise.

The two lower peaks are shorter than the other two; this pattern is also observed in the raw data. Sharp peaks are not observed in the raw data because the ion recirculation is not exactly along a straight line, besides the ions are not monoenergetic as mentioned earlier. This gives some variation to the angle α in the eqn. 8.1 and hence a rather continuous distribution (with a double peak feature) is observed in the raw proton counts.

The present analysis is based on fitting the raw data with the theoretical predictions of the SRIM code and hence is tedious and cannot predict values better than ±10% variation. Despite these limitations is the only method available to measure the average ion energies of the ions at low pressures within the IEC device.

In this case, for an applied voltage of 50 keV, most ions are getting accelerated to a maximum of 30 keV ± 5 keV (60% ± 10% of the applied voltage) at 2 mtorr chamber pressure. The error in

this technique can be reduced by fitting the raw data appropriately using various peaks generated using SRIM code, each of these peaks uses different proton input energies, calculated using eqn. 7.4 by varying both the reactant energy and the angle 'θ' in small variations to a maximum value determined by the grid rotation experiment, (see Chapter 13).

Compared to the measurements at 10 mtorr using visible spectroscopy where the ions were accelerated to roughly 20% of the applied voltage, the average ion energy is approximately 60% of the applied voltage at 2 mtorr and hence by reducing the pressure by a factor of 5, the average ion energy increases by a factor of 3.

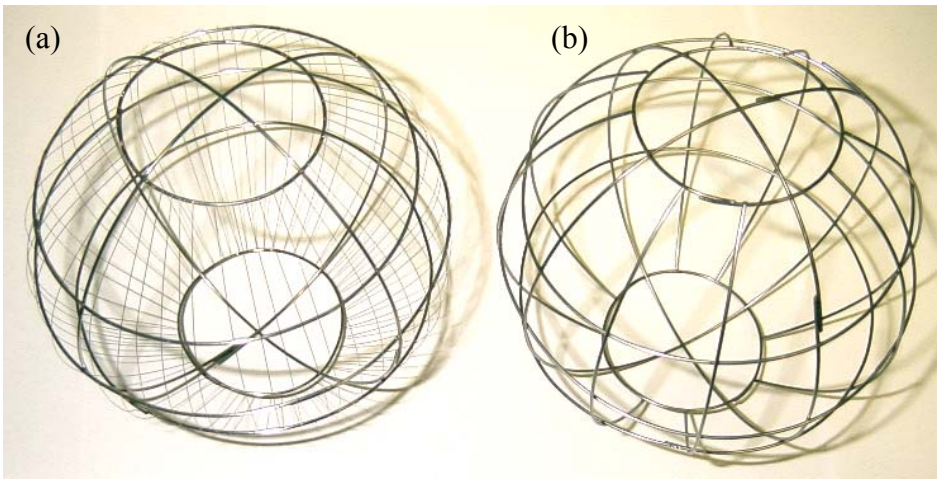

Figure 8.5 (a) Fine mesh grid of equivalent transparency (92%) as the original grid in (b) Grid with regular 5 latitudes and 12 longitudes.

From the above argument it is clear that, when the pressure is decreased, the ions get accelerated to higher energy. This is further supported by the fact that the temperature of the grid wires [fine mesh grid with constant transparency, see figure 8.5 (a)] measured at a constant location on the equator of the grid increases as the pressure is decreased, figure 8.6. This temperature variation is not caused by the convection of heat by the fuel gas to the chamber walls.[4] Calculations (see Appendix B) show that the heat transferred from the grid to the

chamber wall through convection (by drifting chamber pressure) is too small to account for the huge temperature variation in figure 8.6. A fine mesh grid is used to decrease the effects of microchannel formations on the grid temperature.

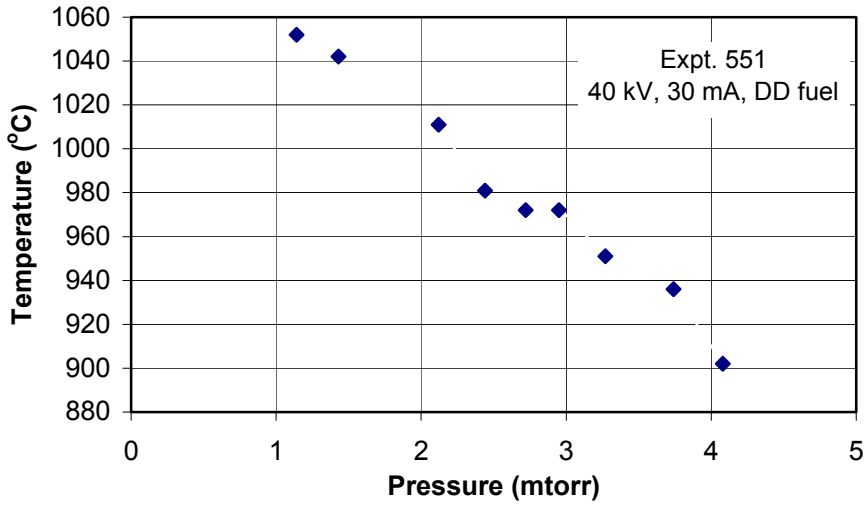

Figure 8.6 Variation of temperature with pressure at 40 kV, 30 mA at a constant spot on the fine mesh cathode.

While the ions inside the chamber at 16 mtorr pressure were accelerated to only 15% of the applied voltage,[3] the ions are now (at 2 mtorr) accelerated to 60% ± 10% of the applied voltage. This can be explained in terms of the mean free path of the ions inside the chamber. At 16 mtorr the mean free path of the particles (D_2 molecules) is only 1 to 2 cm while the mean free path of the ions at 5 mtorr is 5 cm, and at 1 mtorr it is ~100 cm (greater than the dimension of the chamber). Hence the ions have a better chance to gain energy from the electrostatic fields at lower pressures and hence the average ion energy is higher at low pressure. This gives an incentive to aim for lower pressure operation of the IEC device to improve the efficiency of the device.

8.2 References

[1] J. Khachan, and S. Collins, "Measurements of ion energy distributions by Doppler shift spectroscopy in an inertial-electrostatic confinement device," Phys. Plasmas, Vol. 8, No. 4, April 2001.

[2] J. Khachan, D. Moore and S. Bosi, "Spatial distribution of ion energies in an inertial electrostatic confinement device," Phys. Plasmas, Vol.10, No. 3, March 2003.

[3] J. Khachan, and S. Collins, "Measurements of ion energy distributions by Doppler shift spectroscopy in an inertial-electrostatic confinement device," Phys. Plasmas, Vol. 8, No. 4, April 2001.

[4] G. A. Emmert, University of Wisconsin, Madison, Private communications, (2002).

Chapter 9.0: CHORDWIRE EXPERIMENTS

High power (>10 kW) operation of IEC devices can generate secondary, thermionic, photo, and field emission electrons from the cathode grid that are a drain on the system. Methods to study and minimize the thermionic emission current are discussed in this chapter using a new diagnostic called chordwire(s) – wires placed in the form of a chord of a circle inside the central grid to intercept the inflowing ions. Local power balance on the wires can then be used to infer the ion flux from the measured temperature. Experimentally measured ion flow patterns into the central grid and their consequences are also reported.

9.1 Chordwire configurations

Several different configurations of wire arrangements shown in figure 9.1 were used to determine the effect of thermionic electron emission. In the diagwire configuration shown in figure 9.1 the chordwire runs across the spherical cathode along a diameter. This wire intercepts most ions and has been observed to reach the highest temperatures among any other chordwire configuration. The cylinwires configuration is an arrangement of wires 'cylindrically' that runs from the topmost latitude to the bottommost latitude. A picture of such an arrangement is shown

in figure 9.2. These wires are symmetric about the vertical axis and the electrons liberated from these wires populate the central region along the vertical axis.

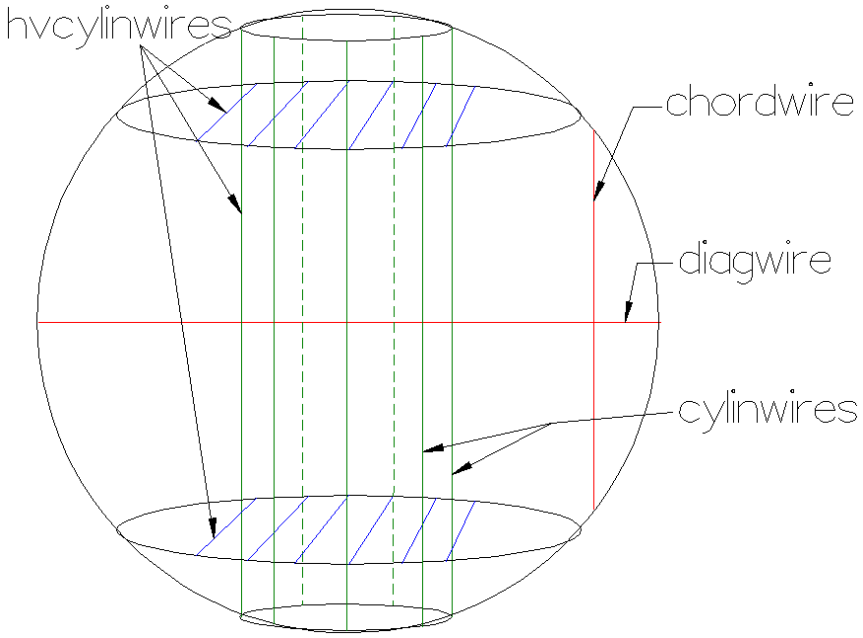

Figure 9.1 Various configurations of the chordwire arrangements inside the cathode used in the chordwire experiment.

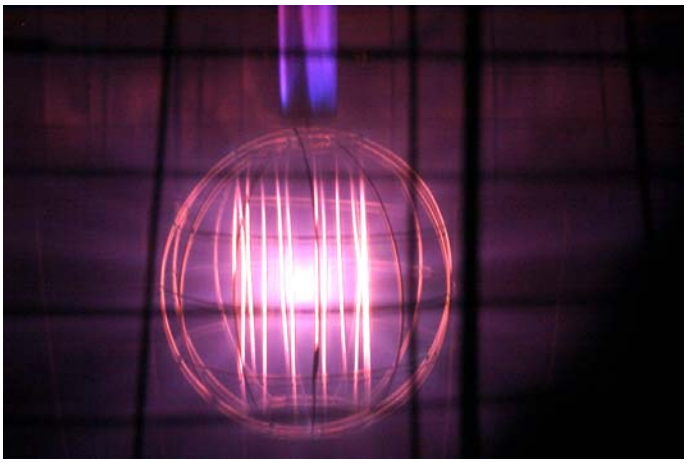

Figure 9.2 Cylinwires configuration. The chordwires are placed such that they run from the topmost latitude to the bottommost latitude. All wires tend to reach approximately the same temperature at a given voltage and current (± 30^{o}C).

With the addition of two sets of wires placed horizontally (horizontal relative to floor) across the two latitudes as shown in figure 9.1 one produces the hvcylinwires configuration.

Each of the above mentioned configurations was studied separately and required that the central grid be removed to change the configurations. After replacement several conditioning runs were performed before the data was acquired in order to reduce the impurity concentration.

A disadvantage with these configurations is that with increasing temperature the wires tend to get deformed due to thermal expansion and the centers of these wires are displaced (~ 1 mm) and have to be accounted for. However, for the ion-flux mapping experiment the wires were placed far from the core (at least 2 cm away). Hence the deformation of such wires was tolerable and no corrections were made for such measurements.

9.2 Thermionic emission

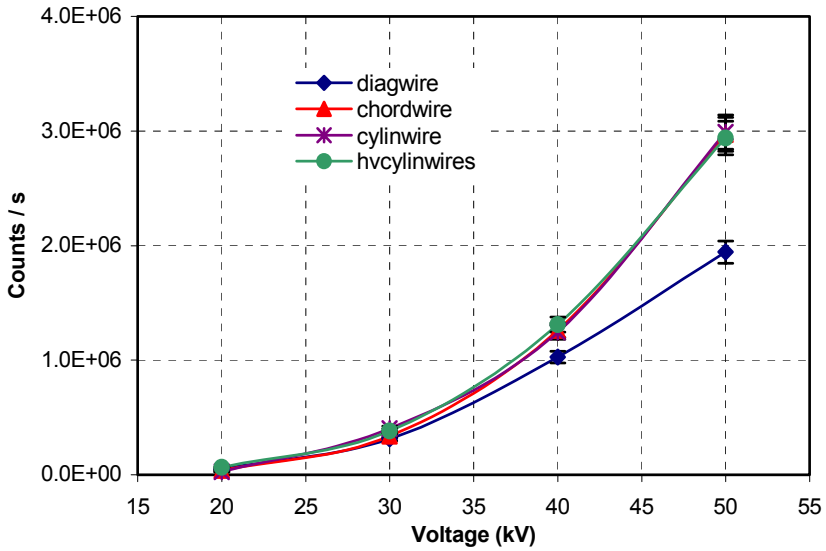

Figure 9.3 The neutron production with various grid configurations. The lowest neutron rate is observed with the diagwire configuration at a constant current of 20 mA.

Owing to their low work function (2.5 eV), thoriated tungsten wires were used to study the influence of thermionic emission on the total fusion rate. As shown in figure 9.3, the diagwire configuration showed the lowest neutron production rate, at 50 kV. The meter current was maintained constant at 30 mA. This is because the wire became extremely hot (≥1170 ^{o}C)

as can be seen in figure 9.4. This caused excessive electron liberation from the wire, and formed concentrated jets. When these electron jets were incident on the view window as shown in figure 9.5, excessive localized heating occurred that cracked the view window. Such electron jets were observed in other configurations but were not intense enough to crack the window.

Figure 9.4 Diagwire configuration. The wire is placed along the diameter across the central grid parallel to the ground surface.

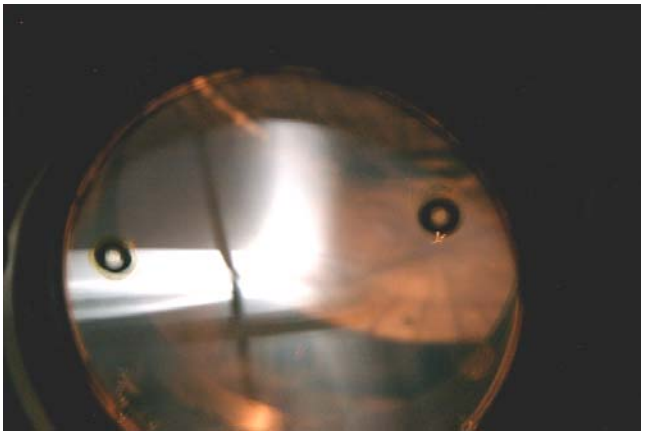

Figure 9.5 Intense electron jet from the diagwire configuration hitting the view window.

The ammeter (in the power-supply) cannot differentiate between the electrons leaving the cathode or the electrons lost due to ions reaching the cathode (recombination). The recombination process does not cause a charge build up because the electron generated during the ionization process completes the circuit. The additional electrons from the thermionic

emission resulted in an effective lower ion current (since the sum of the two currents is a constant, the measured power supply current) and hence an overall lower fusion rate is observed. Therefore thermionic emission has to be minimized to realize higher fusion rates if the grid heating causes a significant heating of the wire.

A general equation for ion recirculation current from Thorson et al.,[1,2] has been modified to account for thermionic emission as follows:

$$I = \frac{\eta\left[I_{meas} - I_{th}\right]}{\left(1-\eta^2\right)\left(1+\delta\right)} \qquad (9.1)$$

$$\text{where } I_{th} = \Lambda \cdot A \cdot T^2 \cdot e^{-e\phi/kT} \qquad (9.2)$$

is known as the Richardson-Dushmann equation[3,4] for thermionic emission, with T the temperature in K, k is the Boltzmann constant, A is the surface area of the heated diagwire monitored by the pyrometer (~ 0.06 cm^2), 'Λ' is a constant (~120 $A \cdot cm^{-2} \cdot K^{-2}$), I_{meas} is the (measured) power-supply current (20 mA, for the diagwire experiment), η is the transparency of the grid (~92%), ϕ is the work-function of the wire (2.5 eV) and δ is the secondary electron emission coefficient, which is assumed[1] to be ~1. All other effects are assumed to be negligible so that they would not change the average ion energy sufficiently to alter the secondary electron emission or the number of passes through the core.

From figure 9.5 we notice that the neutron rate for the diagwire configuration at 50 kV is ~30% lower than for the other configurations. At 50 kV, 20 mA, the temperature of the diagwire configuration was the highest (1170^{o}C) causing excessive electron current liberation, that caused a corresponding decrease in the ion current, which in turn lowered the neutron rate.

The decrease in the recirculation ion current due to the increase in electron current is accommodated in eqn. 9.1. This decrease in the ion current explains the corresponding decrease in the overall fusion rate. Using eqn. 9.2 the thermionic current (I_{th}) is found to be 6.3 mA with the diagwire temperature T = 1170^{o}C and work-function ϕ = 2.5 MeV. However, this is ~ 1 mA less than expected (7.4 mA) for the reaction rate in the diagwire configuration to match the fusion rate of the other configurations. There could be many reasons for such discrepancy, one such reason being that the area surrounding the region monitored by the pyrometer would also contribute additional electrons.

The thermionic emission occurs when the grid is hot (even before reaching the melting temperature). Such electron emission could become significant even at low input powers (< 10 kW) if asymmetric heating exists, as explained in the next section (since the thermionic emission varies exponentially with temperature).

9.3 Asymmetric heating of the cathode grid

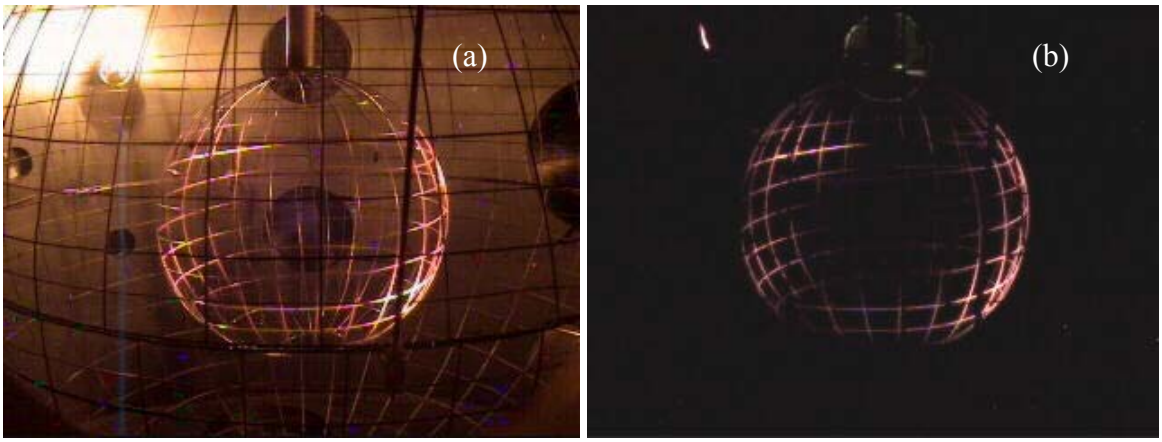

Figure 9.6 (a) Picture of a large 20 cm diameter central cathode grid during operation (b) Picture taken soon after the shutdown shows the heat distribution around the grid.

The asymmetric heating phenomenon is a consequence of uneven distribution of the ionization source that causes localized heating of the grid as shown in figure 9.6. Such heating is caused by the ions from the asymmetric source that bombards the grid and deposits energy locally.

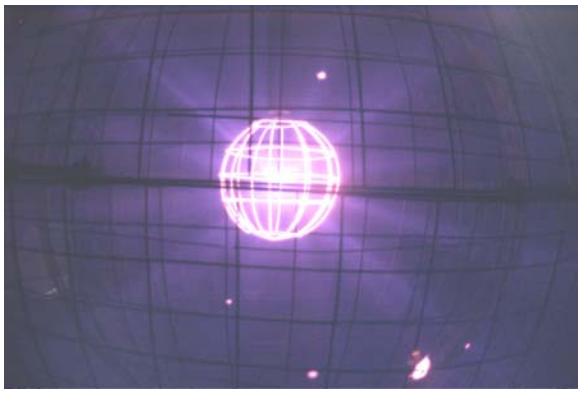

Figure 9.7 Electron jets detected on the wire mesh placed around the intermediate grid (20 kV, 25mA, 7 mtorr chamber pressure).

In the experiment described below an intermediate grid (35 cm diameter) with fine mesh around it (~ 1 mm spacing) as shown in figure 3.1 was used to intercept the outgoing electrons. If there is a concentration of electrons in the form of a jet, it shows up as a hotspot on the fine mesh.

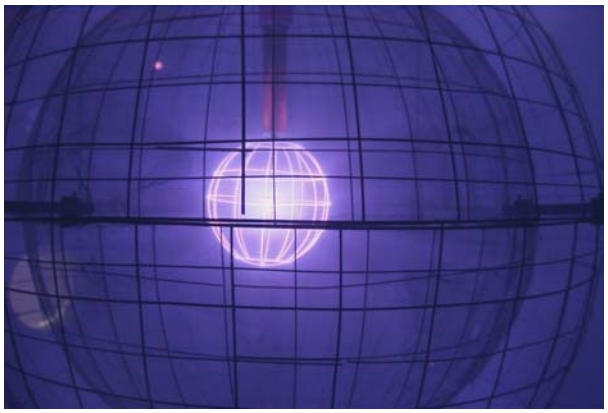

Figure 9.8 Fewer electron jets are observed when RF ionization source is used at 20 kV, 25 mA, 7 mtorr.

In one experiment the IEC device was operated in a Paschen-breakdown regime at a high chamber pressure (~ 7 mtorr). The plasma was sustained by impact ionization by both electrons and ions without the aid of an external ionization source. Several hotspots (regions where electron jets deposit their energy) were observed (figure 9.7) on the intermediate grid (covered with stainless steel mesh with 1 mm wire spacing). Under identical conditions these hotspots vanished (figure 9.8) when an RF ionization source was turned on. The RF source was applied to the intermediate and outer grids simultaneously, as shown in the configuration C, figure 9.1.

The RF source provided a uniform distribution of excited ions around the grid. This proves that uneven ion distribution could cause preferential high ion/electron current channels in an IEC device and that such an effect could be homogenized using a uniform ionization source. The uneven distribution of electrons leaving the grid and recirculating ions could cause asymmetric heating of the cathode. Hence a more uniform ionization source should be used at lower pressures.

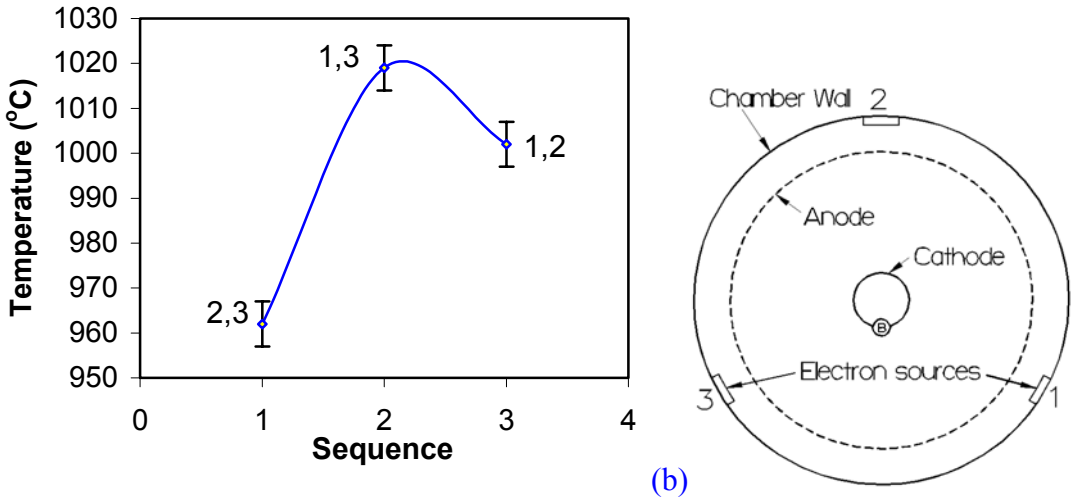

(a) (b)

Figure 9.9 (a) Three experiments conducted in a sequence by switching the electron sources (1, 2 & 3), showed a significant temperature variation of a given spot (B) on the grid. (b) Top view of the IEC cross-section showing the arrangement of filament electron sources.

In a different experiment when a RF ionization source was used at 2 mtorr chamber pressure, for reasons presently not understood, asymmetric heating caused the top and bottom halves to heat while the central region of the cathode remained relatively cold. Furthermore, experiments were conducted by operating two of the three electron filaments in the IEC device at a given time. The temperature of the spot (B) figure 9.9 (b) on the central grid varied significantly as the electron sources were switched (on/off), as shown in figure 9.9 (a).

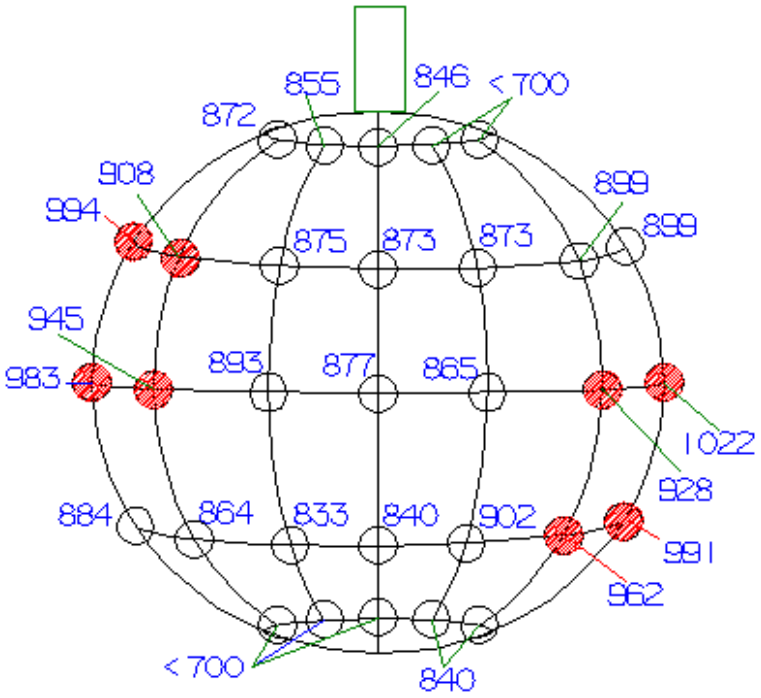

Figure 9.10 Asymmetric temperature distribution as measured on the central grid at 25 kV and 15 mA, 2 mtorr. Shaded circles are the hottest portions of the grid.

This variation in temperature is caused due to preferentially higher ionization in the regions close to the electron sources. The microchannels that form in these regions have higher concentrations of recirculating ions relative to other microchannels (For a detailed treatment of microchannel formation refer to chapter 13). Some of these ions that hit the grid deposit their energy on the portions of the grid wires in their pathway thus resulting in localized grid heating, known as asymmetric heating, see figure 9.6. Sometimes asymmetric heating is observed even

when all three filaments are turned on. The temperature measurements of such an asymmetrically heated grid is shown in figure 9.10.

The selective heating of certain regions of the central grid causes the temperature difference between the different zones to be as high as ~300^{o}C, see figure 9.9. The outcome of such asymmetric heating could cause thermionic electron emission from the hotter regions even at low input power operation. This is especially important when a low work-function material, such as stainless steel, is used in the construction of the cathode grid. The various grid materials used and proposed for future use are analyzed in the next section (9.4).

If the fraction of the grid-surface (f) at high enough temperature for thermionic emission is known it must be included in the expression (9.1). Such measurements are tedious with a single pyrometer and would require a scanning pyrometer that could simultaneously measure the temperature of the entire grid.

The equation for thermionic emission from the cathode now becomes:

$$I_{th} = \sum_i f_i \cdot \Lambda \cdot \alpha \cdot T_i^{\,2} \cdot e^{-e\phi/kT_i} \qquad (9.3)$$

where f_i is the fraction of the grid at a temperature T_i, and approximating the continuous temperature distribution by a set of discrete values.

With asymmetric heating, the thermionic emission could become significant even before grid meltdown/deformation occurs and must be accounted for in any recirculating ion current calculations, especially for higher input powers (> 10 kW for a 10 cm diameter spherical cathode grid). However, the thermionic emission has a negative feedback effect – the increased electron emission causes decreased ion current and hence a decreased heat load. This automatically decreases the grid temperature and thermionic emission. The net effect is that the

recirculating ion current to the grid cannot increase linearly with the power-supply's meter current if the temperature of (portions of) the grid is so high that the thermionic emission becomes significant (eg., T > 1100 ^{o}C for stainless steel and >1600^{o}C for W-25%Re).

9.4 Grid wire material selection

Material properties desired for the cathode grid construction are:

1. High melting point
2. Low sputter yield
3. High work function and
4. Economical.

A material with high work function would emit fewer electrons at high input power (i.e., at higher grid temperature) operation and hence a higher ion current fraction could be achieved for the same power supply current.

If the sputter yield of the material were high, the high-voltage stalk would be coated with sputtered material. For instance, stainless steel sputters profusely at low voltages and deposits on the high voltage stalk as shown in figure 9.11 for a stainless-steel central grid.

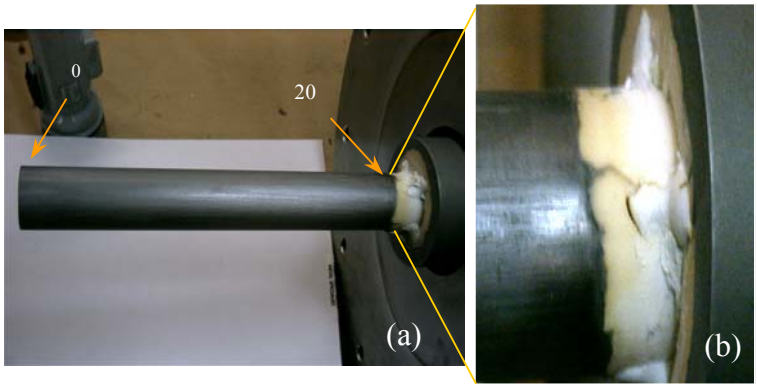

Figure 9.11 (a) Picture of a stalk coated with sputtered stainless steel material from the grid. (b) Zoomed-in view shows the breakdown path from the stalk to the chamber walls.

The variation of the surface resistance as measured along a stalk, used with a stainless steel cathode, between consecutive points spaced equally is shown in figure 9.12.

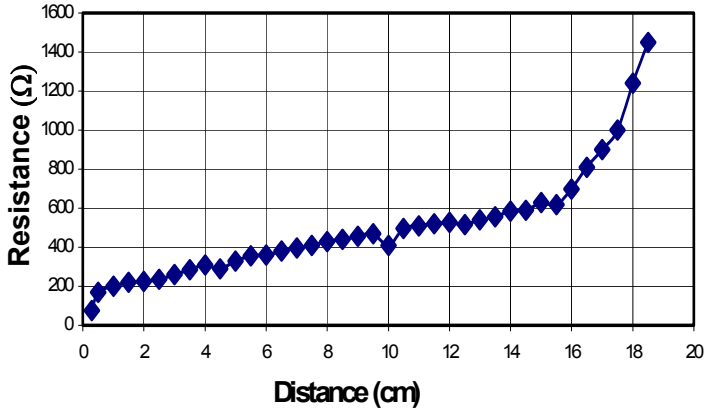

Figure 9.12 Sputter-coated stalk resistance variation with distance. The resistance was measured in small increments of distance along a straight line.

The maximum current a grid can handle depends on the rate at which it can radiate the power (otherwise it would deform and/or melt). This maximum current that a grid of a given material can handle before melting or deforming can be calculated by assuming that all the energy of the ions is deposited into the grid wires and then calculating the current at an equilibrium temperature. For stainless steel the melting point is ~1800 K and the deformation of the grid (sagging) begins much earlier. Assuming the sagging occurs at 1500 K and equating the black body radiation rate to the input power (cathode voltage (V) x power supply current (I) in Amperes) we may calculate maximum current as follows:

$$I = A\varepsilon\sigma T^4/V \qquad (9.4)$$

where A = surface area ~ 76 cm^2 (for a 10 cm grid made of 0.08 cm diameter with 5 latitudes and 12 longitudes), ε is the emissivity of the material (= 0.15), σ is the Stefan-Boltzmann constant (5.67 x 10^{-8} watt.m^{-2}.K^{-4}), and T is the temperature of the grid (~1500 K). This gives 9.5 mA of ion current at 200 kV, whereas the power supply can produce 200 kV at 75 mA. Hence

stainless-steel is not preferred for the cathode grid construction. The above calculation presumed that the whole grid is uniformly heated to 1500 K, if asymmetric heating were to occur, the grid could handle much less input power due to the thermionic emission and hence would further limit its performance.

Of the materials shown in figure 9.13 (below), pure-Re, W, Mo, Ta, and Ti, plus alloys such as W-5%Re, W-25%Re, and Mo-25%Re were analyzed. The W-25%Re was found to be the most suitable for a 10 cm cathode grid construction at the current operating conditions (~ 3 – 15 kW). This is because it is relatively cheap, has a high melting point (2800 K), low sputter yield and is easy to manufacture (W-25%Re alloy can be spot-welded). As a consequence of using this material, very low sputtering was observed and hence enhanced the device's capability of handling much higher voltages for longer durations of time. Any sharp edges that appeared during the manufacture of the grid were removed to avoid premature breakdowns due to high (local) field emission.

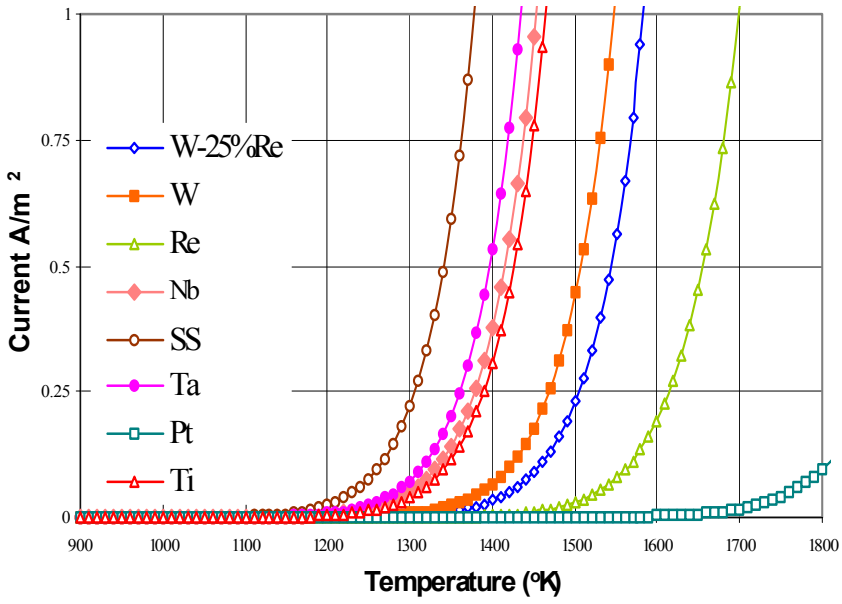

Figure 9.13 Thermionic emission from eqn. (9.1) for various materials vs. temperature

9.5 2-D ion flux mapping

Earlier predictions of ion fluxes in an IEC device using the Simion™ code[5] had many significant limitations: insulators cannot be modeled, it does not compute plasma fields and it cannot model ion and neutral gas collisions, which are major ion scattering mechanisms in an IEC device. As a consequence, the predicted microchannel formations are not very reliable. Hence experimental measurements become indispensable, because such data would provide a better understanding of the ion flow.

Thorson, et al.[1] conducted experiments at low voltage < 13 kV and determined the ion flux reaching the interior of the central grid using an emissive probe. Though this method produced reliable data at low voltages, it failed to do so at higher voltages due to breakdown and melting problems associated with the probe. Also, the emissive probe arrangement was not good at determining the flux distribution since the probe tip was spherical and did not have directional sensitivity (gives the same temperature data irrespective of how the ions reached the probe tip).

In the present experiments a set of wires (made of W-25%Re) is placed in various orientations inside the central grid to intercept the inflowing ions. These wires are at the same potential as the central grid and are less intrusive than probes, causing negligible distortion to the ion flux pattern unless they intersect the origin. The ions outside the central grid do not see the chordwire potential and once inside the grid the ions only see the virtual anode potential. Since, in the presence of the diagwire the virtual anode potential is quenched, this configuration was avoided in the ion flux mapping experiment.

The heat deposited on these wires by the ions is mostly radiated away; this can be deduced by comparing the radiative heat transfer with the convective heat transfer (conduction) across the wire:

$$\frac{Q_c}{Q_r} = \frac{-kA'(T_w - T_g)}{A''\varepsilon\sigma L(T_w^{\,4} - T_c^{\,4})} \approx 0.03 \qquad (9.5)$$

where Q_c is the convective heat flow rate, Q_r is the heat radiation rate, k is the coefficient of thermal conductivity (63.8 at 2073 ^oK), A′ is the cross-sectional area ($\pi \cdot r^2$) with r =0.000127 m, A″ is the radiating surface area ($2\pi r l$), the length of the chordwire across which the heat has to flow is 'L' = 4 cm, T_w is the wire temperature (1800^oC maximum), T_g is the grid wire temperature (~673 ^oK), T_c is the chamber temperature (313 ^oK), ε is the emissivity (~0.45 for tungsten), and σ is the Stefan-Boltzmann constant (5.6697 x 10^{-8} W/m^2K^4). Since this ratio (Q_r/Q_c) is only 0.03, we may neglect the convective heat transfer along the wire for the present purpose.

The ions reach the interior of the central grid with a velocity that would remain constant if their space charge created no potential difference before they exit on the other side of the grid (in the absence of collisions). However, the virtual anode potential that builds up at the core of the central grid determines the final energy of the ions reaching the wires and must be accounted for in absolute ion density calculations.

From figure 9.14 (below), the ions see an increasing potential as they move towards the core due to the virtual anode (but once on the other side of the virtual anode potential the ions regain their lost energy). Hence the ions reaching the chordwires would be affected by the presence of the virtual anode (their energy is reduced) and this has to be accounted for (explained in the next section).

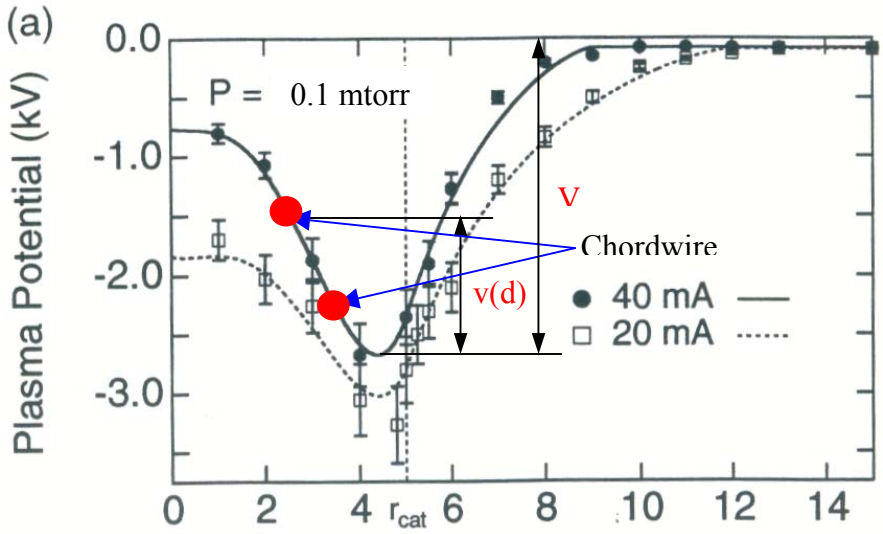

Figure 9.14 The ions impinging on the chordwires have different energies, governed by the virtual anode potential that builds up inside the cathode (after Thorson[2]).

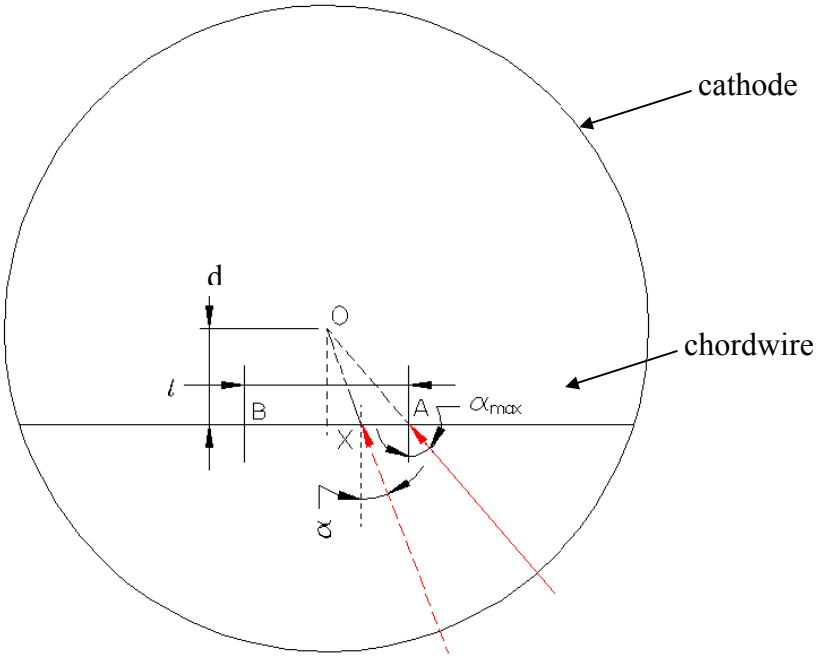

Figure 9.15 The ion converging at the center of the cathode makes an angle α with respect to the chordwire, with the maximum value being α_{max}. The pyrometer monitors the wire length AB.

The ions reach the chordwire at various angles of incidence and this angular dependence causes the ion flux on the chordwire to become increasingly perpendicular as we move closer to

the center of the chordwire for uniform spherical convergence, see figure 9.15. Hence the average ion flux on a chordwire is given by:

$$\left|\dot{N}_{i\,avg}\right| = \frac{2P_{rad}}{q\Phi_c}\int_0^{\alpha_{\max}} \cos\alpha d\alpha = \frac{2\varepsilon\sigma T^4}{q\Phi_c\sqrt{1+\left(\frac{2d}{l}\right)^2}} \qquad (9.6)$$

where 'α' is the angle of incidence and its maximum value is given by $\alpha_{\max} = \sin^{-1}\left(1/\sqrt{1+\left(\frac{2d}{l}\right)^2}\right)$, '*l*' is the length of the wire (~ 2.0 cm) monitored by the pyrometer from outside the chamber, 'd' is the perpendicular distance of the chordwire from the center of the grid. A simple energy balance equation[2] modified to relate the ion density (n_i) to the energy deposited on the wire (~ power radiated by the wire P_{rad}) is given below:

$$n_i \approx \frac{P_{rad}}{v_i E_i} = \frac{\varepsilon\sigma T^4}{\sqrt{\frac{2}{M}}\left(q\Phi_c\right)^{3/2}\sqrt{1+\left(\frac{2d}{l}\right)^2}} \qquad (9.7)$$

where we have assumed that the ion velocity is given by $v_i = \sqrt{\frac{2E_i}{M}}$, where E_i is the ion energy just before reaching the chordwire due to the virtual anode potential ($E_i = q\,\Phi_c$).

It must be noted that the equation (9.6) has been derived assuming that the ion convergence is spherically isotropic, however, due to the presence of the wires and the associated electric fields, the ions do not converge uniformly. This equation would also be valid for IEC schemes where virtual cathodes instead of grid wires are envisaged. However, the presence of chordwires might affect the virtual cathode formation in such schemes. Hence the equation (9.7) should be used cautiously.

The methodology of calculation of the 2D ion flux reaching the cathode from each of the below described configurations is explained in the subsequent section 9.6. In order to map the

2D ion flux, we begin with the planar chordwire configuration as shown in figure 9.16, wherein several wires were placed in the same plane and were used to intercept the counter-streaming ions in that plane. Since perfect alignment of wires in the plane was not achieved, the masking of the ion flow by these wires is neglected.

Figure 9.17 shows the temperature distribution of the wires placed in a single plane. A gradual increase in the temperature as we move towards the center is observed due to increased ion convergence. The topmost wires [6 & 7, in figure 9.16] were not studied since their temperatures remained below the detection capability of the pyrometer (700^{o}C). The data points at chordwire positions 1 & 5 are introduced only to guide the eye (have lower than 700^{o}C temperature). The temperature of the chordwire 4 is higher because this wire deformed towards the core (downwards) under its own weight. However, the chordwire 2 deformed away from the core (downwards) and hence was relatively cooler as shown in figure 9.17. Exact chordwire deformation information is not available at this time.

Similarly, a different set of experiments was conducted using two mutually perpendicular arrangements of chordwires in the same plane, see figure 9.18. This arrangement revealed the ion flux distribution in that plane, computed from the temperature distribution at 50 kV and 30 mA as shown in the figure 9.19. It was observed that the wires on the side D [in figure 9.18 (a)] of the grid were hottest at 2 cm radial distance, consistent with focused flow. The average ion flux into the cathode (see next section for details of calculations) from the four directions [A, B, C & D, in figure 9.18 (a)] are given below:

$$\left.\begin{array}{l} A \rightarrow 9.2 \times 10^{14} \text{ ions/cm}^2\text{s} \\ B \rightarrow 5.8 \times 10^{14} \text{ ions/cm}^2\text{s} \\ C \rightarrow 8.9 \times 10^{14} \text{ ions/cm}^2\text{s} \\ D \rightarrow 9.4 \times 10^{14} \text{ ions/cm}^2\text{s} \end{array}\right\} \qquad (9.8)$$

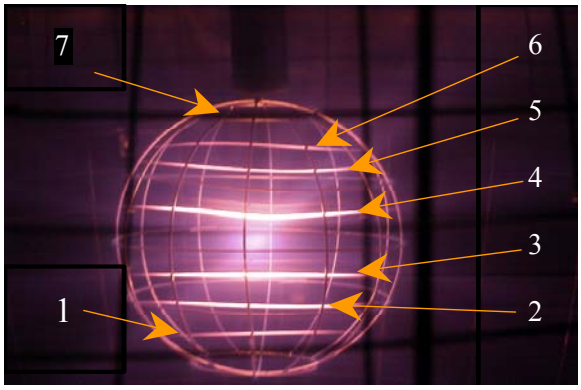

Figure 9.16 Planar chordwire experiment. Several wires are arranged in the same azimuth parallel to each other and to the ground surface.

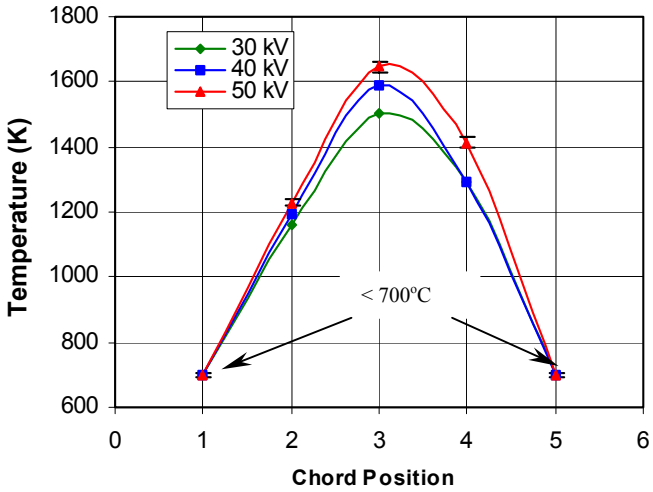

Figure 9.17 The temperature of various wires placed in the planar arrangement (planar chordwires) is plotted against the wire positions at constant current of 30 mA.

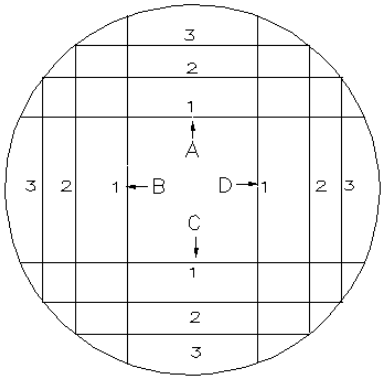

(a)

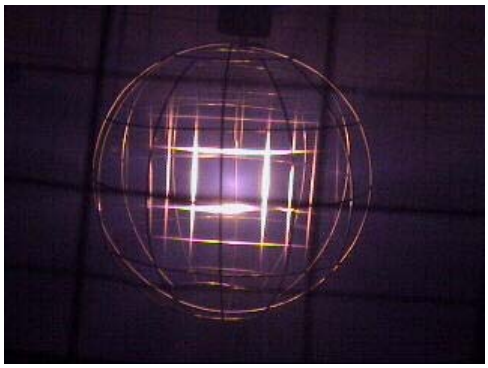

(b)

Figure9.18 (a) The biplanar – chordwire arrangement. Wires are numbered (1,2,3) along each of the orientations (A,B,C and D). All dimensions are in cm, (b) Picture of the biplanar-chordwire arrangement inside the central grid. The picture was taken at 7.32 mtorr, 20 kV and 10 mA.

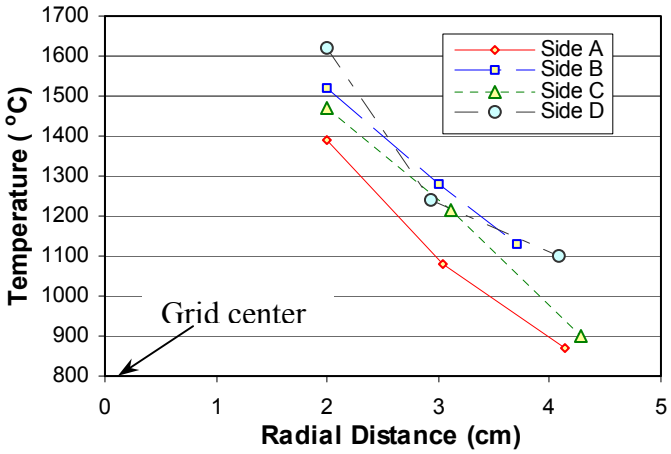

Figure 9.19 The temperature distribution of the bi-planar wire arrangement (Figure 9.18) at 50 kV & 30 mA.

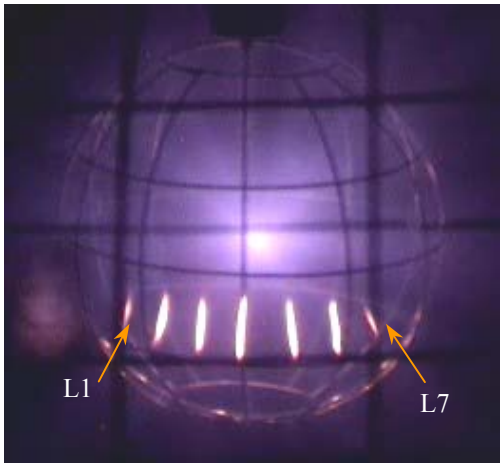

Figure 9.20 Wires arranged inside the central grid in a plane parallel to the ground.

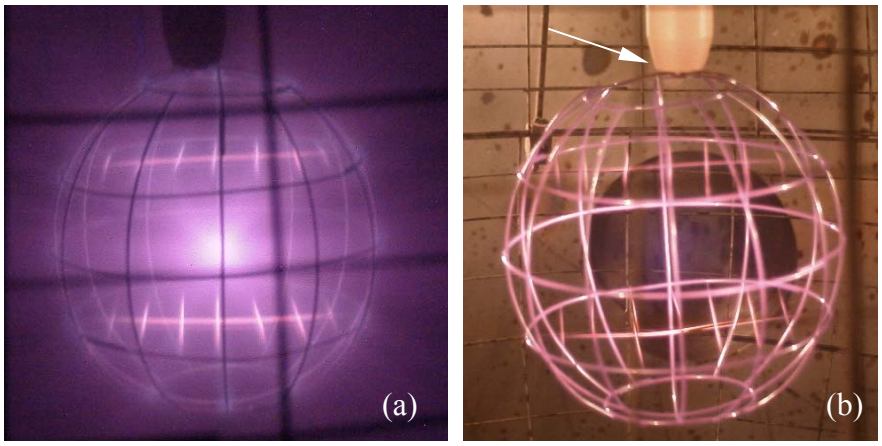

Figure 9.21 Two sets of chordwires were arranged parallel to the ground plane. (b) Due to the erroneous tilt in the grid, the results were abandoned.

In order to map the ion flux reaching the grid from the bottom-up direction, another experiment was performed where the wires were arranged in a plane parallel to the ground, see figure 9.20. In a separate experiment a second set of wires was used on the upper latitude, similar to figure 9.21 without the lower set of chordwires. This was done to minimize the ion flow perturbation by the chordwires, since using too many chordwires tends to affect the ion flux.

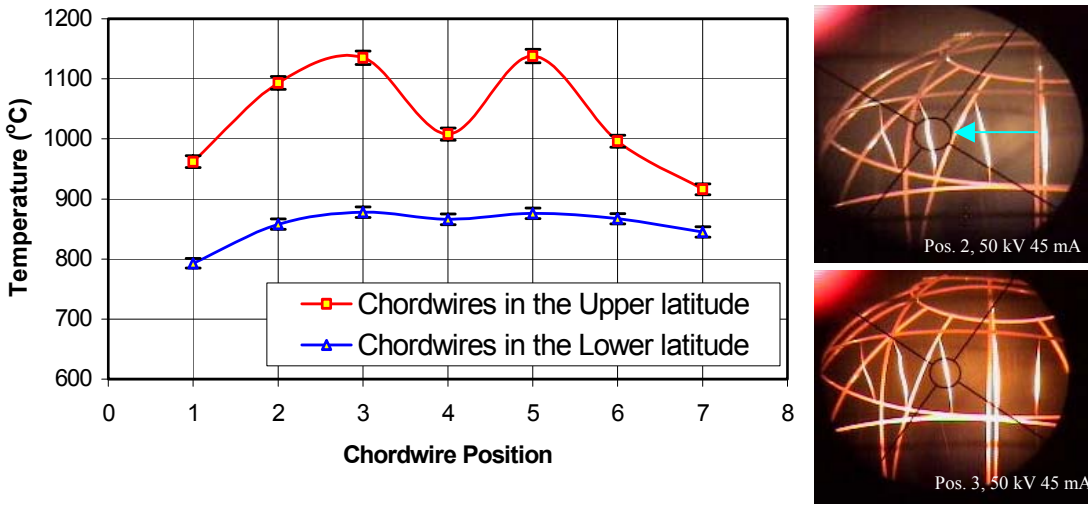

Figure 9.22 (a) Plot of the temperature vs. the chordwire position. The central wire was cold although it is closer to the center of the grid when compared to the rest, showing that the ion flux is lower in that direction. (b) View of the chordwires on the lower latitude from the pyrometer (image is inverted).

The temperature measurements of the two sets of chordwires placed on the upper and lower latitudes are shown in region within the circle of figure 9.22(a). The error bars were generated based on the temperature fluctuations observed and also the error in orientating the pyrometer at the center of the chordwires. The view of the regions monitored by the pyrometer is shown in figure 9.22 (b). The wire closest to the center of the cathode grid (wire 4) is relatively colder showing that this wire intercepted fewer ions. The temperatures of the outer wires (1, 6 & 7) are low owing to their distance from the center. Interestingly, this experiment

revealed that the stalk on the top tends to block the recirculating ions in the vertical direction. This tends to decrease the ion flux coming from the bottom due to crossover (circulating) ion flow. Hence the effective redistribution of ion flow inside the grid is poor, which is expected for the relatively small space charge buildup in the core of the device.

9.6 Calculation of the 2-D ion flux into the cathode

A simple estimate of the expected density profile is given by first assuming a perfectly convergent, non-interacting flow into the core. Angular momentum of the ions at the edge [due to their perpendicular thermal velocity at the edge, $\langle V_{\perp} \rangle$] will prevent the flow from giving an infinite density at r = 0, and to the lowest order one can invoke some constant density inside the core radius, r_c to avoid this divergence. All ions are assumed to flow through the core with a velocity $v_c = \sqrt{\frac{2q\Phi c}{M}}$ where Φ_c is the electric potential energy of the ions in the core (≈ applied cathode voltage), q is the charge of the ion, and M is the ion mass. The core size will then be determined by conserving the average angular momentum of the ions, and the core density is found by particle conservation.

In this model all of the ions are assumed to be launched from a single point towards the core (then effectively a sphere with radius r_c) without loss of generality, a perfect radial convergence is being assumed. The core size is then determined by setting the average momentum of the ions (with ion mass M and the anode radius R) at the edge equal to that of the ions passing through the core:

$$M\langle V_{\perp}\rangle R = \frac{\int_0^{2\pi} d\theta \int_0^{r_c} rdrMv_c r_c}{\int_0^{2\pi} d\theta \int_0^{r_c} rdr} = \frac{2}{3} Mv_c r_c \qquad (9.9)$$

and the core radius is given by: [2,6]

$$r_c = \frac{3}{2} R \frac{\langle V_{\perp} \rangle}{Vc} \approx \frac{3}{2} R \sqrt{\frac{kT_{\perp i}(R)}{q\Phi_c}} \qquad (9.10)$$

where $T_{\perp i}(R)$ is the edge perpendicular ion temperature. Hence r_c should scale as $1/\sqrt{\Phi_c}$.

Comparing the above derived ideal core radius (eqn. 9.10) with experiment shown in figure 9.23 we see that there is little agreement at higher cathode voltages.

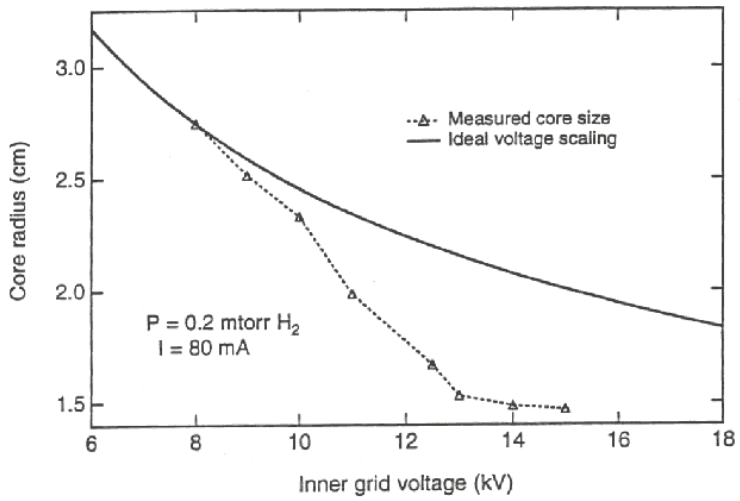

Figure 9.23 Scaling of core size with cathode voltage vs. the expected scaling from ideal convergence (normalized to the point at cathode voltage of 8 kV).[7]

Hence a different approach is taken to calculate the core radius. The present technique is not very accurate in determining the voltage (V′) due to the charge buildup inside the cathode. When other precise methods are developed to calculate (V′), they should replace those calculated from eqn. 9.18 below.

The ion space charge is assumed to stagnate (slow) the flow at some radius $r_{stag} = r_c$ for a purely radial, collisionless flow with single-species injection. This stagnation radius can be determined by solving eqn. 9.11 for α and using eqn. 9.12 to find the appropriate r_c/R where r_c and R are illustrated in figure 9.24, the values of α are plotted for various r_c/R values in figure 9.25.

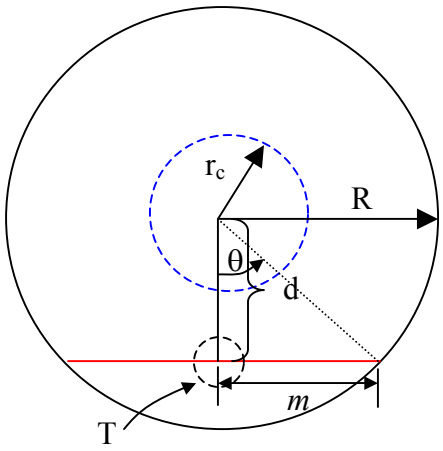

Figure 9.24 The core radius is r_o and the chordwire temperature (T) is measured at the center of the length of the wire.

The ion saturation current in concentric spheres geometry is given by: [8]

$$I_c = \frac{4}{9}\sqrt{\frac{2q}{M_D}}\frac{V^{3/2}}{\alpha^2} \qquad (9.11)$$

where M_D is the mass of the ion (D_2^+), q is the ion charge and α is a geometrical factor that is related to the radii of the spherical electrodes:

$$\alpha = \gamma - 0.3\cdot\gamma^2 + 0.075\cdot\gamma^3 - 0.0143182\cdot\gamma^4 + 0.0021609\cdot\gamma^5 + \ldots \qquad (9.12)$$

with $\gamma = \ln(r_c / R_{cat})$ (9.13)

Assuming no sources or sinks of particles between the electrodes (consistent with low pressure and density), Eq. (9.11) can be solved for the voltage (volts):

$$V(r) = \left[\frac{9I\alpha^2(r)}{4} \sqrt{\frac{M_D}{2q}} \right]^{2/3} \qquad (9.14)$$

where we use I = η x I_i = 7 x 22.5 mA = 157.5 mA in eqn.(9.12) which is the total recirculating ion current inside the cathode that determines the space charge buildup in the core region.

The value of α(r) (where α → 0 as r_c → R_{cat}) is computed using eqn.(9.13) & (9.14) at each radial distance 'd' (= R_{cat} in the eqn. 9.13) for a fixed value of r_c.

The above equations were originally derived for solid electrodes, but they also hold for semi-transparent grids with counter streaming ion flows if I_c represents the total recirculating ion current between the spheres.[2]

If $J = \frac{I_c}{4\pi r_o^2}$ → measured power supply current density, then we may write it as follows:

$$J = \frac{D}{4\pi r_o^2 \alpha^2} \text{ (A/cm}^2\text{)} \qquad (9.15)$$

r_o = radius of the emitter (cm) = r_c (core radius)

where $D = \frac{4\sqrt{2}}{9} \sqrt{\frac{e}{M_D}} V^{3/2} = \frac{68.55 \times 10^{-8} V^{3/2}}{\sqrt{M_D}}$ (9.16)

$\therefore I_c = \frac{D}{\alpha^2}$ = 7.0 x 0.0225 A, assuming half the power supply current is electron current (secondary electron emission coeff. ~1) at 50 kV input voltage and the theoretical recirculation factor[9] for the 92.5 % transparent cathode grid is η ~ 7.[1]

$$\Rightarrow \alpha = \left(\frac{68.55 \times 10^{-8} V^{3/2}}{0.1575 \cdot \sqrt{M_D}} \right)^{1/2} = 9.93 \text{ when V = 50000 volts.} \qquad (9.17)$$

With 15.7 mA input ion current at 50 kV applied cathode voltage, the value of $\alpha \sim 9.93$, from the figure 9.25 we obtain $R_{cat}/r_c = R/r_c \sim 9$. Hence the core radius is $r_c \sim 0.55$ cm for a 5 cm radius cathode grid at the above mentioned parameters (50×10^3 volts cathode voltage, 0.03 amperes power supply current and 2 mtorr chamber pressure). This core radius value is reasonable compared to earlier experimental measurements (at much lower voltage) in figure 9.26, since it is known that the core radius decreases with increasing voltage as shown in figure 9.23.[7]

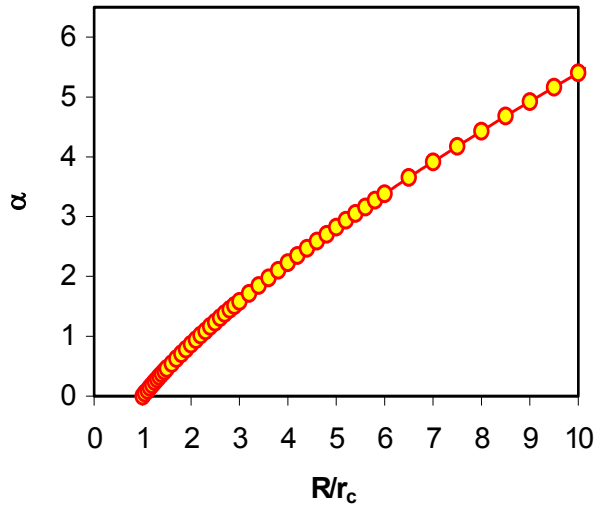

Figure 9.25 Langmuir parameter for concentric spherical grids (α) vs. radius ratio.[8]

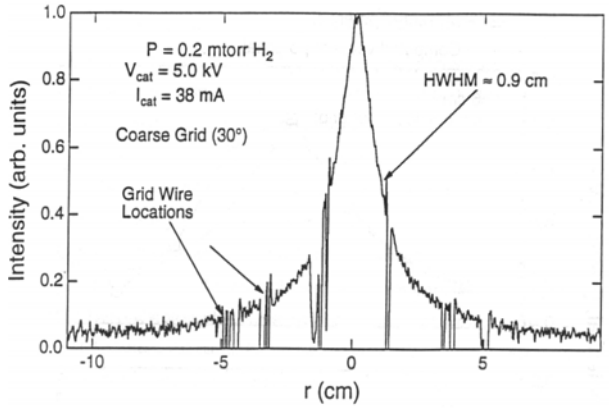

Figure 9.26 The HWHM of the core of a grid with 30° spacing is ~0.9 cm at 5.0 kV for a 30° coarse grid longitude spacing.[2] Hence the computed value of $r_c \sim 0.55$ cm at 50 kV is reasonable.

We can now determine the voltage at various radial distances inside the cathode from the core using eqn. 9.18 with the ion current as shown below:

$$\therefore V(d) = \left(\frac{I_c \alpha^2(r) \sqrt{M_D}}{68.55 \times 10^{-8}} \right)^{2/3} = 5955 \cdot \left[\alpha(r) \right]^{4/3} \qquad (9.18)$$

with R = d = 2.18 cm, I_i = 0.1575 A, $R/r_c = 3.92 \Rightarrow \alpha(r) = 2.4$, $M_D = 9$. Where the value of $\alpha(r)$ in eqn.(9.18) is determined from the figure 9.24 for various radius ratios (R/r_c) with fixed r_c = 0.4 cm, and R = d, the distance from the core to the center of the wire as shown in figure 9.23.

The resulting ion flux reaching the region of the wire that the pyrometer monitors, assuming parallel convergence (i.e., ion paths make small angles with respect to other ion paths, true especially when ions form microchannels), is given by:

$$\frac{\dot{N}}{A} = \frac{\varepsilon \sigma T^4}{q \Phi_c} = \frac{0.15 \times 5.67 \cdot 10^{-8} \times T^4}{[V_{cat} - V(d)] \times 1.6 \cdot 10^{-19}} \text{ (ions·m}^{-2}\text{·s}^{-1}\text{)} \qquad (9.19)$$

where V(d) is evaluated from eqn. 9.14 for corresponding values of $\alpha(r)$ from figure 9.29. The eqn. 9.20 below gives the local density (region close to the chordwire).

$$n_i = \frac{\varepsilon \sigma T^4}{\sqrt{\frac{2}{M_D}} (q \phi)^{3/2}} \qquad (9.20)$$

where T is measured using a pyrometer for each of the chordwires.

In the biplanar chordwire experiment, as shown in figure 9.18, selecting the chordwires farthest from the center in the two mutually opposite directions (B3 & D3), and evaluating the ion flux in those directions from the parameters – R/r_c = 7.52, α = 9.3, V(d) = 87355 volts and R/r_c = 7.42, α = 9.2 and V(d) = 40352 volts are 1.04 x 10^{15} and 5.8 x 10^{14} ions·cm^{2}·s^{-1} respectively with normalized $\dot{N}$ values H1 = 1 and H2 = 0.56 respectively). The resulting ion flux map thus generated from the tabulated values (Table 9.1, 9.2 and H1 & H2) is plotted in figure 9.27(a) below. The asymmetry in the ion flux is due to the fact that the experiment was conducted with three different stalks and two different grids of same geometry, repeating the experiment with the same stalk and grid could help reduce the error in the ion flux map.

Table 9.1 Computation of ion flux in the bottom-up direction into the cathode grid (In Expt. No. 815, Stalk ST-36, without any tapering at its tip was used for this experiment). All $\dot{N}$ values are normalized to the maximum flux 1.04x10^{15} (along the equator H1).

Chordwire #	**d (cm)**	**d/r_c**	**α (r_c ~ 0.55)**	**V(d) (kV)**	**T (K)**	**$\dot{N}$ (#m^{-2}s^{-1})**	**Normalized $\dot{N}$**
L1	3.71	6.75	3.8	35311.2	1235	8.42x10^{14}	0.81
L2	2.957	5.38	3.1	23083.5	1366	6.87x10^{14}	0.66
L3	2.398	9.36	2.55	29259.5	1408	1.01x10^{15}	0.97
L4	2.179	3.96	2.6	21289.5	1281	9.98x10^{14}	0.48
L5	2.398	9.36	2.55	29259.7	1411	1.02x10^{15}	0.98
L6	2.957	5.38	3.1	23083.5	1269	5.12x10^{14}	0.49
L7	3.71	6.75	3.8	35311.3	1189	7.23x10^{14}	0.69

Table 9.2 Computation of ion flux into the cathode grid from upward direction measured in Expt. No. 1143 (the stalk ST-38 had a small tapering at the tip).

Chordwire #	**d (cm)**	**d/r_c**	**α (r_c ~ 0.55)**	**V(d) (kV)**	**T (K)**	**$\dot{N}$ (#cm^{-2}s^{-1})**	**Normalized $\dot{N}$**
U1	3.71	6.75	3.8	35311.2	1066	9.67x10^{14}	0.45
U2	2.957	5.38	3.1	23083.5	1131	3.23x10^{14}	0.31
U3	2.398	9.36	2.55	29259.5	1150	9.48x10^{14}	0.43
U4	2.179	3.96	2.6	21289.5	1139	3.11x10^{14}	0.29
U5	2.398	9.36	2.55	29259.7	1149	9.46x10^{14}	0.43
U6	2.957	5.38	3.1	23083.5	1140	3.33x10^{14}	0.32
U7	3.71	3.71	3.8	35311.3	1118	5.65x10^{14}	0.54

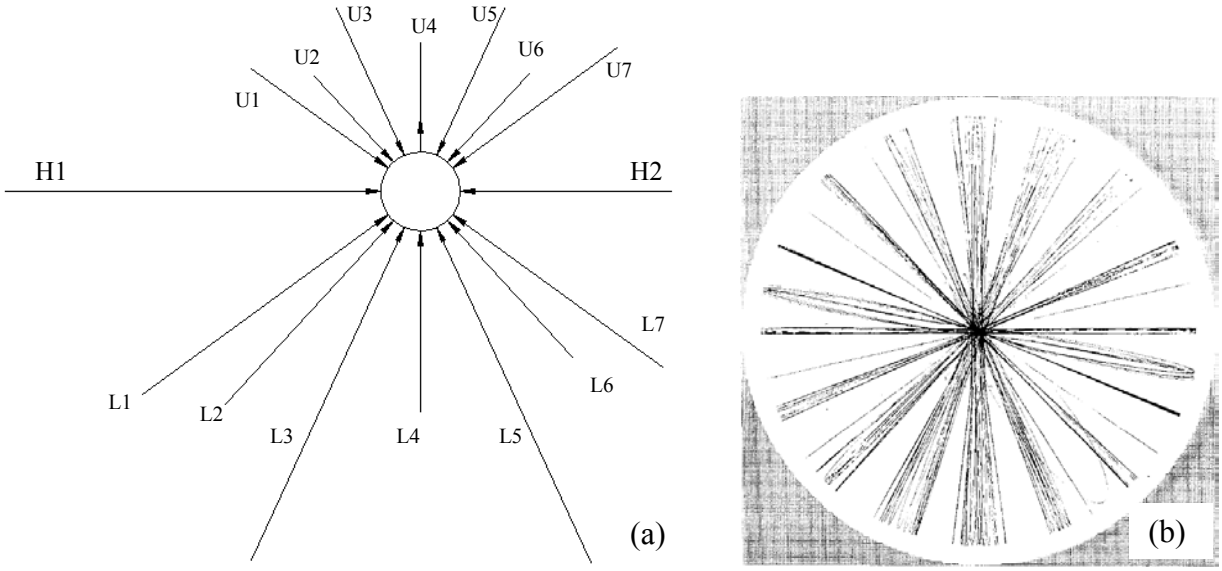

Figure 9.27 (a) Preliminary 2D ion flux map shows non-uniformity in the ion recirculation around the cathode. The flux is higher from left to right. The lowest flux is observed in the up-down direction where the stalk is present. (b) Simion^{TM} prediction[5] of the microchannel formation in an IEC device. Three different stalks and two different grids (of same geometry) were used.

The above calculations presume several approximations that might not be true in their entirety. One such assumption is that the ion saturation current equation (9.9) is derived for an opaque cathode (all ions recombine on the surface of the cathode) is valid for a transparent grid also. The errors that are introduced in the final values of the ion flux could be as large as 80%, but the relative magnitudes would still remain constant, and hence a normalized value of the ion flux would be a good indicator of the relative ion flux behavior around the cathode grid.

The above-derived values are preliminary results and to obtain more accurate values one would have to repeat the experiment with only one chordwire in the grid at a time, this would minimize any perturbation to the ion flow introduced by these wires. However, this would increase the run time and the number of times the device has to be vented to change the wire. The impurity level must be maintained constant through out the experiment.

Several other precautions to be taken while making sensitive ion flux measurements are: A clean window must be used for correct temperature measurement, the pyrometer should be focused on the wire properly, any deformations in the chordwire due to thermal expansion must be accounted in the ion flux calculations (or the input power of operation should be maintained low), the angular distribution of ions in a microchannel must be accounted, the grid must be oriented properly (this is especially important since it was observed that the ion flux was sensitive to small changes (such as a small tilt in the grid orientation, see figure 9.21).

The accuracy of the 2D ion flux map (figure 9.27(a)) can be improved by using several wires in other configurations (limited by the pyrometer's resolution). This map is based on the assumption that the ion flux is uniformly distributed over the entire surface of the central grid and that only the flux magnitudes change. Figure 9.27 (b) shows the Simion^{TM} prediction of a uniform distribution of microchannels around the grid. However, from the experimental measurements the ion flow is non-uniform and the presence of the high voltage stalk adds to the non-uniformity of the ion flow.

9.7 Applications of the chordwire configuration

The chordwire configuration also has other applications. Since focused high electron ejection (governed by the grid geometry) was observed in the diagwire configuration, figure 9.4, it could be used as a focused electron beam source, the cathode grid geometry may be changed to fine tune the shape of the beam.

Ions bombarding the wire tend to produce damage. Given the high temperatures that prevail on these wires, high-temperature ion-impact damage studies can be easily carried out, see figure 9.28. The wire sample could provide information about tensile strength at varying ion

impact rates and fluences. Several different wire samples could be place inside the grid simultaneously for variable ion fluences under identical operational conditions. The sample is not limited to a wire; solid targets of different shapes (shielded from the ambient electric fields of the grid) could also be studied as shown in figure 9.29.

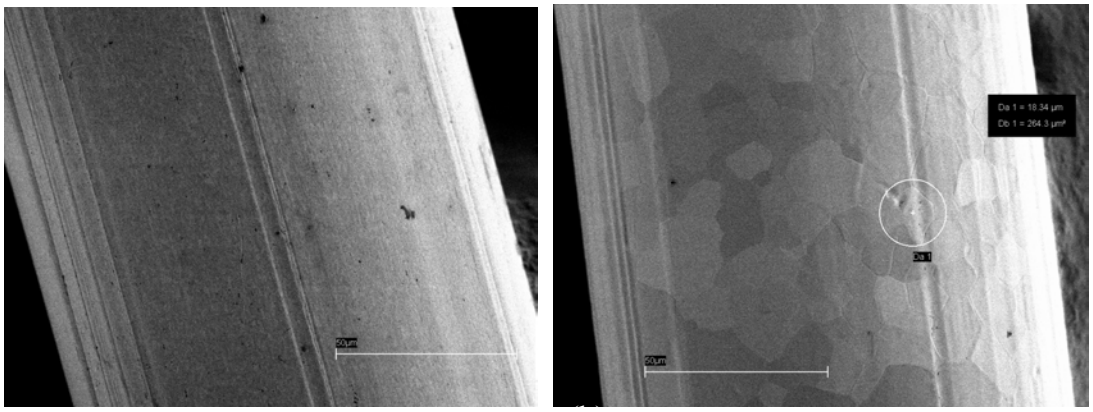

Figure 9.28 (a) Scanning electron microscope picture of the chordwire before exposure to plasma (b) Grain growth is observed after exposing the chordwire to the plasma.

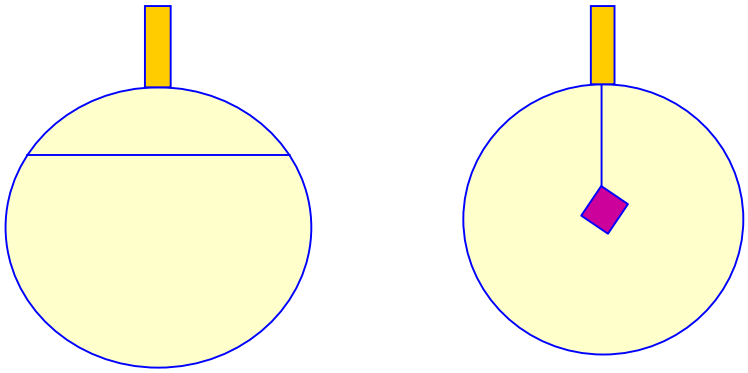

Figure 9.29 Samples of varied shapes and sizes could be irradiated and used for damage analysis.

9.8 Conclusions

A new recirculation current equation has been derived that takes the thermionic electron emissions into account (other electron emission contributions will be covered in chapter 11).

Theoretical predictions show that thermionic emission adversely affects the performance of the device at high power levels (> 10kW), especially if asymmetric heating occurs.

A new diagnostic called “chordwire” has been developed to map the ion flux reaching the interior of an IEC device. Preliminary 2-D mapping of the average ion flux into the central grid shows an uneven distribution of ion flow into the core of the device. The presence of the high voltage stalk in the vicinity of the cathode seems to block the counter-streaming ions, causing a decrease in the crossover (recirculating) ion flow. Using this diagnostic the effect of thermionic emission on the performance of the device has been studied. Thermionic electron emission adversely affects the ion flux and hence the overall performance of an IEC device is hampered.

9.9 References

[1] T. A. Thorson, R.D. Durst, R. J. Fonck and L. P. Wainwright, "Convergence, electrostatic potential, and density measurements in a spherically convergent ion focus," Phys. Plasmas **4** (1), Jan. 1997.

[2] T.A. Thorson, PhD thesis, University of Wisconsin, Madison (1996).

[3] O. W. Richardson O. W. and A. F. A. Young, "The thermionic Work-Functions and Photoelectric Thresholds of the Alkali Metals," Proc. R. Soc. London A (1925) 107, 377-49.

[4] C. Herring and M. H. Nichols, Rev. Mod. Phys. **21**, 185 (1949).

5. J. M. DeMora, R. A. Stubbers and R. A. Anderl, "Study of Ion Microchannels and IEC Grid Effects Using the SIMION Code," Proc. 16th IEEE/NPSS Symp. Fusion Eng. G. H. Miley and C. M. Elliott. Eds. Piseataway, NJ: IEEE 1996, pg. 1486-1489.

[6] M. Rosenberg, and Nicholas A. Krall, "The effect of collisions in maintaining a non-Maxwellian plasma distribution in a spherically convergent ion focus," Phys. Fluids B 4(7), July 1992.

[7] T.A. Thorson, PhD Preliminary examination report, University of Wisconsin, Madison (1996).

[8] I. Langmuir and K. B. Blodgett, "Currents limited by space charge between concentric spheres," Phys. Rev. **24**, 49 (1924).

[9] R. L. Hirsch, "Experimental studies of a deep, negative electrostatic potential well in a spherical geometry," Phys. fluids, **11**, 2486, (1963).

Chapter 10.0. Residual Gas Analyzer

The Closed Ion Source (CIS) Quadrupole Gas Analyzer is a differentially pumped quadrupole mass spectrometer used for direct measurement of minute trace gas impurities. It is usually operated with fuel gas mixtures at pressures from 10^{-12} Torr to ~2 mTorr. The CIS analyzer is a mass spectrometer that analyzes gas mixtures by ionizing some of the gas molecules, separating the resulting ions (positive ions) according to their respective masses, and measuring the ion currents at each mass. Partial pressure measurements are determined with the help of sensitivity (i.e. calibration) factors by reference to the abundance of the individual mass numbers attributed to each gas type, see section 10.3.

The CIS probe consists of a quadrupole mass spectrometer equipped with a high conductance, differentially pumped, CIS ionizer. The total probe equipment consists of three parts: the CIS ionizer (electron impact), the quadrupole mass filter and the ion detector. The CIS sits on top of the quadrupole mass filter and is simply a short, gas-tight tube with two very small openings for the entrance of electrons and the exit of ions. The source is exposed to the process environment (< 10 mTorr) and ions are produced by electron impact directly at the process pressure. The ions enter the quadrupole through a small aperture. A turbomolecular pump,

attached to the pumping system port of the CIS Cover Tee, Figure 10.1, keeps the filament and the rest of the quadrupole mass spectrometer at pressures below 10^{-5} Torr through differential pumping.[1]

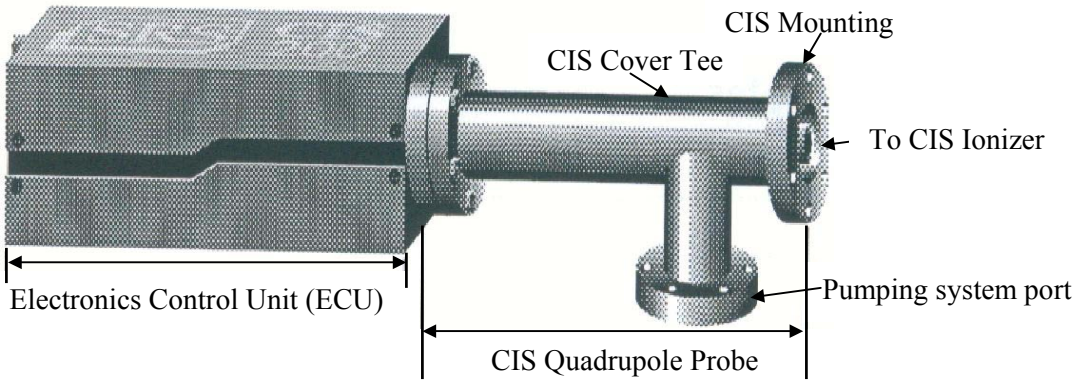

Figure 10.1 The RGA setup showing the Electronic Control Unit and the CIS Quadrupole probe attached to it. A turbomolecular pump is connected to the pumping system port.

The mass filter determines which ions reach the detector at any given time. It is operated by a combination of RF and DC voltages and the filtering action is based on the mass to charge dependency of the ion trajectories in the RF and DC fields. In this device the x-axis acts as the high-pass filter and the y-axis is a low-pass mass filter. The two directions together constitute a mass filter with a certain band pass.

The Electronics Control Unit used in conjunction with this device has an operating range that covers current magnitudes between 10^{-7} A and 10^{-15} A, and allows detectable partial pressures better than 10^{-11} Torr during electron multiplier detection. The electronics of this device are controlled with the help of a computer running the RGA windows software.

The CIS analyzer operating as a mass spectrometer allows operation in two modes, namely the Bar mode and the Analog mode. The Histogram (Bar Mode) scan operation was

preferred to the Analog scanning which tends to be rather slow and only allows a reduced amount of data to get exchanged during the scan.[1]

10.1 Mass Spectra Analysis

The qualitative spectral analysis involves identification of the peaks in the spectrum in agreement with the known fragmentation patterns of the components.

10.1.1 Ionization Source

The most common way of creating ions is using an electron impact ionization source. In general ions are formed by electron bombardment of a sample of the gas under analysis. The electrons radiated from the filament are accelerated towards the cage that is at a higher potential. Many of these electrons collide with the gas molecules within the source and cause ionization. After the ions have been formed, they are drawn from the source into the quadrupole field by the source plate, which is at a relatively negative potential.

It is important to remember that the ionized gases from the chamber do not make it to the CIS Analyzer because they undergo multiple collisions with the tube walls that connect the chamber to the RGA unit. Such collisions neutralize the ionized species and all previous information about ionization levels is lost.

10.2 Cracking Patterns

A cracking pattern is the characteristic spectrum produced by a sample gas introduced into a mass spectrometer. When a gas molecule is bombarded with electrons of a given energy it will always fragment in the same manner, producing ions in a certain ratio. However the exact

ratio between the intensities of the ions is dependent upon the energy of the electrons, in the present case this aspect was maintained constant by fixing the voltage and current input to the filament electron source in the RGA. With the knowledge of the cracking patterns and the processes involved, a mass spectrum is analyzed to reveal the component gases present.

Table 10.1 Composition of various species in a typical RGA spectrum.

Peak number (AMU)	Probable species
2	H_2^+, D^+
3	$^3He^+$, HD^+
4	D_2^+
6	D_3^+
15	CH_3^+
16	O^+, CH_2D^+
17	OH^+, CHD_2^+
18	H_2O^+, OD^+
19	HDO^+
20	D_2O^+
28	N_2^+, CO^+
44	CO_2^+

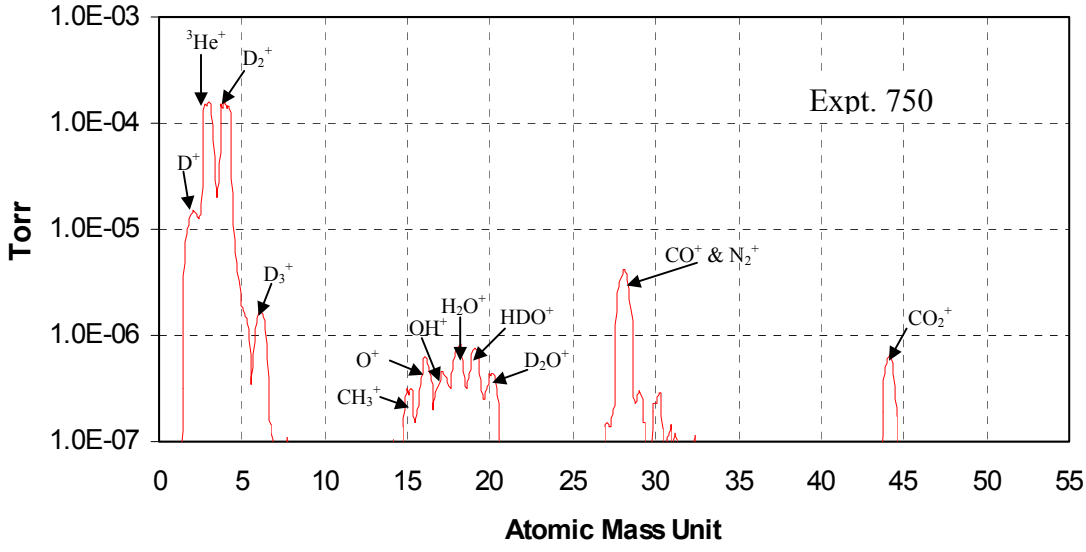

Figure 10.2 Typical RGA data during the first run after venting up to air, with D_2 + ^3He as the fuel gas mixture. Most likely species contributing to various peaks have been identified.

A typical RGA spectrum is shown in Figure 10.2, peaks at 44, 28 and some portions of 15, 16, 17, 18, 19 and 20 are caused by cracking of CO_2 into CO and the carbon from the further breakdown of CO combines with D_2 and H_2 and forms various species shown in Table.10.1.

In figure 10.2 unless ethylene or ethane has been used in the system (for cleaning the grid, stalk or the chamber walls), the most likely source of a mass peak 28 is nitrogen or carbon monoxide or a mixture of the two. The minor peaks at 14 and 12 (if present) could help to estimate the relative amounts of each, although in practice CO is always present to some extent due to the reaction of carbon compounds with oxygen at the heated filament of the mass spectrometer ion source as well as the filaments of ion gauges, etc.[1]

Water is always noticed during the initial runs after venting the chamber up to air. This is because the moisture in the air tends to get adsorbed on the surface of the chamber walls and is subsequently liberated slowly when pumped down. This water, upon dissociation near the electron filament ionizer in the quadrupole mass spectrometer, combines with several species and produces a cracking pattern. The hydrogen (from water) combines with carbon (from the filament) and forms CH_3^+ (peak at 15). Since the carbon has to combine with multiple hydrogen atoms, its formation is relatively scarce and hence the peak intensity (15) is relatively lower. However, the relative sensitivity of this gas with respect to N_2 could also play a role in determining its intensity, as explained in the next section.

The oxygen from water and CO_2 gets ionized, forms O^+ and contributes to a peak (16), along with CD_2^+ and a few CH_4^+ ions (which is even more scarce than CH_3^+). The O+ sometimes combines with D and forms OD^+ (18). If the water molecule were not completely dissociated, OH^+ would show up as a peak at (17). Some of the oxygen atoms recombine with

the D_2 gas and form D_2O^+ (20), while a hydroxyl OH molecule combines with a D atom and forms HDO^+ (19), or simply recombines with hydrogen and forms H_2O^+ (18), see Figure 10.2.

10.3 Relative Sensitivity

The relative height of the base peak of a component compared to nitrogen measured at the same partial pressure is defined as the relative sensitivity. Different gases are ionized with different efficiencies in the ion source of a mass spectrometer. Nitrogen is assigned the relative sensitivity value 1.00. The indicated partial pressure of a peak on a mass spectrum should be divided by the relative sensitivity factor to obtain the "true" partial pressure i.e. that pressure which correctly indicates its actual abundance in the gas sample.

Table 10.2 Typical gas relative sensitivities[2] normalized to N_2

Gas	Relative Sensitivity
H_2	0.70
He	0.23
CH_4	1.08
H_2O	1.17
Ne	0.24
CO	1.09
N_2	1.00
O_2	0.62
Ar	1.16
CO2	0.9

The relative sensitivity of various fuels in use for the current experiments (D_2 + ^{3}He) have to be taken into account (assuming the same relative sensitivity as H_2 + ^{4}He) when the fuel-ratio scan is performed. A fuel ratio scan is required to determine the optimum fuel mixture for highest D-^{3}He proton production. As shown in Figure 10.3 when the fuel ratios are monitored

using a RGA, for the same intensities of ^{3}He and Deuterium, there is more ^{3}He present than the D_2. Since the scale is logarithmic the total amount of ^{3}He is still greater than all the peaks of deuterium (D^+, D_2^+, D_3^+) combined.

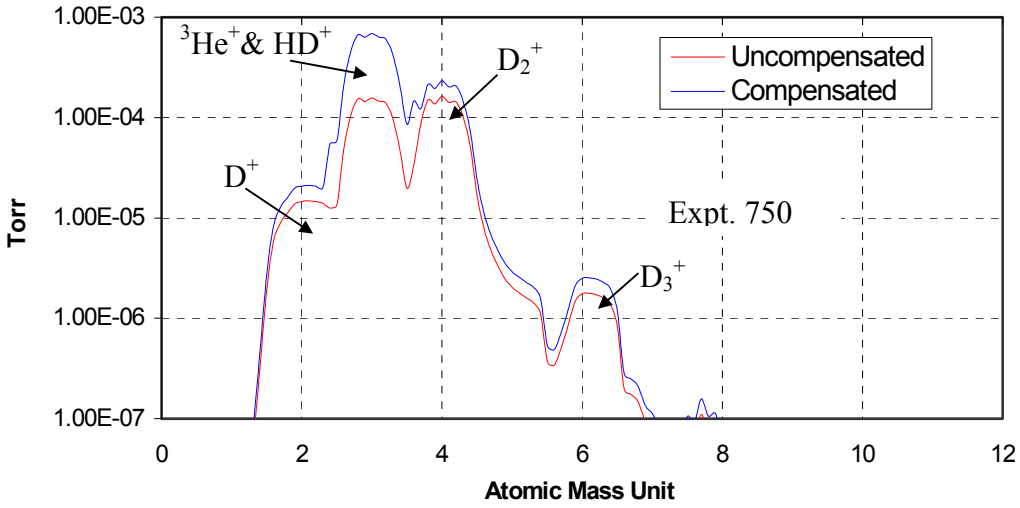

Figure 10.3 The true partial pressure values are reflected in the graph when the relative sensitivities (compensated) are taken into account.

10.4 Flow rate scan (D_2)

The rate of gases flowing into the IEC device's chamber determines the concentration of the impurities within the device. A higher flow rate (measured in standard cubic centimeters per minute, sccm) should flush out the impurities from the system. Though there should be little accumulation of impurities or fusion ash in the IEC plasma, leaks (though small) and the continuous liberation of adsorbed gases contributes to the impurity levels in the system, and a higher flow rate would help purge the system. An experiment was performed to determine the influence of flow rate over the net fusion rate of the system. The neutron and proton rates were

measured as the flow rate was varied gradually. The chamber pressure was maintained constant during the following experiments by controlling the gate valve.

A plot of the normalized proton and neutron counts/s shows a gradual increase with the flow rate as shown in figure 10.4. The flow rate was first decreased gradually (30, 20, 10 sccm) to 5 sccm and then the flow ratio was increased to 30 sccm by filling in the points (15, 25 and 30 sccm). This was done to remove any hysterisis effects. An average of ~15% variation in the fusion rate between max. and min. values of flow rate is observed. The error bars are statistical and are just the inverse square root values of the counts.

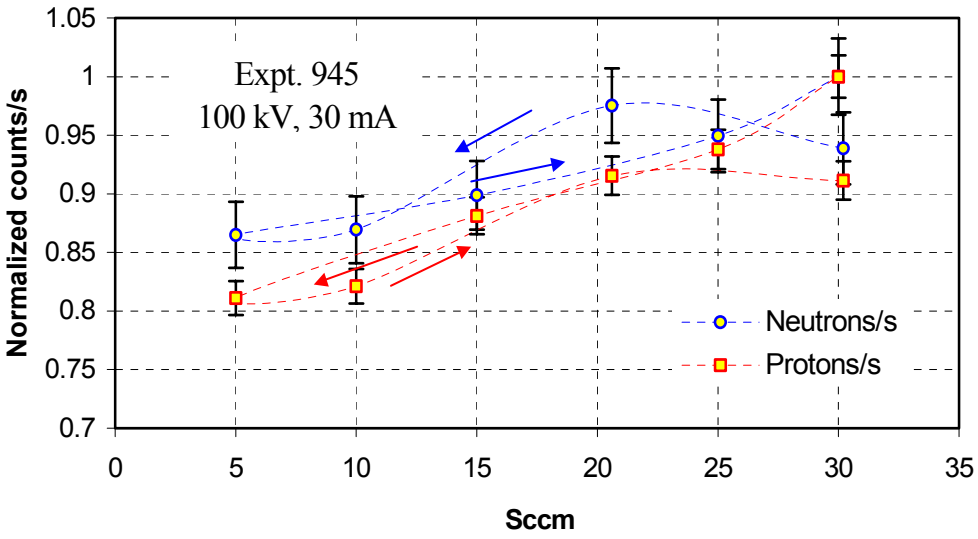

Figure 10.4 Variation of Normalized protons and neutrons with flow rate at constant voltage and current (100 kV, 30 mA) shows on an average a 15% variation. The arrows indicate the direction in which the sccm was varied.

The grid (W-5, made of W-25%Re) was formerly run many times before the experiment no. 945, hence the positive effects of surface cleaning (which causes lesser electron emission) due to sputtering with the extended run is ruled out. A disadvantage of running the

device at high flow rate is that a lot of fuel gas would be wasted (if not reprocessed), and it is crucial especially when ^{3}He is used. Hence the gains from the increased flow rate would be overshadowed by the increased operational costs. Another factor besides the flow rate that governs the fusion rate is the fuel flow ratio if two different gases are used (e.g., D-^{3}He). The effect of such variations on the fusion rate is elaborated in the next section.

10.5 Flow ratio (D_2/^{3}He) scan

In this experiment the ratio of concentrations of D_2 and ^{3}He in the chamber is varied by altering the flow rate of the two gases into the chamber. It was observed that changing the flow ratio of D_2/^{3}He fed to the chamber changed the proton rate and hence a scan was performed to determine the optimum flow ratio for the maximum proton production rate.

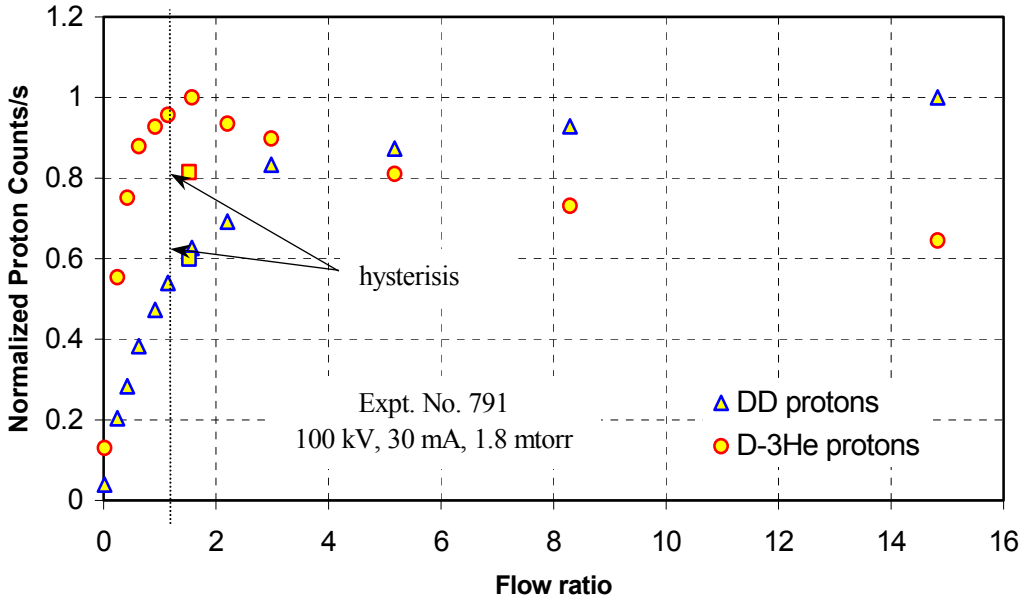

Figure 10.5 Flow ratio (D_2/^{3}He) scan vs. protons/s shows a gradual increase followed by a steep falloff as the ratio decreases for D-^{3}He protons, while it is a constantly decreasing value for DD protons.

Figure 10.5 shows the flow ratio scan performed by varying the flow rate of each of the fuel gases (D & ^{3}He) flowing into the chamber while simultaneously measuring the peaks (D_2 and ^{3}He) using an RGA. The ratio $D_2/^3$He is the ratio of the two peak intensities at 4 and 3 atomic mass unit (amu) respectively, as shown in figure 10.3. However, the values on the x-axis in Figure 10.5 are not compensated for the relative sensitivities. The relative sensitivity of D_2 and ^{3}He from table 10.2 are 0.7 and 0.23 respectively (isotopic dependence is negligible). Hence the flow ratio $D_2/^3$He in Figure 10.5 must be multiplied by $0.23/0.7 \approx 0.33$. Figure 10.5 is plotted again in Figure 10.6 with the values on the x-axis multiplied by 0.33.

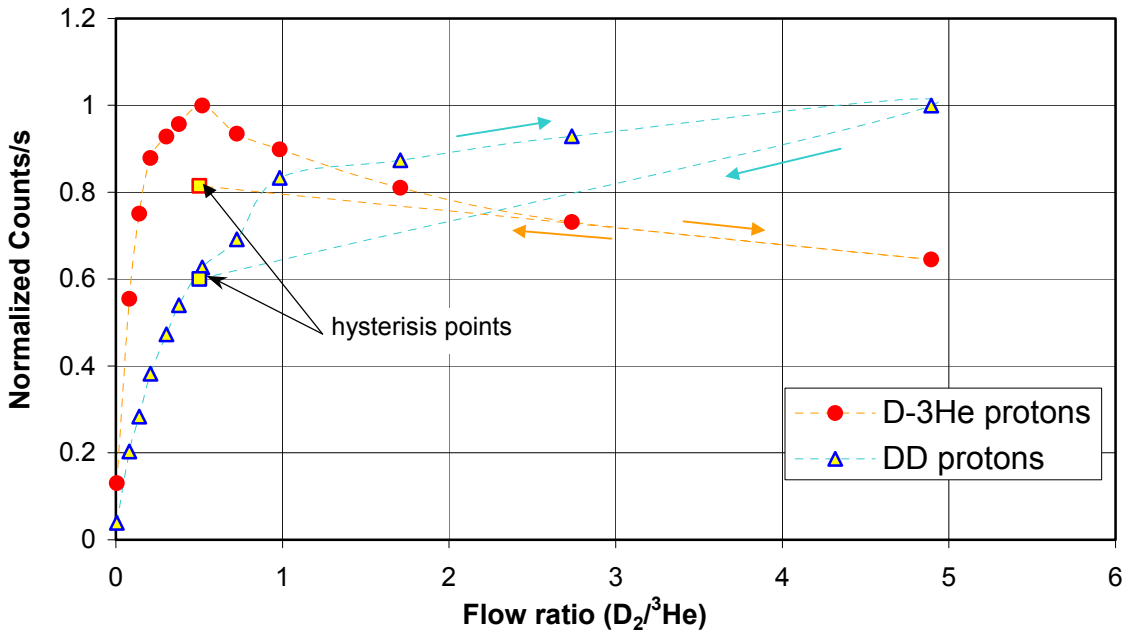

Figure 10.6 Compensated flow ratio ($D_2/^3$He) scan vs. protons/s shows a maximum D-^{3}He production rate at a flow ratio of ~ 0.5. The arrows show the direction in which the flow ratio was varied.

From the Figure 10.6 the optimum ratio for maximum proton production is ~0.5. As the concentration of deuterium gas (i.e., the ratio $D_2/^3$He) is increased, the D-^{3}He proton rate

decreases while the DD proton rate increases because there are more DD reactions due to increased concentration of D_2 gas in the chamber.

When the flow ratio is decreased below 0.5, both the D-D and D-^{3}He proton rates fall, this is because there are fewer deuterium atoms for either D-D or the D-^{3}He reactions to occur. From the earlier argument the increase in D_2 concentration should equally decrease the number of D-^{3}He reactions, but the falloff is more gradual. This is because D-^{3}He reactions are dominated by embedded reactions (see chapter 5.0) and there is only a certain concentration of ^{3}He embedded into the grid surface that is available for D-^{3}He reactions. The D-^{3}He reaction rate also depends on the previous run history of the grid.

Another observation during this experiment was that after increasing the flow ratio to a maximum value, when the system was returned to the flow ratio of 0.5, the DD reaction rate was reproduced but not the D-^{3}He rate. As the flow ratio was increased earlier, much of the embedded ^{3}He was consumed by the deuterium ions bombarding the cathode grid and when the flow ratio was returned back to 0.5, there would be lesser concentration of ^{3}He left in the grid wires. Such behavior could cause the D-^{3}He reaction rate to be lower than the earlier measurement at the same flow ratio. Furthermore, it can be safely predicted that if this scan were performed in the other direction, i.e., after decreasing the fuel ratio to a minimum value, returning back to the fuel ratio of 0.5, the D-^{3}He fusion rate would be higher because there would be a higher concentration of ^{3}He in the wires. A crossover is observed at around a flow ratio of 1.5 in figure 10.6. The DD reaction rate reaches a maximum value at the maximum flow ratio;

this is expected since for higher DD reaction rates one would need a higher concentration of D_2 in the chamber.

10.6 Impurity concentration in an IEC chamber

As an extension to the earlier experiment section 10.4, the partial pressures of each of the constituent gases (including impurities) were monitored as the flow rate scan was performed.

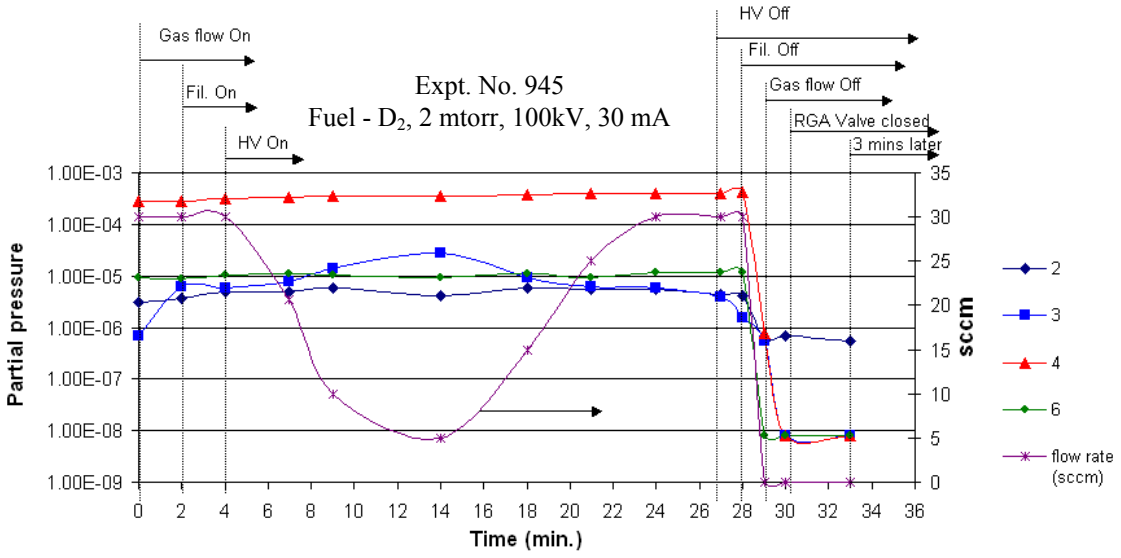

Figure 10.7 Variation of partial pressures with flow rate. Various events (gas flow, filament on/off, high voltage on/off etc.,) were recorded with time.

Figure 10.7 shows the variation of partial pressures of D^+ (2 amu), HD^+ & $^3He^+$ (3), D_2^+ (4) and D_3^+ (6), for the DD experiment no. 949 (the cathode had been previously run with ^3He). The concentration of D_2^+ remains almost constant throughout the scan since the flow rate and the chamber pressure are maintained constant. Two minutes after the gas flow was turned on the filaments inside the IEC chamber were turned on, as a result of which the 3 amu line intensity increases noticeably. This means that the HD^+ concentration is increasing because the hydrogen

from water dissociates and recombines with deuterium atoms to form HD (3 amu), this molecule later forms HD^+ in the ionization source of the RGA. The ^3He is absent in the present run and hence its contribution to the 3 amu peak is ruled out. A decrease in the D_2 flow rate further increases the HD^+ concentration, this is because the ionization process at the RGA filament is more efficient at low flow rates, and once ionized, the formation of HD^+ is favored through the recombination process.

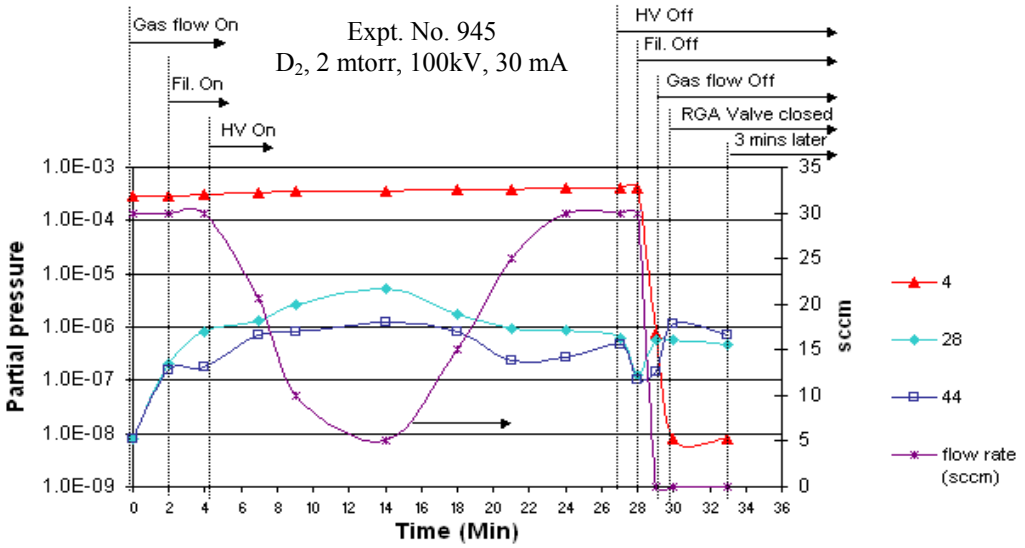

Figure 10.8 Variation of partial pressures of 4, 28 and 44 amu peaks with flow rate.

Figure 10.8 shows the variation of peaks at 28 and 44 amu with time for the experiment described in Figure 10.7. The concentration of D_2 as mentioned earlier is constant. The concentration of both the peak 28 goes up when the filaments inside the chamber are turned on, suggesting that CO is generated mostly from filaments inside the chamber. However, the concentration of CO is observed to increase after the gas flow is shutoff, this is because the CO from the RGA filament builds up in the Ionization source region in the absence of adequate gas flow as explained below.

When the flow rate is decreased, the concentration of these two peaks increases as expected because the chamber is not flushed out quickly. This statement is further supported by the observation that the impurity concentration (28 & 44) decreases with the increasing flow rate. When the high voltage is turned on, the concentration of the two C impurities increases (CO & CO_2) and when it is turned off the concentration goes down. This could mean that the cathode grid is also a source of impurities or that the electrons generated at the cathode accelerate and hit the outer grid and the chamber walls thus releasing the adsorbed gases. When the RGA valve was closed the concentration of these impurities once again increased showing that the filaments inside the RGA also form a source of impurities. The reason it becomes significant after the valve is closed is because the impurity build up occurs in the ionization source due to the lack of gas flow in that region.

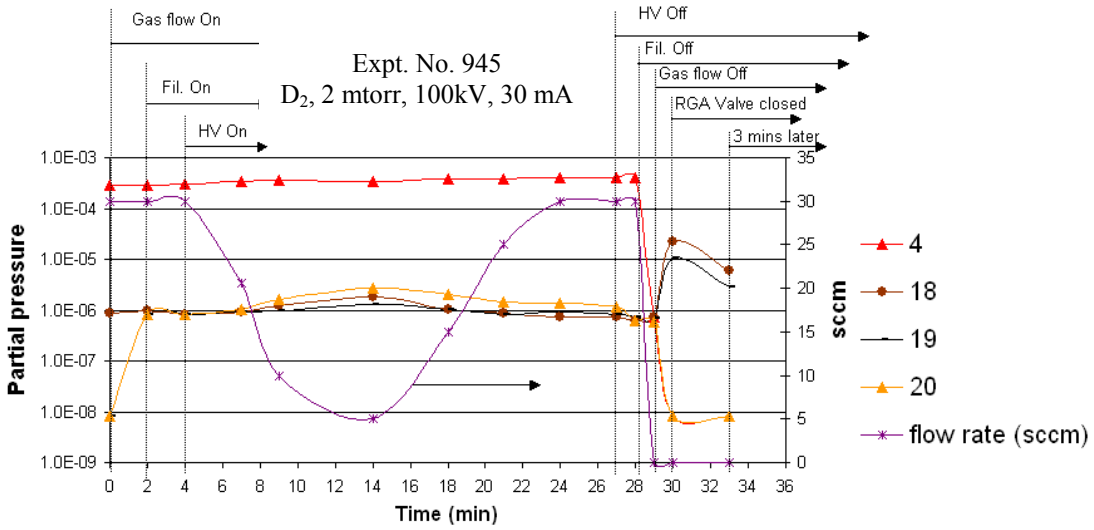

Figure 10.9 Variation of partial pressures of 4, 18, 19 and 20 amu peaks with flow rate.

The concentration of the peaks 18 (H_2O^+), 19 (HDO^+) and 20 (D_2O^+) shown in figure 10.9 remains constant till the high voltage is turned on and the flow rate is decreased. D_2O^+ has relatively higher partial pressure because the dissociated oxygen atoms from the H_2O molecule have a greater probability of recombining with D_2 molecules to form D_2O. The concentration of all three peaks (18, 19 and 20) goes up as the flow rate is decreased because the chamber walls get heated (with time) and release the adsorbed water H_2O molecules that form the other peaks at 19 and 20 amu.

As the flow rate is decreased the impurity molecules thus created are not flushed out quickly allowing their partial pressures to build up. Furthermore, when the high voltage is turned off the concentration of all three impurities mentioned above decreases, this is because the impurities released from the chamber wall due to the electron bombardment (from the cathode) now ceases. A further decrease in the impurity concentration is observed when the filaments are turned off suggesting that the impurities are no longer released from the walls and/or are getting adsorbed back on to the chamber walls.

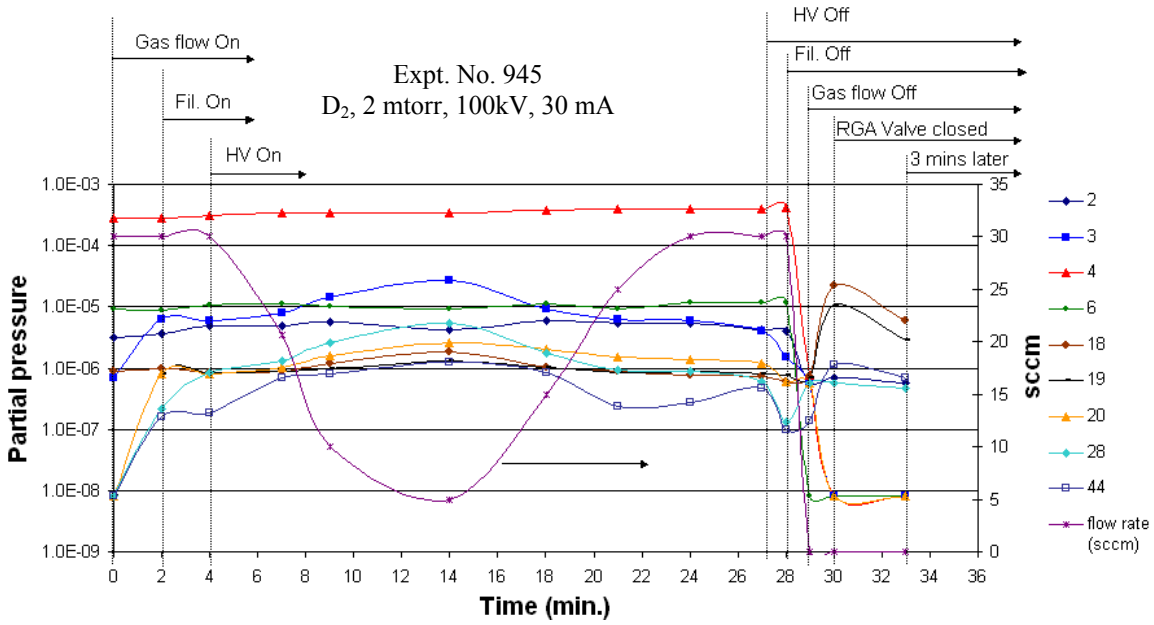

Figure 10.10 Variation of partial pressures of process gases (fuel & impurities) and flow rate, vs. time.

With the gas flow shutoff the concentration of the peaks 18 and 19 go up due to impurity build up, also suggesting that the ionization source of the RGA is also contributing to the impurity peak intensities. The concentration of the peak at 20 amu goes down, since a lesser amount of D_2 is now available for the formation of D_2O. Figure 10.10 summarizes the entire partial pressure scan with flow rate vs. time.

10.7 Conclusions

The RGA filaments seem to contribute to some of the impurity peaks detected by the CIS quadrupole detector. The filament electron source used inside the IEC chamber gives out CO_2 that dissociates and forms CO^+, and the oxygen from both CO_2 and H_2O combines and forms other molecules such as HDO and D_2O. Higher gas flow rate tends to flush out the impurities from the system causing the fusion rate to increase. The flow ratio scan revealed that the

optimum mixture of D_2 with ^3He is D_2:^3He::1:2 (see figure 10.6) for maximum D-^3He proton production. To attain the above mentioned concentration ratio $D_2/^3He$, the flow ratios must be maintained at 1.5 (figure 10.5) for the fuel gases, the relative sensitivity of the flow meter automatically adjusts the concentration inside the chamber to a concentration ratio of 0.5.

10.8 References

[1] Closed Ion Source Quadrupole Gas Analyzer Operating manual and Programming Reference, Stanford research systems, Version 2.3 (3-Sep-97).

[2] O'Hanlon J. F., "A User's Guide to Vacuum Technology," Second Ed., John Wiley & Sons, Chapter 8, pg. 1210.

Chapter 11.0: Single loop experiments

Experiments were conducted using single loop cathode grids (made of Re and W-25%Re). The fusion rate observed using these loops was used to compare the performance of the grid material under identical conditions (same voltage, current, impurity levels, etc.). A general equation that accurately reflects the recirculation ion current should account for the electron loss (see, eqn. 11.10). Earlier discussion on the thermionic emission in chapter 9.0 showed that at high power operation electron emission would be a showstopper even before the grid meltdown occurs. However, the secondary electron emission is an important factor that determines the IEC device's performance even at low power. If the secondary electron emission coefficient were large, the ion current reaching the central grid would be smaller (inversely proportional). Hence, an understanding of this phenomenon would prove helpful.

Though secondary electron emission has been known to be a power drain in the past, it was not accounted for accurately (in a general sense, valid for all voltages).[1] To resolve this problem a general expression for the secondary electron emission coefficient that depends on the stopping power of the electrons[2,3] is used. This new understanding would help enhance the

efficiency of the IEC device through better cathode grid material selection for high power operation (> 10 kW).

The recirculating ions across the face of the single loop grid form a line source (more precisely a cylindrical source). Using the eclipse disc diagnostic[4] the distribution of the ion energies across the loop grid has been characterized.

The description of the IEC experimental setup at the University of Wisconsin, Madison and its principles of operation are given in chapter 2. Only the modifications done to this setup for the current experiments are described here, see figure 11.1 (a). The central mount, that is also a high voltage feed-through, is vacuum-sealed through an o-ring and held in place by gravity. This mount has an axial freedom of rotation necessary for the current set of experiments.

The spherical central grid of the IEC device is replaced by single metallic loops made of either pure Re or W-25%Re, as shown in figure 11.1 (a). This is done so that the ion flux over the loop's surface would remain constant even when grids are replaced. This configuration allows comparison of different grid materials under identical conditions, and orienting the grids in the same direction is a lot easier.

Since a spherical grid has ~10 times more volume of wire (radius being constant) in it than a single loop, the grid wire in the spherical grid tends to remain at relatively low temperatures. For identical input power the single loop grid is subjected to much higher power density, hence projecting the grid performance at higher input powers would be possible using such single loop grids. Building identical loop grids is also easier than building two identical spherical grids unless some special molds are used. Furthermore, using a spherical grid has the

disadvantage that uneven ion flux distribution due to anisotropic ion source distribution can cause asymmetric heating (certain regions of the grid are selectively overheated, see chapter 9) of the central grid that would skew the temperature measurements.

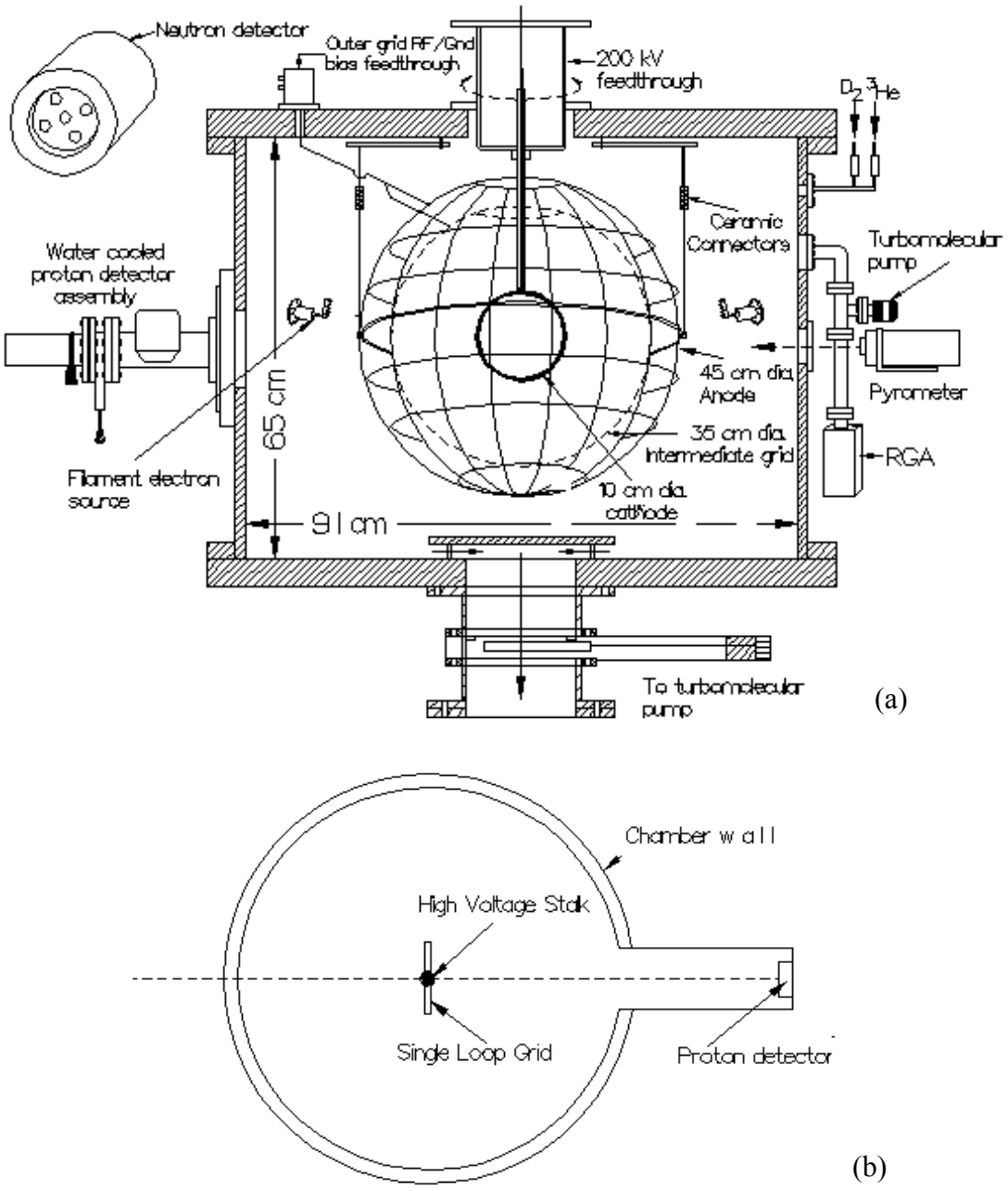

Figure 11.1 (a) Experimental setup for the determination of various electron contributions. (b) The orientation (top view) of the Loop grid inside the IEC chamber.

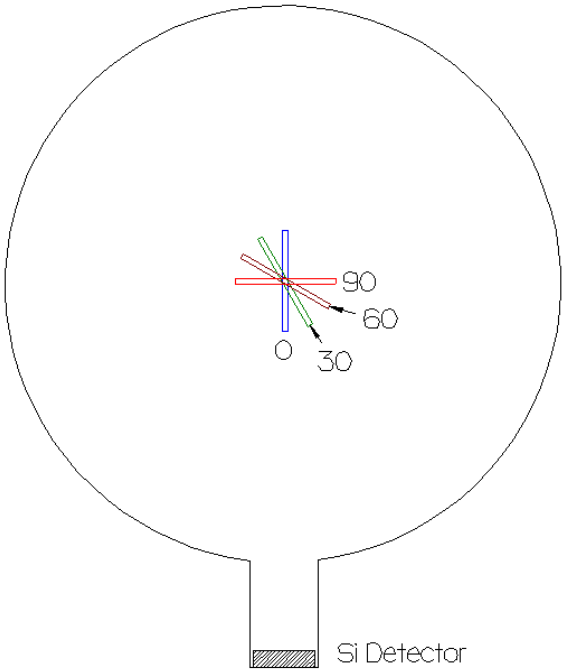

Figure 11.2 Top view of the single loop grid rotation with respect to the Si detector.

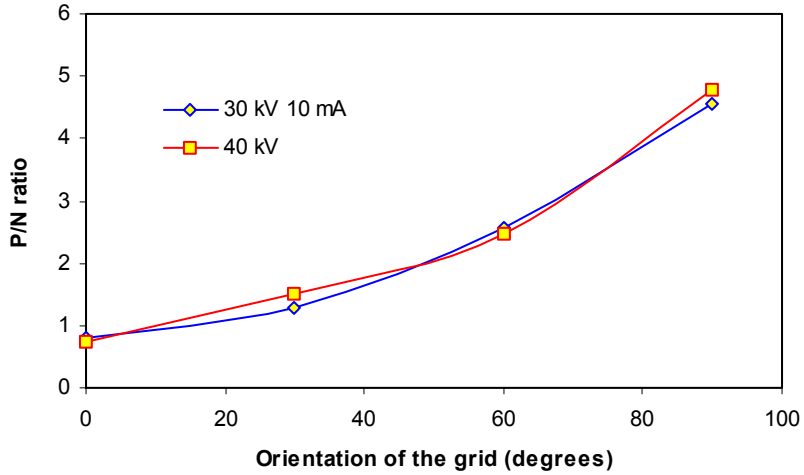

Figure 11.3 The Proton/Neutron ratio increases as the grid is rotated from 0^{o} to 90^{o} showing that a single loop grid behaves like a line source.

In the following section the results of an experimental investigation to determine the secondary electron emission contribution is reported. Two materials (pure Re and W-25%Re) were used in the construction of the Loop grids of 10 cm diameter to evaluate their suitability for the cathode grid construction.

11.1 Characterization of fusion reactions in a single loop grid configuration

To characterize the fusion in a single loop grid, the grid was rotated about the axis using the high voltage stalk supporting it as shown in figure 11.2. The proton and neutron data were recorded simultaneously and are plotted in figure 11.3. The P/N ratio increases as the grid orientation is changed from 0^o to 90^o showing that more protons are detected. This occurs because the proton detector sees more of the volume source with every bit of rotation towards 90^o.

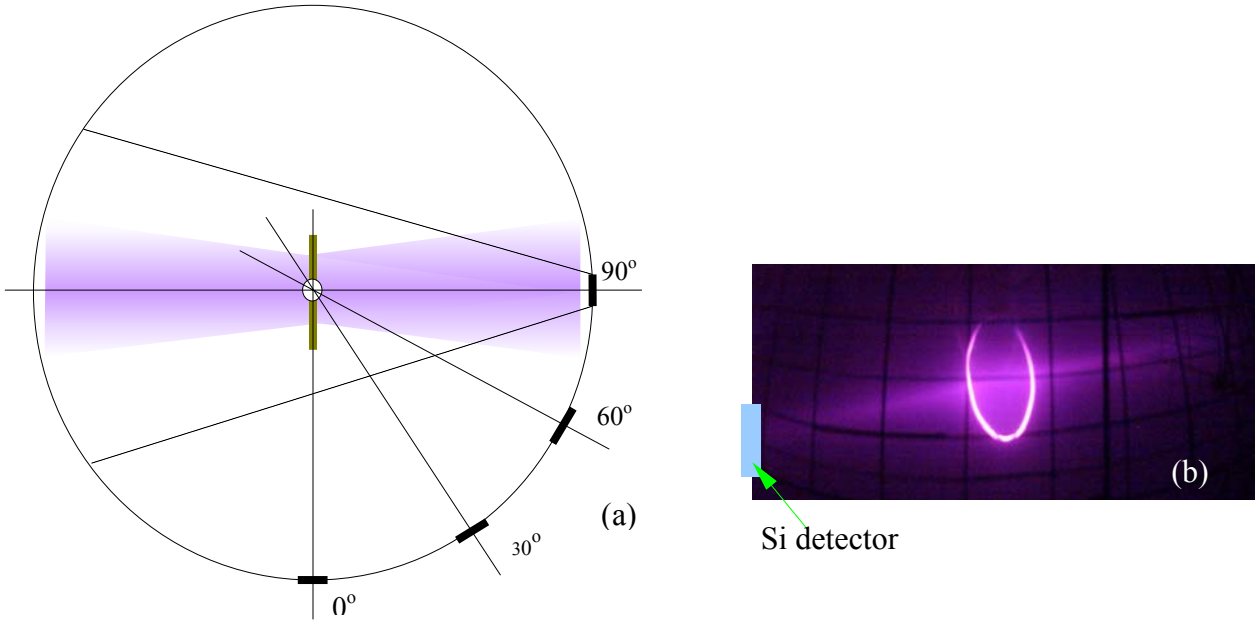

Figure 11.4 (a) In this geometry the loop grid is fixed and the detector is rotated (although physically it is the other way around). The view of the detector is a cone that encompasses greater volume of the line (cylindrical) source as it is rotated from 0^o to 90^o. (b) Picture of the plasma in the single loop grid configuration at 7.35 mtorr, 10 kV taken from the view port that is oriented at 90^o to the axis of the detector port.

From figure 11.4 (a) it is observed that in a single loop grid configuration, the greatest number of fusion reactions is observed by the proton detector when it looks face-on. In this configuration maximum volume of the cylindrical source is covered by the line of sight. This

indicates that the single loop geometry creates a line source. Such a line source is not detected by the neutron detector because it still sees only an effective point source, but the proton detector sees a line source. This would mean that in a cylindrical IEC device[5] higher fusion rate would be observed along the face-on direction.

The temperature of the grid at various points along the loop were measured at 25 kV and 20 mA, figure 11.5 (a). The wire showed a gradual variation in temperature indicating an uneven distribution of ion flux reaching the Loop grid. An identical temperature variation was observed using the pure Re wire loop grid (LoopRe).

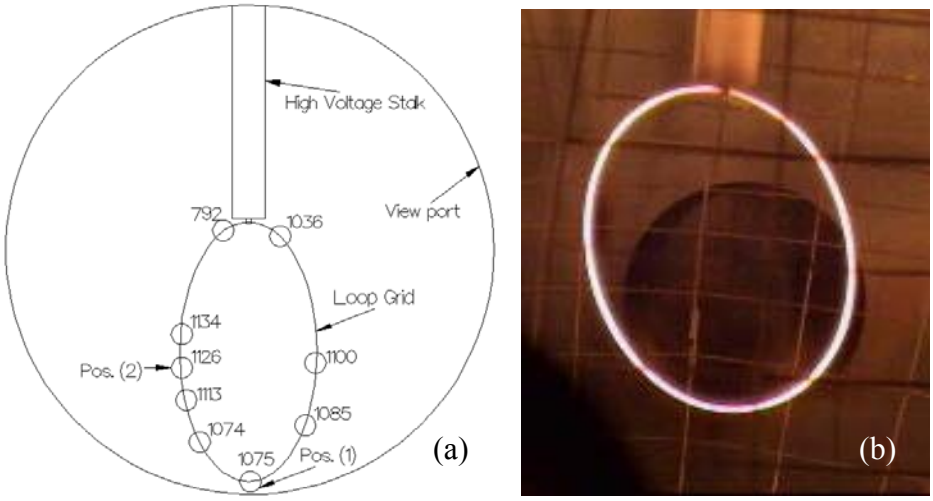

Figure 11.5 (a) Temperature measurement (in ^{o}C) at various locations on the loop, as seen from a view port. (b) Picture of the loop as seen from the view port at 25 kV 10 mA.

The temperatures at one spot (shown in figure 11.6) for LoopW and two different spots (shown in figure 11.7) for LoopRe, on the loop grid were measured while keeping the power constant at 400 W [see figure 11.5 (a)], the voltage and current were varied during this experiment. The temperature varied as shown in figure 11.6 & 11.7. Interestingly it is observed that at higher input voltage and correspondingly low input current (used in maintaining the

power constant), the temperature of the grid remains low; on the other hand, at low input voltage and high current the temperature of the grid is relatively high.

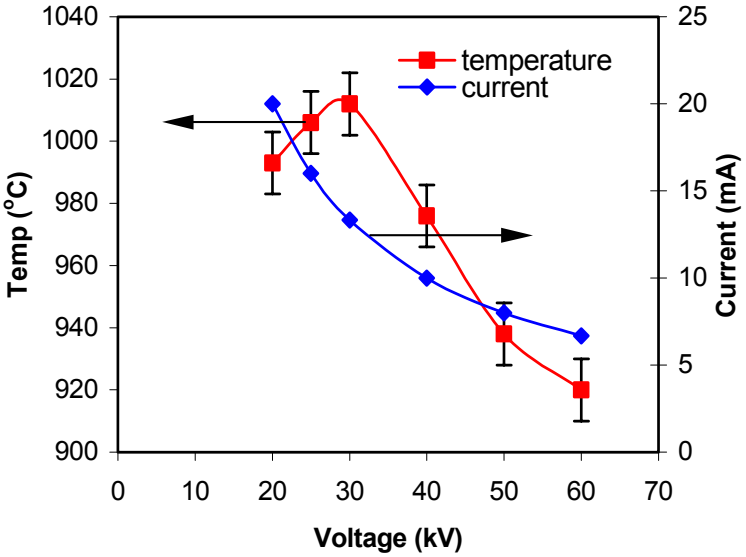

Figure 11.6 Voltage Vs Temperature and current at constant power (400W) for LoopW.

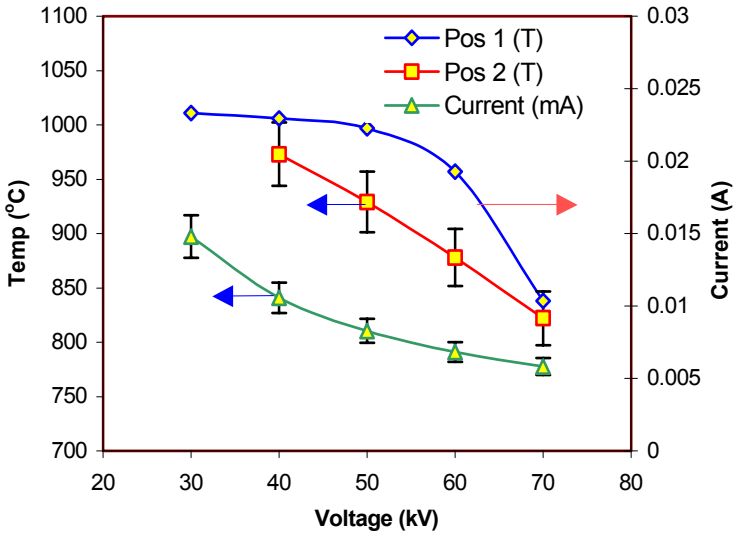

Figure 11.7 Voltage Vs Temperature and current at constant power (400W) at two spots for LoopRe

Although one may expect that the temperatures would remain constant for a constant input power, this was not the case (either with W-25%Re Loop, figure 11.6 or Re Loop, figure 11.7). This could be explained only if the electron current emitted from the cathode were

to increase with voltage causing a corresponding decrease in the ion current, causing the energy deposited on the grid to decrease as well. Since the thermionic emissions at the measured temperatures were negligible their contributions to such are therefore neglected. The only other reason why this could be occurring could be if the secondary electron emission coefficient is changing with voltage, thus causing a higher electron emission at higher voltages and causing the ion current to be lower at higher voltages and hence the energy deposited on the grid is also lower. Although such measurements of the secondary electron emission coefficient are not available for W-25% Re alloy and the Re, they should be similar to that shown in the figure 11.8 for Mo[6] (similar to a W target behavior[7]) because the secondary emission coefficient varies slowly with Z (see figure 11.9). Though not very useful, this figure 11.8 shows how secondary electron emission changes with voltage and ion species.

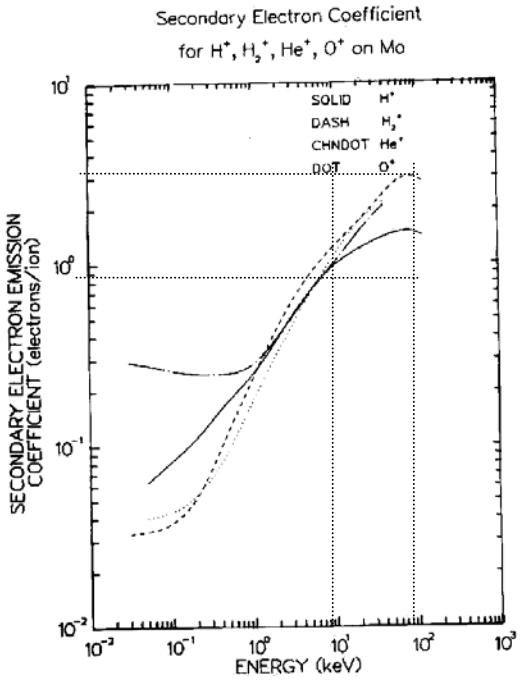

Figure 11.8 Variation of 'γ' with ion energy (keV) for various species (H^+, H_2^+, He^+, O^+) on Mo.[8]

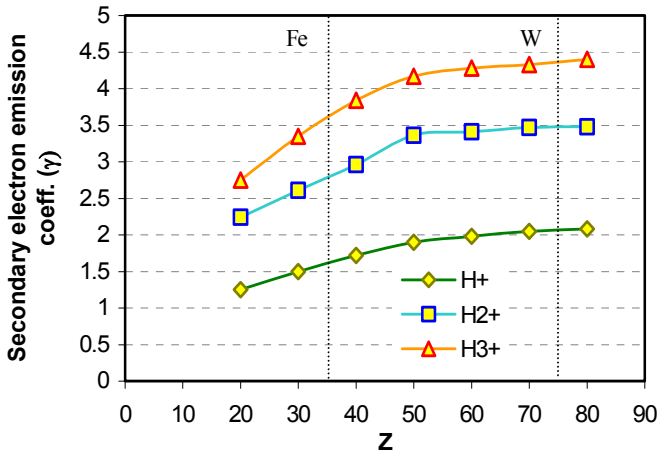

Figure 11.9 Variation of the secondary electron emission vs. the atomic number for various H^+, H_2^+ and H_3^+ ion impact at 100 keV.[9,10,11] $\gamma(H^+) < \gamma(H_2^+) < \gamma(H_3^+)$ irrespective of the material used. Variation of γ with Z is small from 74 (W) to 79 (Au) and hence the data for Au can be used for W without adding huge errors to the final results.

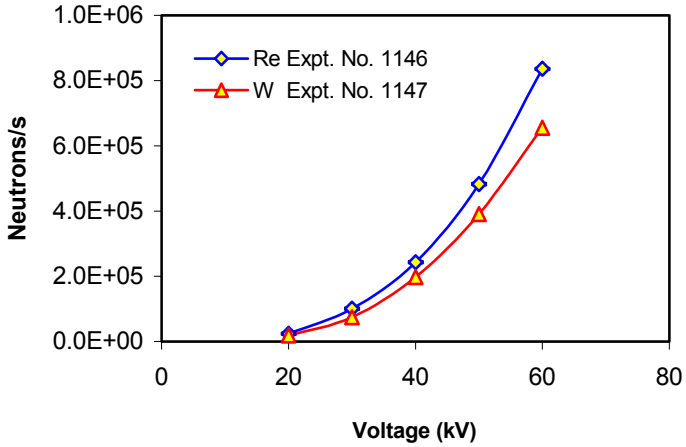

Figure 11.10 The neutron rate vs. voltage for the two Loops (W & Re) at 90° orientation.

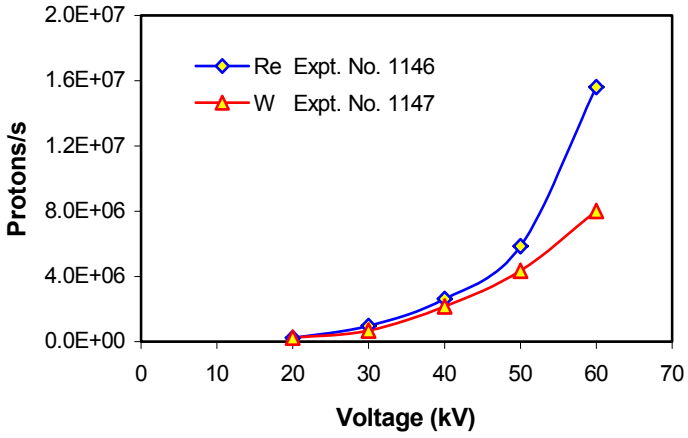

Figure 11.11 The Proton rate Vs Voltage for the two Loops (W & Re) at 90° orientation.

Thorson et al.,[12] accounted for the secondary emission by assuming a constant coefficient $\gamma \approx 1$ in the following expression (assuming randomized orbits[13] of the recirculating ions) for the true ion current (I):

$$I = \frac{\eta[I_{meas}]}{(1-\eta^2)(1+\gamma)} \qquad (11.1)$$

where I_{meas} is the (measured) power-supply current and η is the geometric transparency of the grid.

The fusion rate (as measured using the neutrons) of the two loops measured under similar conditions showed significant differences. The average fusion rate is ~27% higher with Re than with W-25%Re loop grid as shown in figure 11.10 for 90° orientation (face-on with the detector, see figure 11.1 (b)).

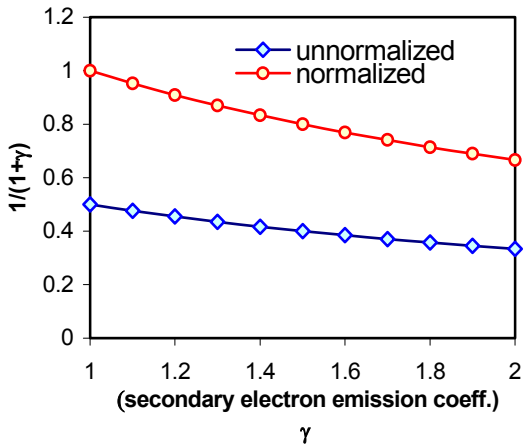

Figure 11.12 Plot shows how the coefficient 1/(1+γ) in eqn.(11.1) is affected by the variation in 'γ'.

The difference in the fusion rates of the two loops is based on the neutron rate because the neutron detector effectively sees a point source (since it is far away) whereas the proton rate is subjected to the line source effect described earlier in this chapter. From figure 11.11 the

proton rate increases with voltage at a faster rate than the neutrons do in figure 11.10, this is because the increased ion current causes a higher amount of ion recirculation, resulting in a higher proton rate along the axis of the loop (also modifying the calibration factors) and an overall increased fusion rate.

If we were to include the variation of γ with voltage in the ion current equation (11.1), its value would change according to figure 11.12. This aspect is evident in the constant power scans wherein the temperature of the loop increased at low voltage and decreased correspondingly at high voltage at constant input power (400 W) see figures 11.6 & 11.7. From figure 11.12 the variation in $1/(1+\gamma)$ is as high as ~40% when γ changes from 1 to 2 and hence we may conclude that at higher voltage an additional amount of current is in the form of secondary electrons and if these electrons were minimized the fusion rate would be further increased (potentially 16% higher if γ is maintained ~ 1 at 100 kV).

Thermionic emission is small at 100 kV, 50 mA as the grid temperature is low, and the field emission is also small since there are no visible sharp edges on the single loops used for the experiments. The sharp edges principally arise at the spots where the wires are spot welded, but in the case of the single loop this was averted by moving the welded portions of the wire into the tip of the stalk. Since the stalk ST-38 was used for these experiments, and this stalk had a ¼″ central molybdenum rod, the welded portions of the loop were inserted into the hole of this rod. This minimized the exposure of the sharp points.

11.2 Secondary electron emission

Inelastic interaction of the atoms or ions entering the uppermost layers of a solid surface cause secondary electron emission (SEE). There are two mechanisms contributing to secondary electron emission.[2] They are known as the potential emission and the kinetic emission. In the former case, the yield γ of secondary electrons is proportional to the potential energy carried by the incident ion. The potential is assumed to be mainly relaxed via the Auger process. On the other hand, in the latter case, γ is said to be proportional to the stopping power for the impinging ion.[14,15]

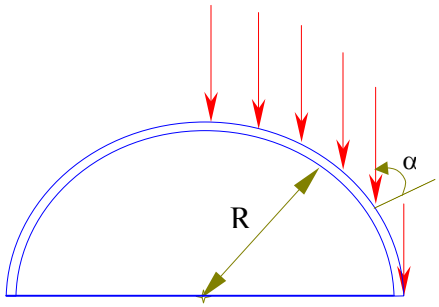

Figure 11.13 The angle of incidence of the ions on the wire varies from -90° to 90° with a singularity at 90°.

An empirical formula to relate the SEE coefficient (γ) with the stopping power $(dE/dx)_e$ led to the following formula:[7,16,3,15]

$$\gamma\left(H^{+}\right)=\frac{\Lambda}{\cos\left(\alpha\right)}\left(\frac{dE}{dx}\right)_{e} \qquad (11.2)$$

where Λ is listed in the table 11.1, Λ(H^+ on W) = 0.07 (assume valid for W-25%Re)and α is the angle of incidence (~0° for radially converging ions) see figure 11.13. The dependence of 'γ' on α is however not yet fully resolved in literature (there is singularity at α = ± 90°.

Table 11.1 Values of Λ for various materials.

k	$\Lambda(H^+ \rightarrow k)$ [3]
Ag	0.13
Al	0.11
Au	0.1
Cu	0.09
W	0.07

The stopping power dE/dx is given by:[17]

$$-\frac{dE}{dx} = \frac{4\pi e^4 z^2}{m_o v^2} NB \qquad (11.3)$$

$$\text{with } B \equiv Z\left[\ln\left(\frac{2m_o v^2}{I}\right) - \ln\left(1-\frac{v^2}{c^2}\right) - \frac{v^2}{c^2}\right] \qquad (11.4)$$

where N is the number density, Z the atomic number of the absorber atoms, m_o is the electron rest mass, and e is the electronic charge. The parameter *I* represents the average excitation and ionization potential of the absorber and is normally treated as an experimentally determined parameter for each element. For a non-relativistic case as in the present case (v<<c) and hence only the first term in the expression for B is significant.

$$B \equiv Z\ln\left(\frac{2m_o v^2}{I}\right) \qquad (11.5)$$

It is known that the secondary electron emission depends on the temperature of the substrate.[18,19,20] Such temperature variations can be determined using the following expression:[2]

$$\frac{\delta(T_1)}{\delta(T_2)} = \frac{1+\beta T_2}{1+\beta T_1} \qquad (11.6)$$

where β is approximately the temperature coefficient of resistivity, T_1 & T_2 are in K.

11.3 Molecular effects on the secondary electron emission

It is observed[3] that the *Z* dependence of the yields for hydrogen and helium projectiles are very similar, that the yields for H^+ and D^+ show the same energy dependence as that of the electronic stopping powers, that molecular ions give lower yields per atom than atomic ions, and that isotope effects are proven to be negligible in the energy range 2-50 keV, and are assumed here to be valid for all energies (up to 150 keV).

It has been suggested that the observed lower secondary emission yield with H^o than H^+, [$\gamma(H^o) \approx 0.85\gamma(H^+)$] for Gold is related to electron liberation within the solid, which is less effective for shielded protons as a consequence of lesser stopping in the first monolayers where the equilibrium projectile charge is not yet reached. Bombardment with molecular ions H_2^+ and H_3^+ should yield similar screening effects as for H^o, due to accompanying electron(s). No distinction is possible whether the H_n^+ molecules dissociate when penetrating the solid into (n-1)·H^o atoms and one proton, or the (n-1) electrons from a screening negatively charged cloud around the n protons. However, the secondary electron yield due to bombardment with molecular ions was expressed by adding the measured yields (n-1)·H^o atoms and one proton according to:[21]

$$\begin{aligned}\gamma\left(H_n^+\right) &= (n-1)\gamma\left(H^o\right)+\gamma\left(H^+\right)\\ &= \left((n-1)\cdot x+1\right)\gamma\left(H^+\right)\end{aligned} \qquad (11.7)$$

Where x is known[21] to be around 15%, hence

$$\therefore \gamma\left(H_n^+\right) \approx \left[0.0595n+0.0105\right]\cdot\left(\frac{dE}{dx}\right)_e \qquad (11.8)$$

We know that the composition of pure H_2 plasma is 20% H^+, 60% H_2^+ and 20% H_3^+ i.e., concentration ratio of 20:60:20 at 5 mtorr chamber pressure.[22] Since the present IEC device is operated at ~2 mtorr, the collisionality is lower and the formation of H_3^+ is less likely.

In the absence of experimental data, we make an educated guess of the concentration ratio as 25:70:5. Therefore, the effective secondary electron emission coefficient is now given by:

$$\gamma_{eff} = 0.25\gamma(H^+) + 0.7(H_2^+) + 0.05(H_3^+)$$

$$=[0.25+0.09065+0.7+0.00945+0.05]\gamma(H^+)$$

$$\approx 1.1\gamma(H^+) \qquad (11.9)$$

Hence the SEE coefficient for typical deuterium IEC plasma is given by:

$$\gamma_{eff} \approx 1.1 \cdot \Lambda \cdot \left(\frac{dE}{dx}\right)_e \qquad (11.10)$$

If the effect of impurities were to be considered this coefficient would be even higher. A general equation for recirculation ion current that accounts for all electron emissions is given below:

$$I = \frac{\eta\left[I_{meas} - I_{th} - I_e - I_f\right]}{\left(1-\eta^2\right)\cdot\left(1+1.1\cdot\Lambda\cdot\left(\frac{dE}{dx}\right)_e\right)} \qquad (11.11)$$

where I_{meas} is the power-supply (measured) current, η is the transparency of the grid. The quantity I_{th} is the thermionic emission current (see chapter 7.0) and 'I_e' accounts for the photoemission, I_f the field emission (explained in the subsequent sections).

The expression for the secondary emission has to be corrected for the temperature variation according to eqn. 11.6.

The core ion density is given by:[1]

$$n_{ic} = \frac{\eta I_{meas}}{(1-\eta^2)\cdot[1+\delta_e]}\left(\frac{1}{e\mathrm{v}_c\pi r_c^2}\right) \qquad (11.12)$$

Based on the earlier argument, accounting for the various electron emissions this eqn. 11.12 could also be modified for accurate estimation of the core ion density as follows:

$$n_{ic} = \frac{\eta(I_{meas} - I_{th} - I_e - I_f)}{(1-\eta^2)\cdot\left[1+1.1\cdot\Lambda\cdot\left(\frac{dE}{dx}\right)_e\right]}\left(\frac{1}{e\mathrm{v}_c\pi r_c^2}\right) \qquad (11.13)$$

11.4 Impurity effects

Table 11.2 Secondary electron emission coefficients by impact of normally incident H^+, H_2^+, He^+ and O^+ ions on Mo.[23,24,25,11,26,27,28,29]

Energy (keV)	H^+	H_2^+	$^4He^+$	O^+
3.0 E-02		3.3 E-02	2.9 E-01	
5.0 E-02	6.3 E-02	3.4 E-02	2.8 E-01	4.0 E-02
7.0 E-02	7.2 E-02	3.5 E-02	2.7 E-01	4.2 E-02
1.0 E-01	8.3 E-02	3.8 E-02	2.6 E-01	4.3 E-02
2.0 E-01	1.1 E-01	5.2 E-01	2.5 E-01	5.4 E-01
4.0 E-01	1.6 E-01	9.8 E-01	2.5 E-01	8.0 E-01
7.0 E-01	2.1 E-01	1.7 E-01	2.6 E-01	1.3 E-01
1.0 E-00	2.5 E-01	2.4 E-01	2.8 E-01	1.8 E-01
2.0 E-00	3.9 E-01	4.5 E-01	4.0 E-01	3.3 E-01
4.0 E-00	6.2 E-01	7.6 E-01	6.0 E-01	5.7 E-01
7.0 E-00	8.4 E-01	1.05 E-00	8.5 E-01	8.7 E-01
1.0 E+01	9.8 E-01	1.25 E 00	1.0 E 00	1.1 E00
2.0 E+01	1.2 E 00	1.7 E 00	1.5 E 00	1.7 E 00
4.0 E+01	1.4 E 00	2.4 E 00	2.1 E 00	2.2 E 00
7.0 E+01	1.5 E 00	3.0 E 00		
1.0 E +02	1.5 E 00	3.0 E 00		
1.2 E+02	1.4 E 00	2.8 E 00		

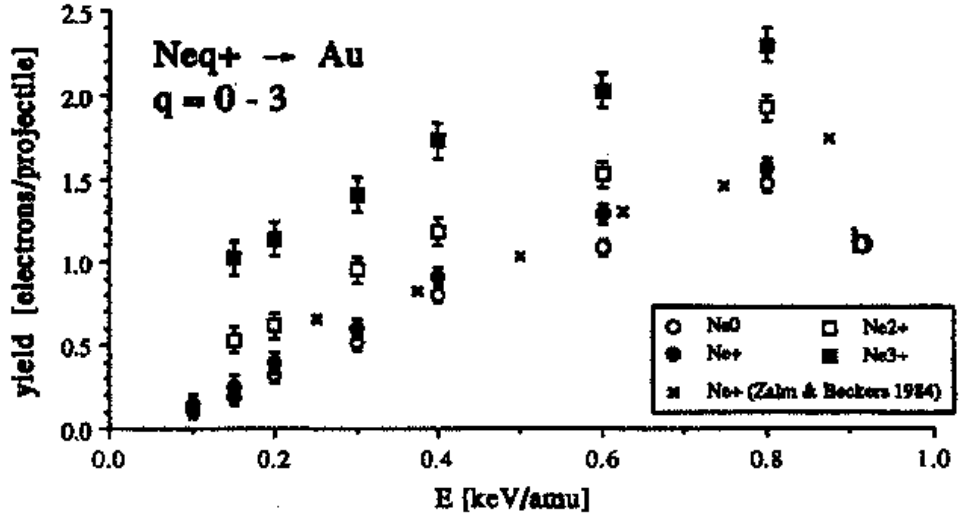

Figure 11.14 Electron emission yields derived from emission statistics measurement for the impact of Ne^{q+}.[21] Behavior of the secondary electron emission coefficients (γ) for other species with W metal surface would be similar to this graph (higher γ for higher ionization state).

It is a general observation that the fusion rate decreases in the presence of impurities. Although impurity buildup does not generally occur in an IEC device, noticeable changes in fusion rates are observed even when trace amounts of impurities are present in the chamber. This is because the secondary electron emission coefficients for the impurity ions are higher than the fuel gas (D^+, same as H^+ in table 11.2) especially at higher ionization states as shown in Figure 11.14 below.

Besides not contributing to the overall fusion rate the impurity ion liberates many more secondary electrons than a single D^+ ion, thus reducing the ion current reaching the cathode for a constant power supply current. Moreover, in terms of secondary electron emission, even D_2^+ and D_3^+ are impurities since they generate more secondary electrons than D^+, see figure 11.14. Hence it is desirable to populate the deuterium plasma with the highest fraction of D^+ ions to improve the efficiency of the device. To realize this ion guns generating D^+ ions may be used.

11.5 Photoemission electrons

The electrons liberated from the cathode accelerate to high energies before hitting the chamber walls where they deposit their energy, as a consequence of which bremsstrahlung radiation is emitted. Since these electrons are not very relativistic, the bremsstrahlung radiation is released in all directions isotropically (if it were relativistic, radiation would occur in the form of two frontal lobes[30]).

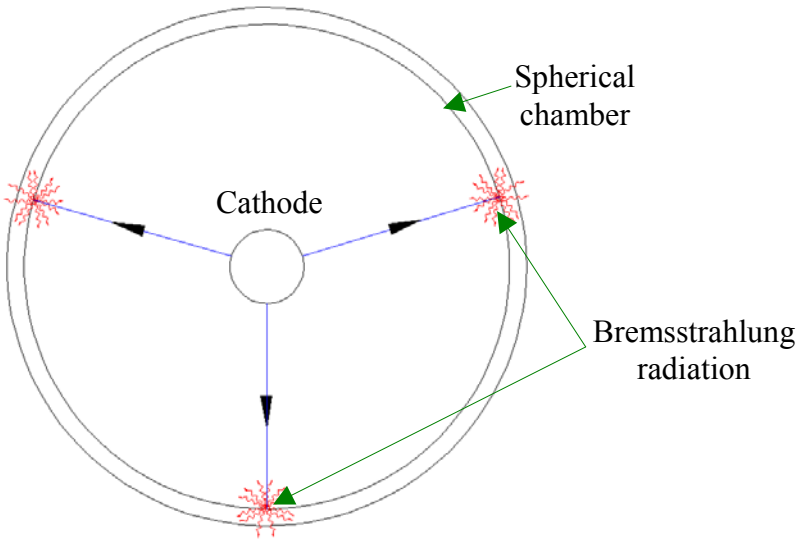

Figure 11.15 The electrons released near the cathode accelerate and deposit their energy on the chamber walls and release bremsstrahlung radiation.

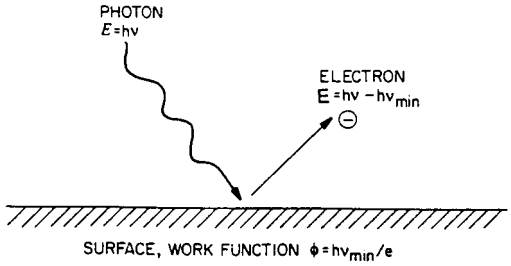

Figure 11.16 Emission of a photoelectron from a surface with work function ϕ (for Al, $\phi = 4.28$ eV)[31]

Each electron is capable of releasing many photons through bremsstrahlung radiation, some of these photons converge back to the center and impinge on the cathode as shown in figure 11.15 and the resulting photo-absorption releases electrons, further reducing the IEC device's efficiency.

The phenomenon responsible for electron emission is the photoelectric effect, illustrated in figure 11.16, in which electrons acquire enough energy from the photons associated with incident electromagnetic radiation to overcome the work function, ϕ, of the solid material. For this process to happen, the frequency of the incident radiation must be above the photoelectric threshold, υ_{min}, given by

$$\upsilon_{\min} = \frac{e\phi}{h} \quad \text{(Hz)} \qquad (11.14)$$

For most metals and insulators, $4eV<\phi<5eV$, thus requiring intense sources of ultraviolet radiation in order to observe the photoelectric effect. The energy of electrons emitted from a surface is given by Einstein's photoelectric equation,

$$\varepsilon = h(\upsilon - \upsilon_{\min}) \quad \text{(J)} \qquad (11.15)$$

Due to photoemission, several more electrons may be released from the cathode and, for constant power supply current, the ion current is further decreased causing the efficiency of the IEC device to decrease even more. This effect would be stronger when the chamber is made of stainless steel since heavy metals generate more bremsstrahlung than light metals such as aluminum.

For the bremsstrahlung x-rays the high-energy primary electrons (electrons emitted without being scattered after excitation) scatter in part before escape, producing large numbers of secondary electrons.[32]

X-rays penetrate matter and excite atoms far below the surface depending on the energy of the photon and hence the electrons could be generated inside the material. The mean free path of the kilovolt x rays in matter is several orders of magnitude greater than for the ejected photoelectrons as shown in figure 11.17.

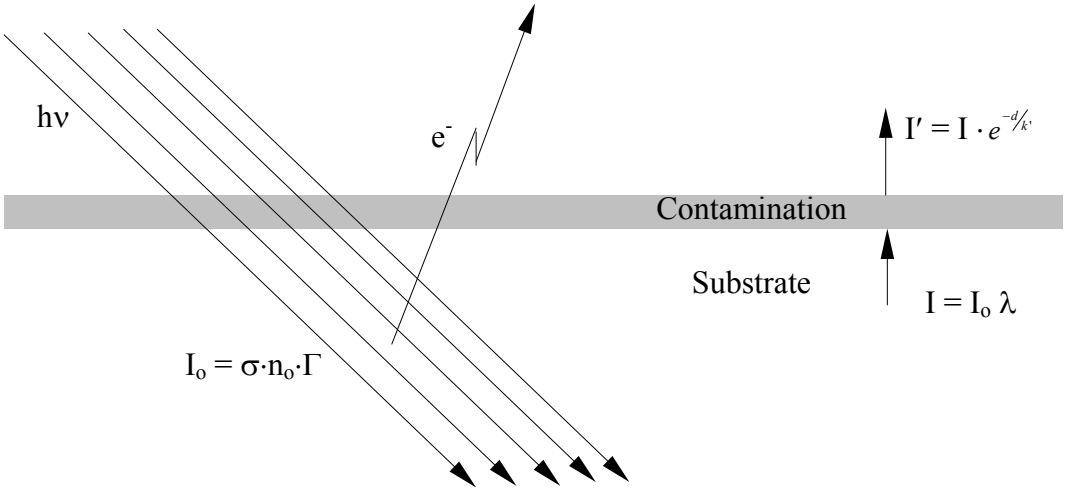

Figure 11.17 Schematic representation of electron emission from matter

The probability for photo-ejecting an electron from a given subshell per unit volume is given by:[33]

$$I_o = \sigma \cdot n_o \cdot \Gamma \qquad (11.16)$$

where σ is the photoelectron (photoionization) cross-section for a given subshell of a given element, figure 11.18 shows a sample of photoionization cross sections of Al and Fe in the energy range of 10 eV to 1 keV,[34,35,36,37,38] Γ is the x-ray flux and n_o is the concentration of the element in terms of atoms per unit volume.

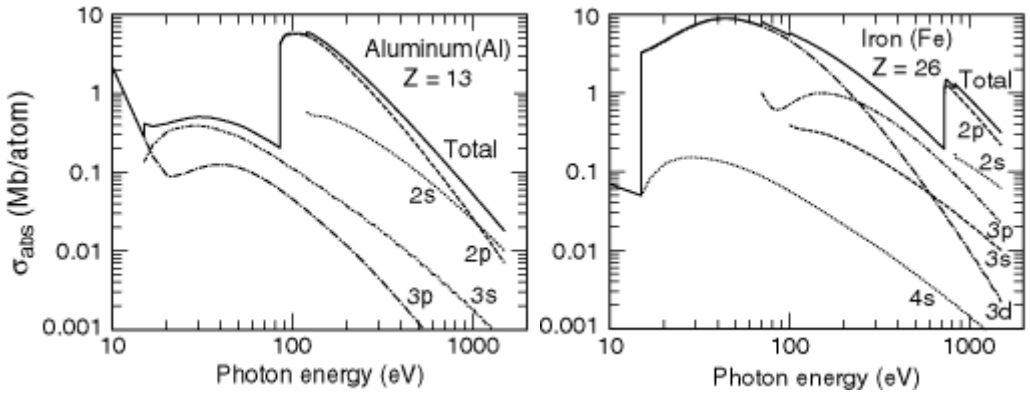

Figure 11.18 The atomic subshell photoionization cross-sections of Al and Fe for various energies[34,35,36,37,38]

Although electrons may be liberated everywhere inside the cathode grid material, it is required that the photoelectron emerges without any energy loss due to an inelastic collision. The intensity is thus equal to

$$dI = I_o e^{-x/\lambda} dx \tag{11.17}$$

where $1/\lambda$ is the reciprocal of the mean-free-path or the cross-section for inelastic scattering, x is the distance below the surface.

The total signal integrated from the surface to an infinite depth gives:

$$I = \int_0^\infty I_o \cdot e^{-x/\lambda} dx = I_o \cdot \lambda = \sigma \cdot n_o \cdot \Gamma \cdot \lambda \tag{11.18}$$

In the case of monoenergetic electrons, which occur whenever electrons are rapidly accelerated across a high potential difference (valid for electrons emitted near the cathode), the fraction of the energy in the electron beam that is converted into X rays (f_x) is given by

$$f_x = 1.0 \times 10^{-7} \cdot Z \cdot E \tag{11.19}$$

where E is the electron energy in keV and Z is the atomic number of the absorber.

Since the bremsstrahlung production increases with the atomic number of the absorber, the chamber wall of the IEC device should preferably be made of Al, or at least be coated with Al or other light materials such as graphite (contamination might be an issue with carbon).

It is suggested that bremsstrahlung radiation is easier to measure than calculate and if such data is available then one could calculate the flux of x-ray photons at the center of the chamber. Although the x-ray flux is usually measured outside the chamber, with necessary corrections for the attenuation in the chamber walls one could estimate the initial flux generated inside the chamber. Only a fraction of this radiation converges on the cathode grid (f_c). One could then estimate the photoemission electrons (I_p) from eqn.11.18 with necessary modifications (using a distribution for n_o (tabulated) & Γ (measured)).

The fraction of the bremsstrahlung radiation that converges on a solid spherical cathode as shown in figure 11.19 is given by:

$$f_c = 6.2/360 = 0.0172 \qquad (11.20)$$

Since the grid is 92% transparent the fraction of the radiation that reaches the cathode grid is given by:

$$f_c' = 0.08 \times 0.0172 = 1.376 \times 10^{-3} \qquad (11.21)$$

Though this is a small number, given that each electron impinging on the chamber wall produces many x-ray photons (eg., ~1000 photons per electron at 50 keV) and since there are many electrons (e.g., 20 mA of electron current for a 30 mA power supply current $= 1.25 \times 10^{17}$ electrons) hitting the chamber wall the number of x-ray photons reaching the cathode grid could become a significant number ($\sim 1.72 \times 10^{14}$). Furthermore, each of the x-ray photons could release multiple numbers of electrons depending on the energy of the photon, thus

further reducing the IEC device's efficiency. This phenomenon could be especially significant in devices that are pulsed to large currents.[39]

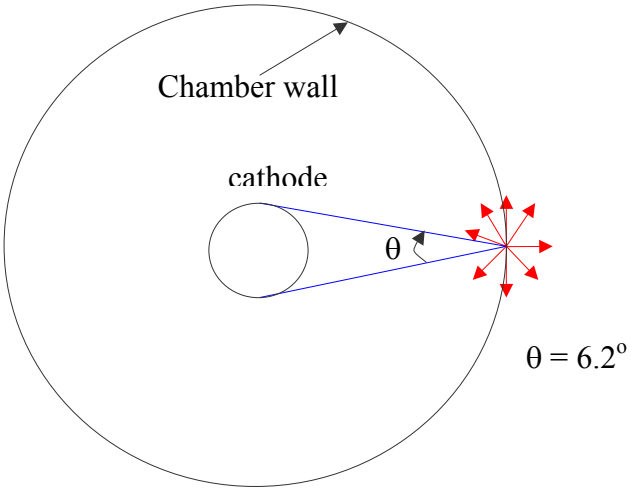

Figure 11.19 A non-relativistic electron hitting the chamber wall releases bremsstrahlung radiation isotropically. Only a small fraction of this radiation (f_c) that subtends a solid angle of 6.2^o converges on the cathode.

11.6 Field emission sources

With the application of an electric field, electrons can be released from a substrate. This effect is known as the Schottky effect.[40] It has been calculated to correspond to a reduction of the work function ϕ by the amount given by: [40,41]

$$\Delta\phi = -(eE)^{1/2} \qquad (11.22)$$

where E is the applied electric field in V/cm, and e is the electronic charge (1.6×10^{-19} C). This would also affect the thermionic emission current.

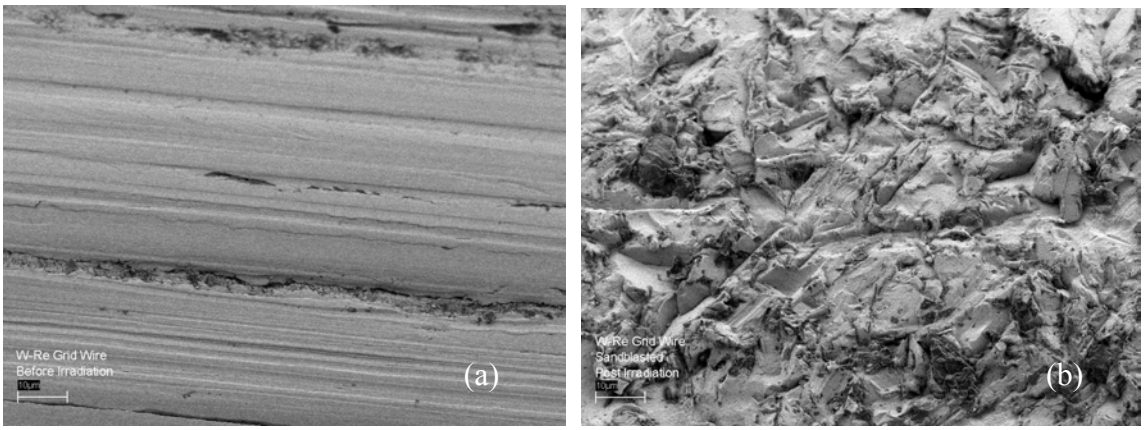

Figure 11.20 (a) W-25%Re grid wire before sandblasting (b) The same wire after sandblasting.

When the applied electric field is high enough (10^7 V/cm), spontaneous electron emission could occur. However, such fields could only prevail at sharp edges (see below) on the cathode grid (since the applied voltage itself does not exceed 200 kV max.). This effect was observed in the present device when the grid wire figure 11.20 (a) was sandblasted (to clean the surface, not recommended), which introduced sharp microstructures as shown in figure 11.20 (b). The grid could no longer be operated at voltages higher than 80 kV.

The electric field is a function of the radius of curvature (of sharp edges), and is given by:[42,43]

$$E = \frac{2V}{r \ln(R/r)} \qquad (11.23)$$

where V is the applied voltage, R is the distance from the tip to the anode and r is the radius of curvature of the tip.

Figure 11.21 shows a schematic energy level diagram for electrons in a metal or insulator, in which the band of electron energies is depressed by the work function ϕ below the reference potential. Imposition of a strong electric field results in a potential as a function of distance above the surface of the metal given by the line ACD.

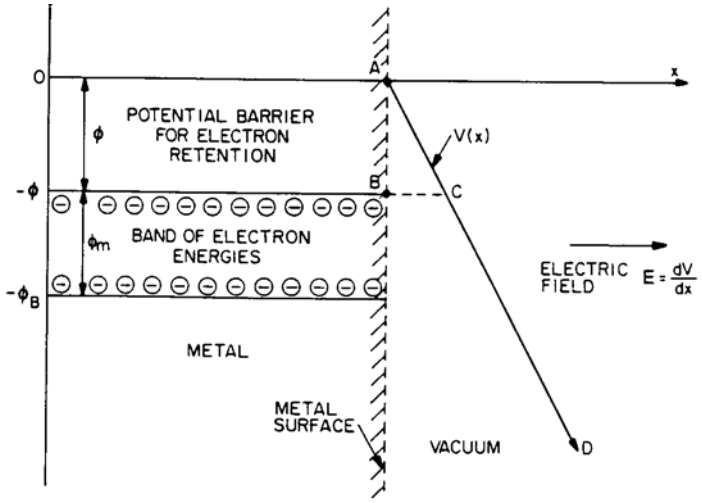

Figure 11.21 Potential-distance diagram at the surface of a metal, given by the hatched line, subject to a very strong electric field. The sloping line AD shows the potential as a function of distance above the surface. If the electric field is strong enough, and the distance CD small enough, electrons in the conduction band can tunnel through the potential barrier BAC and be pulled out of the solid material by the strong electric field.[42]

Beyond the point C, an electron outside the metal would have a potential lower than its value inside the metal; this provides a driving force for quantum mechanical tunneling of electrons from B to C, through the potential barrier immediately above the surface of the material. This process was studied by Fowler and Nordheim[44] and by Fowler,[45] who derived the field emission current density:

$$J_f = CE^2 \exp\left(\frac{-D}{E}\right) \quad (\text{A/m}^2) \qquad (11.24)$$

For ϕ in eV, the constant C is given by:

$$C = \frac{e^2 \phi_m^{1/2}}{2\pi h \phi_b \phi^{1/2}} = 6.16 \times 10^{-6} \times \frac{1}{\phi_b}\sqrt{\frac{\phi_m}{\phi}} \quad \text{A/V}^2 \qquad (11.25)$$

and the constant D by:

$$D = \frac{8\pi}{3h}(2me)^{1/2}\phi^{3/2} = 6.83\times10^9 \phi^{3/2} \quad \text{V/m} \qquad (11.26)$$

From figure 11.20

$$\phi_b = \phi + \phi_m \qquad (11.27)$$

where ϕ is the work function of the metal, and ϕ_m is the band potential.

An estimate of the band potential ϕ_m is given by:

$$\phi_m = \frac{h^2}{2me}\left(\frac{3N}{8\pi}\right)^{2/3} = 3.65\text{x}10^{-19}\ N^{2/3}\ \text{eV} \quad (11.28)$$

where N is the number density in electrons per cubic meter in the metal typically one electron per atom in electrical conductors.

This effect would show up when the grid is not manufactured carefully. Sharp points appear whenever two wires are spot-welded, since the electrode tends to melt (unevenly) the surfaces of contact (electrode-wire, wire-wire and wire-electrode contacts). Such sharp points and those of the wire used in grid construction should be grinded off and polished carefully. Once this is achieved, the field emission effect could be neglected altogether.

11.7 Conclusions

A single loop grid produces a (~line) cylindrical fusion source and higher proton rates are observed when this grid is oriented face on with the proton detector. Hence in a cylindrical IEC the fusion rate observed would be higher along the two faces of the cylinder. At higher input voltages the ions tend to continue recirculation causing a higher fusion rate along the line of sight of the detector in the face-on orientation (90^o) with the single loop grid. The single loop grid appears to produce a line (cylindrical) source rather than a volume or point source. Future research should be directed at selecting material with lower γ (Rhenium seems to be a better choice for this reason) and increasing the D^+ concentration in the chamber to reduce the secondary electron emission. The variation of γ with voltage has to be accounted for in the new

ion circulation current equation. The γ is also affected by the composition of the plasma (D^+:D^{2+}:D^{3+}) even in a chamber with few impurities. The contributions of the other electron emission processes in an IEC device were also investigated and incorporated in the ion current equation. A simple way to test the material properties suitable for building the cathode grid is to use single loop grids built of different materials.

Photoemission is caused by the bremsstrahlung radiation generated by the electrons hitting the chamber walls and is accounted for in the new ion current equation derived in this chapter. Photoemission could be reduced by using appropriate material for the chamber construction or by simply coating the chamber with low-Z material. Another way to accomplish this would be to modify the grid (introduce a hole) such that electrons are ejected in one direction and at the spot where the electrons strike the chamber we could use a low-z material. However, this would be useful for only those electrons leaving the core of the cathode, since all other electrons (secondary, thermionic etc.,) do not converge. Rounding off the sharp edges on the cathode grid could minimize field emission.

11.8 References

[1] T.A. Thorson, PhD thesis, University of Wisconsin, Madison (1996).

[2] E. J. Sternglass, Phys. Rev. **108**, 1 (1957).

[3] R. A. Baragiola, E. V. Alonso, and A. Oliva Florio, "Electron emission from clean metal surfaces induced by low-energy light ions," Phys. Rev. B **19**, 121–129 (1979).

[4] R. P.Ashley, G.L. Kulcinski, J. F. Santarius, S. Krupakar Murali, G. Piefer, B. B. Cipiti and R. Radel, "Recent progress in steady state fusion using D-^{3}He," Fusion Science and Technology, **44**, 559 (Sep. 2003).

[5] Y. Gu, J. B. Javedani and G. H. Miley, "A portable cylindrical electrostatic fusion device for neutronic tomography," Fusion Technol., **26**, 929-932 (1994).

[6] Oak Ridge National Laboratory, Atomic Data for Fusion, Vol.3. (Also available at http://www-cfadc.phy.ornl.gov/redbooks/three/c/3c13.html).

[7] D. Hasselkamp, K. G. Lang, A. Scharmann, and N. Stiller, "Ion induced electron emission from metal surfaces," Nucl Inst. Meth. **180** (1981) 349-356.

[8] Oak Ridge National Laboratory, Atomic Data for Fusion, Vol.3.

[9] U.A. Arifov and R. R. Rakhimov, Bull. Acad. Sci. U.S.S.R Phys. Ser. **24**, 266 (1960) [Mo, Ta, and W].

[10] G. D. Magnuson and C. E. Carlston, Phys. Rev. **129**, 2403 (1963) [Al, Ni, Cu, Zr, Mo, and Ti]

[11] L. N. Large and W. S. Whitlock Proc. Phys. Soc. (London) **79**, 148 (1962) [Ti, Ni, Cu, Zr, Mo, Ag, Au & Pt].

[12] Thorson, T. A., Durst, R. D., Fonck, R. J., and Wainwright, L.P., Phys. Plasmas **4** (1997) 4.

[13] Hirsch, R.L., Phys. Fluids **11**, 2486 (1968).

[14] E. S. Parillis, and L. M. Kishinevskii, Sov. Phys. Solid State 3 (1961) 885.

[15] J. Schou, Phys. Rev. B **22**, 2141 (1980).

[16] E. J. Sternglass, Phys. Rev. **108**, 1 (1957).

[17] G. F. Knoll, "Radiation Detection and Measurement," 3rd edition, John Wiley & Sons, Inc. pg.31, (2000)

[18] A. J. Dekker, "Energy and temperature dependence of the secondary emission of MgO," Phys. Rev. **94**, 5 (1954).

[19] L. H. Linford, Phys. Rev. **47**, 279 (1935).

[20] J. S. Allen, Phys. Rev. **55**, 336 (1939).

[21] Lakits G. and Winter H., "Electron emission from metal surfaces bombarded by slow neutral and ionized particles," Nucl. Inst. Meths. **B48** (1990) 597-603.

[22] J. Khachan and S. Collis, Phys. Plasmas, **8,** No. 4**,** (2001) 1299.

[23] U. A. Arifov, R. R. Rakhimov, and O. V. Khozinskii, Bull. Acad. Sci. USSR-Phys. Ser. **26**, 1422 (1962);

[24] J. Ferron, E. V. Alonso, R. A. Baragiola, and A. Oliva-Florio, J. Phys. D **14**, 1707 (1981);

[25] H. D. Hagstrum, Phys. Rev. **104**, 672 (1956).

[26] W. H. P. Losch, Phys. Stat. Sol. (A) **2**, 123 (1970).

[27] P. Mahadevan, G. D. Magnuson, J. K. Layton, and C. E. Carlston, Phys. Rev. **140**, A1407 (1965);

[28] M. Perdix, S. Paletto, R. Goutte, and C. Guilland, Brit. J. Appl. Phys. **2**, 441 (1969).

[29] D. W. Vance, Phys. Rev. **169**, 252 (1968).

[30] J. D. Jackson, "Classical electrodynamics," 3rd edition, John Wiley & Sons, Inc., New York, London (2002).

[31] H. B. Michaelson, "The work function of the elements and its periodicity," J. Appl. Phys., **48**, 11, 4729 (1977).

[32] M. Cardona and L. Ley, Eds. "Photoemission in Solids I," Springer-Verlag Berlin Heidelberg, New York (1978) Pg. 28.

[33] W. J. Carter and G. K. Schweitzer, "Experimental evaluation of a simple model for quantitative analysis in X-ray photoelectron spectroscopy," J. Electron Spectroscopy **5** (1974) 827-835.

[34] J.-J. Yeh and I. Lindau, "Atomic Subshell Photoionization Cross Sections and Asymmetry Parameters: $1 < Z < 103$," *At. Data Nucl. Data Tables* **32**, 1 (1985).

[35] J.-J. Yeh, *Atomic Calculations of Photoionization Cross Sections and Asymmetry Parameters* (Gordon and Breach, Langhorne, PA, 1993).

[36] J. W. Cooper, *Phys. Rev.* **128**, 681 (1962).

[37] S. T. Manson and J. W. Cooper, *Phys. Rev.* **165**, 126 (1968).

[38] S. T. Manson, *Adv. Electron. Electron Phys.* **41**, 73 (1976).

[39] J.H. Nadler, G. H. Miley, H. Momota, Y. Shaban, Y. Nam and M. Coventry, "Neutron production and ionization efficiency in a gridded IEC device at high currents," Fusion Tech. Vol. **39**, Mar. 2001.

[40] W. Schottky: Ann. Physik **44**, 1011 (1914).

[41] C. Herring, M. H. Nichols: Rev. Mod. Phys. **21**, 185 (1949).

[42] M. Cardona and L.Ley editors, "Photoemission in solids I – General principles," Springer-Verlag, Berlin Heidelberg, New York, pg. 21, (1978).

[43] J. Reece Roth, "Industrial Plasma Physics," Vol. 1, Principles, Institute of Physics Publishing, Bristol and Philadelphia, pg.165, (1995).

[44] R. H. Fowler, L. W. Nordheim: Proc. Roy. Soc. (London) A **119**, 173 (1928).

[45] R. H. Fowler, Phys. Rev. **38**, 45 (1931).

Chapter 12.0: Study of Ion flow dynamics through sequential grid construction

To study the effects of grid symmetry, experiments were performed initially using a single loop grid. More loops were added to it sequentially till a spherical grid with 12 longitudes and 5 latitudes was constructed as shown in figure 12.1. This experiment allows one to monitor the effects of the ion flux into the central grid as the symmetry of the grid is varied.

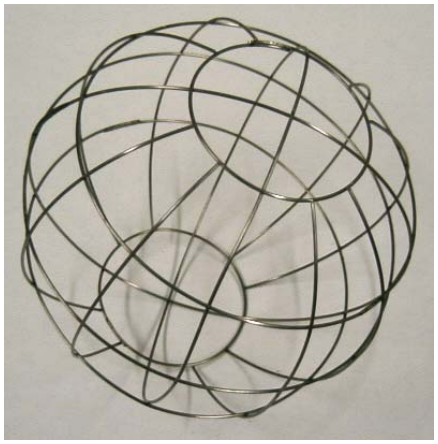

Figure 12.1 Cathode grid with 12 longitudes and 5 latitudes.

Building on the earlier idea of the chordwires diagnostic (see chapter 4.0) for the ion flux determination, several wires were introduced into the single loop in mutually perpendicular directions as shown in figure 12.2. This chordwire configuration was kept constant throughout the experiments as the whole grid was eventually built.

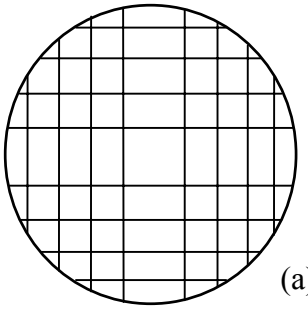

(a)

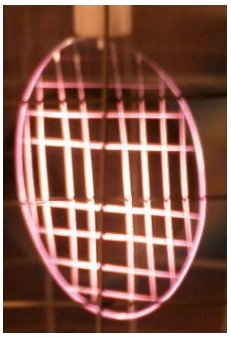

(b)

Figure 12.2 (a) Schematic of the chordwire arrangement across a single loop. (b) Picture of the single loop in operation (20 kV 15 mA, 2 mtorr) with 16 chordwires.

With the introduction of the chordwires the operation of the single loop grid (XWLoopRe-1) was stabilized (less arcing and associated shutdown problems). A picture of the single loop XWLoopRe-1 grid taken at high pressure (in 7 mtorr D_2) is shown in figure 12.3. The additional electrons emitted by the chordwires in the direction perpendicular to the face of the single loop grid seems to help sustain/stabilize the plasma.

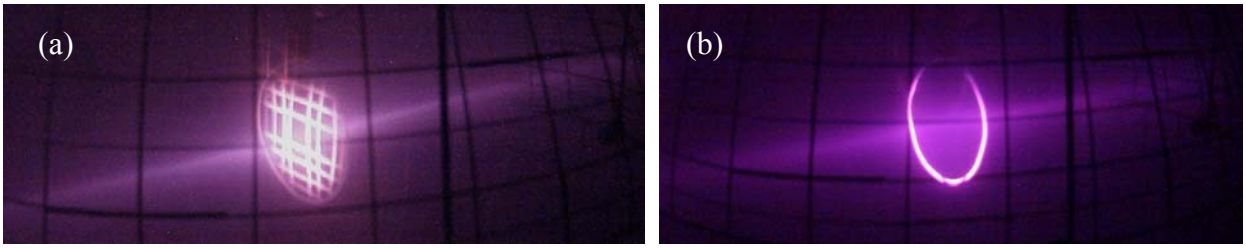

Figure 12.3 (a) Picture of the single loop grid with cross-wires (XWLoopRe-1) during the high-pressure operation (150 kV, 10 mA, 7 mtorr, D_2). The ions seem to recirculate along the straight line perpendicular to the face of the XWLoopRe-1. (b) Picture of the single loop grid without cross-wires at (15 kV, 10 mA, 7.6 mtorr).

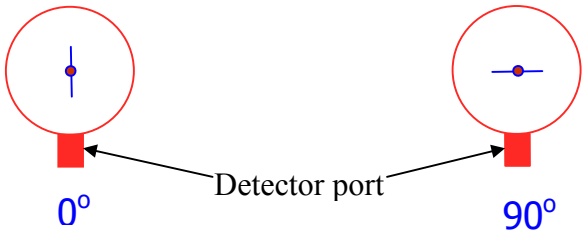

Figure 12.4 Two orientations of the grid face-off (edge-on), 0^o and face-On, 90^o with respect to the detector.

The fusion rate was measured with these grids in two orientations: face-on 90^{o} and face-off (edge-on) 0^{o}, with the detector as shown in figure 12.4. The variation of the neutron rate measured with changes in grid configuration, i.e., addition of more loops as shown in figure 12.5, provides an understanding of the effects of improved grid symmetry on the convergence and hence the overall fusion rate.

Eclipse scans were performed for each of the configurations in the two above-mentioned orientations (0^{o} & 90^{o}). Such scans give an understanding of the effects of ion flow convergence on the fusion rate and give some idea about the dimensions of the core volume and the number of reactions emanating from it.

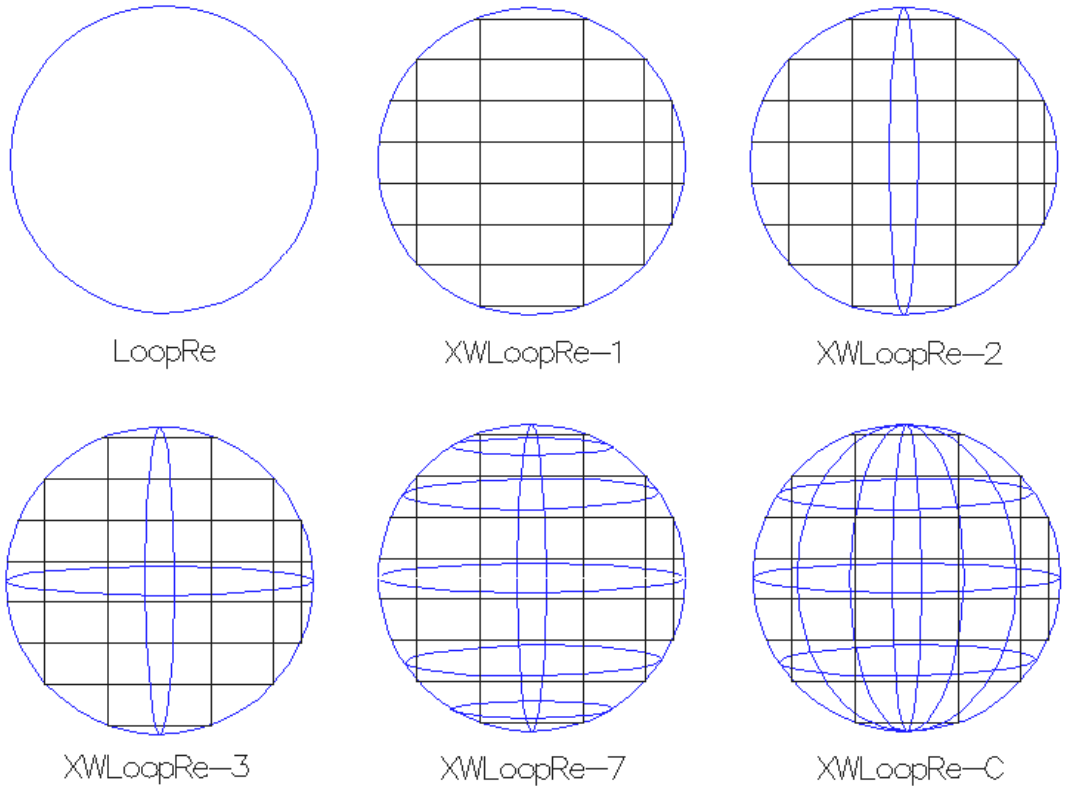

Figure 12.5 Sequential grid construction was performed, along with simultaneous characterization of each of the configurations. Loops are in blue (circle and ellipses) and the chordwires are in black (straight lines).

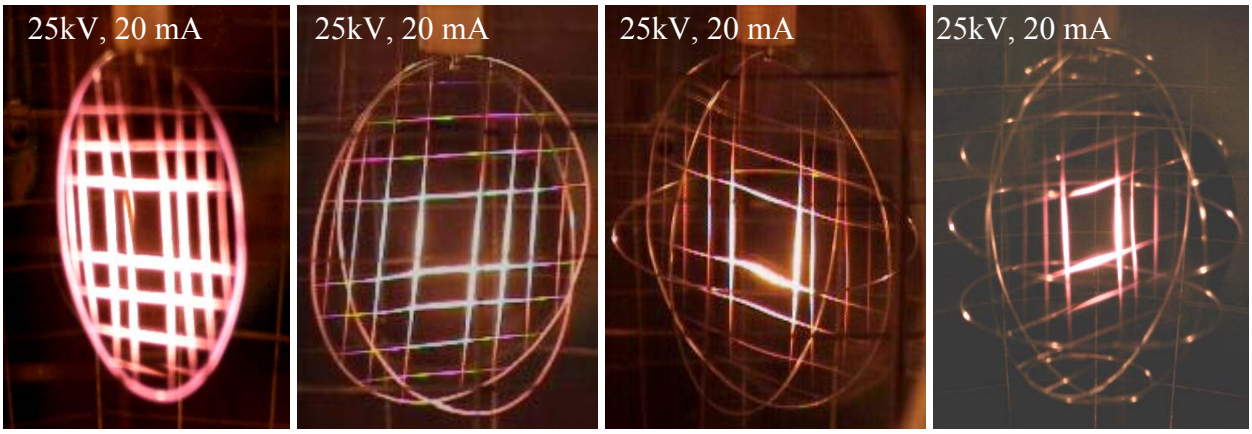

Figure 12.6 The temperature of fewer chordwires is high as the number of loops used in the construction of the grid is increased. Improvement in convergence with increased symmetry is observed.

Several cross wires were introduced into the LoopRe configuration (now called XWLoopRe-1). Pictures taken at 25 kV, 20 mA for various configurations are shown in figure 12.6, the corresponding temperature measurements are shown in figure 12.7. Interestingly, with improved symmetry, only the wires close to the core get hotter. This is expected because the ion flow converges better with improving symmetry. The effects of such improvements in symmetry on the overall fusion rate are explained later in the present chapter.

The temperature of the chordwires is high everywhere for XWLoopRe-1, see figure 12.7. This is because the ion recirculation is not focused. Furthermore, the chordwires close to the high voltage stalk towards the top remained relatively cold. It appears that the stalk perturbation of the electric fields is causing the ions to recirculate preferably along the lower three quarters of the single loop grid.

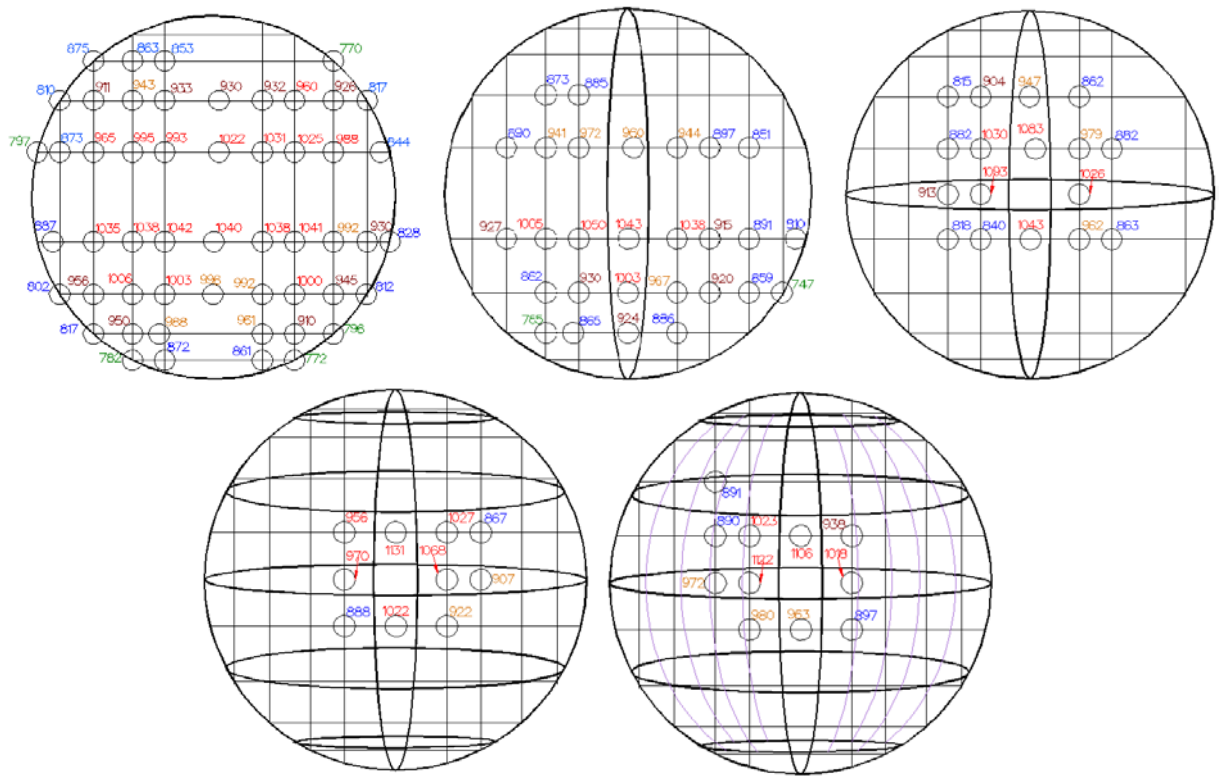

Figure 12.7 Temperature distribution of the chordwires as more loops are being added sequentially. Each of these temperature measurements was taken at 25 kV, 10 mA and 2 mtorr chamber pressure. The pictures taken during the temperature measurements are shown in figure 12.6. Where temperature measurements are not shown, the temperature was below 700°C, the lower limit of the pyrometer.

Eclipse scans were performed with each of the configurations (as shown in figure 12.8 for XWLoopRe-1). Each of these scans were performed from position 0 to 5 only (to save time) see figure 12.8, as it is assumed here that the readings would be more or less similar about the center. Besides, the behavior in one half of the scan (position 1 through 6) would be a good indicator of the convergence effects.

Figure 12.9 shows the eclipse scan (positions 0 to 5) performed with the single loop grid (XWLoopRe-1), there is a drastic difference between the P/N ratios for the two orientations. The calibration factors used are the same as those derived for the complete grid, taking into account

the volume source, converged core and beam target reactions. Although, a converged core does not occur in a single loop grid, the same calibration factors are used for consistency. The P/N ratio is computed by assuming a constant calibration factor ratio of 438,355/22,615 ≈ 19.4. The relative magnitude would be the same even if raw counts were used.

12.1 Eclipse scan in two orientations

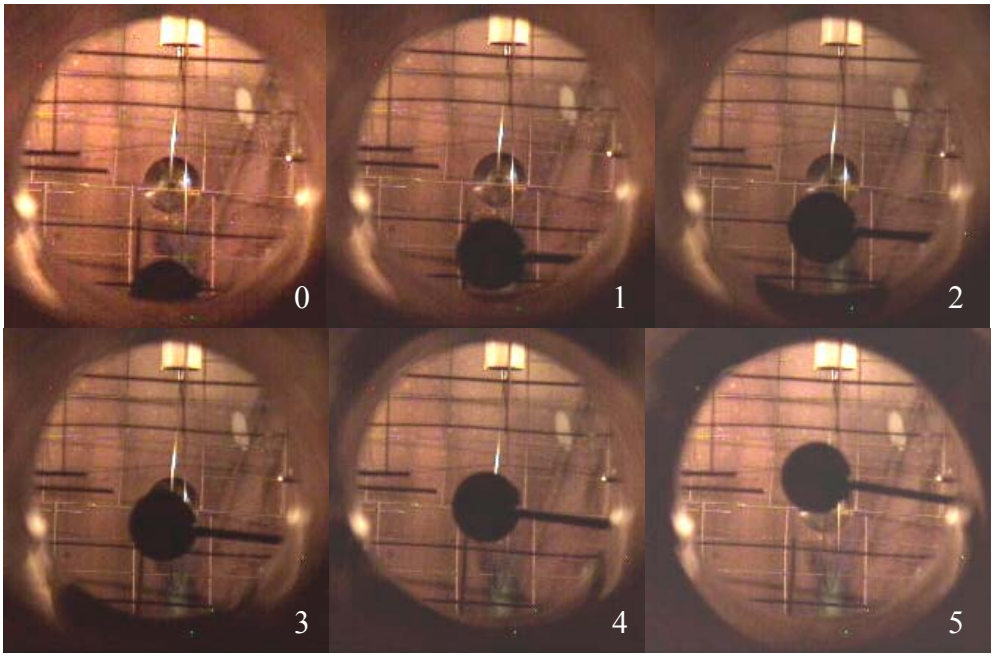

Figure 12.8 Pictures taken with the eclipse in various positions with 0^{o} orientation of the single loop grid.

An interesting feature in this set of measurements, as shown in figure 12.9 (b), is the dip in the P/N ratio at the position-4 where the disc eclipses the center of the grid, see figure 12.8. Hence, there is a positive fusion rate gradient as we move radially towards the center of the single loop grid, confirming that there is some converged core contribution to the overall fusion rate even with a single loop grid, such a converged core is caused by the high energy ions recirculating close to the center of the cathode. This is also evident from figure 12.9 (a), which

further confirms the earlier statement. Error bars are generated only for figure 12.9 (b), since the error bars for all the other data points (for other configurations) are on the same order.

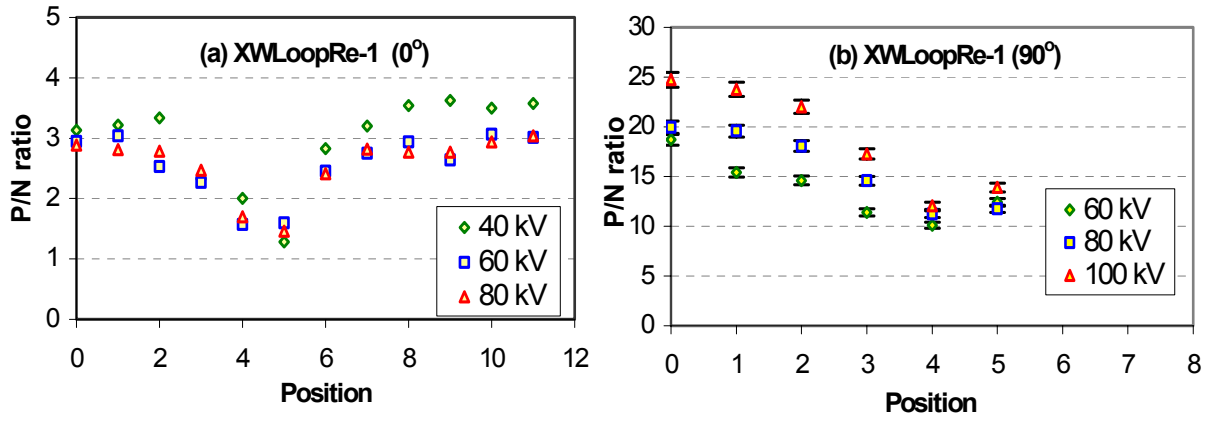

Figure 12.9 Small Eclipse disc scans of the single loop grid made of pure rhenium (XWLoopRe-1) with chordwires, in two orientations [(a) 0° & (b) 90°], shows a higher number of protons from the center of the grid, also see figure 12.8 and figure 7.1.

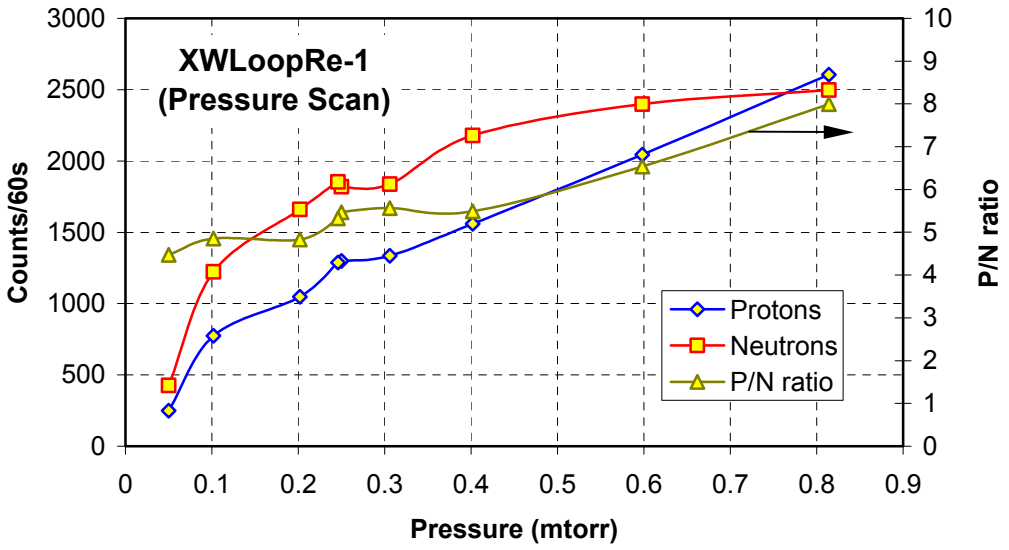

Figure 12.10 Pressure scan performed at 60 kV, 10 mA shows a decrease in reactivity as the chamber pressure decreases. Pressure readings were calibrated for N_2 gas and hence were corrected for the fuel gas D_2 according to figure 12.11.

The pressure readings are from a baratron gauge that is calibrated by the manufacturer for the N_2 gas and is hence corrected for the D_2 gas sensitivity as shown in figure 12.11. The pressure in the chamber was gradually decreased while maintaining the voltage and current constant. The simultaneous measurements of the proton and neutron rate are plotted together with the P/N ratio in figure 12.10. Although, it is possible to sustain the device at low pressures ~0.05 mtorr, the overall fusion rate is lower. This is because, the electrons released from the secondary emission were ionizing neutral gas in the vicinity of the cathode grid, helping sustain the plasma, but the ion current itself is reduced.

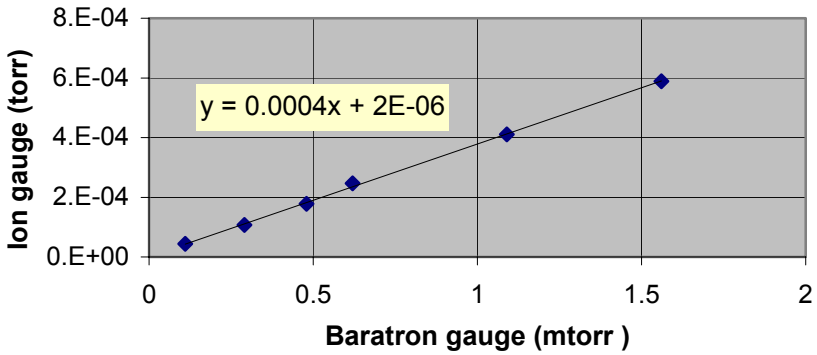

Figure 12.11 The readings of the baratron gauge are corrected for sensitivity, since the manufacture had calibrated it for N_2 gas. Direct ion gauge measurements were not feasible at the time of the experiments.

Furthermore, there is a downside to this kind of ionization, in that these ions are born close to the cathode and fall through a smaller potential gradient and therefore gain relatively lower energy where the fusion cross sections are low as well. This means that the ionization source should be placed away from the cathode. The electron emission from the cathode does ionize some neutral gas, but such ionization is not preferable. Such behavior (operation at lower pressure) is not observed in the absence of the chordwires, for instance, with the whole cathode grid (without chordwires).

The ions recirculating along the microchannels in the spherical grid continue to do so even more at lower pressures and are eventually lost through charge exchange. Very few of these ions bombard the grid and hence fewer secondary electrons are emitted. However, when chordwires are placed inside the grid (so as to intercept the energetic recirculating ions), they release a greater number of secondary electrons that help sustain the plasma even at lower pressures.

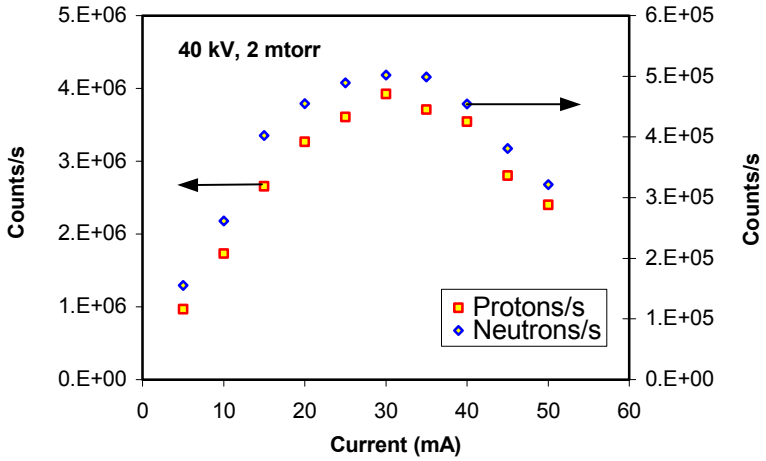

Figure 12.12 Proton and neutron rates tend to rollover at higher currents due to the presence of resistors in the high voltage circuit (~200 kΩ) that drops significant voltages at higher currents causing the overall fusion rate to decrease.

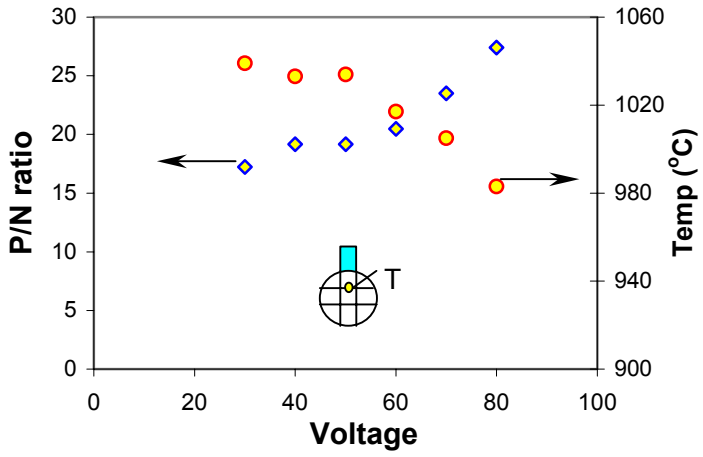

Figure 12.13 P/N ratio and temperature variation with voltage at constant input power (400W) and 2 mtorr.

A current scan was performed at 40 kV, 2 mtorr as shown in figure 12.12. Interestingly, a rollover is observed at higher currents, which is due to the presence of a ~200 kΩ resistor in the high voltage circuit. This resistor was introduced to suppress the transient high voltage arcing.[1] When the presence of the resistor is compensated for, by running the device at predetermined compensating (for the resistor) voltages (solution of $400 + I^2R - V \cdot I = 0$), the rollover was no longer observed during the current scan.

The temperature of one of the chordwires was measured, as shown in figure 12.13. As observed earlier with single-loop grids (without chordwires) in chapter 10, the temperature of the chordwire decreases with voltage due to increased secondary electron emission at higher voltage. Towards the end of the current scan experiment it was observed that the plasma was sustained at 90 kV 35 mA, and 2 mtorr without any filament ionization source. The grid heating that had already occurred during the earlier current scan emitted electrons that were sufficient to sustain the plasma at this voltage. However, the fusion rate was low and hence this mode of operation at low pressures is not very attractive.

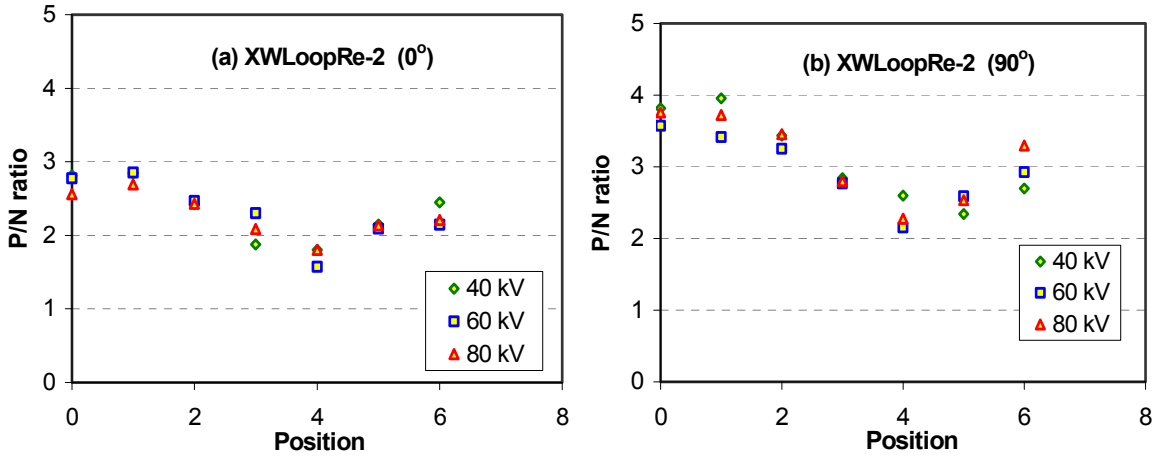

Figure 12.14 Small eclipse scans of the two orientations of double loop configuration shows a similar behavior. The small difference in the P/N ratio is because of the chordwires that cause preferential ionization in the region perpendicular to the face of the loop carrying the chordwires.

With XWLoopRe-2, as shown in figure 12.14, a similar behavior (with the eclipse scan) in both the orientations is observed, however a small difference in the P/N ratio occurs due to the presence of the chordwires (exact details of this behavior are not well understood). These chordwires seem to preferentially ionize the neutrals in the direction normal to their orientation since the electrons are released preferentially in that direction, be it the secondary emission or the thermionic emission electrons.

The dip in the P/N ratio at the center of the grid is not as prominent as in the case of the XWLoopRe-1 grid. This is because now there are four microchannel formations instead of two as in the earlier case with XWLoopRe-1. Figure 12.15 shows the picture of a two-loop grid at high pressure that shows the formation of four microchannels. The P/N ratio is lower with XWLoopRe-2 in the 90^{o} orientation than with XWLoopRe-1 because the fusion reactions are now distributed in four channels.

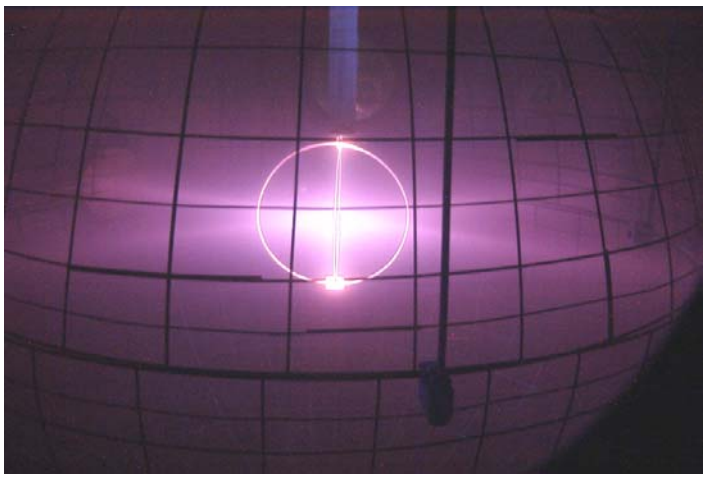

Figure 12.15 High pressure run with the two loop grid (without chordwires) shows the formation of four microchannels, hence the proton (fusion) rate along any single microchannel is decreased for a constant cathode current.

A third loop was added in the equatorial plane (see figure 12.4) to the earlier grid and is now called XWLoopRe-3. The results of the eclipse scan are plotted in figure 12.17. Strangely,

the P/N ratio goes to a very low value (~ 0) with the 90^{o} orientation. This is unexpected, it seems that the grid wires are affecting the fusion reactions occurring in the line of sight of the proton detector.

One possibility is that the microchannels formed in the grid do not fall in the line of sight of the detector causing the overall fusion rate detected by the proton detector to decrease. Also, the grid is offset at the point of suspension (see figure 12.15, where it is connected to the stalk) and a rotation of the grid causes results in uneven orientation and hence the difference in the P/N ratio for two orientations. This result prompted an important set of new experiments to analyze the effects of the cathode grid wire on the fusion rate through grid rotation and is explained in the chapter 13.

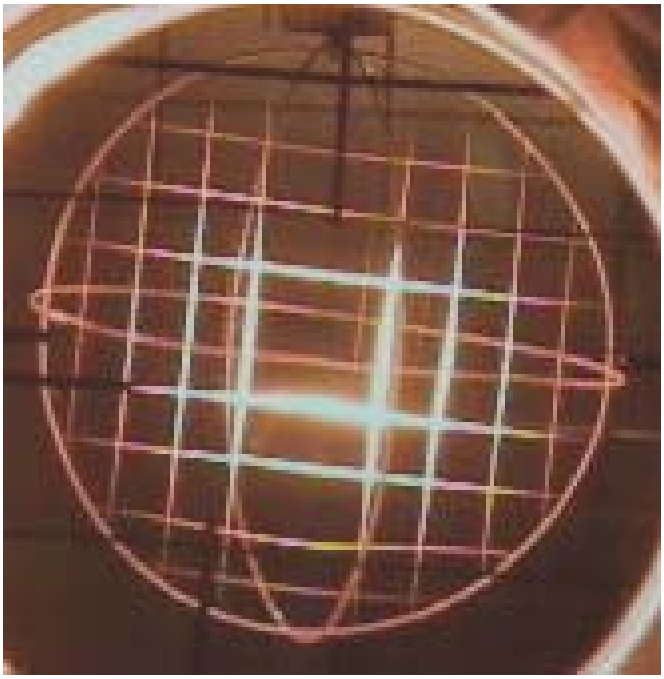

Figure 12.16 Picture of XWLoopRe-3 taken from the proton detector port. The grid appears to be tilted due to the offset at the suspension point of the grid.

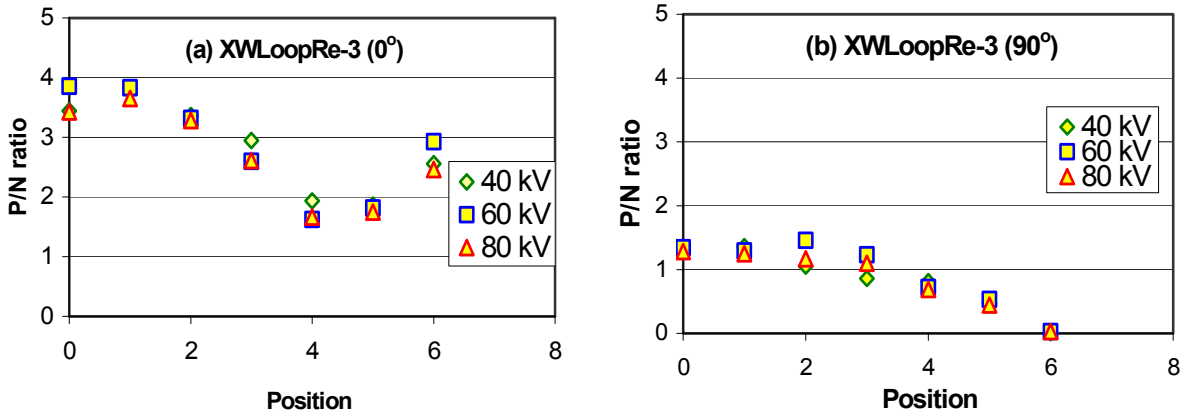

Figure 12.17 Plot of the eclipse scan of the P/N ratios for two orientations of XWLoopRe-3 grid. While the P/N ratio in the 0^o orientation is not much different from figure 12.13, the P/N ratio in the 90^o orientation is much lower and could be due to the fact that the microchannel is not oriented along the line of sight of the proton detector.

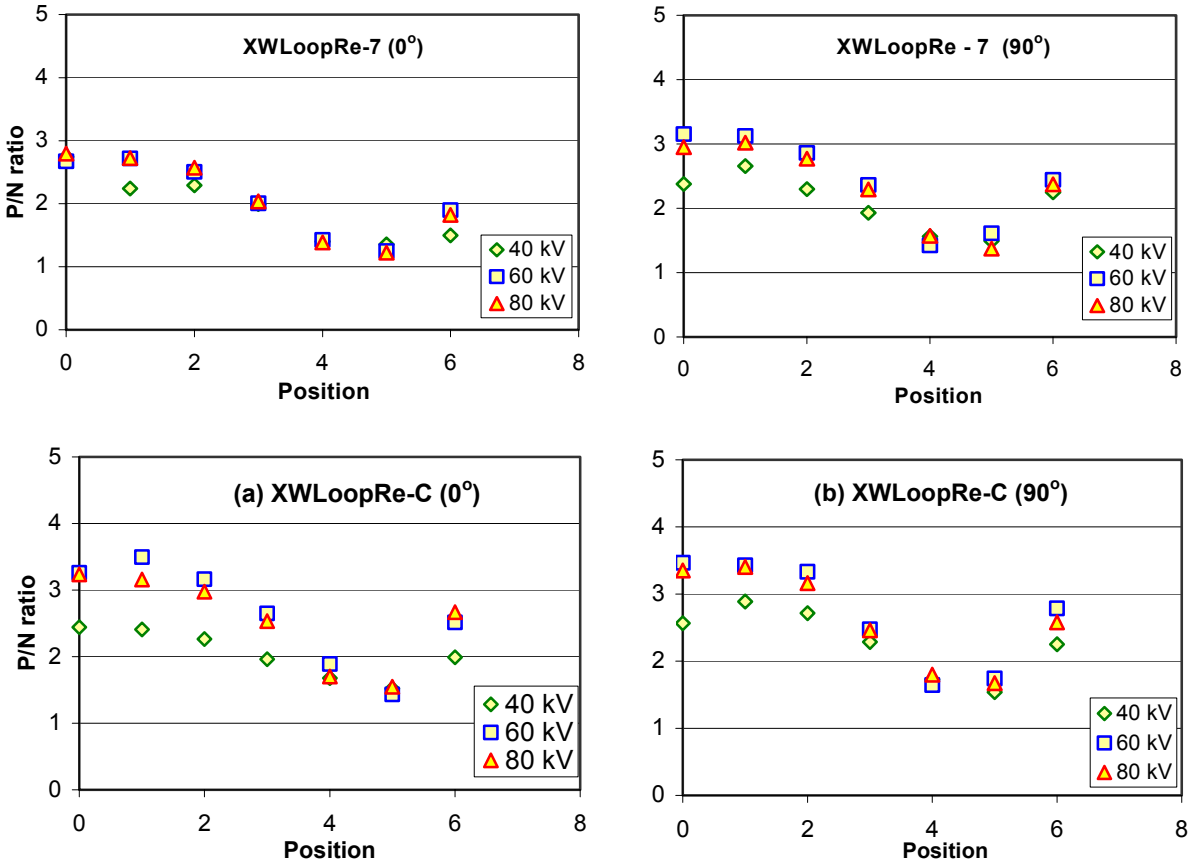

Figure 12.18 Plot of the eclipse scan of the P/N ratios for two orientations of XWLoopRe-7 grid. The P/N ratio scans in both the orientations are almost the same.

As the symmetry of the cathode gets better with the addition of more loops (7 loops and the complete grid with ~12 loops) the P/N ratio looks same as the XWLoop-7 grid. There is little change in the P/N ratio with orientation or with increased symmetry as shown in figure 12.18.

In the following section the effect of increasing symmetry on the total fusion rate is analyzed. Possible reasons for the observed behavior are ventured and a way to calculate the fusion rate of the single loop is proposed.

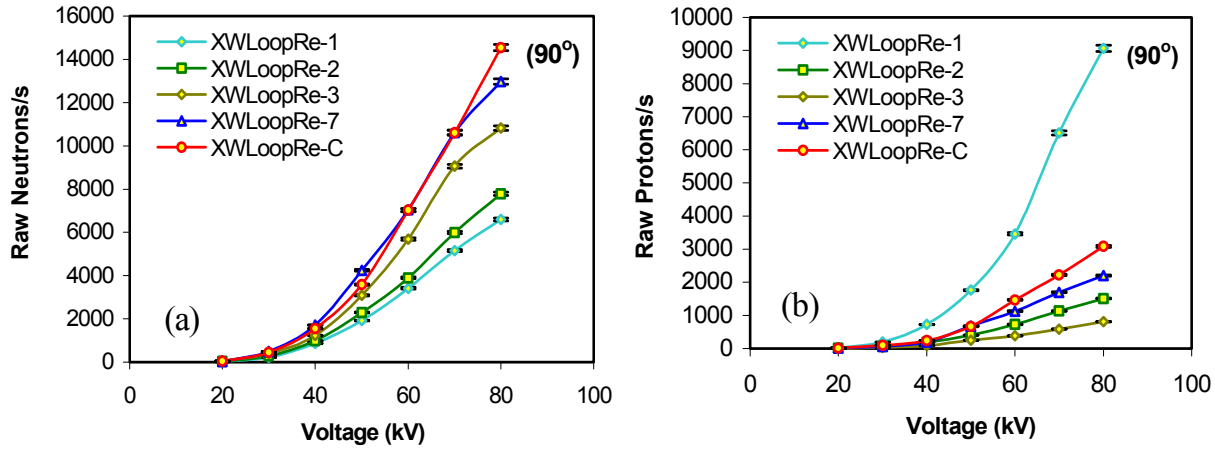

Figure 12.19 Plot of Voltage scans of (a) the neutrons/s and (b) the protons/s at 10 mA, 2 mtorr for various grid configurations in the 90° orientation. While neutrons show an expected trend with increasing symmetry, the protons for XWLoopRe-1 by far produces largest number of protons, contrary to one's expectations.

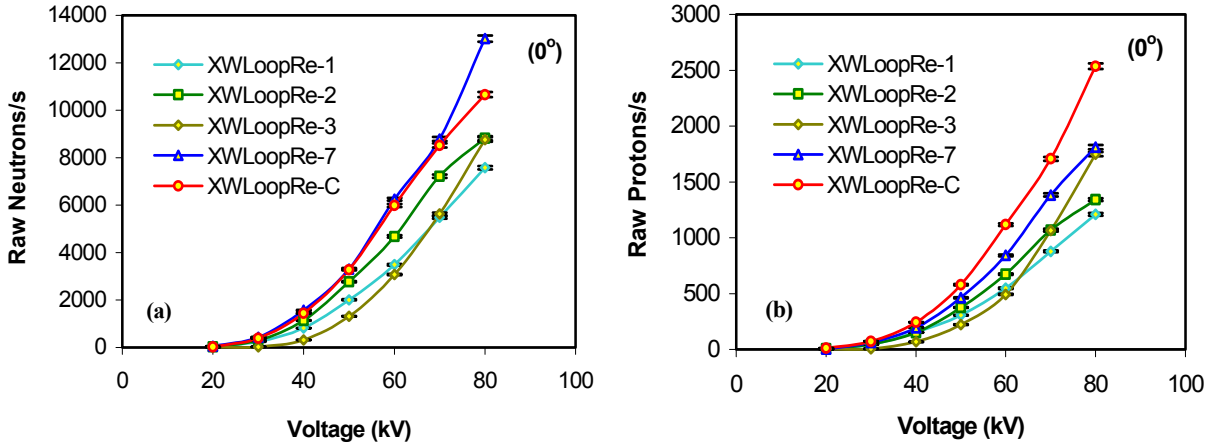

Figure 12.20 Plot of Voltage scans of (a) the neutrons/s and (b) the protons/s at 10 mA, 2 mtorr for various grid configurations in the 0° orientation.

The general trend of neutrons production rates in figure 12.20 (a) is consistent (increases) with increasing symmetry. However, with the protons, XWLoopRe-1 produces maximum number of protons, higher than any other configuration. One reason could be that the only microchannel associated with the XWLoopRe-1 is aligned with the detector and hence the line of sight of the Si detector passes through maximum volume source (for the 90^o orientation) that also has a $1/r^2$ falloff. The earlier explanation is further supported in figure 12.20 (b), where the XWLoopRe-1 has the minimum proton rate (~9 times smaller than the 90^o orientation, figure 12.20 (b)). The neutron rate of XWLoopRe-3 in figure 12.20 (a) is not consistent with the corresponding proton rate and the increasing symmetry in the figure 12.20 (b). It is not known at this time why this behavior persists.

Another set of experiments (current scan) with the changing grid configurations is illustrated in figure 12.21. The fusion rate rolls over with increasing current due to the presence of the 200 kΩ resistor as explained earlier in this chapter. An interesting observation is that the neutron rate in figure 12.21 (a) & (c) increases gradually with symmetry, but it saturates beyond XWLoopRe-7. Hence, the addition of more wires to improve the symmetry does not increase the fusion rate significantly.

The proton rate with XWLoopRe-1 configuration in figure 12.21 (d) is the highest and it reaches a maximum at 30 mA for which the proton rate of the single loop is ~4.6 times higher than the spherical grid with all the wires for maximum symmetry. This suggests that using a single loop grid (rather than a isotropic spherical grid) source would be a better choice for applications where higher neutron/proton rates are desired in small regions of interest.

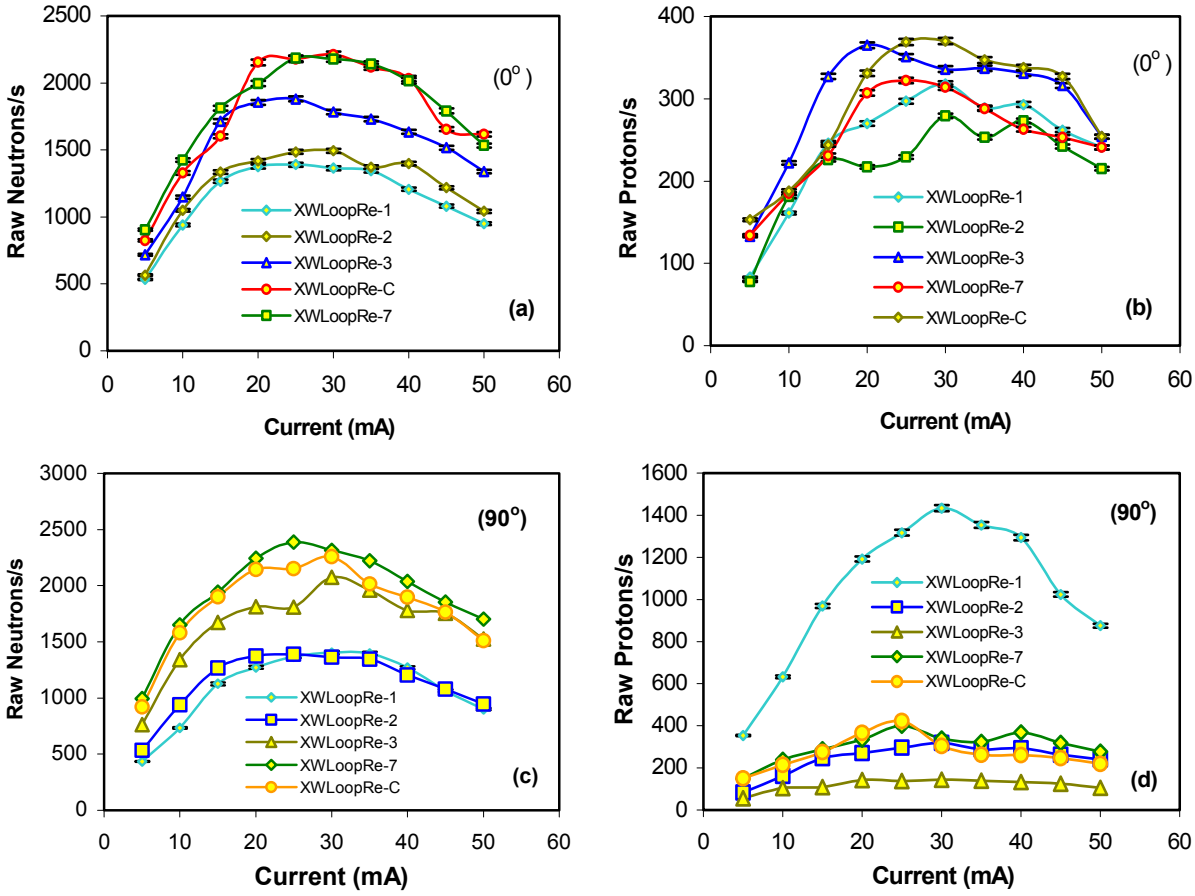

Figure 12.21 Plot of Current scans of (a) & (c) the neutrons/s and (b) & (d) the protons/s at 10 mA, 2 mtorr for various grid configurations in both the 90° and the 0° orientation.

It is important to note that the neutron rates shown in figure 12.21 denote the overall neutron production rate which is lower than those from a spherical grid configuration, but since a higher proton rate is detected (due to $1/r^2$ falloff) using the single loop (90° orientation) using a Si detector, the neutron rate would also be higher in that direction due to the 50% branching ratio of the D-D reactions (see figure 2.1). One such configuration is the C-device[2] used by the University of Illinois IEC group for a line source; a higher fusion rate is possible along the axial direction than in the radial direction and new applications could be developed based on this discovery.

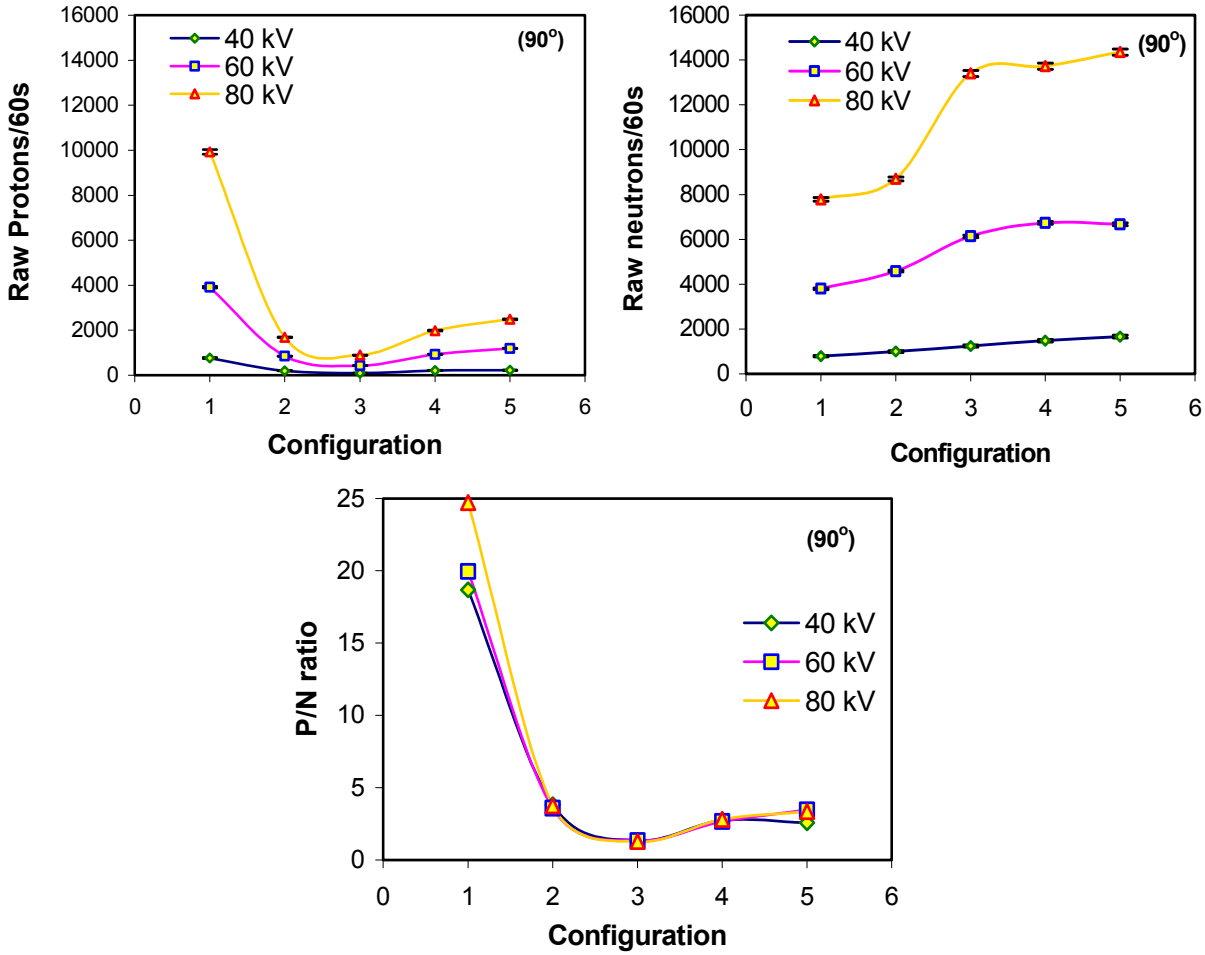

Figure 12.22 Comparison of the proton and neutron counts with various grid configurations (1→XWLoopRe-1, 2→XWLoopRe-2, 3→XWLoopRe-3, 4→XWLoopRe-7, 5→XWLoopRe-C) without the eclipse disc blocking the proton detector's view of the cathode. The chordwires are oriented face-on (90°) with respect to the detector. The P/N ratio follows the proton count and this ratio is higher for higher voltage only for the XWLoopRe-1 configuration.

12.2 Transformation of line source into a volume source

The protons and neutrons for various configurations are plotted for three voltages (40, 60 and 80 kV) in figure 12.22. The transformation of the single loop grid that is a line (cylindrical) source to a spherical grid (a volume source) is evident from figure 12.22 (a), where the proton rate is the highest when the line source is facing the detector. This proton rate decreases and then eventually increases once again. The neutron rate in figure 12.22 (b) further supports this

argument because the neutron rate increases with symmetry irrespective of the orientation of the grid.

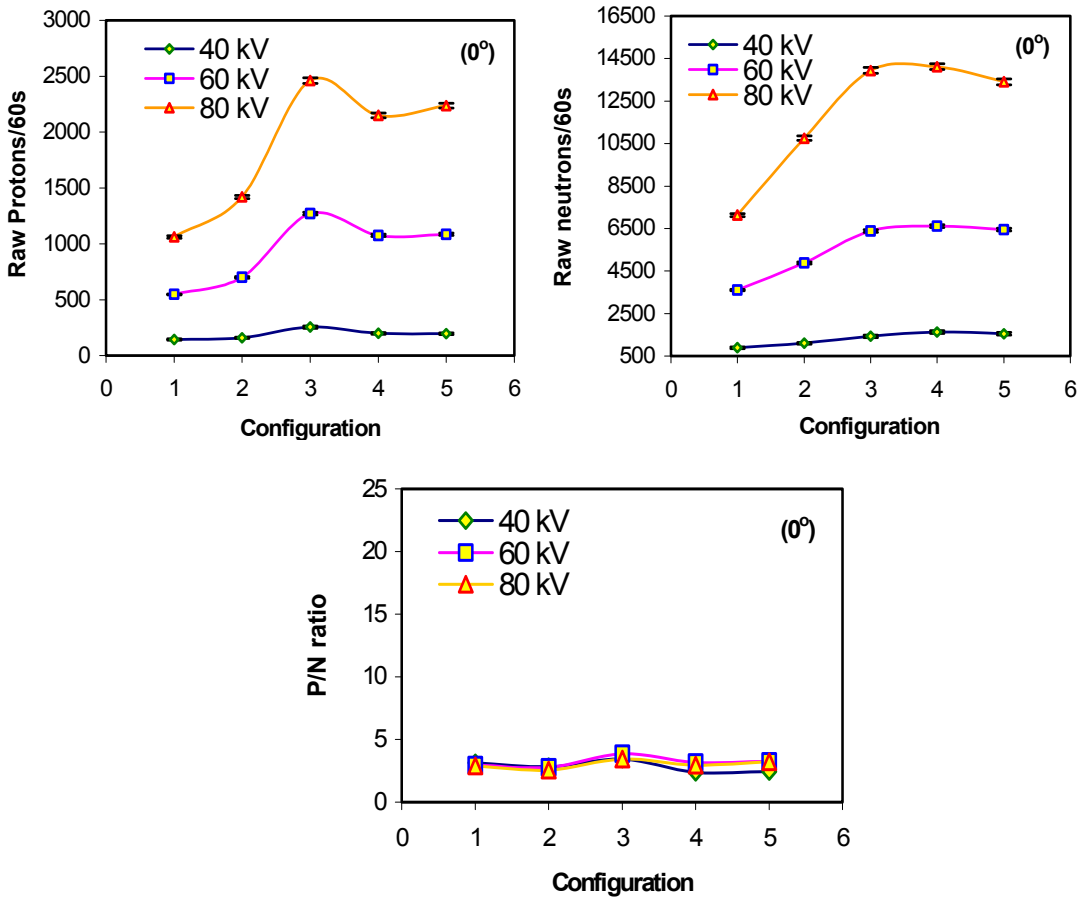

Figure 12.23 Comparison of the proton and neutron counts with various grid configurations without the eclipse disc blocking the proton detectors view of the cathode. The chordwires are oriented face-off (0^o) with respect to the detector. The P/N ratios follow the proton counts and are much smaller than the corresponding values in figure 12.21.

The neutron rate saturation is more prominent at higher voltages and there is no significant increase in the neutron rate beyond the XWLoopRe-7 configuration (4). Hence we may conclude that beyond a certain point the symmetry of the grid is not an issue (for spherical geometries) and huge gains in the fusion rate may not be expected with improved symmetry for high-pressure operation, where volume-source reactions dominate. However, if too many wires

were added, the fusion rate would go down because of the decrease in transparency and the resulting decreased ion recirculation.

With the chordwires oriented at 0^o with respect to the proton detector, the behavior of the neutron counts with voltage is in accordance with one's expectation. However, with the proton detector the values increase with the XWLoopRe-3 configuration, such behavior could be caused by the uneven tilt of the grid about the point of suspension as stated earlier in this chapter, that could cause one of the microchannels to align at least partially with the detector causing the proton rate to increase.

The calculation of the fusion rate detected by a proton detector with a single loop configuration is reported in the next section. The assumption of the line source holds for these calculations.

12.3 Calculation of fusion regimes in a single loop grid

The fusion rate is almost constant beyond the converged core since these reactions are mostly charge exchanged neutral reactions and hence the fusion rate remains constant in this region.

Assuming that all reactions occur along the path that the ions recirculate, the total fusion rate (F_t) detected by the Si detector for the 0^o orientation can be easily derived and is given by:

$$F_t = \frac{A\eta}{4\pi}\left(\int_{-\delta}^{\delta} \frac{\pi \cdot r_{cy}^{\ 2} \cdot f_v}{r_i^{\ 2}} dl + \frac{f_c - f_v}{r^2} \cdot V_c \right) \qquad (12.1)$$

where f_c is the fusion rate (protons·s^{-1}·cm^{-3}) in the core of the chamber (close to the center of the XWLoopRe-1), assuming homogeneity, f_v is the fusion rate (protons·s^{-1}·cm^{-3}) in the volume

excluding the core, η is the detector efficiency, r_i, is the radial distance from the differential volume to the detector as shown in figure 12.24, A is the surface area of the detector (12 cm^2, since all of the detector's surface area is visible to the microchannel) and r_{cy} is the radius of the differential volume. The term $V_c \cdot f_v / r^2$ is subtracted from the second term on the right hand side of the eqn. 12.1 because the core volume is counted twice (already included in $V_c \cdot f_c / r^2$).

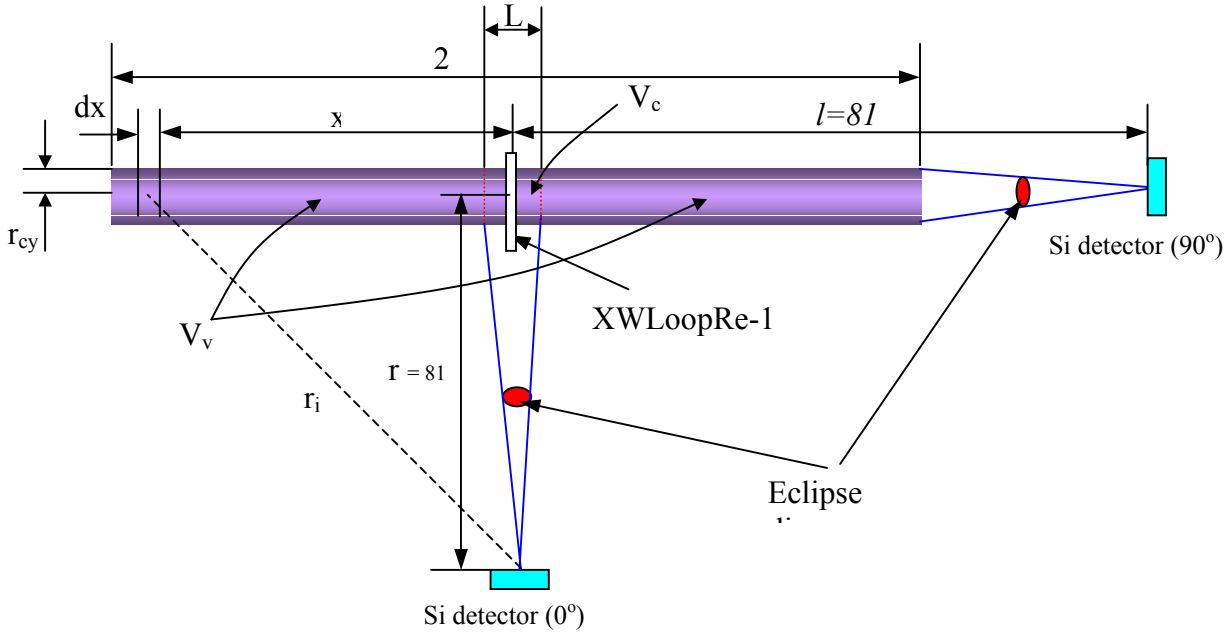

Figure 12.24 Schematic of the line (cylindrical) source from the XWLoopRe-1 single loop grid configuration in two orientations 0° and 90°. Figure not to scale, all dimensions are in cm.

From the table 12.1 the number of protons blocked by the disc in the central position (0° orientation at 60 kV) is 70 (in 60 s) ~ 1.17 /s, while the total counts (without eclipse) registered by the proton detector is (150 in 60 s) ⇒ F_t ~2.5/s. The intersection of the cone projected from the detector to cylindrical source that passes through the LoopRe-1 is L ~1.5 cm wide.

Table 12.1 Protons measured from experiments using LoopRe-1 in two orientations. Eclipsing was performed using the small disc (1.1 cm diameter).

Expt. No.	Orientation	Voltage	Current	Protons with eclipse in the center (60s)	Protons without the eclipse in the center (60s)	No. of protons produced in the core
982	0^o	40 kV	10 mA	13	50	37
		60 kV	10 mA	80	150	70
986	90^o	40 kV	10 mA	372	410	–NA–
		60 kV	10 mA	1632	3604	–NA–

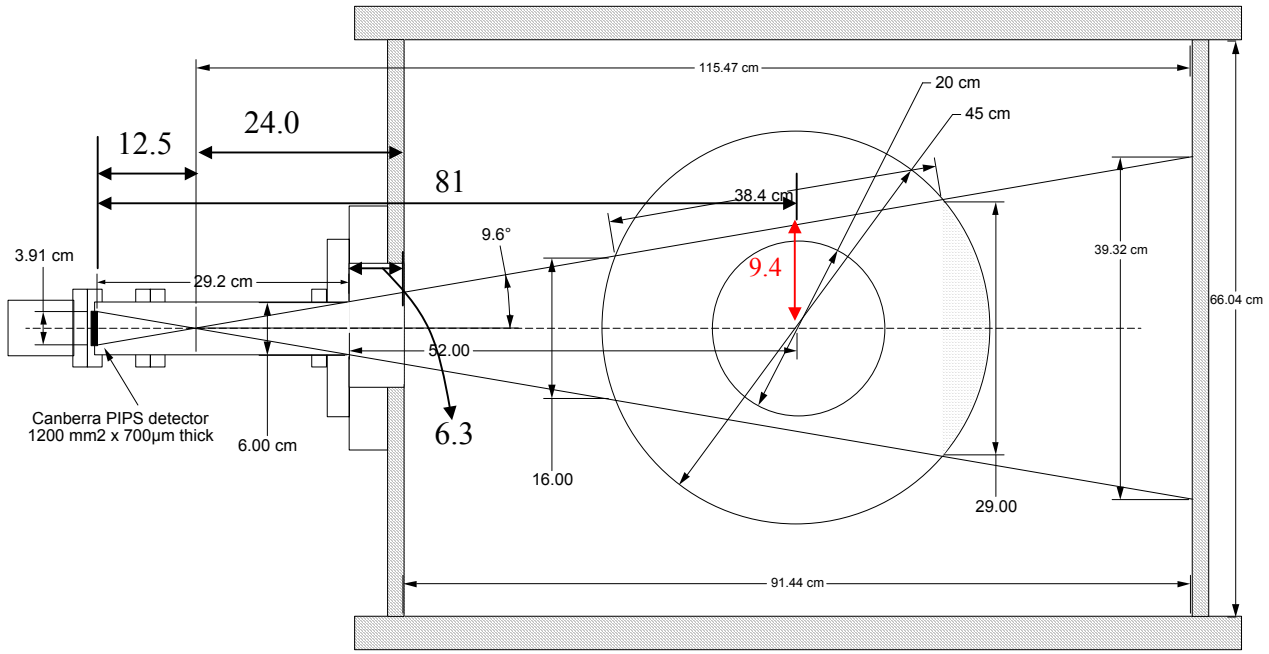

Figure 12.25 Schematic of the IEC device showing the intersection of the line source with the cone of view of the Si detector.

Assuming that a cylinder of diameter 10 cm and length 2 cm as the volume of the core region (with uniform fusion rate). A differential volume of length dx and radius $r_{cy} \sim 5$ cm is assumed (as shown in figure 12.24) to calculate the contribution of the line source formed by the single loop grid, and is calculated using the following equation:

$$F_t = \frac{A\eta}{4\pi}\left(\int_{-\beta}^{\beta} \frac{\pi r_{cy}^{\,2} f_v}{(r^2 + x^2)} dx + \frac{f_c - f_v}{r^2} \cdot V_c \right) \qquad (12.2)$$

where r = 81 cm, β is half the length of the volume source visible to the detector = 9.4 cm, see figure 12.25.

A simplifying assumption is made here – the volume where the reactions occur is assumed to be a cylinder of ~10 cm diameter and is assumed to be uniform in the volume. Hence the volume of the core where additional reactions occur is given by:

$V_c = L \cdot \pi \cdot d^2/4 = 117.8\ cm^3$ (12.3)

where d ~ 10 cm and L ~ 1.5 cm (projection of the 1 cm eclipse disc at the center of the cathode). Hence the second term on the right hand side of eqn. (12.2) is given by:

$$\frac{A \cdot \eta \cdot (f_c - f_v)}{4\pi r^2} \cdot V_c = 1.33$$

$\Rightarrow (f_c - f_v) \sim 71.8\ p/s/cm^3$ (12.4)

$$2.5 = \frac{A \cdot \eta}{4} \int_{-\beta}^{\beta} \frac{r_{cy}^{\ 2} f_v}{(r^2 + x^2)} dx + 1.17 \Rightarrow \frac{2A \cdot \eta}{4} \int_{0}^{\beta} \frac{r_{cy}^{\ 2} f_v}{(r^2 + x^2)} dx = 1.33$$

$\Rightarrow f_v \sim 6.54\ p \cdot s^{-1} \cdot cm^{-3}$ (12.5)

inserting eqn.(12.5) into eqn.(12.4) we get:

$\therefore f_c \sim 65.3\ p \cdot s^{-1} \cdot cm^{-3}$ (12.6)

Hence a large number of reactions still occur very close to the cathode even for a single loop grid. This is expected, because ions have maximum energy close to the cathode (higher reaction cross section) and hence the higher fusion rate in the vicinity of the cathode.

While in the 90° orientation, the total counts are (at 60 kV) $F_{t(90^o)} \sim 60.6$ /s and those registered when the eclipse disc blocked the cathode is ~ 27.2 /s. The later information cannot

be used to characterize the contributions of the core volume segment (as was done earlier) because other volume segments' contributions are also eclipsed in this configuration.

The total fusion rate for the 90^o orientation, is given by:

$$\left(F_t\right)_{90} = \frac{A\eta}{4\pi}\left(\int_{-\delta}^{45.7}\frac{\pi \cdot r_{cy}{}^2 f_v}{(l+x)^2}dx + \frac{f_c - f_v}{l^2}\cdot V_c\right) \qquad (12.7)$$

where l = 81 cm (see figure 12.25) is the distance from the center of the core volume V_c to the Si detector. The upper limit of the integral is limited by the chamber walls 45.7 cm away from the center of the cathode, we have to now determine the lower limit of δ. The total length of the line source would then be (δ + 45.7) cm. Substituting the values obtained above for f_v, f_c, and $F_{t(90^o)}$ in eqn.(12.7) and solving for δ iteratively we obtain δ ~ 78.5. Hence the length of the line source is L ~ 124 cm (extends beyond the outer grid, coming close to the detector).

The above calculations did not account for the variation in the source strength close to the core volume segment where the beam background reactions are significant (although the CX reaction rate would remain constant). For this purpose the eqns.12.1 & 12.2 would have to be modified in future work. However, if we limit the volume source to the confines of the chamber in eqn.(12.6), a discrepancy between the measurements in the two orientations and those predicted by the eqns. 12.1 & 12.2 arises. This would mean that we are having a directed source of protons and this would be contrary to our understanding of this device's operation. Therefore it is concluded that the length of the line source is ~124 cm.

12.4 Conclusions

A single loop grid generates a line (cylindrical) source of protons. The high-energy ions recirculate along the center of the line source. The eclipse scan of the loop grids showed a positive fusion reaction gradient as we move from the edge to the center of the XWLoopRe-1 single loop grid. With improving symmetry (added wires), the fusion rate increases and eventually saturates. The gradual transformation of a line source to a volume source is observed with the increasing symmetry obtained by the addition of more loops to the grid.

The ionization source must be placed away from the cathode for efficient performance. The chordwires provide electrons for ionization even at low pressures and helps sustain plasma. Though low-pressure operation (~0.1 mtorr) is possible when chordwires are used, the fusion rate at such low pressures is much lower and hence is not a recommended approach for low pressure operation of the device.

As the symmetry increases the core plasma radius decreases, this is evident from the chordwire temperature measurements where the wires close to the core get hotter with increasing symmetry. The line source extends beyond the outer grid and the total length of the line source is ~ 124 cm.

The presence of the grid wires seems to affect the fusion rate more drastically than previously thought (was assumed to be uniform around the central grid). The ion microchannels are responsible for most of the fusion reactions in the volume of the chamber and this has prompted another important set of experiments (involving grid rotation) described in the chapter 13.

12.5 References

[1] R. P. Ashley, Private communications, University of Wisconsin, Madison (1999).

[2] Y. Gu, J. B. Javedani, and G. H. Miley, "A portable cylindrical electrostatic fusion device for neutronic tomography," Fusion Technol., 26, 929-932 (1994).

Chapter 13.0 Effects of the cathode grid wires on the fusion rate of the IEC device

The (10 cm dia.) cathode grid used during the present dissertation work has 5 latitudes and 12 longitudes. Figure 11.1 shows a picture of the grid built using wire of 0.08 cm diameter. When this grid is rotated about the z-axis a longitudinal plane sweeps a constant volume in the azimuthal direction about the central axis as shown in figure 13.1, and hence blocks a constant volume along the line of sight of the detector aligned with the converged core.

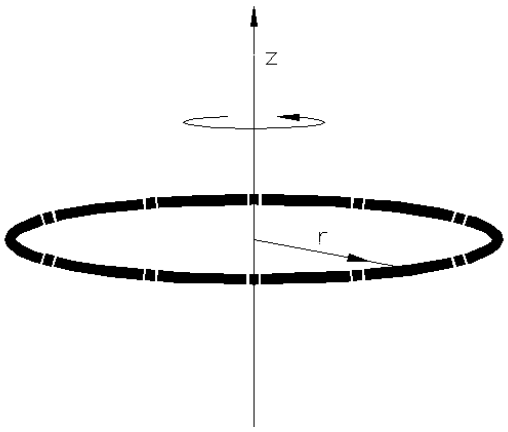

Figure 13.1 Rotation of a longitudinal plane about the z-axis sweeps constant volume along the azimuthal direction

However, as the grid is rotated about the central axis the longitudes sweep different volumes with respect to the line of sight of the detector because, unlike the latitude, the longitude rotates about the diameter as shown in figure 13.2. The longitudes are spaced at equal intervals of 30^{o} and hence with the rotation of every 30^{o} the grid returns to the initial orientation, assuming the grid is symmetric.

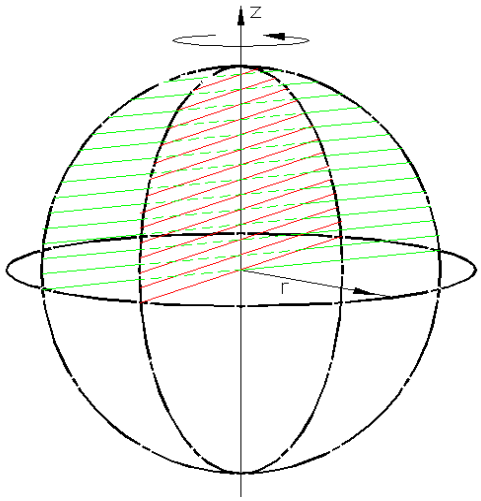

Figure 13.2 Rotation of the longitude along the z-axis sweeps variable areas with respect to a stationary detector along the line of sight in the radial direction.

13.1 Grid rotation experimental setup

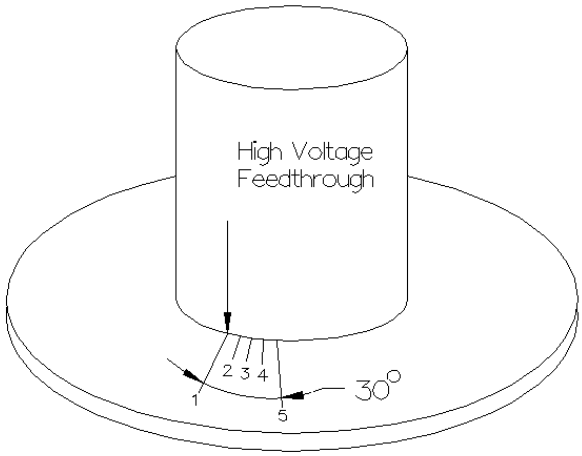

Figure 13.3 The high voltage feedthrough was rotated in intervals of 7.5^{o} up to 30^{o}.

To study the effect of grid wires (eclipsing) on the proton rate from the converged core, it is important that the grid be rotated in small increments of angle. In the present case the angular step sizes adopted were $7.5^{o} \pm 0.5^{o}$ and 2.5 ± 0.3^{o} as shown in figure 13.3. All the other parameters were maintained constant, since the high voltage feedthrough could be rotated under vacuum (without venting), hence the impurity levels in the chamber could be maintained constant during the entire experiment.

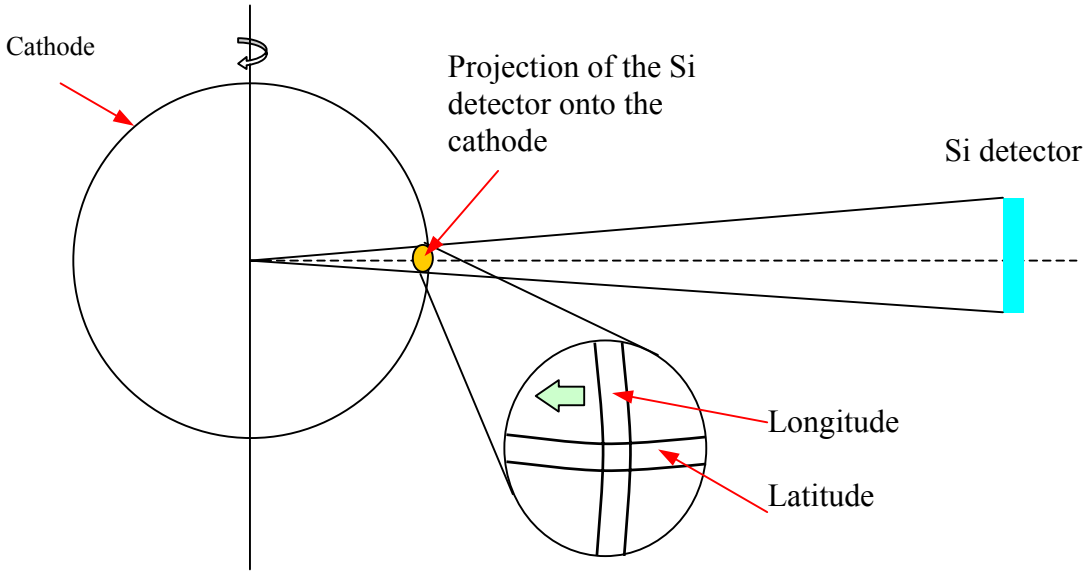

Figure 13.4 The projection of the Si detector onto the cathode is approximately a circle. Assuming a perfect point source, the difference between the projected area and that blocked by the two wires is ~56%. Without the longitude in the view, the difference is ~26%.

If a converged core exists in the center of the IEC device and if this core's dimension is very small (point source), the grid wires would play a major role in masking the counts from such a converged region. The cross wires (one latitude and one longitude) would block approximately 56%, (see figure 13.4), and since the latitude masks half (28%) of the counts (constantly) the longitude alone should mask 28% of the counts when it falls in the line of sight

of the proton detector. Hence the maximum variation in the P/N ratio should not exceed 28%. To verify this aspect, a set of experiments was performed as explained in the next section, by rotating the grid in small increments of angle.

13.2 Results and Discussions

The high-voltage feed-through was rotated in small increments of angle ($7.5^{o} \pm 0.5^{o}$) as shown in figure 13.3, and the protons were recorded by a fixed proton detector simultaneously for each position at various voltages in a sequence as shown in figure 13.5 (a). Two voltage scans were performed at every orientation with varying voltages as shown in figure 13.5 (b).

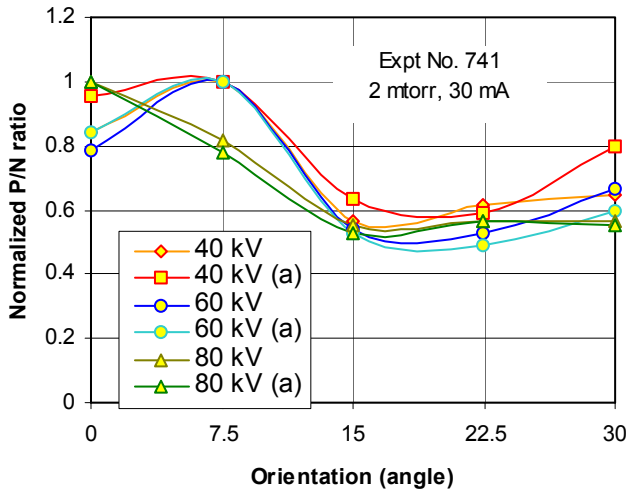

(a)

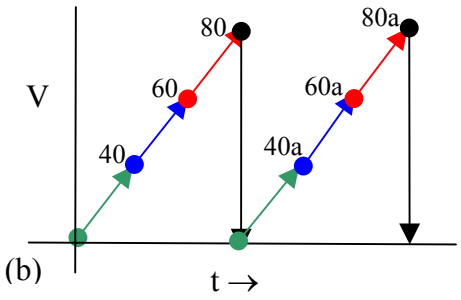

(b)

Figure 13.5 (a) Variation of the P/N ratio with grid orientation. (b) Two voltage scans performed in a sequence (40 – 60 – 80 kV).

The P/N ratio (normalized to the maximum value in a particular scan) measured at each position revealed an average of 40% variation between its maximum and minimum values. This is a source of error (if the proper calibration factor is not used), because the proton detector

would detect fewer protons than the maximum value if the grid were not properly oriented for this factor. This error occurs in addition to the statistical errors (square root of the counts) in the proton counts and is significant. However, this error can be fixed by optimizing the grid orientation.

To verify the above observation another experiment was performed on a similar basis. The grid was rotated in steps of $2.5^{o} \pm 0.3^{o}$, through a total of 42^{o}. The results of this experiment are plotted in the figure 13.6. It is observed that the P/N ratio value repeats itself at an interval of 30^{o}. This is expected because, as mentioned earlier, the cathode grid has longitudes separated by 30^{o} and hence a rotation by 30^{o} would reproduce the original configuration. The value of the P/N ratio in Figure 13.6 varies by about 35 – 40%. The small variation in the data is caused by the small misalignments during rotation within the tolerable limits ($\pm 0.3^{o}$). Hence the grid orientation could affect the proton counts by as much as 45% if the appropriate calibration factor is not used.

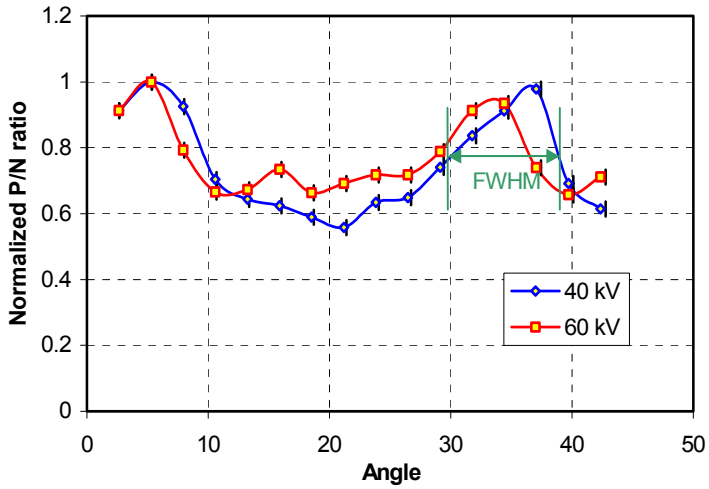

Figure 13.6 Plot of the normalized P/N ratio scan with the angular orientation of the cathode grid is periodic every 30^{o}.

Since the variation in the P/N ratio is greater than the expected 28% for a point converged core it is unlikely that we have a very converged core (almost a perfect point source). Hence, the microchannel that extends towards the proton detector from the cathode should be causing the P/N ratio to increase due to the $1/r^2$ falloff of the fusion rate in such microchannels.

These results (Figure 13.6) suggest that the grid orientation has to be optimized every time the stalk is moved from its original position. Marking the orientation of the feedthrough would help realignment of the grid as long as the stalk itself is not moved with respect to the feedthrough in that we have to repeat the experiment to find the optimum orientation.

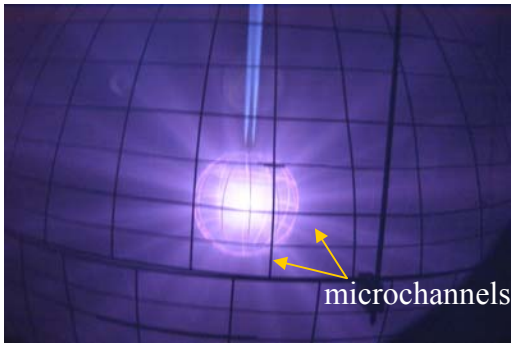

Figure 13.7 Picture of the cathode grid at 25 kV, 30 mA 7.59 mtorr pressure.

The conclusion of the above experiment that the microchannels formed between the longitudinal grid wires affect the DD proton counts suggests that the calibration factors may be a function of the orientation of the grid /proton detector configuration. As shown in figure 13.7, the picture of the cathode at high pressure reveals jet formation (star mode) at high pressure. Since the microchannels are principally constituted of recirculating ions, they form jets, and it would be reasonable to expect that fusion reactions also occur in the pathway of these recirculating ions. CX fusion reactions would also be enhanced along this path, since the CX hot neutrals would continue in straight-line paths along their initial trajectory.

Experiments were not performed to study the effects of vertical alignment of the grid because any misalignment from a concentric position affects the electric fields within the chamber drastically. The only way to do this would be to mount the detector on a moveable port that could be used to scan the cathode grid in the vertical direction.

13.3 Calibration of the IEC device based on the microchannel formation

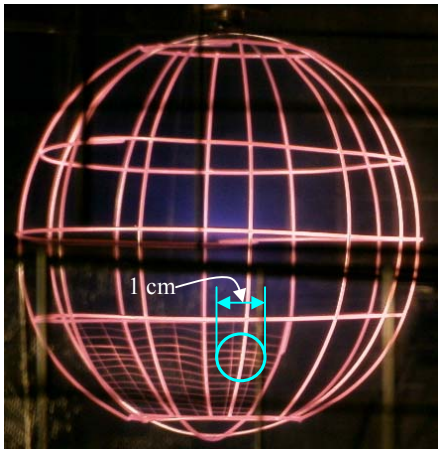

Figure 13.8 Fine wires are introduced on the surface of the grid to intercept the ions leaving the cathode. The dimension of the jet is ~1 cm in diameter.

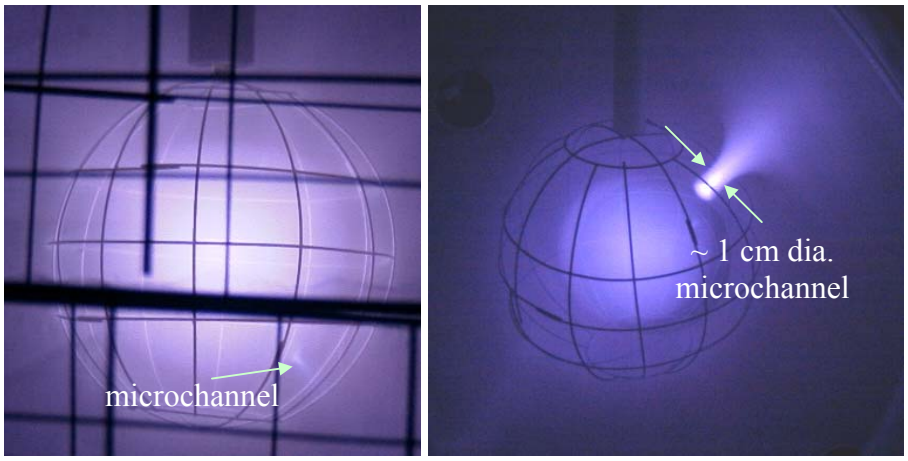

Figure 13.9 Operation of the IEC device in the halo mode allows the measurement of the microchannels' dimensions easily (a) High pressure operation of the grid in the star mode shows the location of the microchannel to be ~ 2/3rd arc distance between the two latitudes (from the lower latitude) (b) the microchannel's diameter is ~ 1 cm and diverges upon exiting the cathode in a spherical chamber at high pressure (~8 mtorr).

Several fine wires were introduced on the surface of the central grid as shown in figure 13.8 to find the microchannel's dimensions as it emerges from the cathode. As shown in figure 13.8 & 13.9, the dimension of this microchannel is ~ 1 cm and that this is the correct dimension of the jet is confirmed in figure 13.9 where the grid is operated in the halo mode.[1] The dimension of the single microchannel that emerges from the grid is easily determined to be ~ 1 cm.

The microchannel that emerges from the cathode diverges and forms a diverging cone. The dimension of the base of this cone was determined from figure 13.6, where the solid angle subtended by the FWHM angular peak width was $\theta \sim 9^o$ (in figure 13.10) at the core of the cathode. The length of the base of the triangle in figure 13.10 is the radius of the cone (microchannel) extending from the core of the cathode to the detector ~ 13.7 cm

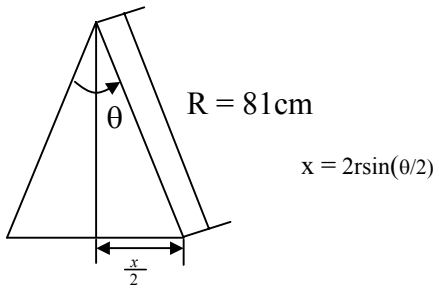

Figure 13.10 The base of the cone calculated from the FWHM in figure 13.5.

Although assuming the microchannel to be cone shaped would give better results, it is approximated by a cylinder (since the divergence is small) for simplifying the calculations. The volume of this assumed cylinder, figure 13.11 (b) is equivalent to the volume of the microchannel, figure 13.11 (a).

It is assumed that the diameter of the converged core is the same as that of the cylinder. The volume of the microchannel in Figure 13.11 (a) is given by:

$$V_m = \frac{2}{3}\pi h(r_c^2 + r_c r + r^2) + \pi r^2 d \qquad (13.1)$$

where h is the height of the cone (l-d)/2, r_c (~ 3.6 cm) is the radius of the cone's base, r (~0.5 cm) is the radius of the cylinder inside the grid, r_{cy} is the radius of the equivalent cylinder in figure 13.11 (b), and d is the diameter of the grid.

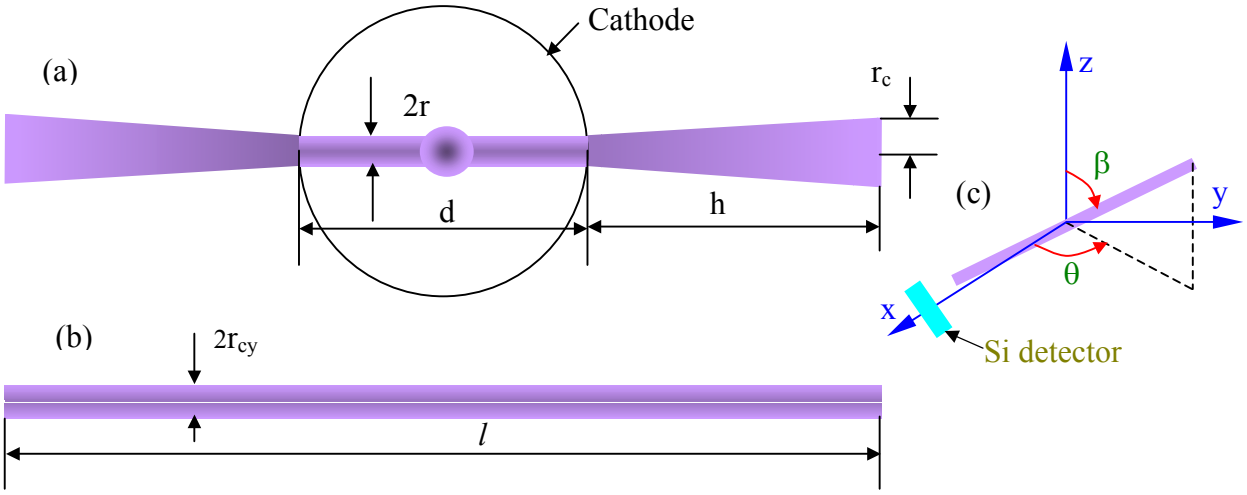

Figure 13.11. (a) Approximate representation of a single microchannel (b) Cylinder of equivalent volume (and hence equivalent number of reactions) of the microchannel (c) Various angles that the microchannel makes with the axis.

Each set of microchannels that forms between any two consecutive latitudes has the same length l (as shown in figure 13.11(b)). Neglecting the variations at the intersections of the cone with the cylinder and chamber, the volume of the equivalent cylinder in figure 13.11 (b) can be evaluated as follows:

$$\frac{2}{3}\pi h(r_c^2 + r_c r + r^2) + \pi r^2 d = \pi \cdot r_{cy}^2 l \qquad (13.2)$$

where l is determined from the orientation of the microchannel (β).

The value of '*l*' is given by:

$$l = \frac{L}{\sin(\beta)} \qquad (13.3)$$

where L is the chamber height = 65 cm. However, for the set of microchannels that fall between the latitudes 2 and 3 in figure 13.12, we have to take the diameter of the cylinder into account and hence

$$l = \frac{L'}{\cos(\beta)} \qquad (13.4)$$

where L′ is the diameter of the chamber = 91.4 cm.

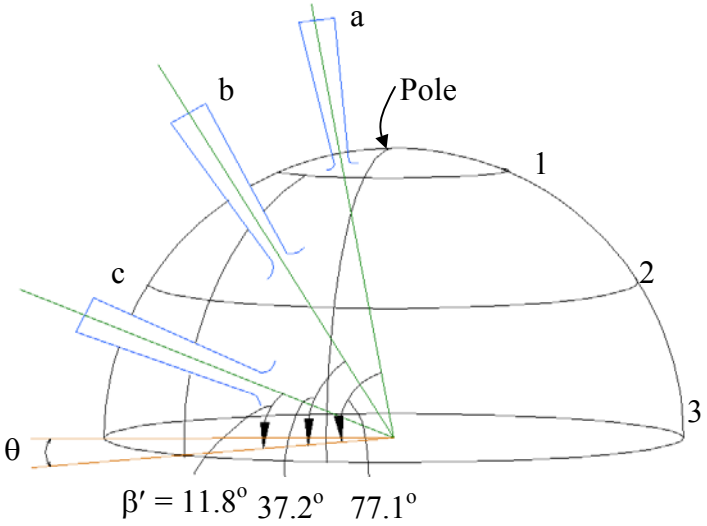

Figure 13.12 Cathode grid showing some latitudes and longitudes along with the microchannels and the corresponding angles of orientation with respect to the core. The latitudes are numbered 1, 2 & 3, while a, b & c are microchannels.

The length of the microchannels are *l* = 66.7 cm for the microchannel a, *l* = 107.5 cm for the microchannel b (evaluated using eqn. 13.3) and *l* = 93.4 cm for the microchannel c (evaluated using eqn. 13.4). Hence the value of r_{cy} for the microchannels a, b and c in figure 13.12 (evaluated using eqn. 13.2) are 2.07 cm, 2.14 cm and 2.12 cm respectively.

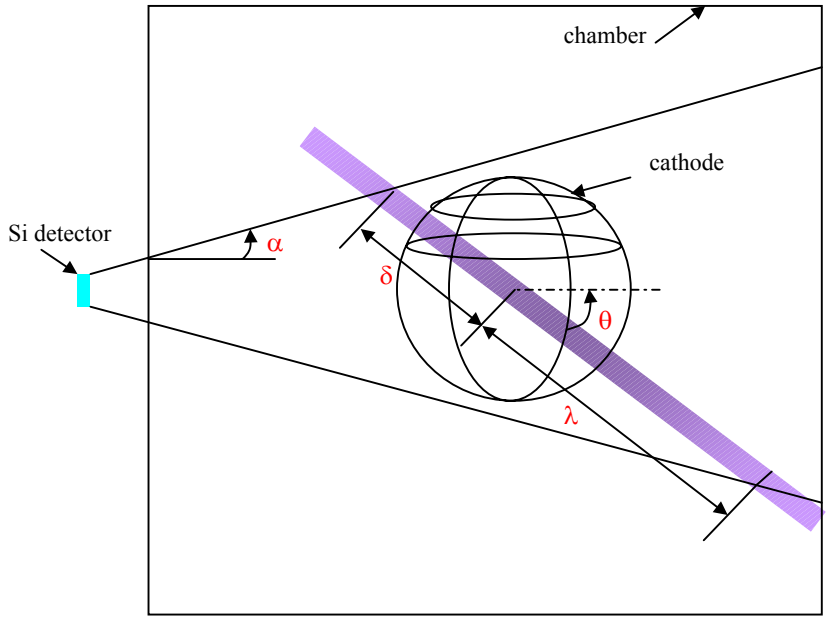

Figure 13.13 The view of the single microchannel is limited by the view cone of the detector.

Assuming that the fusion rate within the differential volume is constant and building on the earlier calculations in Chapter 12, eqns.12.1 & 12.2 are now generalized as follows:

$$F_t = \frac{A\eta}{4\pi}\left(f_v \int_{-\delta}^{\lambda} \frac{\pi \cdot r_{cy}^{\,2} \cos^2(\beta')}{[r^2 + x^2 + 2rx\cos(\theta)]} dx + \frac{f_c - f_v}{r^2} \cdot V_c \right) \qquad (13.5)$$

where θ & β (where β′ = 90 - β, see figure 13.12) are the angles of inclination of the microchannel with y and z axis respectively as shown in Figure 13.11 (c), δ & λ are the lower and upper limits of the cylindrical source respectively that is generally limited by the chamber dimensions and/or the view cone of the detector for the proton detector's view, see figure 13.13.

Although eqn. 13.5 gives an accurate estimate of F_t it is easier to neglect the second term on the right hand side of eqn. 13.5 and account for it later after all calculations are completed. Later in the present section, this simplifying technique will be explained shortly (see eqn. 13.6).

The length of a microchannel is specific for each orientation, however, using symmetry, the length of only half the number of microchannels, i.e., 13 in all, (which is ~ one quarter of the number of holes in the cathode), has to be evaluated since the other half has the same value.

The microchannel tends to form in a region where the electrostatic potentials between the wires are less negative, and hence is away from regions where the wires converge as in the case of the latitudes 1 & 2 illustrated in figure 13.12. The angles that the axes of the microchannels make at the core of the cathode while passing through each of these holes shown in figure 13.12 are $\beta' = (90 - \beta) = 11.8^o, 37.2^o$& 77.1^o.

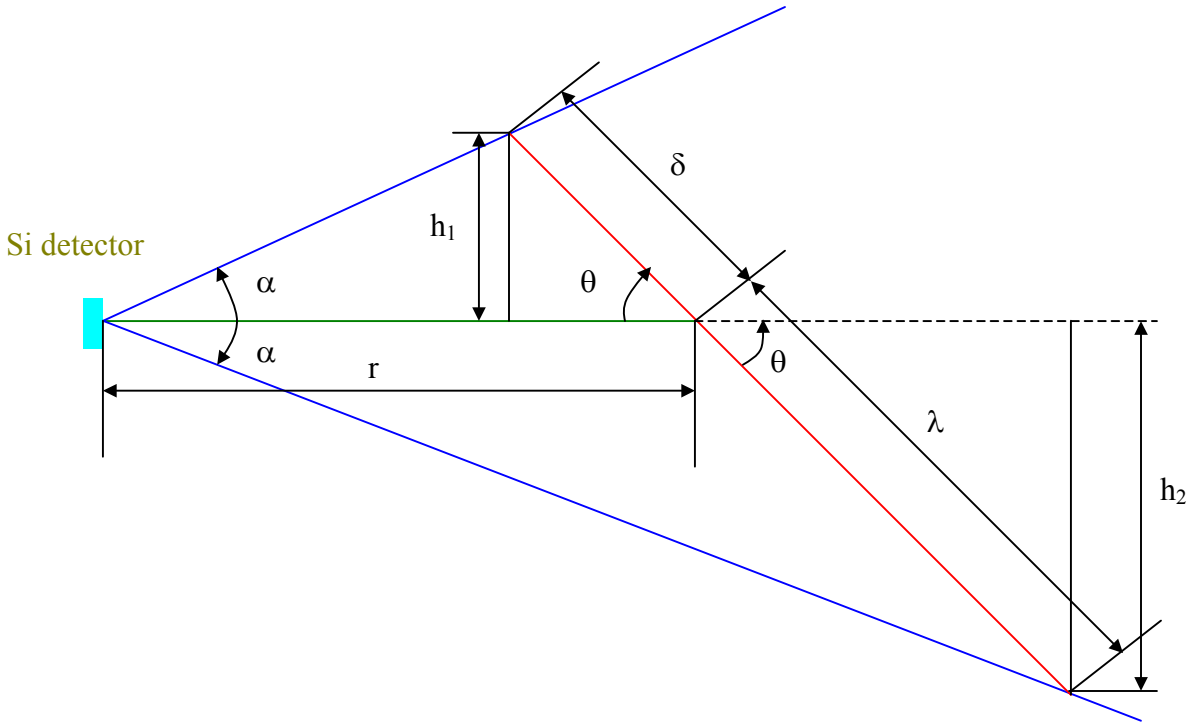

Figure 13.14 Geometry of the detector and the microchannel orientations where $\theta = (15 + n \cdot 30)$, where n = 0,1,...5 and $\alpha = 5.86^o$.

The various lengths from Figure 13.14 are listed below in terms of known quantities:

$$h_1 = r\frac{\sin\alpha\sin\theta}{\sin(\alpha+\theta)} = \frac{r}{\cot\alpha + \cot\theta} \qquad (13.6)$$

$$h_2 = r\frac{\sin\alpha\sin\theta}{\sin(\theta-\alpha)} = \frac{r}{\cot\alpha - \cot\theta} \tag{13.7}$$

$$\delta = \frac{h_1}{\sin\theta} \tag{13.8}$$

$$\lambda = \frac{h_2}{\sin\theta} \tag{13.9}$$

The total length of the line source is δ+λ = L given by:

$$\mathrm{L} = \frac{h_1 + h_2}{\sin\theta} = \frac{2r\cdot\cot\alpha}{\sin\theta\cdot(\cot^2\alpha - \cot^2\theta)} \tag{13.10}$$

The number of segments between the latitude 1 and the pole of the grid in figure 13.14 (also see figure 13.1) is only 4, hence there are only two orientations of the microchannel 'a' that we need to account for in the calibration. All the other microchannels that form between any two consecutive latitudes are 12 in number and 56 in total. Since the area of each of the openings is ~constant, we assume that the diameter of the microchannel remains constant (~ 1 cm).

13.4 Calibration of the IEC chamber assuming the source of the fusion to be the microchannels

The volume source calibration factor calculated using MCNP[2] gave an approximate calibration factor of the form:

$$\frac{4\pi r^2}{A}\left(\frac{21}{\eta_d}\right) \tag{13.11}$$

where the factor 21 was found using MCNP. Figure 13.15 shows a plot of the relative detector calibration factor vs. the spherical source radius, and it includes the extrapolation from the solid angle of the detector to the entire chamber volume.

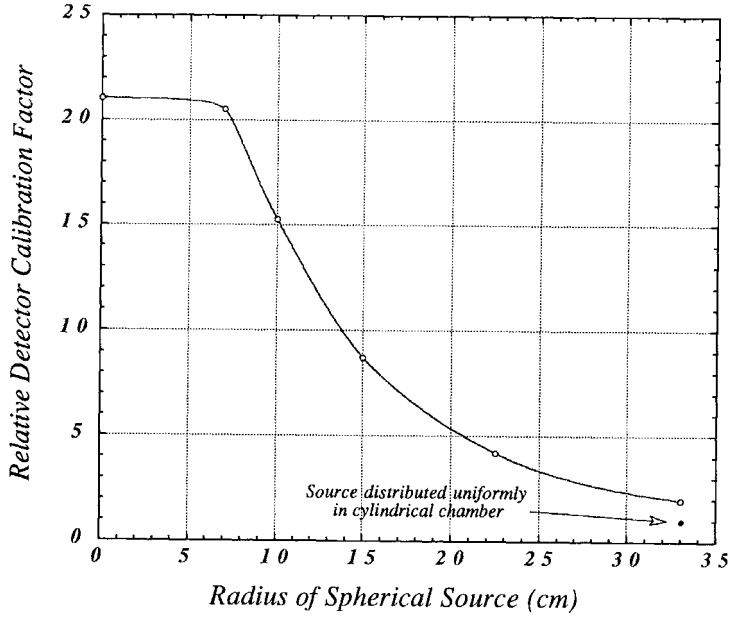

Figure 13.15 Plot of relative detector calibration factor vs. radius of spherical source. For the point source the detector calibration factor is 1, but for a complete volume source the factor is 21.[2]

The converged core source can be approximated to be a point source (as seen by the detector), and can be modeled using the following equation, (modified from Ben Cipiti's work[3]):

$$\frac{4\pi r^2}{A}\left(\frac{1}{\eta_c \eta_d}\right) \sim \mathbf{7818} \qquad (13.12)$$

where A is the surface area of the detector = 12 cm^2 (since the entire detector is visible to the protons born in this region), r is the distance of the proton detector from the center of the chamber ~ 81 cm, η_c is the transparency of the cathode ~0.925, and η_d is the detector efficiency ~0.95. The transparency of the anode η_a is not accounted for because a hole was introduced into the anode in front of the detector that did not block protons, in other words η_a ~1 . The calibration factor for the converged core as calculated from eqn. 13.12 is ~7818.

The embedded source can also be approximated by a point source with an additional factor of 2 since protons born on the far side of a grid wire gets blocked by the wire, and is given by (modified from Ben Cipiti's work[3]):

$$\frac{4\pi r^2}{A}\left(\frac{1}{\eta_d}\right)\times 2 \sim \mathbf{14550} \qquad (13.13)$$

where A = 12 cm^2 (since the entire detector is visible to the protons born in this region).

In the present setup, r ~ 81 cm, A = 12 cm^2, η_d = 0.95 gives a calibration factor of ~164192 (= 151,878 if the anode transparency factor (η_a ~ 0.925), is excluded, since a hole was later introduced in front of the detector). This calibration factor (164,192) was used for all the earlier purposes[3] and in the calculation of this factor the formation of microchannels was neglected; instead a uniform volume source was assumed. In what follows, a new calibration factor is calculated after breaking down the various fusion contributions into volume (microchannel), embedded and converged core source contributions.

The initial orientation of the grid is important for the calibration of the proton detector. It is assumed here that the grid is oriented in such a way that none of the microchannels are pointed at the detector i.e., in an orientation such that the proton rate on the detector is a minimum. This orientation is chosen because if the microchannels were pointing at the detector instead, the $1/r^2$ dependence of the fusion rate would complicate the calculation of the calibration factors. For such an orientation, it is required that the cross wires of the grid are aligned with the line of sight of the proton detector as shown in Figure 13.4.

The above mentioned assumption is important because if we had chosen the orientation where the readings are a maximum (i.e., longitude (wire) is not in the projection of the proton

detector) then we would have to take into account the one microchannel that would extend close to the proton detector and this would complicate the calculations.

Since the grid is spherically symmetric, we can evaluate the fusion rate of the microchannels in only one quadrant of the grid and the total fusion rate would then be given by:

$F_t = 4\cdot(\Sigma F_i) + 2\cdot\Sigma G_j$ (13.14)

where i = 1,2,3 & j = 1,2 and

F_i & G_j are calculated using the equation (modified eqn. 13.5) given below:

$$F_i \text{ or } G_j = \frac{A\eta}{4\pi}\left(f_v \int_{-\delta}^{\lambda} \frac{\pi \cdot r_{cy}^{\,2} \cos^2(\beta')}{[r^2 + x^2 + 2rx\cos(\theta)]} dx \right) \quad (13.15)$$

where A is the surface area of the detector visible to the proton born somewhere within the IEC chamber. The accurate calculation of this area is given in Appendix C. This area A is an intersection of the projection of the entrance port of the Si detector (an ellipse) with the surface area of the Si detector (a circle). It is assumed that the minor radius of the ellipse remains constant.

Since the contributions of the volume source alone is difficult to determine, the data from the large eclipse experiment is used. The large eclipse disc masks 100% of the central grid and hence any protons detected by the Si detector come from the volume source. However, the exact volume of the microchannel is difficult to calculate. The cylinder of the microchannel's equivalent volume is used for the purpose. The length of this cylinder is calculated in two stages. The length of the microchannel when there is no disc is first calculated. In the next step the length of the microchannel blocked by the eclipse disc is calculated. The difference in the two lengths gives the length of the microchannel visible to the detector and is tabulated in the

Table 13.1 below, also see figure 13.16 where $\Delta x_1 = \delta_1 - \delta_2$ and $\Delta x_2 = \lambda_1 - \lambda_2$, $T_{i,j} = F_i/f_v = G_j/f_v$, and F_i & G_j are computed using eqn. 13.13 (without the second term on the right hand side of the eqn.).

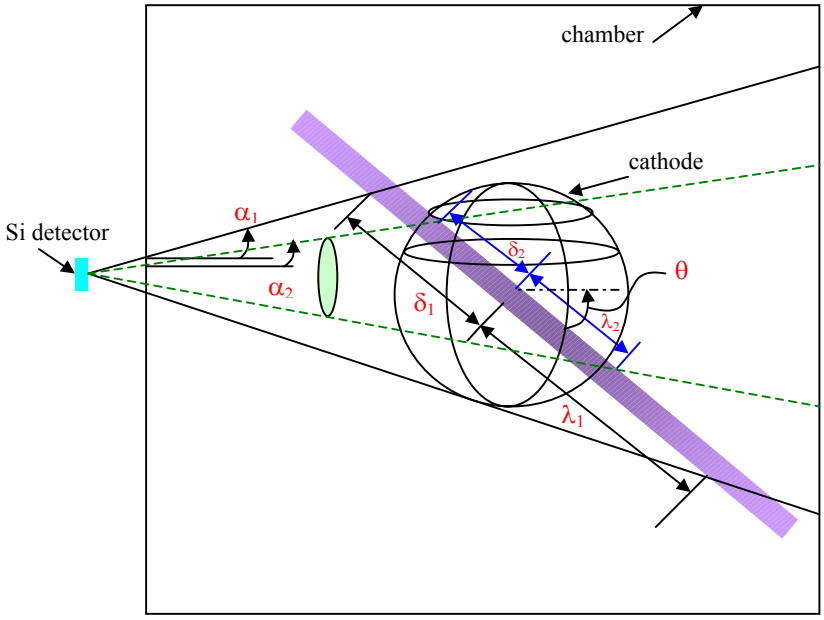

Figure 13.16 Various parameter from the Table 13.1 are schematically represented here, where $\alpha_1 = 5.86^o$, $\alpha_2 = 4.20^o$.

Table 13.1 Various values used in the calculation of the volume source calibration factors using data from the Large eclipse scan experiment.

i	α_1	α_2	θ^o	β^o	l	δ_1	λ_1	δ_2	λ_2	r_{cy}	Δx_1	Δx_2	T_i	T_j
1a	5.86	4.20	15	11.8	93.4	23.2	52.1	18.0	31.6	2.120	5.2	20.5	0.01576	0.01581
2a	5.86	4.20	45	11.8	93.4	10.7	13.1	7.8	9.1	2.120	2.9	4.0	0.00591	0.00573
3a	5.86	4.20	75	11.8	93.4	8.37	8.85	6.04	6.28	2.120	2.33	2.57	0.00420	0.004219
1b	5.86	4.20	15	37.2	107.5	23.2	52.1	18.0	31.6	2.136	5.17	20.45	0.01214	0.01218
2b	5.86	4.20	45	37.2	107.5	10.7	13.1	7.84	9.08	2.136	2.86	4.02	0.00449	0.004434
3b	5.86	4.20	75	37.2	107.5	8.37	8.85	6.04	6.28	2.136	2.33	2.57	0.00324	0.00325
1c	5.86	4.20	45	77.1	66.7	10.7	13.1	7.84	9.08	2.071	2.86	4.02	0.00559	0.00552
2c	5.86	4.20	90	77.1	66.7	8.31	8.31	5.95	5.95	2.071	2.36	2.36	0.00390	0.003896

If f_v is the source strength of the volume source in protons/s/cm^3 and if N is the total number of protons detected by the detector when the large eclipse disc is in position, then from Table 13.1 the relation between f_v and N is given by:

$$(4[\underbrace{\Sigma T_i(a,b) + \Sigma T_j(a,b)}] + 2[\underbrace{\Sigma T_i(c) + \Sigma T_j(c)}])x\ f_v = N \qquad (13.16)$$

$$(4\ x\ 0.091365\ +\ 2\ x\ 0.018902)\ f_v \sim\ 0.403\ f_v = N$$

$$\therefore f_v \sim 2.48 \text{ x (N) protons}\cdot s^{-1}\cdot cm^{-3} \qquad (13.17)$$

The total fusion rate in the volume of the chamber is given by:

$$T_f = f_v \text{ x } V_s \qquad (13.18)$$

Where V_s is the total volume of all the microchannels given by:

$$V_s = 12\pi\ [r_{cy1}{}^2 l_1 + r_{cy2}{}^2 l_2] + 4\pi[r^2{}_{cy3} l_3] - 26\ (4/3\pi cr^3) \sim 36{,}903\ cm^3 \qquad (13.19)$$

where all the parameters are defined in table. 13.1, and cr is the core radius (~2.1 cm, region where the equivalent cylindrical microchannels overlap) and the factor of 26 arises from the fact that there are 26 microchannels in this grid configuration. Hence the volume source calibration factor is ~ **91,520.**

The total contribution of the microchannel (volume) source is given by:

$$T_f = 91520\ N' \qquad (13.20)$$

where N′ is the total number of protons detected by the Si detector.

Hence the total calibration factor for the D-D fusion is given by:

$$\frac{7818\,(x) + 14550\,(y) + 91520\,(z)}{\eta_{mag}} \qquad (13.21)$$

where x, y and z are the percentage contributions of each of the source regimes to the overall fusion rate and η_{mag} is the detector channel efficiency (eqn. 13.9) in the presence of the electron deflector magnetic field.

13.5 Effects of non-uniform ionization source on the microchannel formation

Although, in the earlier calculations in section 13.4 it is assumed that the microchannels are formed uniformly around the cathode, the assumption was that the only factor affecting these microchannels is the area between the wires open for such microchannel formations. In order to verify this assumption another set of experiments was conducted by varying the ionization source around the cathode. This was accomplished by sequentially turning off the filament electron sources (1,2 & 3) as shown below in figure13.17 (also see figure 10.9).

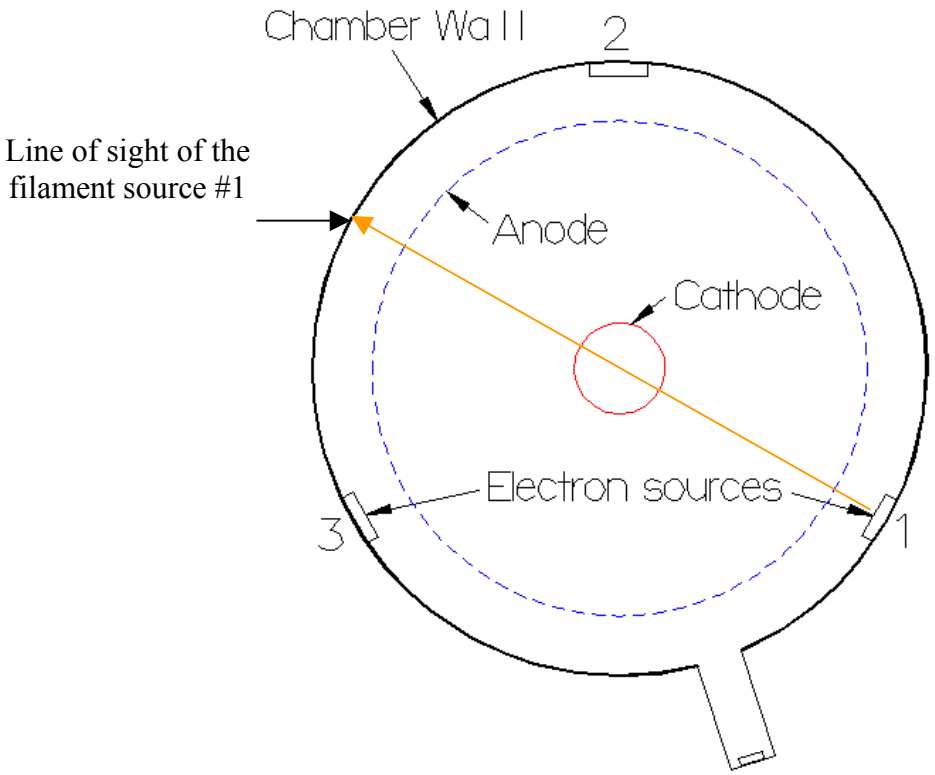

Figure 13.17 Top view of the cross-section of the IEC chamber. The arrangement of the three filament electron sources with respect to the detector is illustrated.

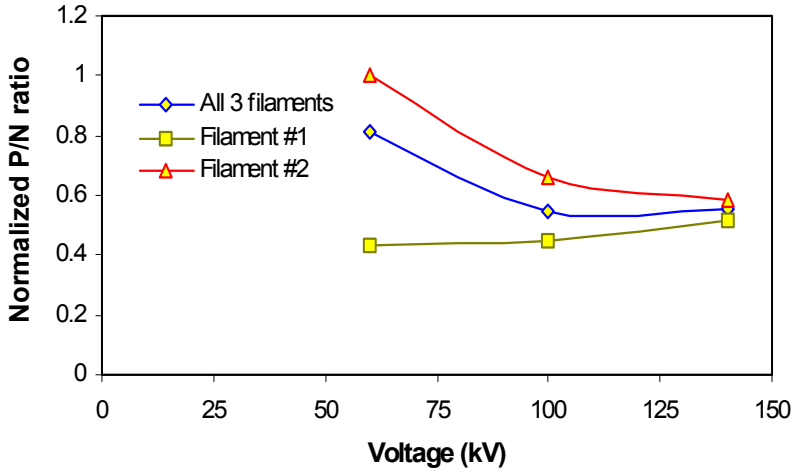

Figure 13.18 Normalized P/N ratio vs. voltage shows a direct correlation with the ionization source (filament source) in operation. (The P/N ratio is normalized to the maximum value of all three voltage scans).

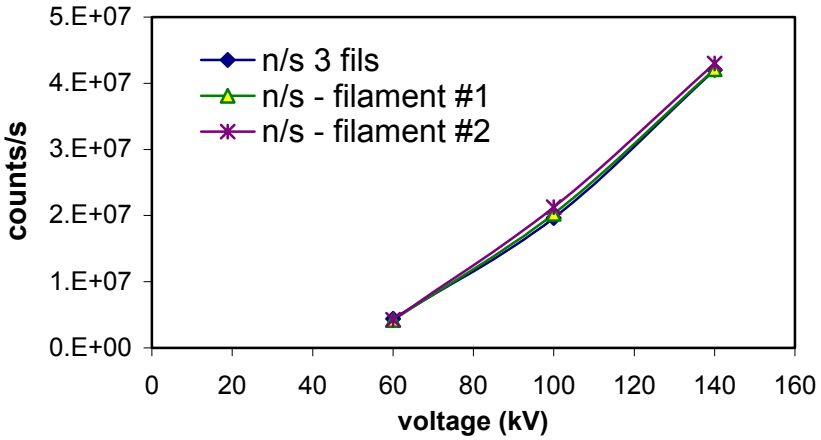

Figure 13.19 Voltage scan with various filament source configuration (also see figure 13.18). Neutron rate remains constant with each of these configurations (i.e., it is independent of the filament electron source in operation)

The filaments (1, 2 & 3) were sequentially turned off, with only one filament in operation at any given time. Figure 13.18 shows the normalized P/N ratio scan with various filaments in operation. Most protons are produced when all three filaments are operating, while the least protons are produced when the filament closest to the Si detector (figure 13.17) is operating. This could be explained only when the formation of microchannels is taken into account. When a single filament source is operating, it provides higher local ionization and hence the

microchannels form easily around the line of sight of the filament source (for instance near the filament source #1, in figure 13.17).

The above observation is confirmed by the fact that with only the filament #2 operating, the proton rate observed is higher than other configurations under study. The line of sight of this filament #2 comes very close to the detector port and hence due to the $1/r^2$ dependence of the fusion rate, the Si detector sees a higher fusion rate. It is noteworthy that the neutron rate remains constant with each of the filament source configurations as shown in figure 13.19, because the neutron source sees a point source. Only the proton rate changes with the filament source configuration.

13.6 Effect of the deflector magnetic fields on the proton rate measurement

A deflector magnet is used to divert the electrons away from the line of sight of the proton detector. The arrangement of this magnet with respect to the proton detector is shown in figure 3.4. However, since the Si detector is sensitive to the magnetic field (due to the Hall effect[4]), a characterization of the magnetic field on the proton rate was performed.

Inside a semiconductor the charge carriers are distributed in energy, and those with higher velocities will be deviated to a greater extent for a given field. Hence the time for which the detector reads a current from a pulse would increase. This increase in pulse length might lead to pulse pileup causing a faulty proton measurement.

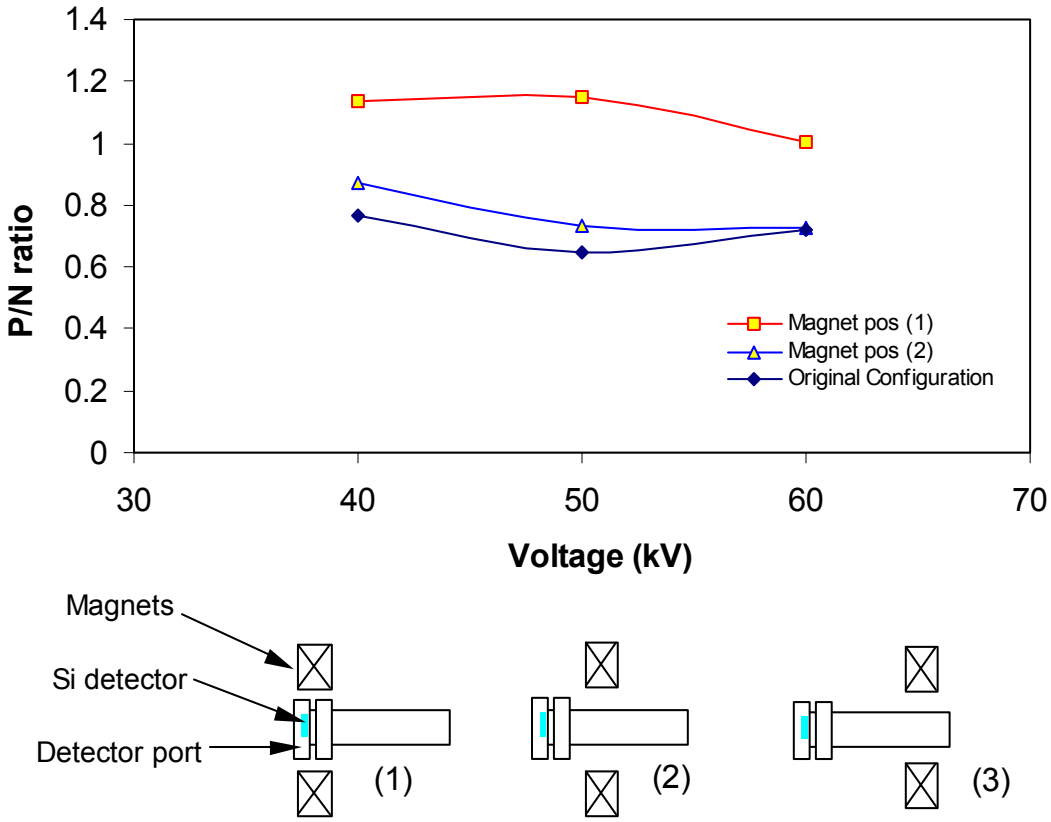

Figure 13.20 (a) Voltage scan of the P/N ratio with various magnetic field configurations. (b) The position of the deflector magnet with respect to the Si detector.

Permanent magnet clusters were prepared by placing several small permanent magnets together to increase the field strength. Once prepared, such magnets were used in various configurations as shown in figure 13.20 (b). From figure 13.20 (a) it is evident that with the increasing magnetic field across the face of the Si detector the number of protons detected is higher. This could be a consequence of the Hall effect as mentioned earlier. The other possibility would be that with the deflector field moving closer to the Si detector, greater numbers of protons reach the detector without being deflected away. Although the protons are very energetic, there is a finite possibility that they would be deflected by the magnetic field. The highest number of protons (higher P/N ratio) is detected with the NNNN configuration since

the field extends for a longer distance and is normal to the direction of propagation of the protons as shown in figure 13.21 (b).

The proton rate measurement with the configuration NSNS beyond 40 kV had noise and is hence not reported. This noise is caused by the electrons that get through the cusp fields that form in this configuration and hence is a bad configuration for electron deflection.

The third configuration NNNN-SSSS was selected with an intension that so that the protons that are deflected in one direction (downwards) by one pair would be reversed by the other pair (in the upward direction). The P/N ratio did not vary much with this configuration and it is perceived to be the best magnetic configuration.

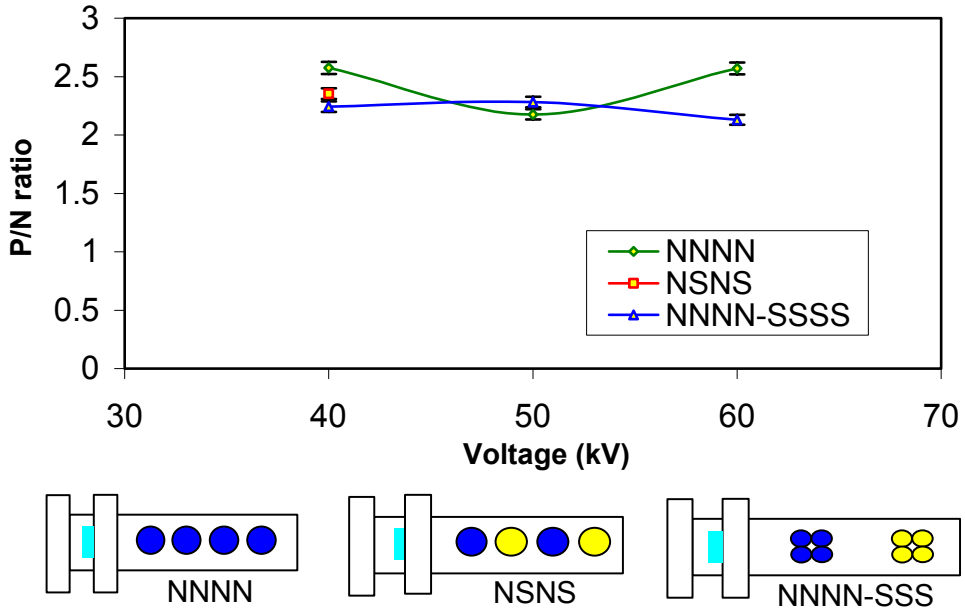

Figure 13.21 (a) The P/N ratio scan with voltage, and the magnetic field configuration confirms that the proton measurements are influenced by the presence of the magnetic field (given that the horseshoe magnet is much more powerful than the magnets used here). (b) Various configurations of the magnetic field used in the experiment (N – north, S – south), the polarity on the far side of the detector port in configuration NNNN is SSSS, and in the configuration NSNS is the same as the one on the near side. The polarity on the far side of the NNNN-SSSS configuration is SSSS-NNNN.

13.7 Calculation of the proton deflection inside the detector port

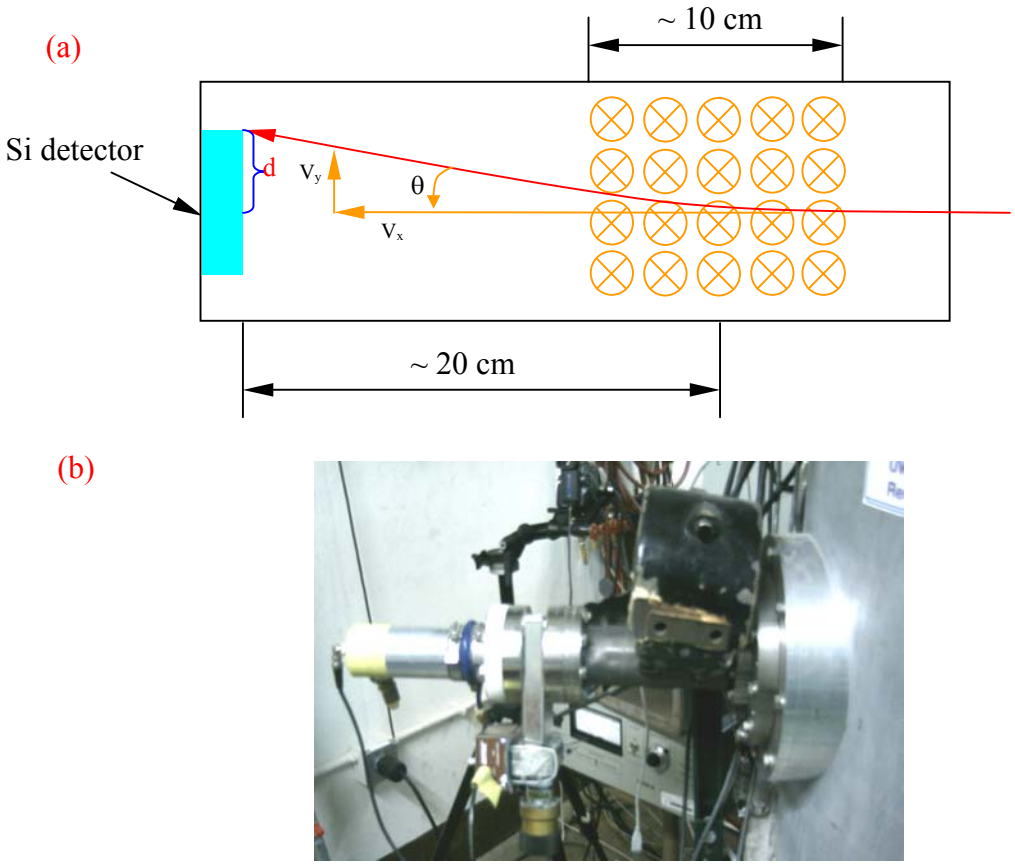

Figure 13.22 (a) Schematic of the approximate dimensions of the detector port with the magnetic field. Though the fields are in general fringing, we assume that it is constant over the 10 cm length of the horseshoe magnet. (b) Side view of the proton detector and the deflector magnet (also see figure 3.4).

The use of a permanent magnet to deflect away the electrons was first suggested by Bob Ashley (Rutherford first used a magnetic field to separate various radiations from the radioactive material). The associated analysis (to calculate the magnetic field efficiency in deflecting protons - η_{mag}) was however done independently.

We now assume that the velocity of the particle is a constant in the x-direction (V_x) and it is on the same order as the initial proton velocity V_p, while the particle accelerates in the y direction, its velocity is V_y and is calculated as follows:

$$V_y = a_y \cdot t \tag{13.22}$$

$$\text{where } a_y = \frac{F_y}{m_p} = \frac{qV_pB}{m_p} \tag{13.23}$$

where B = 0.15 T (measured peak B field inside the detector port), $m_p = 1.67 \times 10^{-27}$ kg, $q = 1.6 \times 10^{-19}$ C,

$$V_x \sim V_p = \sqrt{\frac{3.0 \cdot 10^6 \times 1.6 \cdot 10^{-19}}{1.67 \times 10^{-27}}} = 1.7 \cdot 10^7 \text{ m/s} \tag{13.24}$$

$$\therefore a_y = 2.4 \times 10^{14} \text{ m/s}^2 \tag{13.25}$$

Assuming that the proton is in the influence of the field for 10 cm as shown in figure 13.22 (a), the time that the proton takes to traverse the field is given by:

$$t \sim \frac{0.1}{V_p} \sim 5.9 \times 10^{-9} \text{ s} \tag{13.26}$$

$$\Rightarrow V_y \sim 1.4 \times 10^6 \text{ m/s} \tag{13.27}$$

The angle of deflection ‘θ’ in figure 13.22 (a) is evaluated as follows:

$$\theta = \tan^{-1}\left(\frac{V_y}{V_x}\right) = 4.7^{\circ} \tag{13.28}$$

$$\therefore d = 20 \times \tan\theta = 1.64 \text{ cm} \tag{13.29}$$

The radius of the detector is only 1.955 cm and hence many protons could be potentially lost, especially those that arrive into the detector at an angle.

The B-field distribution inside the proton detector is not known accurately and hence empirical data is used to determine η_{mag}.

The proton rate before and after the B-field is used, which gives an idea of the influence of the B-field. Such an experiment was performed at low cathode voltage to avoid any energetic electron jets from damaging the proton detector. From this measurement it was observed that the proton rate changed by an average of 50%:

$$\therefore \eta_{mag} \sim 0.5 \qquad (13.30)$$

Hence substituting eqn. 13.30 and the corresponding values from table 5.1 in eqn. 13.21, we get a calibration factor of ~**107612** (with the orientation of the grid such that microchannels are oriented away from the detector i.e., lowest number of protons are detected).

13.8 Conclusions

Grid rotation experiments have revealed that the fusion source is non-uniform inside the IEC device. Microchannels form at regular intervals spaced 30^o apart, corresponding to the spacing of the longitudes of the cathode grid. All fusion occurs within these microchannels, since even the charge exchanged neutrals cause fusion within these channels. Proper grid orientation is essential for correct proton rate measurement and interpretation. The calibration factor was calculated for the orientation where the proton rate was a minimum; this was done to avoid the complications that may arise due to $1/r^2$ falloff of the protons.

The magnetic field used to deflect the electrons has been found to deflect the protons also. Hence the final calibration factor included the empirical efficiency factor (η_{mag}) that accounts for the protons lost due to magnetic deflection. The proton data from the off-axis

detector was found to be unreliable because the magnetic fields were significant near the Si detector and the associated Hall effect could easily affect the proton rate measurements. Hence the information from such off-axis detector measurements was not used for the present purpose.

13.9 References

[1] J. H. Nadler, G. H. Miley, Y. Gu and T. Hochberg, "Characterization of an inertial-electrostatic confinement glow discharge (IECGD) neutron generator,"Fusion technol. Vol.21, pg. 1639, May 1992.

[2] Mohamed E. Sawan, Private Communications, University of Wisconsin, Madison, 2000.

[3] Ben B. Cipiti, PhD thesis, University of Wisconsin, (2004).

[4] Lindmayer and Wrigley, "Fundamentals of semiconductor devices," D. Van Nostrand Company, Inc., pg. 395, (1965).

Chapter 14.0: Summary

Chapters 1, 2 and 3 deal with the principle of operation, history and the experimental IEC setup at the University of Wisconsin, Madison. In chapter 4, operational techniques with various ionization sources (RF and filament electron sources) developed to improve the performance of the IEC device are explained. An RF ionization source was avoided during the present study due to the associated noise problems.

There are various ways by which fusion occurs in an IEC device:

1. Beam-beam reactions that occur in the core of the device,
2. Beam target reactions that occur on the surface of the grid wires and the chamber walls, and
3. Beam-background reactions that occur close to the central grid and charge exchanged (CX) neutral-background reactions that occur everywhere inside the chamber.

A beam consists of charged ions such as D^+, D_2^+, D_3^+, He^+ and He^{++} while the background is the neutral fuel gas and the target is the embedded ions that get trapped inside the

lattice structure of either the grid material or the chamber walls. An understanding of the distribution of the various reaction contributions described above to the total fusion reactivity would help further the efficiency of the device and design new applications. This understanding would also help reduce the disparity between experimental and theoretical values. Hence a new diagnostic called the eclipse disc was co-invented.

In Chapter 5 a new diagnostic called the "eclipse disc" is introduced and was used to characterize the various fusion regimes within an IEC device. The Eclipse disc diagnostic allows monitoring the fusion reactivity from regions not eclipsed by the disc using a proton detector. A difference in fusion rate measurements, with and without the disc in position, helps deduce the reaction rate in the eclipsed region, thus allowing selective fusion rate measurements from different regions within the IEC device. While the data from the small eclipse experiment gave insight about the converged core contributions, the large eclipse disc experiment revealed the volume source contributions. Using this diagnostic it was confirmed that a converged core regime exists for the D-D reactions, but the D-^{3}He reactions are mostly beam-target reactions and occur on the surface of the cathode wires (D-^{3}He reactions are rare in the volume of the device due to the penning ionization effect). The effect of fusion convergence with varying voltage and chamber pressures is studied using a small eclipse disc that was scanned across the view of the cathode grid from the Si detector and is reported in Chapter 6. It was observed that there was no significant variation of the P/N ratio with voltage or pressure in the range of operation. Hence a single calibration factor could be used in the range of operation tested during these experiments and such a calibration factor is derived in chapter 13.

Chapter 7 deals with the Monte-Carlo Stopping and Range of Ions in Matter (SRIM) code, which is used to simulate the proton energy spectrum of both the DD and D-^{3}He and is

compared with the experimental observations. A Si (semiconductor) detector detects the protons from the fusion reactions. These protons are energy broadened due to collisions and Doppler broadening. Though the Doppler broadening is a simple calculation, the collisional broadening could be accommodated into theoretical predictions using Monte-Carlo SRIM code calculations. Building on Chapter 7, Chapter 8 explains a new technique to measure the average ion energy in an IEC device using Doppler broadening of the proton energy spectrum using a single loop cathode.

The fusion rate as measured with these grids, showed Doppler broadening, that contains a double peak (characteristic of linear doppler broadening). SRIM calculations revealed that the ions were getting accelerated to 60% of the applied grid voltage. This is a new method of determining the average ion energy while the earlier methods used visible spectroscopy at higher pressures, and were not suitable at lower pressures. The average ion energy information is used in the energy balance equation calculations (in chapter 9) and would also be useful for all the codes that predict the fusion rates in an IEC device.

A new diagnostic called the "chordwire" is introduced in Chapter 9. The chordwire diagnostic is a wire that is placed in the form of a chord of a circle inside the cathode. The energy balance on the surface of this wire using temperature measurements via a pyrometer gives the ion flux. This diagnostic was used to study the effects of thermionic emission on the performance of the IEC device, and this diagnostic also gives insights into the ion flux reaching the central grid. Various chordwire arrangements were used to calculate the ion flux from different directions and a preliminary 2D ion flux map was generated. The chordwire diagnostic has also helped understand the non-uniformity of the ion flux in an IEC device and guided the research effort towards finding new ways to homogenize these ion-fluxes. To homogenize the

ion fluxes the RF ionization source was used that provided homogeneous distribution of ions around the central grid. The effects of asymmetric grid heating and the grid wire material selection process are also reported in this chapter. Associated with the stalk is the breakdown problem due to sputter deposition of grid material that forms a conductive path from the central grid to the grounded chamber wall. Earlier cathode grids were built using stainless-steel (SS) wires, such wires melt at low temperature and hence operation beyond an input power ~ 4 to 5 kW was difficult and the grid also sputters significantly. This problem has been reduced drastically by selecting new refractory grid material (W-25%Re) that, due to reduced sputtering, allowed the device's operational voltage to be raised from 60 kV to 180 kV (with improvements in the stalk design) and has allowed the operational power level to be increased to 12 kW (limited by power supply capabilities). Using this new material resulted in 5 orders of magnitude improvement in the D-^{3}He reactions and ~3 orders of magnitude improvement in the D-D reaction rate when compared to the earlier performance of the device with stainless-steel grids.

The fusion reactivity is severely affected by the impurities present inside an IEC chamber and the effect of such impurity concentrations is studied using a residual gas analyzer in chapter 10. Highly ionized impurity ion liberates more secondary electrons than a single fuel ion and hence even small concentrations of impurities could lower the total ion current and hence the lower fusion rate. Increasing the fuels' flow rate flushes the system and helps reduce the concentration of the ions within the chamber at any given time. The fuel ratio (D_2/^{3}He) affects the performance of the D-^{3}He reactions and the optimum ratio was found to be ~0.5.

Experiments with a single loop cathode grid are reported in Chapter 11. Since energy drain occurs in an IEC device through electrons, various electron sources are identified and studied in this chapter. Thorson's equation for the ion recirculation current in an IEC device was

updated. Single loop grid experiments were then performed, and these experiments revealed the importance of secondary emission and their role in ion recirculation current. These single loop grids generated a line (~cylindrical) source inside a spherical outer grid.

Furthermore, in Chapter 12, the fusion contributions of the single loop grid are characterized and appropriate equations for the fusion reactivity are derived. Sequential grid manufacturing experiments showed that the fusion reactivity of the IEC grid is not very sensitive to the cathode grid's symmetry. The single loop was replaced by another single loop with cross-wires that intercepted the recirculating ions. Experiments were performed at every stage of grid construction after adding more loops to the earlier grid (sequentially 1, 1, 2, 2, 2, and 2 loops in various orientations were added to the single loop) thus constructing the whole grid with 11 loops. This experiment revealed the structure of the converged core with the variation of the grids' surface electric field and showed an improved fusion rate with increasing symmetry of the grid surface's electric fields up to 3 loop grid, however no significant improvements in neutron rate was observed with addition of more loops. The observation that the grid wires influence the fusion reactivity in the earlier sequential grid construction experiment led to the grid rotation experiments in Chapter 13. In this set of experiments, rotating the high voltage stalk in small increments of angle rotated the grid about its axis. The results of this experiment revealed that the volume source reactions occur mostly in the microchannels that form in the open spaces between the wires of a cathode grid in an IEC device. Based on the results from the grid rotation experiment a new calibration factor was derived. It was observed that all the volume source reactions occur in the microchannels that form in the open.

Finally, Chapter 14 summarizes all the experiments while the Chapter 15 lists the major contributions of the present dissertation work.

Chapter15: Overall Conclusions

The following are the major accomplishments of the present dissertation work:

1. The first simultaneous measurement of DD and D-^{3}He protons was accomplished during the present dissertation work confirming that D-^{3}He reactions indeed occurs in an IEC device.

2. The steady-state fusion of D-^{3}He fuels was studied at rates 4 – 5 orders of magnitude higher than previously accomplished (900 protons/s) at University of Wisconsin, Madison.

3. Proton energy spectrum from both DD and D-^{3}He reactions were characterized and theoretically explained.

4. Three new diagnostics were newly devised and used to understand the physics behind the operation of the device.

    a. Doppler shift proton energy spectroscopy for average ion energy measurement.

    b. Eclipse disc diagnostic used in characterizing the various fusion regimes (volume, embedded & converged core) within an IEC device at 2 mtorr chamber pressure.

    c. Chordwire diagnostic for characterizing the various electron emission contributions and providing a 2D map of the ion flux into the central cathode.

5. Thorson's equation for ion recirculation in an IEC device has been improved.

6. More efficient materials have been selected (W-25%Re & pure Re) for the IEC grid increasing the life of the cathode grid by several orders of magnitude. These new

materials mitigated the contamination of the stalk due to sputtering and paved the way for higher voltage operation.

7. The fusion rate (proton to neutron rate ratio) from the IEC device was used to study the changes in ion current due to increased electron emission (secondary electron, photo, thermionic and field electron emissions).

8. The volume fusion source in an IEC device has been found to be due to non-uniform ion fluxes, contrary to earlier beliefs. Microchannels formation was established at relatively low pressures (2 mtorr) and was used to calibrate the fusion rate contribution of the volume source. A new formula was derived for the purpose.

Appendix A: Volume eclipsed by the various discs

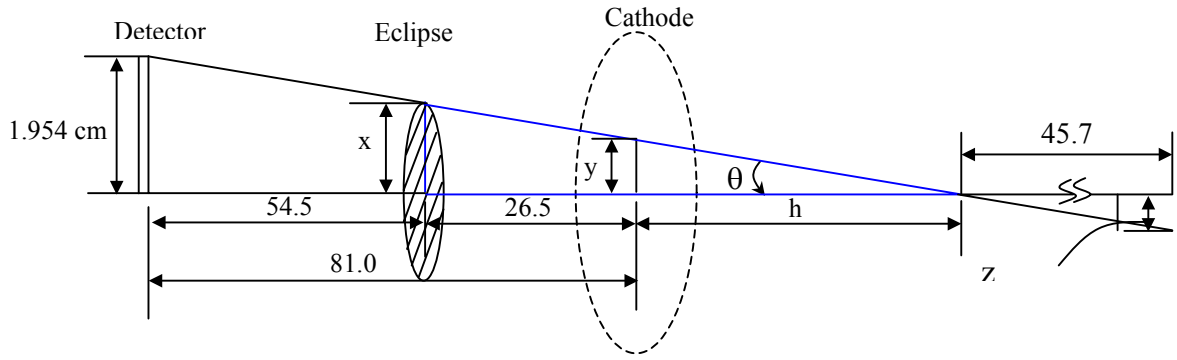

Figure A.1 Geometry of the small eclipse disc (x = 1.1 cm diameter). Since the geometry is symmetric only half the dimensions are shown for the detector, disc and grid radii.

Since the dimension of the small eclipse disc is smaller than the radius of the detector, we may simply approximate the volume eclipsed by it as a cylinder of diameter equal to the diameter of the eclipse disc. The error involved in such calculation would be small. For this approximation the volume eclipsed by the eclipse disc = $\pi r^2 l = \pi(0.55)^2 \cdot (26.5+45.7) = 68.6\ cm^3$

In light of the converged core scenario, this argument is valid when the contributions of the volume source on either side of the converged core remain constant. Hence for all relative measurements this approximation will not introduce much error in the data. Such measurements are reported in chapter (5.0). Accurate volume calculations are given below.

Small disc

When a small disc is used it is smaller in size than the detector and hence it would mask only a cone (shown in blue), figure A.1.

$$\tan\theta = \frac{y}{h} = \frac{x}{26.5+h} = \frac{1.95}{81+h} = \frac{z}{45.7} \qquad \text{(a.1)}$$

substituting x = 0.55 cm for the (1.1 cm diameter small disc) in the above eqn. (a.1)

$$\frac{0.55}{26.5+h}=\frac{1.95}{81+h}$$

we get h = -5.15 cm (a.2)

A negative value denotes that the crossover point is before 26.5 cm from the eclipse disc. Substituting in eqn.(a.1) and solving for y , z and θ we get

y = 0.08 cm, z = 1.458 cm and θ ~ 0.45°

The volume eclipsed by the small disc $V_s = \frac{\pi}{3}[r^2 l + z^2(45.7)]$ = 101.78 cm^3

where l = 26.5 - h = 21.35 cm, z = 1.458 cm and r = 0.55 cm

$\therefore$ V_s = 119.96 cm^3 (a.3)

When a small eclipse disc is used the contributions of the volume source to the overall counts blocked by the disc are not all that important because the bulk of the counts blocked by the disc come from the converged core reactions.

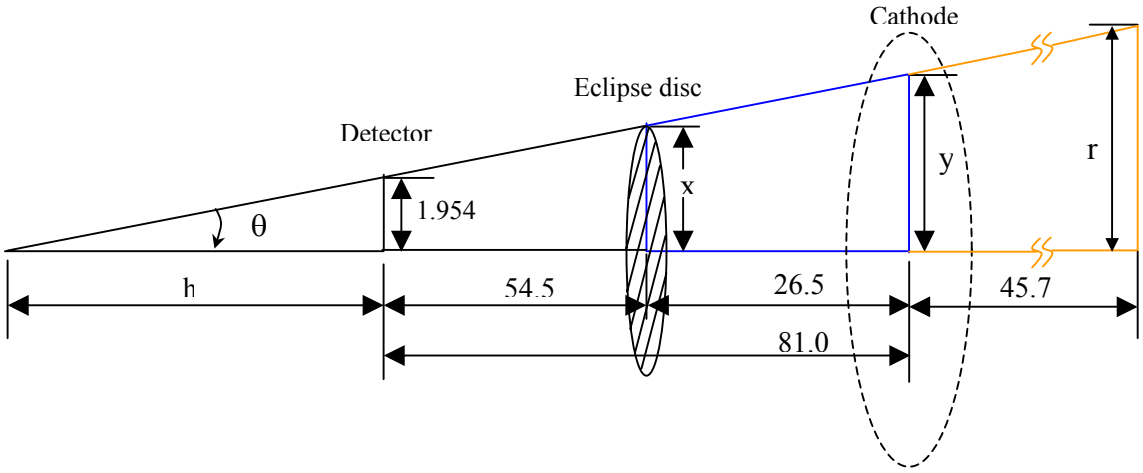

Figure A.2 Geometry of the intermediate (x = 2.4 cm diameter) and large eclipse (x = 4.0 cm diameter) discs.

For the intermediate and the large discs, the geometry in figure A.2 applies. In this case the size of the disc is larger than the detector and hence the volume eclipsed by these discs are diverging cones.

$$\tan\theta=\frac{1.954}{h}=\frac{x}{54.5+h}=\frac{y}{81+h}=\frac{r}{h+126.7} \quad \text{(a.4)}$$

Intermediate disc

Substituting x = 1.2 cm (for the intermediate disc of 2.4 cm diameter) in the eqn.(2)

$\frac{1.954}{h} = \frac{1.2}{54.5 + h}$ we get h = 141.3 cm inserting this back into eqn. (2) and solving for y and r we get y = 3.074 cm and r = 3.706 cm.

The volume of the cone blocked by the intermediate disc is given by:

$$V_I = \frac{1}{3}\pi\left[r^2 l - x^2(h + 54.5)\right] \approx 3559.3 \text{ cm}^3 \qquad \text{(a.5)}$$

where l = 268 cm and the small volume correction at the base of the cone due to the curvature of the cylindrical chamber is neglected.

Large disc

Similarly substituting x = 2.0 cm for the large disc in eqn. (2) we obtain h ≈ 2315 cm, y = 2.022 cm and r = 2.061 cm

The volume blocked by the large disc is given by: $V_L = \frac{1}{3}\pi\left[r^2 l - x^2(h + 54.5)\right] \approx 8733.5 \text{ cm}^3$

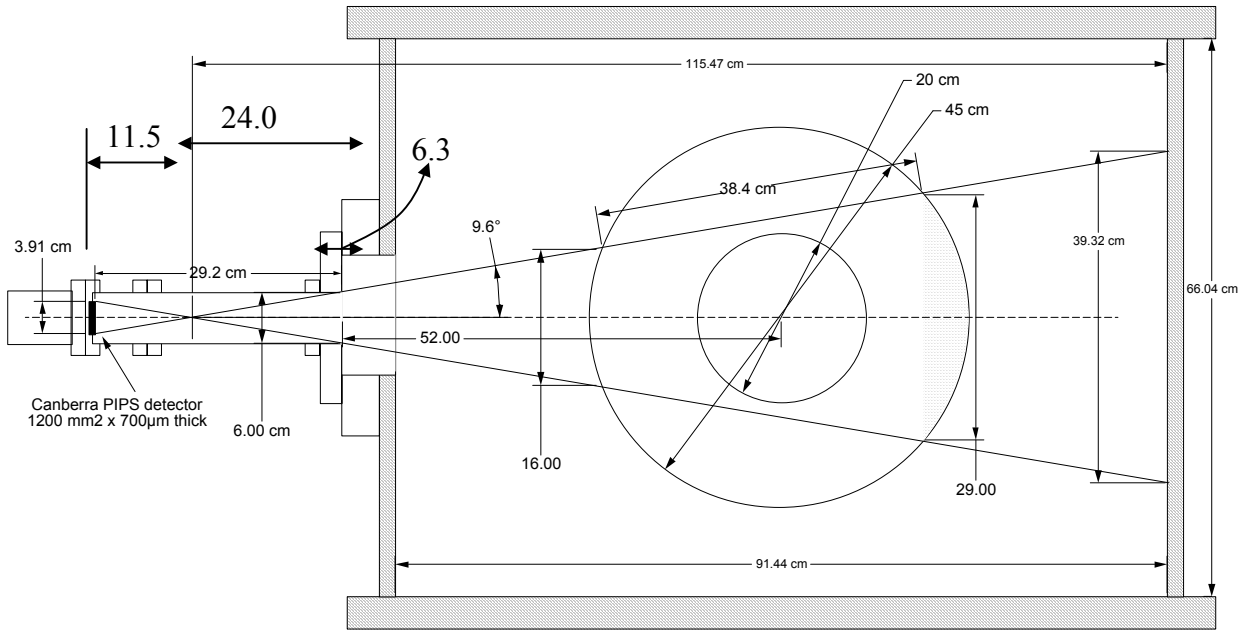

Figure A.3 The volume fractions blocked by each of the discs

The volume fraction (see figure A.3) masked by a disc = $\frac{V_{tot} - V_{disc}}{V_{tot}}$

where V_{tot} is the total volume visible to the detector.

From eqn. a.4 we have

$$\tan\theta = \frac{1.954}{29.2 - x} = \frac{3}{x} = \frac{y}{52 + 45.72 - x} \Rightarrow \theta = 9.63^{o} \qquad \text{(a.6)}$$

solving the above equation we get x = 17.685 cm and y = 19.56 cm.

Total volume seen by the detector

$$V_{tot} = \frac{1}{3}\pi\left[(19.56)^2 \cdot (x + 52 + 45.72) + (1.954)^2 \cdot (29.2 - x)\right] = 46283.17 \text{ cm}^3 \qquad \text{(a.7)}$$

$\therefore$ The fraction of the total volume seen by the detector that each of the discs eclipses is given by

V_{small} = 119.96/46283.17 = 0.26% (a.9)

$V_{intermediate}$ = 3559.3/46283.17 = 7.71% (a.10)

V_{Large} = 8733.5/46283.17 = 18.86 % (a.11)

Appendix B: Natural gas cooling of surfaces

Particle Distributions - Maxwellian (3D)

$$f = n\left(\frac{\alpha}{\pi}\right)^{3/2} e^{-\alpha v^2} \quad \text{where } \alpha = \frac{m}{2kT} \tag{b.1}$$

Particle flux in 1D is given by:

$$\Gamma = \int_{N_x>0} f \cdot v_x \cdot d^3v \tag{b.2}$$

$$\Gamma = \int_0^{\pi/2} \int_{N>0} fv\cos(\theta) \cdot 2\pi \cdot v^2 \sin\theta d\theta dv \tag{b.3}$$

$$\Gamma = 2\pi \int_0^{\infty} n\left(\frac{\alpha}{\pi}\right)^{3/2} v^3 e^{-\alpha v^2} dv \int_0^{\pi/2} \sin\theta\cos\theta d\theta \tag{b.4}$$

$$\Gamma = 2\pi n\left(\frac{\alpha}{\pi}\right)^{3/2} \frac{1}{2\alpha^2} \cdot \frac{\sin^2\theta}{2}\bigg|_0^{\pi/2} = \frac{n}{2}\frac{1}{\sqrt{\pi\alpha}} = \frac{n}{2\sqrt{\pi}}\left(\frac{2kT}{m}\right)^{1/2} = n\sqrt{\frac{kT}{2\pi m}} \tag{b.5}$$

Energy Flux in 1D

$$Q = \int_{N_x>0} \frac{1}{2} m v^2 v_x f d^3v \tag{b.6}$$

where $v_x = v\cos\theta$ and $dv = 2\pi v^2 \sin\theta d\theta d\phi$

$$Q = \frac{mn}{2}\left(\frac{\alpha}{\pi}\right)^{3/2} \int_0^\infty v^5 e^{-\alpha v^2} dv \int_0^{\pi/2} 2\pi \sin\theta \cos\theta d\theta \tag{b.7}$$

$$= \frac{2\pi nm}{2}\left(\frac{\alpha}{\pi}\right)^{3/2} \frac{2}{2\alpha^3}\left(\frac{1}{2}\right) = \frac{n}{\sqrt{\pi}} \frac{1}{\alpha^{3/2}} = n\sqrt{\frac{kT}{2\pi m}}(2kT) \tag{b.8}$$

$$\therefore Q = 2kT\,\Gamma \tag{b.9}$$

Consider a small object surrounded by a neutral gas of density ‘n’. By small, we mean that the mean free path ‘λ’, of the gas molecules is much greater than the dimension of the object. In this case the characteristic rate of gas molecules arriving at the surface is

$$\dot{N} = A \cdot \Gamma \tag{b.10}$$

and the rate of energy arriving is

$$\dot{E} = A \cdot Q = 2A \cdot \Gamma \cdot h \cdot T_g \tag{b.11}$$

We assume the surface saturates with gas. Once this occurs, for every molecule hitting the surface, another molecule leaves. Hence molecules hit the surface with an energy distribution characteristic of a Maxwellian at the gas temperature.

We assume the typical molecules stick on the surface long enough to thermalize with the object material. When dislodged they leave with an energy distribution characteristic of the surface temperature. Thus

$$\dot{E}_{out} = A \cdot \Gamma \cdot 2k \cdot T_s \tag{b.12}$$

$$\dot{E}_{in} = A \cdot n_g \cdot \sqrt{\frac{k \cdot T_g}{2\pi m}}\left(2h \cdot T_g\right) \tag{b.13}$$

$$\Gamma_{out} = n'\sqrt{\frac{kT_s}{2\pi m}} = n_g\sqrt{\frac{kT_g}{2\pi m}} \tag{b.14}$$

$$\dot{E}_{out} = A \cdot n' \cdot 2h \cdot T_s \sqrt{\frac{kT_s}{2\pi m}} = A \cdot n_g \sqrt{\frac{kT_g}{2\pi m}} \cdot 2hT_s \quad \text{(b.15)}$$

$$\dot{E}_{net} = An_g \sqrt{\frac{kT_g}{2\pi m}} [2k \cdot T_s - 2k \cdot T_g] \quad \text{where } k = 1.38 \times 10^{-23} \, J/K \quad \text{(b.16)}$$

For D_2 molecules

$M = 4(1.67\text{x } 10^{-27})$ kg (b.17)

$p = nkT_g = 2.0 mTorr$ (b.18)

where p = 0.266 Pascal = n_g (1.38x10^{-23}x300) and n_g = 6.4 x 10^{19} molecules/cm^3

$$P_g = \frac{\dot{E}}{A} = 6.4 \times 10^{19} \sqrt{\frac{1.38 \times 10^{-23} \times 300}{2\pi \cdot 4 \cdot 1.67 \times 10^{-29}}} \times 2 \times 1.38 \times 10^{-23} \cdot [T_s - T_g] \quad \text{(b.19)}$$
$$= 0.554 \cdot [T_s - T_g]$$

Radiation

$$\sigma = 5.67 \times 10^{-8} \frac{W}{m^2 K^4} \quad \text{(b.20)}$$

$$P_{rad} = e\sigma A T^4 \quad \text{(b.21)}$$

For Tungsten

e = 0.23 at 1500^{o}C
e = 0.28 at 2000^{o}C

$$\frac{P_g}{P_{rad}} = \frac{0.554 \times [T_s - T_g]}{0.28 \times 5.67 \times 10^{-8} \times T_s^4} = 3.5 \times 10^7 \left(\frac{T_s - T_g}{T_s^4} \right) \quad \text{(b.22)}$$

Table B.1 Power radiated vs. convection power (by gas) at low pressures (~2 mtorr) at various temperatures.[1]

T_s (^{o}K)	P_{gas} (W/m^2)	P_{rad} (W/m^2)
1000	388	1.3x10^4
1500	665	6.6x10^4
2000	941	7.59x10^5

B.1 References

[1] Gil Emmert, Private communications, University of Wisconsin, Madison (2000).

Appendix C: Detector's surface area visible to the protons born inside the IEC device

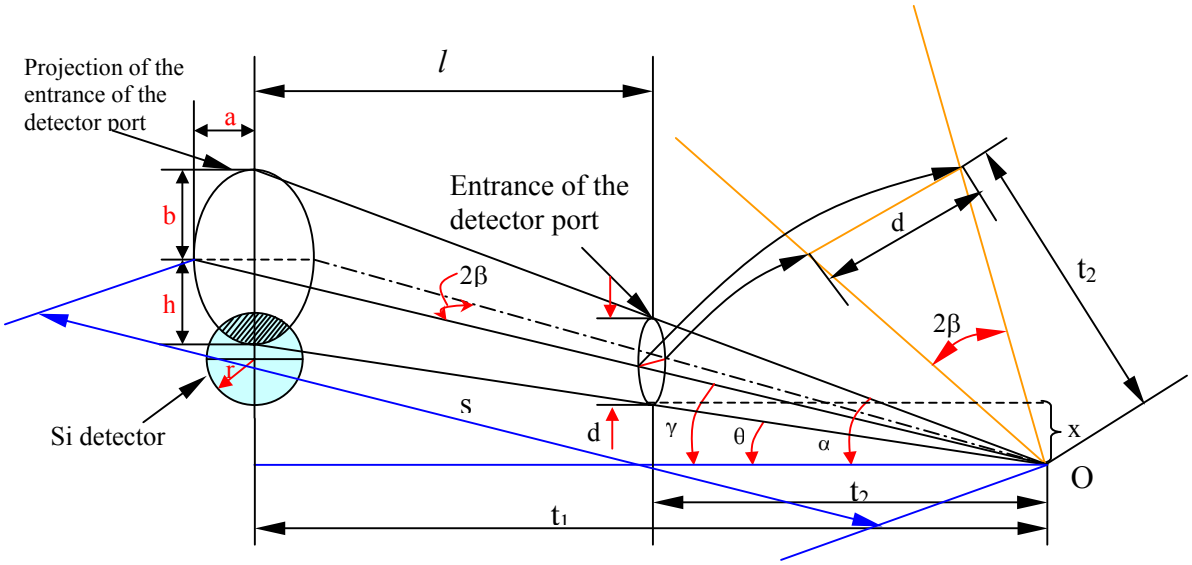

Figure c.1 Illustration of various parameters used in the equations (c.12) to (c.17). The intersection of the ellipse and circle is the shaded area visible to the proton born at the point O

Equation of a circle with center at (0,0):

$$x^2 + y^2 = r^2 \qquad \text{(c.1)}$$

For a point moving in the y direction, the projection of the entrance of the detector port (circle) on to the detector is an ellipse as shown in the figure c.1.

An ellipse with center at (0,h), is the graph of

$$\frac{x^2}{a^2} + \frac{(y-h)^2}{b^2} = 1 \text{ with a > b > 0} \qquad \text{(c.2)}$$

The length of the major axis is 2a, and the length of the minor axis is 2b. The two foci (foci is the plural of focus) are at (± c, 0), where $c^2 = a^2 - b^2$. It is assumed that 'b' remains constant for all the protons born in the same plane.

$\theta = \tan^{-1}\left[{}^{(2r+d)}/_{2l}\right]$ (c.3)

$\alpha = \tan^{-1}\left[{}^{(x+d)}/_{t_2}\right]$ (c.4)

$\beta = \tan^{-1}({}^{d}/_{2t_2}) = 1.88^{o}$ (c.5)

$\gamma = \tan^{-1}\left[{}^{(2x+d)}/_{t_2}\right] = 11.45^{o}$ (c.6)

$h = l\tan\alpha + r$ (c.7)

$d = l\tan\theta$ (c.8)

Solving the two equation given above we get

$$h = \left(\frac{d\tan\alpha}{\tan\theta}\right) + r \qquad \text{(c.9)}$$

$a = t_1 \cdot \tan\alpha \cdot \tan\beta$ (c.10)

$b = t_1 (\tan\alpha - \tan\theta)$ (c.11)

where r = 1.955 cm, d = 6 cm, t_2 = 91.4 cm, and t_1 = 126 cm (changes with proton birth point 'O').

We now derive a general equation for the area of intersection of the projection of the entrance (an ellipse) and the Si detector (a circle).

The following maple program evaluates the point of intersection of the circle and the ellipse. The origin is at the center of the circle.

```
> restart;
> ((y^2-r^2)/a^2)+((y-h)^2/b^2)-1;
```

$$\frac{y^2-r^2}{a^2}+\frac{(y-h)^2}{b^2}-1$$

```
> solve(((y^2-r^2)/a^2)+((y-h)^2/b^2)-1,y);
```

$$\left.\begin{array}{c} \dfrac{2\,a^2\,h+2\sqrt{a^2\,b^2\,r^2+b^2\,a^4-b^2\,a^2\,h^2+b^4\,r^2+b^4\,a^2}}{2\,(a^2+b^2)}, \\ \dfrac{2\,a^2\,h-2\sqrt{a^2\,b^2\,r^2+b^2\,a^4-b^2\,a^2\,h^2+b^4\,r^2+b^4\,a^2}}{2\,(a^2+b^2)} \end{array}\right\} \quad \text{(c.12)}$$

The equation of the ellipse could be written in the following form (as a function of x):

$$y_1 = h \pm b\sqrt{1-\frac{x^2}{a^2}} \quad \text{(c.13)}$$

The equation of the circle may be written as follows:

$$y_2 = \sqrt{r^2-x^2} \quad \text{(c.14)}$$

Hence the values of y at the points of intersection (of the two curves, circle and ellipse) are:

$$y = \frac{a^2 h \pm \sqrt{D}}{(a^2+b^2)} \quad \text{(c.15)}$$

where $D = a^2b^2(r^2 + a^2 - h^2) + b^4(r^2 + a^2)$ (c.16)

The values of the x coordinates are obtained by substituting the y from eqn.(c.1) into

$$x = \sqrt{r^2 - y^2} \qquad \text{(c.17)}$$

where the parameters in the eqn.(c.13) are illustrated in figure c.1 and defined in eqns.(c.3) - (c.11).

The shaded area (visible to the proton born at the point 'O') in figure c.1 is given by the following equation:

$$\text{A} = 2\int_0^{x_1} (y_2 - y_1)dx \qquad \text{(c.18)}$$

where y_2 is obtained from equation (c.12), the equation of an ellipse and y_1 is obtained from equation (c.16), the equation of a circle and x1 is obtained from eqns. c.15 – c.17.

VITA

S. Krupakar Murali was born on 10th September 1975 in New Delhi, India, the son of P. Subramanian and T. A. Bhagyam. He was married to Kasthuri Priya M. on 13th June 2002. After graduating from Durga Bhavani High School, Hyderabad, India he attended the intermediate college in Loyola Academy, Hyderabad. He then joined the K. L. College of Engineering, affiliated to Nagarjuna University, Guntur, India in 1992 and received his Bachelor of technology in Electronics and Communication Engineering in June 1996. Following which he joined North Carolina State University (NCSU), Raleigh, USA in Jan. 1997 and received his first M.S. degree in Nuclear Engineering in Dec. 1998. During this time he was inducted into Alpha Nu Sigma honorary society and was funded 100 % of his education. He also received the Leadership achievement award from NCSU. He then moved to University of Wisconsin, Madison in Dec. 1998 and received his second M.S. degree in Nuclear Engineering and Engineering Physics in Dec. 2002. He also received a third master's degree (M.A.) in (Plasma) Physics in Dec. 2003. He received the best presentation award from American Nuclear Society, University of California, Berkeley in 2002. He had an opportunity to work at Los Alamos National Lab, as a summer intern and at the end of the 3 month period he received the Student Distinguished Performance Award, 2003. Finally he received his PhD in Plasma Physics from University of Wisconsin, Madison in August 2004. During the entire period of education he has co-authored many articles related to his research. Hopefully he will now stop attending graduate school !?